ANNUAL PERFORMANCE REPORT

Title: Use of Suction Piles for Mooring of Mobile Offshore Bases (ONR Grant No. N00014-97-1-0887)

Period: June 1, 1997 – May 31, 1998

Principal Investigator:

Sangchul Bang
Department of Civil and Environmental Engineering
South Dakota School of Mines and Technology
Rapid City, SD 57701

Date: June 11, 1998

Described below are the research activities completed during the first year of the study, from June 1, 1997 to May 31, 1998.

1. Literature Review

The literature study on suction piles has been completed and the final report has been submitted to the Naval Facilities Engineering Service Center (NFESC) after an extensive review. A copy of the task completion report on literature review is included in this report.

2. Analytical Performance Study of Suction Piles

The suction pile performance study using linear elastic soil material properties has been completed. Results of the analysis have been reported as a quarterly progress report to NFESC in March 1998 and a copy is included in this report. Appendix - A of the quarterly progress report describes the results of the analytical performance study of suction piles.

3. Analysis and Design Method of Suction Piles

An analytical solution previously developed by the principal investigator for the analysis of laterally loaded piles and subsequently modified for suction piles has been used to study the behaviors of suction piles under lateral loads and to identify the effect of the location of mooring line attachment under various conditions. Six different soil types so far have been investigated. They include; sands with friction angles of 30, 35 and 40 degrees and clays with average cohesions along the entire length of the pile of 100, 250, and 500 psf. The pile diameters studied vary from 10 ft. to 50 ft. with the length to diameter ratio varying from 1 to 4.

From the results of the analysis with sands, it was found that the ratio between the depth to the mooring line attachment point and the pile length (H"/L) that corresponded to the ultimate pile lateral resistance (P_{ult}) increased with the pile length to diameter ratio (L/D) but with a decreasing rate. The H"/L ratio at P_{ult} also varied only with the ratio L/D and remained almost independent of the soil friction angle and the pile diameter. The ratio between the depth to the pile rotation point and the pile length at P_{ult} was about 0.45 to 0.6 in all cases.

For clay soils with relatively low cohesion values, the H"/L ratio decreased as the L/D ratio increased with a faster rate for larger pile diameters. With high cohesion, the H"/L ratio increased as the L/D ratio increased with a faster rate for smaller diameter piles. The ratio between the depth to the pile rotation point and the pile length at P_{ult} generally increased as the ratio L/D increased, resulting in 0.94 – 0.965 in almost all

cases.

4. Model Testing

A model testing apparatus has been built and used to test four series of suction piles in sand. The model box was constructed from a heavy-duty plastic pipe with dimensions of 6 ft. in height and 2 ft. in diameter. It can contain approximately 1,500 lbs of fine sand inside. For easy mobility, wheels were placed underneath the pipe. The model box has a perforated bottom plate with a space underneath for proper water collection and drainage.

A 5 ft. high model suction pile was constructed with a 4.5 inch transparent plastic tube. It has a relatively large aspect ratio, i.e., the length to diameter ratio, to avoid any possible soil boiling problem associated with short piles. Additional components of the model test apparatus include; a pile guide for straight pile travel, scaffolding, a series of water collection reservoirs between the pile and the vacuum pump, a large displacement measurement system to measure the pile penetration, pore pressure transducers, and data acquisition system.

Each suction pile model test series consisted of four to five almost identical tests (except a slight variation in initial pile penetration depth) in order to minimize any potential error. The main variables in these series of tests were the suction pile initial penetration depth and the amount of surcharge applied at the top of the pile as shown below.

Series	Initial Pile Penetration (ft.)	Surcharge (lbs)
1	1.0	48.8
2	1.0	61.0
3	1.0	73.2
4	3.0	73.2

Please note that the surcharge of 48.8 lbs is an additional weight on top of the plastic model pile to simulate the equivalent weight of the steel pile with equal dimensions. Appendix – B of the March 1998 quarterly report to NFESC includes the complete measurements of the first three series model tests. The measurements include the pile penetration history as a function of the applied suction pressure inside the pile.

An analytical solution method has also been developed to simulate the suction pile installation procedure. It describes and establishes the relationship between the

suction pressure inside the pile and the pile penetration depth under given material and geometric conditions.

Appendix – C of the March 1998 quarterly report includes the calibration of the mobilized soil friction angle parameter, alpha, from the results of series 1 through 3 model tests. The parameter (alpha) describes the average mobilized effective soil friction angle at the tip and inside the pile where the soil friction values may be lower than that of the outside surface of the pile due to the water flow caused by the suction pressure application. In Appendix – C, the alpha values are plotted as a function of the total head gradient between the tip of the pile and the inside soil surface within the pile. The results indicate that the values of alpha mostly lie within a band between 0.75 and 1.10 with a slight decrease in its value as the total head gradient increases. These are in agreement with generally expected soil behaviors influenced by the flow of water.

5. Verification of Cable Mooring Line Centrifuge Tests

The results of the centrifuge model tests on mooring cables have been visited again to identify the effect of the chasing wires and to provide necessary validation of the analytical solution. Four chasing wires were connected to the cable mooring line during the tests for the purpose of identifying the geometries of the mooring cable. Appendix – D of the March 1998 quarterly report provides the details of the centrifuge test validation procedures and the results.

USE OF SUCTION PILES FOR MOORING OF MOBILE OFFSHORE BASES

(ONR Grant No. N00014-97-1-0887)

Task 1 Completion Report: Literature Review

(July 1 – Dec. 31, 1997)

Submitted to

Naval Facilities Engineering Service Center
Port Hueneme, CA

by

Sangchul Bang and Graham Smith

Department of Civil and Environmental Engineering
South Dakota School of Mines and Technology
Rapid City, SD 57701

May, 1998

Table of Contents

Introduction

The following is a summary of literature studies on large cylindrical caissons driven into the seabed by hydrostatic underpressure. These caissons are referred to as "suction piles." Suction piles have been in existence since at least the 1950's. The genesis of suction piles and their study will be covered in a historical review of research on this system This report also includes discussions of other relevant parameters relating to the installation and retention of suction piles. Soil stresses relevant to the installation and use of suction piles will also be examined. Installation procedures, including a discussion of critical suction pressures for installation in clay and sand will also be surveyed.

In the area of suction pile retention after emplacement, tensile failure in the soil beneath the pile, reverse end bearing capacity of the system, pile wall friction, pore water pressure, static and cyclic loading conditions, lateral loading of the pile, and tether attachment point will all be considered. These subjects all relate to the installation and performance of suction piles for use in deep sea mooring points for floating structures such as mobile offshore bases.

Description of Suction Piles

Suction piles are usually composed of a single or multiple cylinders of large diameter and relatively shallow penetration depths (a length to diameter ratio of 2:1 is common). Fig. 1 shows a schematic cross-section of a typical suction pile. "Suction" is a reference to both the negative pressure created within the pile during the installation process, and the passive reduction of pressure mobilized during uplift (Morrison and Clukey, 1994).

During the installation process the pressure within the pile is reduced by pumping out water. The vacuum that is created overcomes the resistance of the soil, allowing the pile to be driven, hydrostatically, by the pressure of the water column above it (Morrison and Clukey,

1994). Fig. 2 shows one method of installation.

After pile emplacement, several factors come into play to maintain its position in the seabed. During normal operations the weight of the pile and ballast, the weight of the soil plug inside the pile, and the skin friction between the pile and the surrounding soil all act to keep the pile in place. During severe situations such as storms passive suction is mobilized. The passive suction develops at the top of the pile, and is translated down through the soil plug to the bottom of the unit. At the base of the pile, passive suction is manifested as reverse end bearing capacity .

Some of the more important advantages of suction pile anchoring systems over traditionally driven piles are the following: 1) ease of installation; 2) reliance on pumps rather than underwater pile drivers for installation; 3) reduced installation time; 4) significant cost savings; and 5) final penetration depth is substantially shallower making installation easier and quicker (Morrison and Clukey, 1994).

Historical Overview

Marine anchors have been used for many centuries. Until the last several decades, dead weight anchors, drag anchors, and permanent anchors were commonly used (Brown and Nacci, 1971). More recently, the concept of suction emplaced anchors has emerged. Initial studies on the subject were carried out several decades ago using suction anchors; anchor structures where active suction is maintained throughout the use of the unit. Recent interest has, however, encouraged more intense research on suction emplacement of piles, where the active suction is terminated after installation. The following is a listing of many of the advances seen in the technology of suction emplaced anchors and piles.

The first use of suction anchoring i.e., an anchor emplaced using pumps to create a vacuum inside the structure, was by Mackereth (1958) for holding down a piston corer during lake bed sampling operations. Later model testing was performed by Goodman et al. (1961) to

evaluate the pullout resistance of an inverted cup-type anchor subjected to different vacuum pressures in various moist soils. This group (Goodman et al., 1961) confirmed that vacuum anchorage in moist soil was feasible.

A decade later, Brown and Nacci (1971) conducted model tests on suction anchoring systems. The anchoring system was described as an inverted can with five basic elements: an anchor housing, a penetration skirt, a pump, a load transmission element, and a fixed porous stone mounted inside the skirt to prevent liquefaction of the sand.

The researchers were able to obtain "excellent" anchorages on clays and silts. However, anchorage on unsaturated sand was reportedly poor, and liquefaction was encountered when saturated sands were tested. Baird and Nacci (1972) continued their studies utilizing triaxial tests to model failure conditions on simulated clay and silt. Their model was used to investigate shear strength parameters useful for the prediction of ultimate pullout forces on a hydrostatic anchor.

Schofield (1974) proposed a slightly different anchor type from the one being tested by Baird and Nacci. Schofield's (1974) model consisted of an anchor structure built of interconnecting beams, and covered by an extended impermeable sheet for increasing the anchor break-out resistance. Most subsequent research has, however, involved steel or concrete piles of the type tested by Baird and Nacci (1972).

By the mid 1970's, the offshore oil industry was beginning to proliferate, as was the technology involved in placing large structures in marine environments. Research conducted on marine sit-on-bottom structures was undertaken by Clausen et al. (1975). A great deal was learned about the bearing capacity of large sit-on-bottom type structures by observation of the Ekofisk tank; a concrete gravity structure placed on the bed of the North Sea. With a submerged weight of 190,000 metric tons, the tank was reported to exert sizable forces on the sea bottom. Along with the static forces generated on the seabed by this large structure, wave action compounded the forces translated to the seabed. The 100-year wave used for design purposes had been estimated to be 24 m high, and was predicted to exert a horizontal force at the seafloor of 78,600 tons, and a moment of 2,800,000 ton-meters. These large forces were accompanied by

another problem envisioned during the design process; the possibility of sand liquefaction, and loss of strength when subjected to cyclical loads.

The design was to be severely tested within a year of emplacement. During a storm, the tank was subjected to waves up to 90% of the 100-year design wave. Measurements during that major storm period showed that excess pore-water-pressures developed, and that their dissipation was accompanied by settlement of the tank (Clausen et al., 1975). These observations were to play a role in later studies of the bearing capacity of gravity based structures implementing suction pile foundations.

Along with sit-on-bottom type fixtures, interest in suction emplaced marine structures continued. In 1976, Helfrich et al. (1976) examined the failure mode of a suction anchor tested in a medium to fine grained sand closely approximating that of Atlantic continental shelf materials. The purpose of this study was to delineate pullout characteristics and failure modes of suction anchors in sand. The degree of dependence of anchor performance on the flow rate of water through the anchor chamber was also observed.

The experiments involved a pile model with the dimensions of 400 mm in diameter and 250 mm in depth. Using this model, the pullout force in submerged sand, and the weight of sand plug retained by the anchor were found to be linearly related to the suction pressure. Both the maximum pullout force, and the weight of sand pulled out were found to be directly related to the flow rate as well. Failure of the sand occurred in the vicinity of the cutting edge of the suction anchor. The mode of failure consisted of many small shear failures that appeared as a "horizontal bumpy surface".

Helfrich et al. (1976) felt that, based on the anchor length / diameter ratio used in their study, the size of suction anchors appropriate for the generation of large reaction forces could be scaled up to prototype size by extrapolation. As an example, a 200 kN reaction force in similar soils, using a factor of safety of two, would require a system of three anchors, each anchor being nearly two meters in diameter and operated at a flow rate of about 6.4 $\mu m^3/s$.

Examination of the suction anchor concept continued into the late 1970's. In 1978,

Wilson and Sahota reported the result of experiments with embedded cup anchors in sand. Difficulties were encountered when trying to get the anchor models to embed. To allow for anchor self-burial, the addition of water jets to their original model was necessary. Sand fluidization was induced by a ring of downward-acting jets around the edge of the anchor skirt.

Results of the study indicated that the forces required for pull-out involved normal and shear stresses applied to the outer surfaces of the anchor by the soil, coupled with the force required to cause failure of the soil below the anchor. Wilson and Sahota recognized this force as a new parameter-relating pullout to the reduction of pore-pressure in the surrounding soil.

In other research reported, Wang et al. (1978) developed a general breakout capacity equation, providing a prediction method for the holding capacity of an anchor. This method used anchor geometry, suction pressure intensity, and soil properties to define breakout capacity.

Throughout the late 1970's and early 1980's, Wilson and Sahota (1977, 1978, 1980), investigated inverted cup-type, and hemispherical-type suction anchors equipped with jets for embedment in cohesionless soils. These authors noted that scaling the results from tests on suction anchors would require geometric similarity of the model and prototype anchors. A similarity would also be required in the position of the anchor with respect to the top, bottom and lateral boundaries of the soil bed. The buoyant weight of the model anchors tested was found to be small in comparison with the pullout forces, so it was felt that scaling of this parameter could be ignored.

Data comparisons between model and prototype anchors were used to make a preliminary investigation of an anchor system with a 1,000 kN vertical pullout force capacity in granular soil (Wilson and Sahota, 1980). With four interconnected anchor footings of one meter in diameter, buried in a four-meter deep bed of granular soil, vertical and horizontal force reactions in excess of 1,000 kN were estimated to be attainable.

Although work had been reported on suction anchoring systems throughout the 1970's, initial literature dealing with suction piles, i.e. large diameter, short piles closed at the top end, which are installed, but not maintained in place using underpressure, first appeared in 1980. In a

study by Hogervorst it was concluded that the features of a pile installed by suction would be a promising solution for mooring marine structures.

The proposed method for installing anchor piles by means of a suction process was investigated extensively by Hogervorst. A systematic research program was implemented to evaluate the potential of suction piles for both the suction emplacement process and the load carrying capacities. Based on soil mechanics considerations, and the findings of their experiments, it was felt that a reasonably accurate prediction of holding capacities could be achieved. Furthermore, Hogervorst conducted tests on large diameter suction piles of 3.8-m diameter, and varying lengths of between five meters and ten meters. Holding capacities of up to two MN were observed in these studies (Hogervorst, 1980). Burgess et al. (1981,1983), Senpere and Auvergne (1982), and Tjelta and Guttormsen (1986) further explored the concept of a suction pile.

In 1981, Cuckson proposed that large suction piles should find a place in soils at 70-200 m water depth in situations requiring large uplift and lateral resistance.

By 1982, as reported by Sahota and Wilson (1982), the largest suction pile installed in the field was the Shell/S.B.M. suction pile. It was detailed by these authors that the weight of the anchor was sufficient to make the skirt tip penetrate the top soil layers, allowing water pressure within the cup to be reduced by pumping. This allowed the hydrostatic pressure difference to drive the suction pile into the sea bottom. The pump could then be removed after anchor installation with the pressure difference no longer being maintained.

Interest in suction piles and their interaction with the soil around them continued. In 1983, Andersen, reporting on soil-pile interaction, stated that laboratory tests showed that the undrained shear strength of Haga clay was dependent upon stress path, and whether the load was applied with constant rate of stress or constant rate of strain. Calculated and measured bearing capacities were found to agree well if the calculations were based on the stress-path-dependent shear strength from laboratory tests with constant rate of stress loading.

The interest in suction piles by the oil industry was on the rise in the mid 1980's. In 1986,

Tjelta et al. reported the results of testing for the placement of suction piles to be used for the foundation of the Gulfaks C gravity platform. Tests were conducted at sea utilizing two locations that were 300 m apart, both approximately 150 m from the center of the target area for placement of the platform. A system of two piles connected with a concrete panel was employed. Observation of tip resistance and wall friction on the concrete skirt panel, and verification of the predictions were major goals of the study.

Tjelta et al. (1986) made several geotechnical observations: The tip penetration resistance in clay was found to correspond to the undrained bearing capacity, but was not affected by suction. Observation in sand showed a significant influence on wall friction by skirt compartment water pressure. In sand there was a decrease of wall friction by suction and an increase by excess pressure, however, it was not believed to have been influenced in clay by suction. The variation of penetration rate had little influence on tip penetration resistance. The seafloor heave inside the suction piles was approximately 1 m; 60% of this was thought to be due to displaced soil, while 40% was due to suction.

Up to this point in time, the standard technology of offshore oil production involved large, gravity-based platforms. Due to the increasing water depths of newly discovered offshore oil fields, it was becoming increasingly evident to oil interests that a new technology for recovery platforms would soon be needed. The offspring of this need was the concept of the tension leg platform (TLP).

Initial interest in the idea of a TLP was seen in 1987 (Albert et al., 1987). The TLP proposed by Albert et al. consisted of a floating structure connected to the seabed by tethers. This type of platform would require an anchoring system to secure it to the seabed Due to the large expense of driving piles at extreme water depths, exploration of the idea of using suction piles for mooring points was instituted. Although the initial study by Albert et al. was purely theoretical, it was based on conventional principles of soil mechanics and soil behavior. From a detailed feasibility analysis of the suction pile system they concluded that the penetration under self-weight of all suction piles is great, especially with possible help of suction and ballast. And,

the weight of the soil inside the piles is large. It was also mentioned that the passive suction caused by the reduction in pore pressure within the pile, and the soil adhesion on the internal wall would ensure that the soil plug "moves" with the pile when subjected to tension.

Although the use of suction piles for anchoring TLP's was the emerging technology, they were already being used for the foundations of gravity-based platforms in the late 1980's. Further research was conducted by Andreasson et al. (1988) to study suction pile capacity for gravity platforms where cyclic loading was used to simulate wave loading of the platform. These researchers found that capacity under cyclic loading was on the order of 70% of the static capacity. The failure mode was identified to be a rotational type of failure only involving the soil directly underneath the base.

In a further effort to improve the design process, a procedure to calculate the foundation capacity of gravity platforms under combined static and cyclic loads was proposed by Andersen and Lauritzsen (1988). The procedure can be used both for undrained and partly drained cyclic loading conditions (Andersen and Lauritzsen, 1988).

To further the usefulness of the calculation procedure, the same principles used above were modified for the calculation of the pullout capacity for anchors (Andersen and Lauritzsen, 1988). Adaptations of the procedure to calculate the pullout capacity for anchors were to use extension shear strengths instead of compression shear strengths in the soil beneath the pile, and compression shear strengths instead of extension shear strengths in the soil outside the pile. This procedure did not, however, take into account the passive suction developed by the pile.

Investigation of soil interaction with suction piles for gravity platform foundations continued. Dyvik et al. (1989) conducted studies on static and cyclic behaviors for the simulation of offshore gravity platforms on soft clay in deep water. Five model tests were performed including one static, one static after cyclic, and three cyclic tests. Moment arm and cyclic loading history were varied from test to test. Based on the measured results, the following conclusions were drawn: The researchers found that there was a reduction in static load capacity after the cyclic loading program. It was also observed that the cyclic load capacity was smaller than the

static load capacity. Furthermore, the cyclic stiffness decreases with increasing cyclic load level the number of cycles at a given cyclic load level. The cyclic stiffness at small cyclic load levels was also found to be reduced by previous cycling at higher cyclic load levels. Cyclic rotation was stated to be the dominant displacement mode.

Finally, tests were conducted in reverse order, starting at maximum cyclic load, with decreasing cyclic loads. These studies achieved large displacements before all of the load history was completed. Dyvik et al. felt that this implied that a design storm composition with increasing cyclic loads, and the largest load last was not necessarily more critical.

In 1990, Tjelta et al. reported on the Gulfaks C concrete platform, which was successfully installed on a soft soil site in 1989. This was the first time the foundation concept of suction piles was implemented for a gravity base structure. The soil profile consisted of 45 meters of normally consolidated soft clay and loose clayey and silty sands with interbedded dense sand layers. The skirt piles were comprised of 16 circular concrete cells of diameter 28 m and wall thickness 0.4 meters. The platform foundation base area totaled 16,000 m^2 with 1,400 running meters of concrete skirts penetrated 22 meters into the seabed.

As the new technology of suction piles was emerging, it was necessary to further characterize their behavior. To this end, a centrifuge study was undertaken by Renzi et al. (1991). It was observed that when the soil was capable of resisting the working load, application of a cyclic load simulating tidal variations did not cause critical conditions in the soil. The observed pore-pressures and pile displacement was negligible.

Also in 1991, Fuglsang and Steensen-Bach reported on laboratory model tests and centrifuge tests utilizing piles of 65 mm and 80 mm in diameter, but with unreported pile depths. In all tests the pile was loaded vertically in a strain-controlled manner until breakout failure occurred. Two different loading rates were used to prove that no significant drainage took place in the rupture zone beneath the pile. In the case of both laboratory model tests and centrifuge tests, failure of the piles was gradual. The failure mechanism in the clay at the base of the pile was found to be similar to reversed-bearing capacity.

Further examinations of the use of suction piles for anchors for TLP's were conducted by Clukey (1991), Fines et al. (1991), Andersen et al (1992), and Hansteen and Hoeg (1994). 1991 was also the year when the first gravity foundation templates ever installed for a tension leg platform were placed on the seabed 310 m below water level at Norway's Snorre field (Cotril, 1991).

Sixteen tethers used to hold down the Snorre platform were to be tied in to four suction pile foundation templates (Cotril, 1991). Wall thickness of the concrete piles was 350 mm. The piles sank 4-6 m into the sea bed under self-weight, with further penetration to 12 m being achieved by pumping water out of the enclosed chambers beneath the skirt cells.

With the technology now proven feasible, the refinement of the design of suction piles as tension resisting foundations began. Research was now being carried out mostly in clays, as that was the soil type being encountered in the deep-sea oil fields. Skirted suction piles used for foundations of deep-sea oil platforms were reported by Aas and Andersen (1992), By and Skomedal (1992), and Christophersen (1992). Clukey et al. (1993), and Renzi et al. (1994) also carried out studies examining the suction pile skirt penetration using geo-centrifuge. Further investigation and testing of suction pile models subjected to static and cyclic loading in both clay and sand were carried out by Fuglsang et al. (1991), Steensen-Bach (1992), Dyvik et al. (1993), Iskander et al. (1993), Pavilicek (1993), Clukey et al. (1995), Morrison (1994), Jostad et al. (1997), and Rao (1997). Svano et al. (1992), Jones et al. (1994), and Keaveny et al. (1994) carried out studies of the axial capacity of suction piles.

In order to study the suction pile penetration behavior in clays, Hjortnaes-Pedersen and Bezuijen constructed miniature prototype skirt piles with a scaled length of 36 m, an inside/outside scaled diameter of 10.5 m/13 m which were scaled at 1:150 and 1:300. Tests were then run in a geo-centrifuge with clay and sand layers in a container having an internal diameter of 0.60 m. From the centrifuge tests it was concluded that there was good agreement between penetration forces and heave measured in models, as well as when values were converted to prototype size.

In 1992, Andersen (1992) performed investigations involving monotonic and cyclic loading in clay that examined failure loads and failure surface locations. Predicted failure loads were within 6% of the measured failure loads for both the monotonic and cyclic model loading (Andersen, 1992). The type and location of predicted failure surfaces were also found to be consistent with measured displacements.

Further analysis by Andersen et al. explored a procedure to calculate the bearing capacity of offshore gravity platforms under combined static and cyclic loading. It was found to be equally applicable to calculate the pullout capacity of suction piles. Verification was by a series of four field model tests. Calculated pullout capacities were within 0-6% higher than measured. The model tests also indicated that the suction could be maintained beneath the piles for a relatively long period of time. It was noted that with higher horizontal load components, soil layering, or small skirt depth/diameter ratio, a tension crack might form at the windward side of the pile leading to a reduced pullout capacity.

Tests to further characterize the penetration, and failure mechanisms of a suction pile in soft clay for the TLP at the Snorre site in the North Sea were performed by Dyvik et al. (1993). The model tests included one static and three cyclic tests, and were performed at a test site outside of Oslo, Norway. The differences between the tests included different geometries and eccentric loading, with all tests loaded in tension at an angle of 10° from the vertical.

Results indicated that the penetration resistance at full penetration was approximately equal to the submerged weight of the model (≈33 kN). Also, the cyclic load capacity was smaller than the static load capacity with a larger number of cycles at a given load producing failure at a lower cyclic load. The primary failure mode was by small cyclic displacements and large permanent (average) displacements. Eccentric loading generated lower cyclic failure loads and larger displacements. A decrease in cyclic stiffness was noted with increasing cyclic load level and with the number of cycles at a given cyclic load level. Previous cycling at higher cyclic load levels reduced the cyclic stiffness at small cyclic load levels. The difference in geometry tested had no significant effect on the cyclic displacements.

Initial tests of suction piles in sand were also first reported in 1993. The conclusions from all work performed, both theoretical and experimental, implied that the undrained suction capacity in sand was dependent on permeability, or more accurately the coefficient of consolidation, (C_v). Realistic model tests in sand required not only acquiring realistic effective stresses, but also getting realistic drainage conditions in relation to load periods. This was felt to be very critical as drained, partly drained or undrained behavior is difficult to predict.

Along with the work being done to anchor production platforms in the Snorre field, the development of the Tordis field was also being conducted using the TLP technology. The Tordis field is located in 200 m water, south of the Snorre field (Christophersen, 1992). The foundation systems for this project were subjected to extensive design, verification, and test programs

Research was also being carried out by Iskander et al. (1993) in 1993 involving the utilization of suction pressures for installation and development of pullout capacity of model piles in sand. Substantial increases in the pullout capacity of suction piles over traditional piles were attained.

The following observations were made during the installation and pullout of model suction piles in sand by Iskander et al. (1993). One problem encountered was that it is was not possible to perform suction installations on an unballasted model suction pile without developing a quick condition, and liquefying the soil inside. Furthermore, it was stated that the formation of a quick condition would be likely during field installations, particularly at shallow penetrations. The quick condition encountered resulted in a substantial reduction in the soil's penetration resistance. Accordingly, a small pressure difference was sufficient for suction pile installation in sand. The existence of a quick condition also led to reduced penetration distance due to soil heaving.

It was also suggested by Iskander et al., that mechanisms involved in suction installations result in a reduction in the frictional capacity of suction piles. Reduction of the hydraulic gradient during the installation was found to improve the frictional capacity but increased installation time.

Passive suction was found to be the dominant parameter contributing to the short term pull-out capacity of sealed top suction piles by Iskander et al. Frictional capacity was

substantially increased during pullout by the gradient associated with the suction pressures.

Clukey and Morrison (1993) performed further centrifuge tests investigating the behavior of suction piles in normally consolidated clays in 1993. This study involved typical Gulf of Mexico (GOM) loading conditions for TLP's. According to Clukey and Morrison, high and low frequency cyclic loads associated with TLP loading for a pile about 15.2 m in diameter and 32.8 m deep in soils with shear strengths similar to GOM clays resulted in a static capacity of about 89.0 MN. Capacity prediction involved traditional methods with a suction efficiency of about 80% being used to determine the reverse end bearing capacity.

Clukey and Morrison (1993) also performed finite element analyses. Using this method the researchers were able to accurately predicted the load-displacement behavior up to 0.6-m vertical displacement. This agreement was achieved despite the centrifuge test having a suction efficiency of 92%. Clukey and Morrison suggested that the methods used to calculate the full reverse end bearing may correspond to displacements beyond the acceptable range for TLP applications. The use of a suction efficiency factor of 80%, however, was felt to maintain a conservative estimate of the ultimate capacity.

Up until the early 1990's, little emphasis had been placed on the point of attachment to suction piles. In 1994 Keaveny et al. reported studies involving the point of tether attachment and its effect on the load capacity of suction piles. Lowering the point of attachment between the tether and anchor from the mudline to midway between mudline and skirt tip reportedly nearly doubled the capacity for static loading. It was also found that, disregarding the small effect of cycling, the difference in capacity was mainly a function of load point for predominantly horizontally loaded anchors.

A majority of the work on suction piles through the 1980's and early 1990's concerned clay and silt seabed materials. Tjelta (1994) was one of the first to pose the questions, " Is uplift capacity available in the sand?", and "Can skirts be penetrated to the necessary depth to achieve this capacity?"

The first question was felt to be resolvable in both a qualitative and a quantitative way

(Tjelta, 1994). It was noted by Tjelta that there were several good examples of structures resting on the sea bottom that resisted uplift forces in excess of their own weight. The uplift resistance was much higher than the expected value based on contemporary design methods. Furthermore, Tjelta stated that model tests of bucket foundations in sand possessed a pullout capacity in excess of the drained capacity. The increased capacity was felt to be a function of both the degree of drainage and the dilatant behavior of the sand.

Much of the data on suction piles garnered through the late 1980's and early 1990's went into the design of the foundation of the Troll gravity platform. As part of the foundation for the Troll platform, the largest suction piles to that date were successfully installed in the floor of the North Sea. The piles were 32 m in diameter and were embedded approximately 36 meters into the sea floor, with the last eight feet of installation being aided by active suction.

During the same year that the Troll platform was being installed in the North Sea, Clukey and Morrison (1995) reported on a centrifuge testing program, which was initiated in 1989. This study was designed to elucidate the behavior of a suction pile foundation system in soils with a shear strength profile specified typical of normally consolidated Gulf of Mexico clays.

The response of a suction pile foundation to the full range of monotonic and cyclic loading conditions was observed. Small-scale models of a 50-ft diameter prototype installed at a depth 100-ft were examined in the centrifuge. A large degree of suction was noted during uplift trials, of which approximately 65% were attributed to passive suction. Finite element comparisons of the load versus displacement results agreed with the centrifuge results for vertical prototype displacements greater than 2 ft .

Clukey and Morrison concluded that there was no evidence that the foundation would fail suddenly failure for a given cyclic load level. Furthermore, all post-cyclic static uplift tests exceeded the static uplift calculated from centrifuge tests, due to the loss of passive suction at the bottom of the pile. Also, combined loading, where the angle of inclination was varied during the cyclic loading, didn't cause a reduction in the number of cycles required to cause capacity This was felt by Clukey and Morrison to suggest that if sufficient time was allowed for consolidation,

the suction pile performance would not progressively degrade as a result of successive storms.

Another series of tests, this time involving suction piles in sand, were reported in 1995 (Bye et al., 1995). These field tests, performed in December, 1992, addressed two important issues as critical with respect to the design of the bucket foundation. These issues were (1) penetration of the skirts through the very dense sand, and (2) tension capacity, particularly under cyclic loading.

Field tests were conducted on a 1.5-m diameter cylinder with a height of 1.7 m and a wall thickness of 12 mm. The pile was penetrated by self-weight and a hydraulic pushing device to refusal, then suction was applied in the closed cylinder and penetration continued. After penetration, static pullout tests and cyclic load tests were performed.

Bye et al. compared the penetration resistance of field tests with cone penetration tip resistance (q_c) leading to the derivation of correlation factors relating q_c to skirt tip and skirt friction resistance. The effect of suction on tip resistance was found to be dramatic, as the tip resistance in the field tests measured close to zero. Bye et al. surmised that this was caused by the high suction used, resulting in critical gradients around the skirt tip. Static pullout capacity from field tests was evaluated based on the classical bearing capacity theory. It was deduced from the tests that the sand dilatancy was a dominant factor, along with the drainage characteristics of the soil and the length of the test. Cyclic loading studies proved that the static pullout capacity did not decrease after cycling, and that some compaction of the soil took place during cyclic loading.

One of the most recent studies involving suction piles was authored by Rao et al. (1997). According to Rao et al. these studies were designed to: (1) bring out the load-displacement behavior of the suction anchor under short-term loading conditions, (2) study the variation of passive suction (underpressure) at the top of the soil plug and anchor base during the break-out process under both short-term and sustained loadings, and (3) study the failure pattern of the suction anchor system.

One conclusion drawn from this study was that displacements corresponding to 16 % of the anchor diameter were necessary to mobilize the ultimate pullout capacities in suction anchors

under short term loading. This large deformation enabled the mobilization of skin friction, suction induced reversed-end-bearing and the tensile strength of the soil at the anchor base. In combination with these factors, as the soil plug moved with the anchor up to the failure point, it contributed to the breakout capacity as long as the adequate passive suction pressure remained at the anchor top to hold the soil plug in position.

Rao et al., also determined that under short term monotonic loading, the suction pressure at the top of the soil plug increased with the increase in the anchor displacement up to failure with no well defined peak in the suction pressure mobilized. Conversely, at the anchor bottom, the suction pressure increased with displacement to reach a maximum value. The peak pressure value was mobilized at relatively low displacements followed by a drop to a constant value at larger displacements.

To date, much work has been accomplished on both suction anchors and on suction piles. More research is ongoing to make the system safer, cheaper, and more reliable. To understand better the geotechnical mechanisms responsible for the suction pile, it is necessary to understand the basic mechanisms of soils stresses related to the structures.

Soil Stresses

Wilson and Sahota (1980) presented early considerations of soil stresses related to suction anchors. These researchers stated that in regards to suction anchors the stresses in a soil bed might be regarded as functions of four quantities: 1) the buoyant unit weight of the soil, 2) the buoyant weight of the anchor, 3) the pressure reduction within the anchor, or at some reference position, due to pumping, and 4) the pull-out force. The buoyant weights of the anchors are small in comparison with the pull-out forces, the vertical pull-out force, P, being taken as the total applied vertical force less the buoyant weight of the anchor.

The standard practice in numerous studies on the pull-out behavior of plate anchors has

been to relate a non-dimensional pull-out force coefficient such as $P/\gamma' AD$ to the burial depth ratio D/B, where $P/\gamma' AD$ is the ratio of the average bearing stress P/A (with P equivalent to pull-out force) to a soil reference stress $\gamma' D$. This reference stress is the vertical stress at a depth of D in a soil bed with buoyant unit weight, γ'.

Suction anchors introduce a cavity suction or other reference pressure, Δp. This can be included in a non-dimensional group such as $\Delta p/\gamma' D$, the ratio of the anchor reference pressure Δp to the soil reference stress $\gamma' D$. Since non-dimensional groups may be multiplied together, $\Delta p/\gamma' D * D/B$ provides an alternative parameter $\Delta p/\gamma' B$ which has proved to be more convenient in experiments in which Δp and B are the primary independent variables according to Wilson and Sahota (1980).

The condition of geometric similarity includes the anchor, the boundaries of the soil bed and also the flow net around the anchor. If the equal pressure surfaces are defined for specific proportions of Δp (Fig. 3), and the distance between these surfaces is to the same linear scale as B, then the group $\Delta p/\gamma' B$ can be regarded as a combination of a pressure gradient parameter Dp/B and the soil vertical stress gradient γ'.

Two further factors, which are of concern (since they relate to pump capacity), are the total flow of the pore water into the anchor and the corresponding net power requirement. The volume flow rate of water into the anchor is proportional to the pressure gradient parameter $\Delta p/B$ and a reference area such as the filter area (Wilson and Sahota, 1980).

Andersen and Lauritzen (1988) reported initial work on soil stresses associated with skirt-pile foundations. According to these researchers, static and cyclic movements of the pile cause a complex stress situation in the soil beneath the platform. Soil elements in the vicinity of the pile are subjected to both the average shear stress, τ_a, and the cyclic shear stress, τ_{cy}. Examples given by Andersen and Lauritzen of simplified stress conditions for a few typical elements along a potential failure surface are shown in Fig. 4. In their paper, τ, denotes the shear stress on the horizontal plane in the direct simple shear (DSS) test and on the 45° plane in the triaxial test .

The average shear stress, τ_a, is composed of two components: (1) The initial shear stress

of the soil prior to the installation of the platform i.e.,

$$\tau_o = 0.5\,(1 - K_o)p_o', \qquad [1]$$

where

p_o' = the effective overburden stress.

K_o = the coefficient of earth pressure at rest;

and (2) the additional shear stress, $\Delta\tau_a$, which is induced by the submerged weight of the platform.

The initial shear stress, τ_o, develops under drained conditions, and the soil is consolidated under this stress. The shear stress due to the weight of the platform, $\Delta\tau_a$, initially acts under undrained conditions, but will also act under drained conditions as the soil consolidates under the weight of the platform.

The cyclic wave loads cause the cyclic shear stress, τ_{cy}, therefore, as the wave height and period vary, the cyclic shear stress will also vary.

Further research on effective stress related to skirt piles was reported by Dyvik et al. (1989). These researchers performed a model study using clay. The effective stress history of the model clay was determined from the following: (1) the known stresses applied at the top and base of the sample, (2) pore-pressure transducers in the clay and on the test tank side wall, and (3) earth-pressure transducers in the teat tank side wall and base.

In Fig. 5 the effective vertical stress profile after primary consolidation for the maximum stress increment is illustrated. This is the combined effect of the applied dead load plus hydraulic surcharge and self-weight of the clay. The curve labeled as σ'_{vcpo} applies to the maximum state of stress, assuming no friction between the clay and the sidewall of the test tank. Dyvik et al. state that the curvature of the profile was caused by the hydraulic surcharge component, and supported by the pore-pressure measurements within the clay.

Dyvik et al. noted, however, that friction was found to be present, and diminished the effective vertical stress by as much as 25% (Dyvik et al., 1989). The friction was assumed to be distributed with depth according to the σ'_{vpco} distribution. The resulting σ'_{vpc} distribution, which accounts for friction, is also shown in Fig. 5.

The effective vertical stress profile within the clay just before the model test was performed (σ'_{vc}) is also shown in Fig. 5. Dyvik et al. based this on pore-pressure measurements from five model tests, and the unit weight of the clay. Final depths of the model clay beds (Table 1) were all trimmed to 200 mm. The σ'_{vc} profile includes the effects of penetrating the model skirts into the clay. Since less than 5% consolidation occurred below the models during the 30 minute test period, the σ'_{vc} profile was assumed by Dyvik et al. to be valid for the entire model testing time.

According to Dyvik et al., the overconsolidation ratio (OCR) for the model clay (based on the σ'_{vpc} and σ'_{vc} profiles shown in Fig. 5) was nearly constant with depth at a value of approximately 3.4.

Dyvik and his colleagues also discussed the shear strength profile of the model clay. Five static and two cyclic direct simple shear tests, and seven static and 24 cyclic triaxial tests were performed at OCR values of 1.0, 1.57, and 2.09, while the clay used in the model tests had an OCR of about 3.4. The reason for this difference was that some effects during consolidation of the model clay were difficult to quantify beforehand (i.e., friction along the sidewalls of the test tanks and some swelling and pore-pressure development due to model skirt penetration). Consequently, Dyvik et al. corrected the laboratory results to OCR = 3.4.

Dyvik et al. presented Fig. 6 showing the triaxial compression, direct simple shear (DSS), and triaxial extension undrained shear strength profiles (s_u^c, s_u^{DSS}, and s_u^E, respectively) for the model clay. These profiles were based on static triaxial (shear strain rate of approximately 3%/hr) and static DSS (shear strain of 5%/hr) results extrapolated to the effective stress and OCR of the model clay during the actual model tests. Miniature cone penetration tests and laboratory vane tests performed in the test tank immediately after each model test upheld the shear strength

gradients. The shear strength was found to be rate-dependent. Fig. 6 also shows the shear strength profiles for the model clay loaded to failure in one minute.

A paper involving effective stresses and soil dilatancy was presented by Bye et al. (1995). In this paper, Bye and his coworkers discuss soil dilatancy and contractancy. According to these researchers, real soils do not generally behave in the idealized elastic-plastic, non-dilatant manner. As shear stresses are applied to elements of soil, there is a tendency for volume change as well. This cross coupling between shear and volumetric behavior is termed "dilatancy" when the soil tries to increase volume, and "contractancy" when the soil tries to decrease volume during shearing.

According to Bye et al. (1995), for soil at any given density, both contractancy and dilatancy will occur depending on the magnitude of the applied mean effective stresses. For one particular mean effective stress magnitude, neither phenomena occurs--this is termed the "critical state."

When dilational behavior is coupled with consolidation mechanisms the consequences can be dramatic. The tendency for volumetric expansion is resisted by suction generated due to the incompressible nature of the pore water. Bye et al. stated that therefore only with substantial flow of water into the soil elements could expansion occur. If the water flow is insufficient, the mean effective stresses in the soil will be increased, along with an increase in the mobilized shear stress. The research suggested that only when the soil effective stress and density have altered such that the "critical state" is reached, will a true limiting strength be attained. For fully undrained conditions, this is usually termed the "steady state" strength. If the water flow is completely prevented, the ultimate soil strength will be several orders of magnitude higher than its initial value. Bye et al. therefore concluded that it was evident that coupling between the consolidation and dilational soil behaviors was important in determining the actual performance of skirt pile foundations.

Although much work had been done on the interaction of cohesive soils and piling systems, research on soil stresses in cohesionless soils was also taking place. Jardine et al. (1993)

discussed the assessment of the shaft capacity of piles in sand by three possible routes; methods by Briaud and Tucker (1988), Poulos (1989) or Jardine and Christoulas (1991). The researchers went on to describe one popular approach which would be to assume a direct relationship between the local skin friction (τ_f) and in-situ test parameters such as the N value from the standard penetration test, q_c from the cone penetrometer test, and P_{lim} from the pressuremeter test. As a second possibility, τ_f, was assumed to be a simple multiple (β) of the initial free-field vertical effective stress (σ'_{vo}). A third route was to assume the Coulomb failure criterion and to assess the normal effective stresses and frictional coefficients acting at failure separately, i.e.,

$$\tau_f = \sigma'_{r,f} \tan\delta' \qquad [2]$$

where:

$\sigma'_{r,f}$ = effective stress

δ' = effective friction angle between the soil and pile

Jardine et al. noted that, although, the third route was the most attractive analytically, it was not clear how $\sigma'_{r,f}$ should be evaluated and that δ' was rarely measured in appropriate laboratory tests. As a result, approximate rules of thumb such as taking $\delta' = 0.8\phi'$, (Potyondy, 1961) must be adopted for design calculations.

The API RP2A recommendations for offshore piles in sand suggest that Eqn. [2] should be evaluated assuming that $\sigma'_{r,f}/\sigma'_{vo}$, or K_f, is equal to 0.8 and 1.0 for open and closed-ended piles, respectively, and that δ' varies with the soil type and relative density (D_r). A graphical interpretation of the implied variations of δ' with D_r and the mean grain size (D_{50}) is given by Jardine et al. in Fig. 7. Upper limits of τ are also specified, but the researchers noted that the API RP2A recommendations were derived by back-analyzing tests on un-instrumented piles, and the individual parameters might not be realistic.

Jardine et al. asserted that it was necessary to establish real values for $\sigma'_{r,f}$ and δ'. From

tests conducted by the researchers, five conclusions were made:

1. The controlling frictional parameter for piles in sands and silts is the critical state interface angle δ'_{cs}.

2. δ'_{cs} does not depend on relative density and, for a given interface roughness, reduces sharply as D_{50} increases.

3: For uniform soils a linear relationship exists between tan δ'_{cs} and normalized interface roughness.

4. Direct interface shear tests are relatively simple to perform and should be incorporated into many more offshore site investigations.

5. Ring-shear tests in which the normal stiffness is controlled may provide the best method of assessing the potential effects of dilation on drained pile loading.

Modeling of soil stresses related to suction piles was not always of a physical nature. Bye et al. (1995) completed a finite element analysis of deep-sea foundation behavior. The in-place foundation design included the soil stiffness representation for the structural in-place and wave load analyses, and bucket capacity calculations for combined loading.

The researchers represented the foundation stiffness by using 6 x 6 stiffness matrices in the structural analysis. Their stiffness matrix was generated from a linear elastic analysis, using a high estimate of soil modulus. They reported that this resulted in conservative (high) moment restraint, which was on the conservative side with respect to the soil capacity calculations.

Bye et al. based their pile bearing capacity analyses on the undrained shear strength of the soil. They calculated the undrained shear strength in the soil volume surrounding the skirt pile (τ_f) based on effective stress distribution (σ') and effective soil friction angle (ψ'_u):

$$\tau_f = \sigma' \tan\psi'_u \qquad [3]$$

Substituting expressions for dilatancy, and using the definitions in Fig. 8, the researchers were

able to express the specific value of undrained shear strength for an arbitrary plane as:

$$\tau_{f_\alpha} = \sigma' \tan\psi'_u + \tau' \tan\psi'_u \cos 2(\alpha-\theta) + \Delta\tau' \tan\psi'_u (2D+\cos 2(\alpha-\theta)) \quad [4]$$

where:

τ_{f_α}	=	shear strength on plane α
σ'	=	initial mean effective stress
ψ'_u	=	undrained friction angle
τ'	=	initial shear stress
α	=	angle of shear plane
θ	=	rotation of principal stress
$\Delta\tau'$	=	change in shear stress
D	=	dilatancy parameter

Bye et al. (1995) stated that for the specific analyses, the effective stresses (σ' and τ) should be corrected with respect to:

1) Accumulated pore-pressure during the design storm.

2) Pore-pressure induced for design load cycle .

3) Dissipation of pore-pressure components.

According to Bye et al., the capacity analysis should be performed by a slip surface type method as illustrated in Fig. 9. External forces were transformed to pile skirt-tip level, accounting for active/passive soil pressures and skirt friction components.

The principles used by Bye and his colleagues in the stability calculation are as follows:

1) Foundation is transformed to a rectangle.

2) Permanent structural load applied is based on the drained condition.

3) Environmental loads are transformed to the skirt tip level, subtracting soil reactions on skirt walls.

4) Environmental loads applied are based on undrained conditions.

5) Loads applied at the skirt tip level are on the effective foundation area.

6) The soil volume limited by the slip surface is divided in triangular elements.

7) Iteration on force equilibrium between the soil elements is performed until the equilibrium shear stress is determined.

Bye et al. used the pore-pressure accumulation technique of Andersen et al. (1988) to calculate the cumulative pore-pressure during a design storm. The generated and resulting pore-pressure during their design storm is presented in Fig. 10, showing a remaining pore-pressure of 25 % of the undrained pore-pressure. The corresponding reduction in mean effective stress along the slip surface was reported as 4%, resulting in a decrease in both compression and tension capacity.

Pore-pressure during the design load cycle was calculated for four different soil elements. The analysis was performed using a two dimensional finite element method of analysis, determining the effective stress distribution for structural weight, assuming drained conditions, and then total stress changes for environmental loading assuming undrained conditions. The undrained pore-pressure amplitudes were then calculated according to Janbu, (1979). A reduction in pore-pressure along the slip surface was observed to vary from 4% to 20 % (from inside to outside foundation area). An average value of 10 % reduction was therefore used for the bearing capacity correction.

The researchers corrected for compression and tension capacity in undrained conditions by correcting the dilatancy parameter D, in the undrained capacity calculations. The correction in D

equals the effective stress changes, which was considered to be the simplest way to perform the correction with the computer codes used for capacity calculations. The original design dilatancy value was D = 0.3. The corrected D values were:

Tension: $D_c = 0.12$

Compression: $D_c = 0.48$

The strength of saturated soil was allowed to be controlled by the effective stresses, which were defined as the total applied stresses minus the or pore-pressure:

$$\sigma' = \sigma * uI \qquad [5]$$

where:

σ' = effective stress tensor

σ = total stress tensor

u = pore-pressure

I = identity matrix

These effective stresses and the soil friction angle (ϕ'), define the soil strength. The simplest soil strength model is that of Coulomb:

$$\tau = \sigma' \tan \phi' \qquad [6]$$

where:

τ = soil shear strength

σ' = normal effective stress on the failure surface

The pore-water pressure was assumed by the researchers to be dependent on the rate at

which the load was applied to the soil. Bye et al. suggested that for an idealized elastic and non-dilatant plastic soil, an instantaneous change in load would cause no change in the mean effective stresses. However, they also noted that an instantaneous change in pore-water-pressure would arise, and, unless the loading increment was isotropic, there would also be a change in the shear (or deviator) stresses in the soil. These effects were said to leave the soil strength unchanged from the values existing prior to loading.

With the passage of time, it was said that the induced pore-pressures would dissipate as the fluid flowed through the soil so as to equalize the pore-water-pressure. During this process the effective stresses in the soil would change, with consequent effects on the soil strength. The time required for dissipating such pore-pressures is a function of three parameters; the foundation size, the soil permeability, and the soil skeleton bulk stiffness.

Considering a skirt-pile foundation, it can be visualized that a compression load would lead to increases in the mean effective stresses as time passed, and therefore an increase in soil strength with time. However, according to Bye et al. tensile loads would cause a decrease in mean effective stress with time, and therefore a decrease in strength. Ultimately, it was felt that when full dissipation of all generated pore-pressures had occurred, the only tensile resistance that could be mobilized would be a very small component resulting from the friction on the skirt walls. This was forwarded as the principal reason why the tensile capacity for such foundations had always previously been considered negligible. However, if the loads were applied for a very short duration, substantial capacities might be possible.

Soil stresses are an important factor in designing a suction pile foundation. A thorough knowledge of soil stresses around a skirt pile can not only help engineers design safe skirt-pile foundations, it can also aid in the installation procedures.

Installation Procedures

The suction pile is a large-diameter pile, which is closed at the top, and has the hydrostatic thrust capacity for total penetration into the sea bottom. The pile tip is allowed to sink into the sediments under self-weight in order to seal itself to the seabed. Water inside the caisson is then pumped out creating an underpressure. The hydrostatic force exerted on the top of the pile due to the underpressure inside the pile drives it into the soil.

In order to drive the suction pile into the seafloor, soil resistance must be overcome. Early attempts to understand the penetration resistance of suction piles during emplacement were based on traditional pile theory (Hogervorst, 1980). The penetration resistance of the pile is the sum of the skin and tip resistance's. Calculation of the penetration resistance may be based on the results of soil measurements, preferably obtained by in-situ testing methods. However, even then there remain some uncertainties with respect to the conversion from one type of penetration resistance to the other, due to the differences in penetration rates, excess pore-pressures, geometrical shapes, etc. Hogervorst states that the penetration resistance may thus be expressed as:

$$R = \pi D \left[2k_f \int_0^h f \, dz + k_p \, q_{ch} \, t \right] \qquad [7]$$

where

D	=	diameter of pile
k_f	=	empirical coefficient relating f to skin friction
f	=	local friction as measured by the penetrometer
h	=	penetrated depth
k_p	=	empirical coefficient relating q_{ch} to end resistance
q_{ch}	=	average cone resistance of identified strata
t	=	thickness of pile rim

Ultimate penetration depth is reached when the resistance at a certain depth equals the available thrust capacity of the pile. The available thrust capacity of a pile is calculated from the following expression presented by Hogervorst:

$$T = G' + (\pi/4)\, D^2\, \Delta p \qquad [8]$$

where

G' = underwater weight of pile

Δp = pressure difference between ambient and internal pile area

Based on Eqns. 7 and 8, the main pile dimensions can be calculated. However, according to Hogervorst, for an adequate design, the effect of the groundwater flow on the soil resistance should also be considered. Hogervorst (1980) had not investigated these effects before, necessitating full-scale field experiments.

Later attempts to model the skirt tip penetration resistance were performed by Tjelta et al. (1986) An empirical method (Fig. 11) was applied to predict the penetration resistance of a concrete panel tip. Measured and predicted penetration resistance's agreed well as shown in Fig. 12.

A more concise method of calculating the penetration resistance during installation of suction piles was proposed by Andreasson et al. (1988). The theoretical skirt penetration resistance is calculated as the sum of tip resistance, q_{tip} and side friction, f_s:

$$q_{tip} = N_c S_u \qquad [9]$$

$$f_s = \alpha\, s_u \qquad [10]$$

where

N_c = bearing capacity factor

s_u = undrained shear strength

α = friction factor

In order to speed calculation of penetration and heave within the suction pile, Hjortnaes-Pedersen and Bezuijen (1992) presented a computer program called PIAPA. In this program, the total resistance force is calculated by adding the friction force to the tip force. The friction force is determined by the local friction resistance developed along the shaft of the skirt, integrated by the shaft area. The tip resistance, multiplied with the tip area determines the tip force. In the program, the additional vertical stress due to the friction and heave is taken into account.

To further analyze penetration resistance, Guttormsen and Wikdal (1994) estimated the penetration resistance, Q, as the sum of the wall friction along the skirt wall, Q_s, and the skirt tip resistance, Q_t. Penetration resistance in clay layers was calculated with a traditional bearing capacity approach for the tip resistance (Brinch-Hansen, 1970), and a remolded shear strength approach for the wall friction (Guttormsen and Wikdal, 1994). The methods for calculation of the penetration resistance presented by Guttormsen and Wikdal are summarized below:

$$Q = A_t * k_p * q_c + A_s * k_f * q_c \qquad [11]$$

where:

q_c = Sand cone penetration resistance

k_p = Empirical coefficient for prediction of tip resistance

k_f = Empirical coefficient for prediction of wall friction

A_s = Wall area in contact with soil

A_t = Skirt tip area

The empirical factors are taken as 0.6 for tip resistance and 0.003 for side friction. For clay layers Guttormsen and Wikdal presented the following equation:

$$Q = A_t * (N_c * s_u^{DSS} + \gamma' * z) + A_s * \alpha * s_u^{DSS} \quad [12]$$

where:

A_t, A_s = Tip and side area of pile in contact with soil

N_c = Bearing capacity factor

γ' = Average effective unit weight of soil above skirt tip level

z = Depth to pile tip

α = Empirical friction coefficient accounting for remolding of clay during continuous penetration

s_u^{DSS} = Direct undrained shear strength, taken as 0.8 times the triaxial undrained shear strength.

Penetration resistance calculations are important for the installation of suction piles. These can be related to another factor important during installation; critical suction.

Critical Suction Pressures

Limiting factors during the soil penetration of a suction pile consist of either inward failure of the soil or movement of the clay plug as a sand layer is approached (Guttormsen and Wikdal, 1994). For inward failure in the clay layer, Guttormsen and Wikdal calculated the limiting suction value, Ulim, with a reversed bearing capacity formula :

$$U_{lim} = N_c * s_u + Q_{si}/A_b \quad [13]$$

where:

N_c = Bearing capacity factor ranging from 6.0 to 6.7 with depth

s_u = Active undrained shear strength at pile tip level

Q_{si} = Inside wall friction of clay

A_b = Inner base area of pile

If a sand layer is encountered during penetration, the limiting suction is governed by the case where the applied suction force exceeds the weight of the clay plug, W_{clay}, and friction forces inside the pile wall (Guttormsen and Wikdal, 1994) Consequently, the clay plug will tend to lift due to suction, and water will invade the space between the sand and clay layers. The limiting suction for this case may theoretically be estimated as:

$$U_{lim} = (W_{clay} + Q_{si})/ A_b \quad [14]$$

In a situation where the seabed is sandy, an unstable, quick condition may occur when the upward seepage force within the pile exceeds the submerged weight of the soil within the pile. The critical gradient, i_{cr}, is given by Iskander et al. (1993):

$$i_{cr} = \gamma'/\gamma_w \quad [15]$$

where:

γ' = buoyant unit weight

γ_w = unit weight of water

When a quick condition occurs, the soil within the pile liquefies, possibly causing the

upwelling of soil into the pile. The pressure, which causes critical gradient, has been considered up to the present as the critical suction pressure in sands.

Once the pile has been installed, failure mechanisms of the soil around and within the pile must be considered for a safe design. One of these failure modes is tensile fracture of the soil beneath the pile tip.

Tensile Failure

Tension failure related to suction piles is a consideration mainly for clay soils, however, it is of interest when designing suction anchors for sandy soils due to some similarities. Failure under tensile loads occurs when the inside soil-wall friction force and suction force of a suction anchor or suction pile exceed the tensile strength of the soil (Steensen-Bach, 1992). The soil plug Inside the pile is then torn out of the seafloor leaving a hole.

Brown and Nacci (1971) conducted one of the earliest studies dealing with the tensile fracture of soil beneath a suction emplaced structure. This study involved the use of a suction anchor in sand. Suction was maintained throughout the study. During the anchor breakout, the intergranular stress normal to the (conical) failure surface was the tensile stress, which was taken as zero for granular soils. Consequently, the effective stress acting on the failure surface was a function of the excess pore-pressure developed by the pump. A reduced excess pore-pressure acted on the failure plane because of the pressure loss related to viscous and turbulent flow through the cone of failure.

In 1991, Fuglsang and Steensen-Bach conducted centrifuge and 1 g studies, using suction pile models in clay. A tensile total stress σ_t was assumed to act across the base of the clay plug. An equation of vertical equilibrium was then derived:

$$F = W_p + W_s + W_w + \alpha c_{um} A_c + \sigma_t A_b \qquad [16]$$

where:

W_p	=	total weight of pile
W_s	=	total weight of soil plug inside pile
W_w	=	total weight of water on pile top
α	=	adhesion coefficient
c_{um}	=	mean undrained shear strength along the pile shaft
A_e	=	exterior cross-sectional area
σ_t	=	tensile strength
A_b	=	area of the base of the clay plug

σ_t is used over the total base area, although it is only defined for the base of the clay plug.

According to Fuglsang and Steensen-Bach (1991) it can be defined that

$$\sigma_t = Nc_{ub} - q \qquad [17]$$

where:

N	=	bearing capacity factor
c_{ub}	=	shear strength at the base of the pile
q	=	total stress at pile point

Therefore, σ_t can be calculated from N_t in Table 2. In laboratory model tests, Fuglsang and Steensen-Bach found the mean tensile stress at the base was 61 kPa in the weak clay and 105 kPa in the stronger clay. In centrifuge tests, it was observed that there was a compressive stress at the base both in the weak clay and in the stronger clay tested, explaining why the tensile failure did not occur in the centrifuge tests, while it was likely in 1 g tests.

It should be noted that the values of σ_t in Table 2 are based on the maximum break-out resistance, which was mobilized prior to tensile fracture. This may lead to a somewhat different

σ_t at the moment of fracture. Another failure mechanism found when dealing with pull-out behavior of suction piles is reverse end bearing capacity.

Reverse End Bearing Capacity

After proper installation of the suction pile, it is subjected to various environmental loads. Such factors include waves, tides, currents, and interaction with ships loading and unloading the platform. More rare events include storms. For day-to-day operations, the holding capacity is handled by the weight of the pile, the weight of the ballast, the weight of the internal soil plug (more so for cohesive soils), and the skin friction on external pile surface.

During storm events, holding capacity is achieved through passive suction. Passive suction can be described as follows: At the top of pile, negative pore-water pressures and high ambient pressures generate a large negative internal pressure called passive suction. The suction force generated at the top of the pile is transferred to the bottom of pile through the soil plug. The transmitted force of the passive suction is known as break-out resistance, or referred to as suction induced reverse end bearing capacity.

Original theories for the suction pile bearing capacity were developed during work on gravity based platforms. However, the pattern of plastic deformation during failure of suction piles corresponds to a reversed end bearing capacity failure, i.e. the shearing of the soil is similar to a bearing capacity failure beneath an embedded footing, but the direction is reversed (Renzi et al., 1991, Fuglsang and Steensen-Bach, 1991). If this is the case, the break-out capacity of the pile can be written as:

$$F = W_p + W_s + W_w + \alpha c_{um} A_e + (N c_{ub} - q) A_b \qquad [18]$$

where:

W_p	=	pile weight
W_s	=	soil weight
W_w	=	weight of water above the pile
α	≈	0.3
c_{um}	=	mean undrained shear along the shaft of the pile
A_e	=	exterior cross-sectional area
N	=	bearing capacity factor
c_{ub}	=	strength at the base of the pile
q	=	total stress in the clay beside the pile
A_b	=	area of the base

The bearing capacity factor N may be derived from the measured break-out force (Fuglsang and Steensen-Bach, 1991). It should be noted that the value of N is highly affected by the uncertainty of c_{um} and c_{ub}.

The N value in each test appears in Table 2 where it is designated N_1 (Fuglsang and Steensen-Bach, 1991). The average N_1 is 8.3 in the weak clay, and 6.4 in the stronger clay. Centrifuge tests did not indicate different values.

The N value may also be calculated from the equilibrium of vertical forces on the clay plug:

$$|-u\,A_p + \alpha c_{um} A_i| = W_s + (Nc_{ub} - q)A_p \qquad [19]$$

where:

u	=	pore pressure below top of pile
A_p	=	cross-sectional area on the clay plug
Ai	=	interior cross-sectional area

α = adhesion coefficient

c_{um} = mean undrained shear along the shaft of the pile

c_{ub} = strength at the base of the pile

W_s = total weight of soil plug inside pile

q = total stress at pile tip

i.e., the pore-water tension at the top, plus the inner skin friction equals the weight of soil plus the reversed undrained bearing capacity at the base. A_p is the cross sectional area of the clay plug. The N value calculated in this manner is given in Table 2 and named N_2 (Fuglsang and Steensen-Bach, 1991). The average value of N_2 is 9.2 in the weak clay and 8.1 in the stronger clay. It is seen that N_2 is larger than N_1 (Fuglsang and Steensen-Bach, 1991). It may be because it is incorrect to assume that the inner skin friction is fully mobilized, as the clay plug follows the pile. If zero skin friction is assumed, N_2 is reduced by some 15% in the weak clay and 30% in the stronger clay (Fuglsang and Steensen-Bach, 1991).

Another approach to reverse end bearing capacity was taken by Clukey and Morrison (1993). To understand the reverse end bearing capacity, one needs to examine the compressive end bearing capacity. The compressive load to the end bearing at the bottom of the caisson, F_c, is calculated from:

$$F_c = qA \qquad [20]$$

where q is the unit end bearing and A is the cross sectional area at the bottom of the caisson. The unit end bearing can be determined from:

$$q = N_c S_u \zeta_s \zeta_i \zeta_d + N_\gamma \gamma' L \qquad [21]$$

where for an undrained ($\phi = 0$) total stress case, N_c is the bearing capacity factor for a strip footing

resting at the ground surface, S_u is the undrained shear strength averaged at a depth of D/2 below the caisson rim (where D is the pile diameter), ζ_s is the caisson shape factor, ζ_i is the inclination factor, and ζ_d is the depth factor which takes into account the shearing that occurs above the base of the caisson rim.

The bearing capacity factor is 5.14 for a soil deposit with a uniform shear strength. For determining the bearing capacity factor for a foundation on a linearly increasing shear strength profile, a generally conservative approach is to average the shear strength over a depth of D/2 below the bottom of the foundation.

The inclination factor, ζ_i, on the reverse end bearing is approximated by the following expression:

$$\zeta_i = (6T)/(S_u N_c \pi D^2) \qquad [22]$$

where T is the horizontal component of the load transferred to the base of the caisson.

The shape factor, ζ_s, for a cylindrical footing equals 1.2. For compressive loading, the following expression was used for the depth factor with a linearly increasing shear strength profile:

$$\zeta_d = 1+0.18\tan^{-1}(D/L) \qquad [23]$$

where D is the caisson diameter and L is the caisson length.

The second term on the right hand side of Eqn. 21, S_u, is equal to the overburden stress ($\gamma' L$) because the N_γ term is 1.0 for a clay under undrained loading conditions. However, this term is canceled by the weight of the internal soil plug where the net unit and bearing capacity is used. The total resistance provided by the soil in uplift is therefore equal to the first term on the right hand side of Eqn. 21, N_c, times the cross-sectional area of the caisson plus the external skin friction.

Along with reverse-end bearing capacity, pile wall friction is an important factor in keeping a suction pile in place.

Pile Wall Friction

Shaft friction in terms of effective stress is the basis for wall friction in suction piles. One relatively early work involved the examination of pile friction in driven piles is by Chandler (1968). Chandler described that when a pile is loaded, the probable mechanism of deformation involves a narrow cylinder of clay immediately around the pile shaft subject to simple shear. Provided that the rate of loading is fairly slow, drained conditions will exist in the clay along the pile shaft. On this zone the effective normal pressure will be the horizontal effective stress, σ_h'.

The drained strength of the clay around the pile shaft may be given by

$$\tau = c' + \sigma_h' \tan \phi' \qquad [24]$$

where:

c' = effective cohesion

σ_h' = horizontal effective stress

ϕ' = effective friction angle

Considering the whole length of the pile shaft., diameter, D, and length, L, the maximum shaft resistance, R, will be

$$R = \pi D \int_0^L (c' + \sigma_h' \tan \phi') dl \qquad [25]$$

In terms of the ultimate friction resistance per unit area, f_u, Eqn.24 can be expressed as

$$f_u = c' + K_o\sigma_v' \tan \phi' \qquad [26]$$

where K_o and σ_v' are the mean values along the entire pile shaft, with K_o being the ratio of the horizontal to vertical effective stresses at rest, σ_v'.

Shaft friction in normally consolidated soils typically follows a linear relation between the undrained strength, c_u, and depth. This relation, expressed by the ratio c_u/p where p is the effective overburden pressure. It was found that for many marine clays, c_u/p increases with increasing plasticity index. In terms of the drained strength along the pile shaft, the shear strength, τ, at any depth can be expressed as

$$\tau = K_o\sigma_v' \tan \phi' \qquad [27]$$

Using the semi-empirical relation of $K_o = 1\text{-}\sin\phi'$ the following equation is obtained:

$$\tau/p = (1\text{-}\sin\phi')\tan\phi' \qquad [28]$$

which enables the strength versus depth relations in terms of both immediate (in-situ) and drained conditions to be compared at different values of plasticity index.

An effective stress approach to estimate the shaft friction in stiff clays is more complex than for soft clays. The major problem is to estimate the value of K (Burland, 1973). In the undisturbed state, the value of K_o for heavily overconsolidated clay varies with depth and can be as high as 3 near the surface, decreasing to less than 1 at great depth.

The first step is to estimate the shaft friction corresponding to K_o state (Burland, 1973). This may be thought of as the shaft friction of an "ideal" pile, which has been installed without altering the initial stress conditions in the ground. Since the value of K_o varies with depth, the

total shaft resistance, R_u, is given as:

$$R_u = \int_0^1 \pi d \Sigma p K_o \tan \delta \, \Delta l \qquad [29]$$

where d is the diameter, δ is the effective angle of friction between the clay and the pile shaft, and l is the length of the pile. According to Burland (1973), the mean shaft friction τ_s is therefore:

$$\tau_s = R_u/\pi d l = 1 \int_0^1 \Sigma p K_o \tan \delta \, \Delta 1 \qquad [30]$$

As before, it was assumed that the failure takes place in the remolded soil close to the shaft surface so that δ is equal to the remolded drained angle of friction.

Later studies dealt with the shaft friction in suction piles more directly. Back-calculated values of wall friction from a study by Tjelta et al. (1986) demonstrated that applied suction reduced inside wall friction significantly. Furthermore, it was observed that the soil may be dragged down from one layer into another during penetration.

A more contemporary approach to evaluate skin friction in suction piles was presented by Iskander et al. (1993). For example, using the API RP2A criterion, the side friction for fully drained conditions would be:

$$f_s = \sigma'_v K \tan(\delta) \qquad [31]$$

The increase in the vertical stress due to a downward vertical gradient is given by γ_w per unit volume (Iskander et al., 1993).

Another approach is to assume the Coulomb failure criterion and to assess the normal effective stresses and frictional coefficients acting at failure separately (Jardine et al., 1993):

$$\tau_f = \sigma'_{rf}\tan\delta' \quad [32]$$

where:

σ'_{rf} = effective stress

δ' = effective friction angle between the soil and pile

Although this approach is one of the most attractive analytically, it is not clear how σ'_{rf} could be evaluated and δ' is rarely measured in appropriate laboratory tests. As a result, approximate rules of thumb (such as taking $\delta' = 0.8\phi'$), are adopted for design calculations (Jardine et al., 1993).

The API RP2A recommendations for offshore piles in sand suggest that Eqn 32 should be evaluated assuming that $\sigma'_{rf}/\sigma'_{vo}$, or K_f, is equal to 1.0 for closed-ended piles and that δ' varies with the soil type and the relative density (D_r). Upper limits of τ are also specified, but it should be noted that the API RP2A recommendations were derived by back-analyzing tests on un-instrumented piles and the individual parameters may not be realistic (Jardine et al., 1993). For advances to be made, it is necessary to establish real values for σ'_{rf} and δ'

In an effort to observe the actual skin friction in a suction pile, Clukey and Morrison (1993) examined the internal and external skin frictions in more detail. This test was performed on a cylindrical single-cell pile with strain gages attached at the one-third points along the outside of the pile. Vertical and horizontally oriented strain gages were mounted at 90° intervals at each third point location. Total pressure measurements were take inside the pile under the pile head. The pile weight, the pressure on top of the pile, the pressure under the pile head, and the strain gage data were used to determine the distribution of skin friction along the pile. The skin friction in this case was the average internal and external skin friction.

Results indicated that the skin friction mobilized in the top third of the pile is very small and acts in the upward direction on the pile. In the middle third of the pile, however, the average skin friction values are in very good agreement with the undrained shear strengths and act in the downward direction, opposite to the direction of loading. The skin friction in the bottom third of

the pile also acts in the downward direction and is about 64% of the average undrained shear strength for that portion of the pile.

The lower skin friction on the inside of the pile is probably related to a reduction in horizontal effective stresses against the walls of the pile. Although the internal pore-pressures are reduced during loading, the soil plug is subjected to an uplift force, which will tend to reduce the effective stresses, causing decreased skin friction against the sides of the pile.

As may be noted, pore water pressure has an effect on both the installation and retention of suction piles in the sea bed.

Pore Water Pressure

Long before the suction pile foundation system was conceived, there was interest in the effects of cyclic wave action on the pore-pressure in the foundations of sit-on-bottom type marine structures (Clausen et al., 1975). In an effort to monitor the pore-pressure changes induced by cyclic wave loading, measurements were made at the Ekofisk tank site by Clausen et al. (1975). The researchers began monitoring the pore-water-pressures in the sands under that tank on the 10th of July, 1973, 10 days after the installation. Measurements were made nearly continuously until the 8th of September, and then discontinued until the 31st of October, 1973. Readings then were taken during scattered periods until the 16th of November, 1973. During the final period, measurements were taken during a severe storm on the 6th of November, 1973.

During calm periods with significant wave heights no greater than 6.5 m, measured pore-water-pressure changes exhibited regular fluctuations in accordance with the tidal variations. During the storm on the 6th of November, 1973 pore-water-pressure rose noticeably. This is illustrated for typical piezometric readings at four different depths in Fig. 13. During the calm period on the 4th of November, nearly hydrostatic pore-water-pressures were observed. On the 6th of November, the pore-water-pressures had risen by 1-2 t/m^2 in the upper sand layer present.

These measurements demonstrated that for sand, repeated loading generates excess pore-water-pressures, although the increase was relatively modest .

Wilson and Sahota performed Work on pore water-pressures somewhat more applicable to the suction pile concept. (1980). This research examined flow rates and pore-water-pressures during continuous pumping of a suction anchor in sand. During a 1978 test with a 600 mm anchor, typical flow rates of 0.22 m^3/hour to 0.81 m^3 /hour were measured at anchor suction pressures up to 52 kN/m^2. Similar results were obtained with a 420 mm anchor during a 1979 test (Wilson and Sahota., 1980). The flow rate for the test in 1979, for instance, was about 1 m^3/hour when the anchor suction pressure was 74 kN/m^2.

Sahota and Wilson (1982) completed a further examination of pore-water-pressure changes during installation of suction anchors. Three pressure transducers were used to measure the pore-water-pressures underneath the anchor (p_1), on top of the anchor (p_2) and above the top (p_3) of a 102 mm suction anchor. A water manometer was used to measure the anchor cavity pressure Δp. Variations of pressures with anchor forces during steady pull-out at 0.6 mm/s are shown in Fig. 14, along with values of the anchor displacement ratio.

The association between the pore-pressures, p_1, beneath and, p_2, above the 102 mm suction anchor for various cavity suction pressures and embedment depth ratios is found in Fig. 15. Pressure, p_2, became zero when the anchor was at or above the soil surface but the pressure, p_1, retained a value as long as the anchor cavity was covered with the soil. At an anchor embedment depth ratio of more than 2.5 a pressure reading of p_2 nearly 80% that of p_1 was recorded. This suggested that the pore-pressure field was most sensitive to the proximity of the soil bed surface when D/B = 2.5.

During pull-out the pressure changes were related to the movement of the anchor towards the surface of the sand bed, as well as pressure/flow characteristics of the suction pump. The trend was towards decreasing suction pressures as the maximum pull-out force was approached.

Albert et al. discussed pore-water-pressures related to skirt piles in their 1982 report. It

was related that during pull-out even small upward movements of a pile in a saturated system would result in large, negative pore-pressures in the soil. The researchers stated that negative pore-pressures are usually limited by the vapor pressure of water (-1 Atm), although the pore-pressure can be reduced by 8400 kPa [827m+ 19m+ 1 Atm. (=10m) =856 m of water = 8395 kPa] at the base of the skirt pile. Only after reaching that point would cavitation occur in sand. Fine grained soils exhibit extremely high cavitation pressures, making the suction pile even safer in clay sites. Thus, extremely large forces can develop at the top of the pile due to the area of its closed end. Therefore, relatively small negative pore-pressures acting over this area are sufficient to keep soil inside the pile.

Using centrifuge tests at both 150 g and 300 g to study the changes in pore pressure during suction pile penetration in clay, the following results were generated by Hjortnaes-Pedersen and Bezuijen (1992). Penetration performance based on the results of the measurements of a 150 g test is shown in Figs. 16 (a), 16 (b) and 16 (c). As the skirt penetrated, the penetration force (friction and tip force) increased. Coincidentally, the soil rose inside and outside the skirt, with the highest excess pore-pressures being generated just before the tip of the skirt reached the level of the measuring devices. Directly beyond the tip, a rapid decrease of pore-pressure was detected. Fig. 16 shows a load cell and strain gages used to measure the forces along the skirt

Not unlike a driven pile, penetration of a suction pile into clay causes a region around the tip to be remolded, with the peak values of the excess pore-pressures in that region between pore-pressures calculated with spherical and cylindrical cavity expansion theories. After penetration, the excess pore-pressures generated along the shaft and in the clay at different distances from the shaft (r/r_o) can be described by the theory of cylindrical cavity expansion. The initial excess pore-pressure developed, just after the skirt has been placed and has come to rest, can be described by the cylindrical cavity expansion theory and is given below:

$$\Delta u_i = \Delta\sigma_m = \begin{cases} 2c_u \ln R/r & \text{if } r_o \le r \le R \\ 0 & \text{if } r > R \end{cases} \qquad [33]$$

where:

$\Delta\sigma_m$ = $[\Delta\sigma_z+\Delta\sigma_r+\Delta\sigma_q]/3$, the increase in total stress.

R = the extent of the plastic zone being defined as $R = r_o\sqrt{G/c_u}$, with G the shear modulus and G/c_u the rigidity index I_r.

r_o = the outer radius of the pile .

When the pile is open ended, as in the case of the skirt, r_o is replaced with the corresponding massive pile radius, $r_{mas} = r_o\sqrt{\beta}$, where β is the relative displaced area, calculated from $\beta = [r_o-r_i]/r_o$ (Hjortnaes-Pedersen and Bezuijen, 1992). The cavity is then expanded from the inside radius, r_i, to the outside radius, r_o. However, the inner radius, r_i, should not be the inner radius of the skirt, but the radius from which the soil underneath the skirt moves outside the skirt during penetration. Observations by Hjortnaes-Pedersen and Bezuijen of the heave in the centrifuge tests indicated that during penetration, roughly 25% of the clay from underneath the skirt went inside and 75% went outside the skirt both in the 150 g tests and the 300 g test. Therefore, the created cavity outward is not 100% but 75% of the skirt wall thickness.

Measured excess pore-pressures with the average c_u measured at the indicated level are plotted in Fig.17 together with the results of calculations using the theory of cylindrical cavity, Eqn. 33. In the calculations, a rigidity index of I_r =200, which was determined from triaxial tests done in the laboratory on samples from the preconsolidated clay layers, was used. For saturated clay (soft to stiff), it can vary between 10 to 300.

Measurements at the moment of total rest of the skirt in the first 150 g test were in good agreement with the calculations. Results of the 300 g test close to the shaft were comparable with calculated findings, but deviated more as the comparison point moves further away from the shaft.

In the second 150 g test ,the opposite is observed. In this case, the deviation was largest close to the shaft and becomes less with greater r/r_o. Reasons were provided by the researchers for the deviations between the measurements and the calculations. One major reason was the choice of c_u.

The measured decay of pore-pressures in the test happened rapidly. Around 90% of the dissipation of the excess pore-pressures at r/r_o=1.36, r/r_o=2.16 and r/r_o=3.31 occurred at a consolidation time, t, (150 g) between $8 * 10^3$ and $1 * 10^4$ seconds. Assuming the similar consolidation coefficients in vertical and horizontal directions, an estimate was made of the time factor, T, from the second 150 g test. Using the relation $T = c * t/r^2$, T_{90} is between 10 and 15 . With $I_r = 200$, T_{90} is close to 50 or t is close to $4 * 10^4$ seconds. The shortcoming of this analytical solution is the assumption that the dissipation takes place only in radial direction and not in the vertical. It was therefore decided by Hjortnaes-Pedersen and Bezuijen to perform finite element (FEM) calculations in order to compare the measured decay of pore-pressures in the second 150 g test with the theoretical, also including the vertical dissipation.

The pore-pressures inside the skirt can be described by assuming that before penetration the clay is normally consolidated, meaning that the effective stress is denoted as: $\sigma'_h = K_o\sigma'$. After penetration, the clay inside the skirt will be deformed, making the horizontal stress the major principle stress. The total horizontal stress, σ'_h, will be larger than the total vertical stress, σ_v, by $2c_u$. The mean normal stress (p) will then be $p = [\sigma_v + 2(\sigma_v + 2c_u)]/3$. The total vertical stress at a certain depth is determined by the wet weight of the clay above, which also determines the vertical stress before penetration, plus the increase in vertical stress due to the heave and adhesion. The contribution of the heave is calculated from the amount of heave, multiplied with the wet weight of the clay. The assumption that the increase in vertical stress caused by adhesion is equally distributed over the clay inside the skirt is made to calculate the contribution of the adhesion forces. Assuming that the increase in isotropic stress in the clay would lead to the same increase in pore-pressure, the following relation was found by Hjortnaes-Pedersen and Bezuijen for the excess pore-pressure in the skirt after penetration to a depth, z:

$$\Delta u = [2(1-K_0)\sigma_v+4c_u]/3 + [h\rho_c ng] + \int[2/r_i]\tau_{ad}(z)dz \quad [34]$$

Where: h is the height of heave, ρ_c is the wet density of the clay (1730 kg/m^3), g the acceleration of gravity, n the factor with which the acceleration of gravity is increased in the centrifuge and τ_{ad}, the adhesion (= $0.35c_u$) (Hjortnaes-Pedersen and Bezuijen, 1992). The results were plotted in figure 15 for K_0=0.61 together with the measured values for transducer u13. Good agreement was obtained between measurements and calculations.

The pore-pressures along the outside of the shaft were simulated with Eqn. 33 with r/r_0 = 1, but also during penetration there will be an increase in the vertical stress, and thus the isotropic stress due to the adhesion. The magnitude of this increase is not known exactly, but is dependent on the stress strain behavior of the clay. The assumption was made by Hjortnaes-Pedersen and Bezuijen that it would not be too different from the stress increase due to the adhesion inside the skirt, and the same contribution as mentioned in Eqn. 34. However, the horizontal stress would not be influenced by the adhesion, and the increase in isotropic stress would only be 1/3 of the increase in the vertical stress. This leads to the following relation presented by Hjortnaes-Pedersen and Bezuijen for the excess pore-pressure outside:

$$\Delta u = c_u ln(\beta G/c_u) + 1/3 \int[2/r_i]\tau_{ad}(z)dz \quad [35]$$

Results of this equation are also shown in Fig. 18 and show reasonable agreement.

Pore-pressure near the tip can also be calculated using Eqn. 33 but then the deformation caused by the tip is schematicized to a cylindrical cavity expansion from r = 0 to r = half the width of the tip. The excess pore-pressure is then determined by the increase in isotropic stress due to cavity expansion. However, the isotropic stress near the tip is already increased due to deformation of the clay, heave, and adhesion, as described above. Therefore the total increase in isotropic stress and the measured excess pore-pressure is the sum of both the pore-pressure inside the skirt and the contribution of the cavity expansion, leading to the following equation presented

by Hjortnaes-Pedersen and Bezuijen:

$$\Delta_u = \Delta_u\text{inside} + c_u ln(G/c_u) \quad [36]$$

Where $\Delta_u$inside is determined by Eqn. 34. In Fig. 18 the results of this equation are shown together with the measurements. According to the researchers, it appeared, that there was reasonable agreement during the second part of the penetration, which supports the notion that such high pore-pressures as measured at the tip can really be expected. However, there is disagreement during the first part of the penetration. The model used would never lead to negative values of the excess pore-pressure.

The modeling done by Hjortnaes-Pedersen and Bezuijen involved mainly static pull-out of the pile, and was involved mainly with the installation of the pile system. The calculation of the accumulated pore-pressure due to cyclic loading was presented by Jardenier et al. (1994) and is based on a resistance concept, where the gross effect from parcels of cycles is treated. The resistance against the pore-pressure build up is defined as

$$R_u = \Delta\sigma_d \; dN/ du_{cu} = r_u(N_0+N) \quad [37]$$

where R_u is the "pore-pressure resistance", N is the number of cycles, u_{cu} is the accumulated pore-pressure, and $\Delta\sigma_d$ is the double amplitude of the deviator stress. The assumption of $\Delta\sigma_d = 4\tau_{cy}$ is made, where τ_{cy} is the cyclic shear stress amplitude. In general, Jardenier et al. found that with increasing cyclic mobilization, the pore-pressure resistance parameters decrease, giving higher rates of pore-pressure generation.

The above mechanisms resist the failure of suction pile foundations. Failure of suction piles can occur during cyclic loading and under static loading.

Static Load Tests

The function of suction anchoring and suction piling is to provide a solid anchor point under tension loads. Many studies have been done to examine the behavior of static loading of these structures. The research on static loading is also the basis for more advanced work on the cyclic behavior of suction piles as well. Tension loading tests were performed as early as the 1960's with suction anchors. This initial work was done merely to test if the concept was viable. After the viability of suction anchoring and piling was established, a greater effort to better understand the mechanisms involved was undertaken.

Studies in the mid 1970's by Helfrich et al. (1976) were designed to observe visually, the failure mechanism in the sand below the anchor and to measure the maximum anchor pull-out force under static loading. In this study, the anchor was sealed into the sand by pushing it approximately 50 mm. Water was then pumped out of the anchor causing it to draw itself into the sand up to the level of an internal filter. Flow rate, anchor movement, and the reaction force on the anchor were measured and recorded at timed intervals. Pressure differences, p_o-p_f, and, p_o-p_c, (Fig. 19), were taken from mercury manometers attached to the anchor. Observations of the failure pattern, and subsequent crater formation in the sand were made during and after the tests.

Another test sequence was performed, identical to the first, except that p_o-p_s was measured (Helfrich et al., 1976). This change in protocol was to permit the calculation of the pressure drop across the filter (Fig. 19). The pore-water pressure at the failure surface was approximated from a linear extrapolation of these data, which in turn allowed the approximation of effective stress on the failure surface.

A final battery of tests were made to determine the anchor side friction. After the pile was fully embedded, the pump was turned off and the test was performed without suction. Table 3 summarizes the test results. Maximum pull-out force for each test occurred at a 10 to 20 mm vertical deflection of the anchor (Fig. 20). The force then decreased at a constant rate until a deflection of 110 to 210 mm was reached. At this point, the force declined rapidly with

increasing deflection, leveling off at the combined buoyant weight of the anchor and sand plug. The maximum pull-out force and the weight of sand pulled out by the anchor were both directly related to the flow rate.

For the tests without the pump running, sand was not pulled up with the anchor, and the maximum pull-out force was about 390 N.

A failure surface occurred near the bottom of the anchor cutting edge, and a plug of sand was pulled out with the anchor during the tests with the pump operating. Sand outside the anchor slumped to fill the void, forming a crater. The position of the failure surface with respect to the anchor cutting edge was dependent upon the flow rate. The shape of this failure surface is called a local shear failure in Fig. 21.

The pull-out force in medium to fine sand, in the laboratory, by a suction anchor of 400 mm in diameter and 250 mm in depth to the filter was found to be linearly related to the suction pressure for the range of values tested. Additionally, the weight of sand pulled out by the anchor was also found to be linearly related to the suction pressure. Both the maximum pull-out force and the weight of sand pulled out were directly related to the flow rate.

Helfrich et al. estimated that to achieve a 200 kN (20 metric ton) reaction force in the typical sandy soils of the continental shelf, utilizing three suction anchors having a L/D ratio of 0.65 and a factor of safety of two would result in each anchor being nearly 2 m in diameter and operated at a flow rate of about 6.4 $\mu m^3/s$.

In the late 1970's, Wang et al. (1978) made one of the early attempts to quantify break-out capacity of a suction anchor during static loading. Breakout capacity of a suction anchor was quantified by estimating the vertical soil pressure, p', required to reduce the original effective vertical pressure, σ_0', to the effective stress at failure, σ_{3f}', i.e. $p = \sigma_0' - \delta_{3f}'$. The vertical soil pressure, p', was expressed in terms of forces acting on the anchor, plus the attached soil wedge as shown in Fig. 22. Accordingly, at the state of failure, the vertical force equilibrium yields

$$p' = (Q - W_A - W_S - F)/A \qquad [38]$$

where Q = break-out force, W_A = buoyant weight of the anchor, W_s = buoyant weight of the attached soil wedge, F = friction and adhesion along the exterior anchor surface, and A = cross section area of the anchor.

The original effective vertical pressure, σ_0', equals the effective overburden pressure due to buoyant weights of the anchor and the soil wedge, plus the additional intergranular pressure induced by the steady-state pumping. The portion of intergranular pressure resulting from pumping was expressed as a function of the suction pressure, Δp. According to Wang et al.(1978), the vertical effective stress at failure, σ_{3f}', could be estimated using the Mohr-Coulomb failure theory together with a consideration of the excess pore-pressure developed during the anchor pull-out. The magnitude of the excess pore-pressure at failure varied with the rate of uplifting, and could be expressed in terms of the consolidation ratio, U_z, and the pore-pressure parameter at failure, A_f.

Wang et al. also stated that the friction and adhesion, F, which is mobilized along the exterior anchor wall surface is equal to the sum of adhesion, C_a, and the frictional resistance. The frictional resistance is directly proportional to the effective stress normal to the anchor wall, and is composed of the horizontal effective stress from overburden and the horizontal effective stress induced by steady state pumping. The portion of the horizontal effective stress due to pumping can be expressed in terms of suction, Δp.

Substituting all of the preceding information into Eqn. 38 and expressing in terms of the pressure yield the following break-out capacity equation proposed by Wang et al.:

$$
\begin{aligned}
q \quad = \quad & [(W_A + W_S)/A]\,[2 - Y_2'(\phi')] + \\
& 2c'\,[1 - (1 - U_z)A_f]\tan\alpha'/Y_1`(\phi') + \\
& 4\,(L/D)[C_a + (K_o g' L/2)\tan\delta] + \\
& \{C_1\,[1 - Y_2'(\phi)] + 4(L/D)C_2\tan\delta\}\Delta p
\end{aligned}
\qquad [39]
$$

where:

$Y_1'(\phi')$	=	$1 - (1 - U_z)A_f(1 - \tan^2\alpha')$
$Y_2'(\phi')$	=	$1 + [1 - (1 - U_z)A_f](K_o\tan^2\alpha' - 1)/Y_1'(\phi')$
c'	=	cohesion of test clay
U_z	=	consolidation ratio
α'	=	$45° - \phi'/2$
K_o	=	ratio of horizontal stress to vertical stress
γ'	=	submerged unit weight of test soil
δ	=	friction angle between soil and anchor wall
C_a	=	adhesion between soil and anchor wall
ϕ'	=	effective internal friction angle of the test soil

Deducting the buoyant weight of the anchor and letting $W_s \approx \gamma'L$, where L is the skirt length, Wang et al. (1978) obtained the following net break-out capacity equation:

$$q_{net} = \gamma'L[2 - Y_2'(\phi')] + 2c'[1 - (1 - U_z)A_f]\tan\alpha'/Y_1'(\phi') + 4(L/D)[C_a + (K_o\gamma'L/2)\tan\delta] + \{C_1[1 - Y_2'(\phi')] + 4(L/D)C_2\tan\delta\}\Delta p \quad [40]$$

Incorporating the previously determined anchor behavior into Eqn. 40, the following equation for the net break-out capacity results was established by Wang et al.:

$$q_{net} = q_o + \lambda\Delta p \quad [41]$$

where:

λ = slope of linear relationship between anchor capacity and suction

q_0 = $\gamma' L N_\gamma + c' N_c + (L/D) N_A$

N_γ = $2 - Y_2'(\phi')$

N_c = $2[1 - (1 - U_z) A_f] \tan \alpha' / Y_1'(\phi')$

N_A = $4(C_a + 0.5 K_0 \gamma' L \tan \delta)$

γ = $N_1 [1 - Y_2'(\phi')] + N_2 \tan \delta$

N_1 = $0.45 e^{-0.90(L/D)}$

N_2 = $0.44 (L/D) e^{-L/D}$

Here, c' = effective soil cohesion, ϕ' = effective soil internal friction, $\alpha' = 45° - \phi'/2$, δ = friction angle between the anchor wall and the soil and γ' = submerged unit weight of soil.

The equation for $Y_1'(\phi')$, suggests that the anchor resistance is composed of two components: one independent of, and the other dependent upon suction. The component, q_0, which is independent of suction, increases with increasing cohesion, c', and the skirt length to diameter ratio, L/D. λ physically represents the slope of the relation between the break-out capacity and the suction, Δp . Both q_0 and λ are dependent upon the dimension of the anchor and the shear strength property of the soil. To facilitate the direct application of the general break-out capacity equation, the equations for $Y_1'(\phi')$, $Y_2'(\phi')$ and N_c are given in graphical form for various values of A_f and K_0 in Figs. 23, 24, and 25, respectively. Also, N_1 and N_2 are plotted in Fig. 26. These figures provided a basis for practical suction anchor design.

Later, Sahota and Wilson (1982) proposed a non-dimensional break-out force parameter such as $P_u/\gamma' AD$, as well as the burial depth ratio, D/B, and the soil density or friction angle to permit collation of anchor tests data from a variety of sources. Suction anchors further required an additional quantity, the reference suction pressures, which was the internal pile suction pressure Δp. Wilson and Sahota suggested the use of non-dimensional pressure parameters $\Delta p/\gamma' B$ and $\Delta p/\gamma' D$. $\Delta p/\gamma' D$ was interpreted as the ratio of the reference pressure, Δp, to the

vertical stress, $\gamma' D$ in the soil at depth D. The related quantity $\Delta p/\gamma' B$ was felt to be more convenient in experiments in which Δp and D were the primary variables.

By fitting a family of curves to the break-out-force measurements from a 102 mm diameter buried suction anchor at seven different suction pressures, and D/B values up to 5.5, it was observed by Sahota and Wilson that the break-out force P_u varied linearly with Δp, except at very low suction pressures and deep burials. These fitted curves were described as:

$$P_u/\gamma' AD = 3.252(D/B)^{0.143} + [\Delta p/\gamma' B](0.563[D/B]^{-1} + 0.446[D/B]^{0.748}) \qquad [42]$$

When $\Delta p = 0$ Eqn. 42 reduces to

$$P_u/\gamma' AD = 3.252(D/B)^{0.143} \qquad [43]$$

For D/B values of up to about 3.5, Eqn. 43 is closely related to the measured break-out forces reported by Wilson and Sahota (1980) for a 102 mm anchor tested without applied suction.

Sahota and Wilson (1982), using a 600 mm diameter prototype suction anchor, performed sea trials. This anchor was hemispherical in form, cast in concrete, and fitted with internal flap valves so that jetting and suction flows could be passed along a single armored hose. The researchers carried out a number of tests with this anchor, but the pull-out forces proved to be greater than the loading capacity of the 60 ton research vessel being used, except at shallow burials or low applied suction pressures. In order to extend the ranges of tests, a 420 mm diameter anchor was also used. The smaller sized anchor prevented the use of valves and the concept reverted to the two-hose design illustrated in Fig. 27. The shapes of this anchor was more like a truncated cone-shaped hemisphere, and was cast in concrete.

The test site was in the Inverness Firth, Scotland, on an almost-level bed of medium sand, which contained some stones and overlay a bed of much harder material. The sand gradations are shown in Fig. 28, and other relevant data are listed in Table 4 (Sahota and Wilson, 1982).

Initially, during the burial of the prototype anchors a crater was formed at the entry point of the anchor into the soil bed. This was similar to what was observed with previous laboratory tests, but the crater was removed by leveling. The sea trials showed that this crater was of greater significance than was realized during the work with the models. The most obvious effect was the reduction in the depth of the soil bed directly above the prototype anchors. The bottom of the crater was estimated to be 0.58 m below the original soil level. This redistribution of the overburden was felt unlikely to be important at the higher values of D/B, but could be very significant when the anchor was at low burial depth ratios.

When break-out forces were normalized as shown in Fig. 29, initial observations indicated that the sea trial data were substantially below the values that might be anticipated from the model tests (Sahota and Wilson, 1982). If allowance was made, however, for the reduction in burial depth due to the crater formed by the anchor embedment procedure, the plotted points moved to a lower D/B and a higher value of the parameter $[P_u-P_{u0}]/\gamma' AD(\gamma' B/\Delta p)]$.

In the region where $0.9 \leq D/B \leq 2.6$, the corrected points lie in the same scatter band as the model data, and on both sides of the line defined by :

$$(P_u - P_{u0})/\gamma' AD *(\gamma' B/DB) = 0.563*(D/B)^{-1} + 0.446*(D/B)^{0.748} \qquad [44]$$

Sahota and Wilson conducted only two tests at higher D/B values. One of these was with the 600 mm anchor and the other with the 420 mm anchor. The results of these trials plotted in the upper part of the scatter band, or above the scatter band, suggesting that the prototype anchors at the higher D/B values developed greater break-out forces than would be predicted by model data and Eqn. 42.

Albert et al. (1987) also reported interest in the break-out capacity of suction piles. The major areas of interest of these researchers were the tension resisting forces of the weight of the soil inside the pile and the passive suction that developed when a pile was subjected to vertical tensile loads. This group found that very large forces could develop at the top of the pile by

virtue of the area of its closed end. Even relatively small negative pore-pressures acting over this area were sufficient to keep the pile in place.

Albert et al. were interested in the static uplift capacity of suction piles because they were designing an anchoring system for a TLP. Suction piles at its four corners would anchor the TLP. This group estimated that the permanent static pretension of the platform would be 18,950 kN, with a maximum axial tension for a 100-yr storm at 32,150 kN per corner. It was suggested that for a multiple pile system, only modest values of negative pressure would be required to resist storm loadings and to provide adequate factors of safety.

They also contended that even without a sealed top the internal soil adhesion forces (p_{int}) were significant. Internal adhesions would not be subjected to cyclic tensions as the external ones were, therefore limiting skin friction was calculated using API rules for static tension and the soil data. Referring to Table 5, for D = 6 m, p_{int} is of the same order of magnitude as the self weight of the soil plug, and more than half of its weight when D = 12 m. These values would be even greater with closed ends, therefore, with a sealed top, the soil inside the pile would only add to the self weight of the suction pile.

Albert et al. proposed the following factors of safety for suction piles:

Extreme Environment (associated with a 100-year storm):	FS = 1.5 B.
Operating Environment (associated to 1 year storm):	FS = 2.0 B.

B is the "bias factor" that is a function of eight aspects of pile design and performance, as indicated in Table 6, from where an average value of B of 1.28 to 1.3 could be derived.

The approach chosen for the calculations of the factor of safety assumed that there was a limited degree of uncertainty associated with the system dead weight. Therefore, a small partial factor of safety F_1 = 1.1 was applied (Albert et al., 1987). The force tending to cause the piles to pull-out, could then be obtained by directly subtracting from the tendon tension such contributions (weight of the template, piles, and related ballast / F_1). The resistance forces were then entirely a

function of the soil only, i.e., the weight of soil plug, W_{soil}, and external adhesion forces, P_f, therefore:

$$FS = \text{Resistance forces / Net tensile force}$$

$$= [\Sigma(W_{soil} + P_f)]/[T_{max} - (\{W_{template} + \Sigma(W_{pile} + W_{ballast})\}/F_1)] \quad [45]$$

$$= 1.95(\text{FS for 100 yrs}) \text{ or } 2.6(\text{FS for 1 yr})$$

where:

T_{max} = maximum tensile force

F_1 = partial factor of safety = 1.1

Further examination of the break-out capacity of suction piles under sustained loading in both clays and sand was conducted by Steensen-Bach (1987). At larger embedment ratios three different failure mechanisms for clays have been recognized as illustrated in Flg. 30:

(i) Local shear failure. If no suction is allowed to develop inside the pile, the soil-wall friction cannot exceed the tensile strength of the soil and failure develops as a local shear failure along the pile shaft the break-out force of the shaft is expressed as:

$$F = \alpha c_u(A_{se}+A_{si}) + W_p + W_w + A_t u_t \quad [46]$$

where:

α = adhesion coefficient

c_u = mean undrained shear strength

A_{se} = exterior soil/wall area

A_{si} = interior soil/wall area

W_p = total weight of the pile

W_w = total weight of water on top of the pile

A_t = tip area

u_t = pore pressure below the pile tip

The quantity obtained by inserting α as the ultimate value for N, which fulfills the vertical equilibrium Eqn. 19 for the clay plug at maximum break-out force, is termed N_2. The quantity obtained by inserting α as the ultimate value for N in Eqn. 49 which is determined at maximum break-out force, F, is termed N_1.

$$|-uA_i+\alpha c_u A_{si}| = W_s + (Nc_u-q)A_i \qquad [19]$$

(ii) Local tension failure. This occurs when the inside soil-wall friction and suction exceed the tensile strength of the soil Eqn. 47. A clay plug inside the pile is then torn apart from the seafloor leaving a hole. The break-out force is expressed as:

$$F = W_p + W_s + W_w + \alpha c_u A_{se} + \sigma_t A_c \qquad [47]$$

where:

W_s = total weight of soil plug inside the pile

σ_t = tensile strength

(iii) General shear failure. In terms of the reversed bearing capacity failure. In this case, the break-out force, F, is expressed as:

$$F = W_p + W_s + W_w + ac_u A_{se} + (Nc_u - q)A_c \qquad [48]$$

Notations used are explained in Fig. 31.

Breakout from sands is somewhat different than the case of clays. The determination of the break-out capacity of suction piles usually regards only the unit shaft resistance, τ_o, as expressed below:

$$\tau_o = a+\sigma_n \tan\delta \qquad [49]$$

For piles in sand, the adhesion term, a, is zero and the shaft resistance is entirely frictional. Suction at pile point is usually not considered, and the tensile pile capacity is calculated with the assumption of drained conditions. Depending on the break-out velocity, a transient state between the drained state (no suction at all) and the entirely undrained failure can be defined, and increased break-out capacity due to suction has been suggested. This can be calculated from Eqn. 50:

$$F = W_p + T_e + T_i + uA_i \qquad [50]$$

where:

T_e = contribution to breakout capacity from exterior shear stresses

T_i = contribution to breakout capacity from interior shear stresses

u = pore pressure below top of pile

A_i = interior cross-sectional area

In order to validate these equations, Steensen-Bach conducted monotonic break-out tests. The goal of the monotonic tests was to determine the effects on the break-out force of the soil type, strength, pile type and embedment, and break-out velocity.

Piles were pulled out of the seafloor shortly after installation at constant velocities ranging from 6 to 20,500 mm/min. 25 monotonic break-out tests were performed in Nlvaa Clay, 19 tests in Speswhite Kaolin, and 27 tests in G12 sand.

Steensen-Bach performed 6 tests in Nivaa Clay under constant tensile loading at forces

larger than the acting soil-wall friction force. Monotonic tests were analyzed with respect to the observed failure mechanisms, (i),(ii) and (iii). It was noted that the analysis and conclusions were only valid for the specific conditions of the presented tests.

The first parameter discussed was the adhesion coefficient. Tests with local shear failure along the pile shaft (i), i.e., suction was not allowed to occur at the pile top, were used to determine the values for the unitless, ultimate adhesion coefficient, α.

$$\alpha = \begin{cases} 0.36 & \text{for Nivaa Clay} \\ 0.30 & \text{for Speswhite Kaolin} \end{cases} \qquad [51]$$

When suction was allowed to develop inside the piles during upward pile displacement, the failure mode changed from local shear (i) to general shear (iii). For piles with an embedment ratio of 1.67, the maximum suction occurred at larger pile displacements than maximum break-out resistance. For an embedment ratio of 3.33, these displacements coincided. Maximum suction at an embedment ratio of 1.67 was close to the "theoretical" maximum of -100 kPa. At embedment ratio of 3.33, maximum values were significantly less (values up to -65 kPa).

Besides the embedment ratio, the magnitude of suction might depend on the strength of the clay, as indicated in tests on Kaolin 1, with stronger clay exhibiting a higher suction necessary to generate a failure in the soil.

Break-out under a sustained load was also studied. Suction piles under sustained loading generally failed in the general shear mode, except at high load levels where instantaneous transition to sliding failure took place. A plateau value for the suction which remained constant until the tensile failure, (ii), occurred, was obtained early in each test.

A logarithmic relationship between the break-out time, t, (i.e. the time to occurrence of tensile failure) and the sustained load, F, was obtained at c_u= 22 kPa for tests which failed in general shear mode was indicated by the results:

$$[F/1N] = [c_u/1kPa]\{12.65 - 0.48\log(t/1min)\} \quad [52]$$

where:

F = total break-out force

N = bearing capacity factor

t = break-out time under sustained load

Drained failure was also considered by Steensen-Bach. Six tests were carried out under drained conditions with no suction developing below the pile top. The following equations describe the observed drained break-out capacity:

$$T_e = 0.1\,\gamma'\,(a_2 - \delta)^2\,De\pi \quad [53]$$

$$T_i = 0.1\,\gamma'\,(a_2 - \delta)^2\,Di\pi \quad [54]$$

where:

T_e = contribution to breakout capacity from exterior shear stresses

T_i = contribution to breakout capacity from interior shear stresses

γ' = bulk density

a_2 = pile penetration

δ = interface friction angle (pile/soil)

De = exterior diameter of the pile

Di = interior diameter of the pile

Undrained break-out capacity was also explored by closing the pile top. This allowed suction to develop during break-out, leading to a significant increase in maximum break-out force with break-out velocity. At very high velocity, break-out capacity of 5 to 6 times the drained

break-out capacity was attained.

Eqns. 53 and 54 need to be modified, before they are used in Eqn. 50 by taking into account the upward and downward gradients outside and Inside the pile.

At failure in undrained state, Eqn. 50 was found generally to underestimate the break-out capacity.

Fig. 32 shows the velocity dependency of the suction inside the suction piles. Steensen-Bach observed that the maximum suction occurred simultaneously with the maximum break-out resistance. An almost linear increase in maximum suction with pull-out velocity was observed, which can be described as:

$$u_{max} = - 3.41 \text{ kPa} - v_p\, 0.00259 \text{ kPa mln/mm} \qquad [55]$$

where:

u_{max} = maximum suction

v_p = break-out velocity

The displacement at the time of maximum suction, Δ, increases with the pull-out velocity, varying almost linearly with the velocity, i.e.:

$$(\Delta/a_2)100\% = 8.12\% + 0.00249(v_p/1\text{mm/min})\% \qquad [56]$$

where:

a_2 = pile penetration

By combining Eqns. 55 and 56, Steensen-Bach was able to determine that the theoretical maximum suction of - 100 kPa would be reached at the time of 100% pull-out at a velocity of 36,900 mm/min.

In the range of embedment ratios 1.67 to 3.33 no significant effect on maximum suction was observed (Steensen-Bach, 1987).

Steensen-Bach was able to conclude that if suction is allowed to develop below the pile top, general shear failure, in terms of the reversed bearing capacity failure, is dominant in clays. Also, the tensile strength was only exceeded after some displacement in general shear failure mode. Furthermore, the bearing capacity factors, N, were shown to be sensitive to the undrained shear strength time of regeneration, break-out velocity and embedment ratio, but seemingly insensitive to whether Nivaa Clay or Kaolin was used as a soil deposit.

Conclusions for sands included that the reversed bearing capacity failure is of no importance. Failure occurred as the local shear failure developed along the pile shaft. However, due to the development of suction below the pile top, significantly increased break-out capacity could be obtained at break-out velocities above a certain level.

Clukey and Morrison (1993) conducted further studies on the subject of monotonic loading of TLP foundations in clay. The monotonic load tests were performed by applying a constant rate of loading to a caisson to simulate the actual TLP tendon-foundation interaction.

Each test was performed with a standard set of measurements which included: (1) measurements of the surface displacement, (2) free-field pore-pressure measurements at three different elevations, (3) pressure measurements at the caisson head (inside) and in the water column above the caisson, (4) vertical displacement measurements at two locations on top of the caisson, (5) measurement of the applied load, and (6) a set of pore-pressure measurements located inside and just below the bottom of the caisson. One test was performed with strain gauges attached at the third points along the sides of the caisson.

The uplift test results are presented in Table 7. A total of 5 tests were performed with various loading rates and caisson configurations. The results indicate that the suction force or the reverse end bearing mobilized during the tests was about 73% of the predicted reverse end bearing capacity. This ratio is referred to as the suction efficiency. To determine the reverse end bearing from the centrifuge tests, the buoyant unit weight of the caisson and the calculated

external skin friction were subtracted from the total measured uplift force.

Skin friction was determined by using an undrained shear strength equal to 75% of the undrained shear strength, since laboratory tests on normally consolidated clays typically have 70 to 80% of the undrained shear strengths determined from the in-situ measurements. This strength reduction was also verified by the strain gage and pore-pressure measurements.

The rate of loading achieved in centrifuge tests varied, but could be categorized into two ranges. Three tests were loaded to failure in times varying from 23 to 37 seconds. In terms of the pore-pressure diffusion, these times would correspond to between 2.6 to 4.1 days on a prototype scale. Two tests were performed in times varying between 118 to 176 seconds, which in terms of the pore-pressure diffusion would correspond to 13.7 to 14.7 days. The suction efficiency for the more rapidly loaded tests was 80.5%. The more slowly loaded tests had a suction efficiency of 60.8%. Clukey and Morrison felt that this suggested that the pore-pressure diffusion could reduce the suction efficiency by about 25% for increases in loading times from a few days to about 2 weeks.

Except for the long term pre-tension force, the times associated with all the applied loads (low and high frequency cyclic) were even less than the times for the tests with the most rapidly applied loads. Therefore, according to Clukey and Morrison, the most appropriate suction efficiency for design for these loads would appear to correspond to the efficiency derived from the tests with the most rapidly applied loads.

Multi-cell and simple cylindrical single-cell caissons had suction efficiencies of 63.2 and 78.9%, respectively. The researchers noted, however, that one of the two multi-cell tests was also the most slowly loaded test and had the lowest overall suction efficiency of 55.6%. The multi-cell average therefore was probably overly influenced by the results from this one test. Nonetheless, the other multi-cell test also had a suction efficiency of 70.7%, which was also slightly less than the average for all the tests. The lower suction efficiency for the multi-cell tests suggests some disturbance effects at the bottom of the caisson.

Clukey and Morrison (1993) also conducted finite element modeling comparisons. An

analysis was made to simulate uplift tests, which had an overall suction efficiency of 92.3%. The finite element analysis was performed with the ABAQUS computer program using 8-noded quadrilateral axi-symmetric elements with reduced integration. Full suction was implied in the analysis by maintaining contact between soil and caisson nodes at the top of the caisson during loading. The soil response was assumed to be undrained, therefore, pore-pressures were not taken into account explicitly.

The non-linear soil response was modeled with a tri-linear representation of the stress vs. strain behavior. The basis for selecting the appropriate stiffnesses and stress limits for each soil layer in the finite element model was provided by four isotropically consolidated triaxial compression tests. A von Mises soil model was used to approximate the soil response under varying stress conditions. For each test a trilinear curve was selected which appeared to provide the best fit to the data. Normalized soil stiffness to undrained shear strength parameters (G/S_u) were then developed and used as the basis for interpolating between layers. The S_u values were based on the undrained shear strength results obtained from centrifuge tests. For the elements adjacent to the caisson wall the value of S_u used in the analyses was 75% of the previous value . The undrained shear strength was reduced for these elements to more accurately model the skin friction along the side of the caisson.

A comparison of Clukey and Morrison's (1993) results obtained from the finite element analysis and the centrifuge testing is shown on Fig. 33. They indicated that the finite element analyses and the centrifuge data were in very good agreement to about 2-ft (0.8-m) vertical displacement. At this level of displacement the researchers noted that the two curves began to diverge with the finite element results suggesting an increase in load as the caisson continued to displace.

This prompted Clukey and Morrison to suggest that for the 0 to 2-ft (0 to 0.6-m) range of displacement, the caisson could be modeled assuming perfect suction. It was felt that the range of acceptable displacements for the caisson would most likely be within the 2-ft (0.6-m) limit. Consequently, the reduction in efficiency may correspond to displacements beyond the operational

range of interest for TLP applications.

Clukey and Morrison (1993) concluded from the results of this study that for the high and low frequency cyclic loads associated with TLP loading, the static capacity of a caisson about 50 ft (15.2 m) in diameter and 100 ft (32.8 m) deep in soils with shear strengths similar to Gulf of Mexico clays would be about 20,000 kips (89.0 MN). Prediction of this capacity is possible with traditional methods when a suction efficiency of about 80%is used to determine the reverse end bearing.

Also, a slow rate of loading led to the reduction of suction efficiency to 61% for the caissons tested, corresponding to about two weeks on a prototype time scale for pore-pressure diffusion. It was, therefore, not felt to be representative of either the low or high frequency cyclic TLP loads.

They also concluded that the finite element analysis was able to accurately predict the load-displacement behavior up to 2-ft. (0.6 m) vertical displacement. This agreement was achieved despite the centrifuge test having a suction efficiency of 92%. Clukey and Morrison therefore suggested that the methods used to calculate the full reverse end bearing might correspond to displacements beyond the acceptable range for TLP applications. The use of a suction efficiency factor of 80%, however, will maintain a conservative measure.

In another study, Iskander et al. (1993) conducted a study involving the comparison of closed top-end and open top-end piles in sand. Pull-out tests were performed on the model suction pile after the dissipation of the installation suction pressures. Piles were pulled out at a constant rate of displacement of 0.76 cm/sec. Sealed-top ("undrained") tests resulted in the creation of a suction pressure beneath the pile top causing the plug to be pulled out with the pile. Open-top ("drained") tests tended to cause the pile to pull-out, leaving the plug behind.

A typical set of pull-out data from Iskander et al. for a test with a sealed top is shown in Fig. 34. The numerical average of all of the pull-out data for the different test series is summarized in Table 8. Typical data from this study for open-top tests are presented in Fig. 35.

In Table 8, the side shear (f_s) for the tests with sealed tops was calculated as follows:

$$f_s = (Q_a - Q_s - W_p - W_{plug})/A_{so} \quad [57]$$

where: Q_a is the applied tensile force, Q_s is the suction force (pressure differential across the pile top times the top internal area), W_p is the submerged weight of the pile in water, W_{plug} is the submerged weight of the plug, and A_{so} is the outer side area of the pile. They noted that this computation ignored any suction capacity of the tip of the plug and thus resulted in elevated values of side shear. Conditions in the sand under the plug, therefore require further study and measurements.

For the tests with open tops, the plug remained in place during withdrawal so the side shear stress was calculated from:

$$f_s = (Q - W_p)/(A_{si} - A_{so}) \quad [58]$$

where A_{si} and A_{so} are the inner and outer side areas, and other terms are defined as above in Eqn. 58.

Iskander et al. state that it was clear that the development of internal suction resulted in a substantial increase in pile capacity (col. 3 in Table 8). In sealed top tests, the side shear was low for test series 1 where high vacuums during installation loosened the sand on the inside and outside of the pile. Side shears were higher for series 3 where piles were pushed into place and series 4 where minimum vacuum was used.

The increase in the side shear capacity of sealed top piles was felt to be due to the downward hydraulic gradient acting outside the pile. The pore-pressures on the outside wall of the suction pile were not measured in this study. As a first approximation, the head value at the tip was obtained using the steady state solution developed by Pavlicek (1993). The steady state solution (Fig. 36) was developed for the test condition represented by a unit suction, S, below the pile's sealed top and a water pressure head of 0.12S at the sea floor. The pressure measured at the top of the pile was therefore multiplied by 0.044 (Fig. 36) to obtain the head at the tip of the pile.

For example, in test series 1, using API RP2A, the side friction for fully drained conditions would be:

$$f_s = \sigma'_v K \tan(\delta) \quad [59]$$

$$f_s \text{ (open top)} = (0.07^* (20.7-9.81)) ^*0.8 * \tan (25) = 0.28 \text{ Pa} \quad [60]$$

The increase in the vertical stress due to the downward vertical water flow is given by γ_w/unit volume. A hydraulic gradient, i, of 2.1 was calculated from the steady state solution during the pull-out tests in the first test series. According to Iskander et al., the increase in the effective stress would result in the following increase in the skin friction, f_s:

$$f_s \text{ (sealed top)} = (0.07^*((2.1^*9.81)+ (20.7-9.81))^*0.8^*\tan(25))= 0.82 \text{ Pa} \quad [61]$$

The calculated values of the skin friction for drained and undrained conditions (0.28 kPa and 0.82 kPa respectively) were in agreement with the measured values (0.31 kPa and 0.78 kPa, respectively). It was therefore suggested that the gradient associated with pull-out suctions is responsible for the increase in the frictional resistance of suction piles.

Iskander et al. also stated that the displacement at the maximum load of open top piles was 0.4 cm (Fig. 35), which was consistent with typical displacements required to mobilize side shear of driven pipe piles in sand. Maximum suction developed for closed top piles was found at displacement of about 2 cm (Fig 34) with a sharp peak followed by slow dissipation.

Iskander et al. noted that the development and dissipation of suction pressures is a function of the rate of tensile loading, hydraulic conductivity, and the drainage length. Since all three parameters were constant throughout the testing program, the measured suctions were equal in test series 1, 3 and 4. It was felt likely that larger suctions could be sustained for longer durations in clays with lower hydraulic conductivities and in full scale installation with longer drainage lengths.

Conclusions drawn by Iskander et al. from this study include that it was not possible to perform suction installations on an unballasted model suction pile without developing a quick condition and liquefying the soil. It was felt that formation of a quick condition would be likely during field installations, particularly at shallow penetrations.

The occurrence of this quick condition resulted in a substantial reduction in the soil's penetration resistance, and accordingly a small pressure difference was sufficient to install suction piles. However, the quick condition also resulted in a reduction in the penetration distance due to the formation of an excess soil plug.

Iskander et al. also concluded that the mechanisms involved in suction installation resulted in a reduction in the frictional capacity of suction piles. Reducing the hydraulic gradient during installation resulted in an improvement of the frictional capacity but resulted in longer installation times.

Finally, suction was the dominant parameter contributing to the short term pull-out capacity of sealed top suction piles. During pull-out, the gradient associated with the suction pressures resulted in a marked increase in the frictional capacity of the suction piles. The suction developed during pull-out was also sufficient to retain the soil plug inside the pile, causing an increase in the dead weight of the pile, and eliminating the internal side shear.

In an attempt to relate previous pile loading research on gravity based platforms to suction piles, Andersen et al. (1993) conducted the following study on pile static pull-out capacity. The static failure load for the model testing was calculated with the undrained static shear strengths presented in Fig. 37. These strengths depended on the stress path and accounts for strain compatibility along a potential failure surface. The shear strength at a given point on the failure surface was interpolated between triaxial compression, DSS, and triaxial extension according to the inclination of the failure surface at that point. The strengths were representative for the constant rate of displacement and the time to failure in the model tests.

According to Andersen et al., the actual value of the measured static failure load depends on the definition of failure. The researchers based their assumption on the measured static load-

displacement curve, and suggested it was reasonable to define failure as a rotation of about $4*10^{-2}$ to $6 * 10^{-2}$ radians.

It was also stated that the calculated failure load depends on the load inclination. In the static model test it was observed that the load inclination gradually decreased as the model rotated, and the load inclination was reduced to about 7.5° from the vertical at failure. This produced a smaller horizontal-load component and a smaller overturning moment for a given actuator load, and it caused the calculated static failure load to increase. This predicted a static failure load in close agreement with the measured static failure load.

The predicted critical failure surface for the static test is shown in Fig. 38(a). The measured displacements of the model and the surrounding clay surface, also shown in Fig. 38(a), were reasonably consistent with the predicted critical failure surfaces. Epoxy columns used to measure the deformations within the soil (Dyvik et al. 1993) also seemed to indicate agreement between the actual failure surface and the predicted one for most of the failure surface.

The weight of the soil did not cause displacements, and the displacements of the anchor were due to the loads from the anchor to the soil. Andersen et al. assumed the clay was weightless for simplicity. For the soil parameters to be consistent with this, the shear strength and the stress-strain relationships were defined relative to the initial shear stress due to the weight of the soil, τ_o . The modified static shear strengths used in the calculations were then $(s_u - \tau_o)$.

Both s_u and τ_o varied with the angle, α, between the major principal stress and the vertical axis, and the modified shear strength was expressed as

$$(s_u - \tau_o)_\alpha = S_o + S_1\cos(2\alpha) + S_2\cos(4\alpha) \qquad [62]$$

where: $\tau_o = (1 - K_o)p_o \sin(\alpha)\cos(\alpha)$; p_o = effective vertical overburden stress from the weight of the soil; and K_o = coefficient of lateral earth pressure at rest. The same numerical values of K_o as used for consolidation of the laboratory specimens were used in the calculations.

The constants, S_1 and S_2, were determined such that the expression fitted the triaxial

compression, DSS, and triaxial extension static shear strengths for α = 0°, 45°, and 90°, respectively.

The expression used by Andersen et al. for the tangential shear modulus was:

$$\log G_t/(s_u - \tau_0)_\alpha = \log [G_0/(s_u - \tau_0)_\alpha] - C_1\zeta - C_2\zeta^2 - C_3\zeta^3 \quad [63]$$

where G_t = tangential shear modulus, $\zeta = (\tau - \tau_0)_{max}/(s_u - \tau_0)_\alpha$. The constants, C_1 through C_3, were determined based on the normalized stress-strain curve for DSS tests, as shown in Fig. 39 (a). It can be seen from Fig. 39 (a) that using the DSS curve both for DSS and triaxial conditions is likely to give somewhat higher calculated displacements for loads in the range of 75 - 100% of the failure load.

As stated by Andersen et al. (1989), Eqns. 62 and 63 are meant to be valid for any type of undrained loading, (independent of direction of loading). Similar equations were previously successfully used to back-calculate the displacements measured in model tests of gravity platforms on clay .

The predicted displacements at mudline elevation for model test 1 are plotted versus the pull-out load and compared to the measured displacements in Fig. 40. For all the displacement components (rotation, horizontal, and vertical), the predicted displacements are in agreement with the measured displacements for loads up to about 75% of the failure load. This was felt to be within the working load range for a typical prototype.

For loads in excess of 75% of the failure load the predicted displacements are greater than measured. This is probably because the normalized stress-strain curve for DSS tests was used for all stress paths in the calculations.

A finite element analysis also accompanied this study. The calculated displacement pattern is consistent with measurements presented in Fig. 38 (a). The predicted failure loads were within 6% of the measured failure loads for the model tests. The type and location of the predicted failure surfaces were reasonably consistent with the measured displacements, but the epoxy

columns used to monitor the deformations within the soil seemed to indicate that the failure surface might deviate somewhat from the predictions.

The predicted rotational, horizontal, and vertical model displacements were in good agreement with the measured displacements. In the static model test, the agreement was very good for loads below 75% of the failure load. At higher loads the predicted displacements were somewhat higher than measured.

Dyvik et al. (1993) also reported on model tests of a suction anchor in soft clay for the tension-leg platform at the Snorre site in the North Sea. The model tests included one static test. The test was loaded in tension at an angle of 10° from the vertical.

Some of the results from the static model test after the application of the inclined load are shown in Fig. 41. The abscissa in each plot represents time. The first plot shows the variation of the actuator load. The next plot shows the pore-pressure variation measured at the skirt tip on the back side of the model). The third plot shows the cell pressure variation measured in the top of the skirt compartment on the back side of the model. The last three plots are the predominant components of displacement derived from the measurements made by six LVDTs. These displacements were referenced to a point at the center of the model in plan and at the level of the clay surface surrounding the model in elevation. The horizontal displacement (x axis) is in the direction of the horizontal component of the inclined tension applied to the model, the vertical displacement (z-axis) is upward, and the rotation is about the horizontal y-axis.

Based on the measurements, an observation was made by Dyvik et al. that the penetration resistance at full penetration was approximately equal to the submerged weight of the model (33 kN).

Continuing the research on suction anchors, Tjelta and Haaland (1993) tried to answer the question "Is tension or uplift capacity in sand possible?" Tjelta and Haaland were interested not in an anchor with active suction, but rather in a skirt pile with no active suction being applied.

It was felt necessary by Tjelta and Haaland to initially define whether the nature of the actual problem was drained or undrained. They were also interested to discover whether, in an

undrained soil, what maximum gradient could be allowed in order to avoid erosion, local failure, and loss of capacity.

Small scale testing by Tjelta and Haaland took place in the years from 1989 to 1991. All tests indicated that the suction capacity of plate-skirt foundations in sand was a real phenomenon, but difficult to investigate in small scale testing, since tests behaved partly drained due to short drainage paths.

The conclusion from all work performed, both theoretical and experimental, pointed in the direction that the undrained suction capacity in sand is very dependent on permeability, or more precisely coefficient of consolidation (Tjelta and Haaland, 1993). There was also the problem of performing realistic model tests in sand and of getting realistic effective stresses, as well as realistic drainage conditions in relation to load periods. This was deemed very fundamental as drained, partly drained, or undrained behavior is difficult to predict. Consequently, only large scale tests were believed to be able to provide convincing test results that could support necessary model development. Further, only field tests could provide realistic penetration results.

Tjelta and Haaland saw two primary needs which both concerned the feasibility of an economical plate-skirt foundation, i.e. the penetration and the suction capacity in sand. The problem of the skirt penetration caused the researchers much concern prior to the field tests as the limited initial penetration calculated was not felt to be sufficient to provide a good seal for continued suction penetration.

The test structure utilized was 3 x 3 meters cross sectional area with the caisson simulating the plate-skirt foundation model being 1.5 meters in diameter and 1.7 meters in height (Fig. 43, Tjelta and Haaland, 1993). This caisson was fitted within four legs and could be penetrated to its full depth with suction alone or in combination with deadweight. The caisson was penetrated by weight to an initial penetration of up to 0.9 meters followed by suction penetration to the full depth.

Tests were carried out at three different sites, one at block 16/11 and two at the Sleipner field. Soil conditions at the sites were dominated by sand. At Sleipner T and block 16/11 the sand

was very dense and at Sleipner B silty and clayey and of medium density.

A total of 15 test locations at the three sites were carried out and the assorted test parameters were systematically varied. Examples of test results are shown in Fig. 44 (penetration results). According to Tjelta and Haaland, the comparison between Figs. 42 and 44 is quite interesting from a geotechnical point of view, and clearly shows the limitations of using empirical relations. This comparison also shows the benefits of performing site-specific field tests. In short, the problem of achieving sufficient skirt penetration is almost eliminated.

The effect of cyclic loading on the static pull-out capacity is shown in Figure 45. Pull 1 is the static pull-out capacity after initial penetration; Pull 2 is after a first cyclic program; Pull 3 after a second cyclic program, etc.. The cyclic program led to an increased pull-out capacity. Test 5 gave an even higher capacity, showing the effect of a different penetration techniques in addition to a comprehensive cyclic program.

In 1994, Morrison and Clukey reported on the results of 1 g and centrifuge model tests. The tests used a stainless steel pile model with dimensions of 18.8 cm by 9 cm depth. The surface area to be embedded in the soil was roughened to provide a pile roughness similar to that from the 1 g model program. The test set-up allowed the pile to be installed, and subsequently loaded without stopping the centrifuge to change out any of the equipment. In all, a total of seventeen different measurements were made during the course of these tests.

The pile was initially allowed to penetrate the soil under its own self-weight, reaching from 79% to 97% of the required penetration of about 82 mm. During this phase, the pile head valves were kept open to prevent build-up of pressure. The valves were then closed and the pressure in the cells was reduced until the pressure differential between the outside and the inside caused the pile to reach the final penetration depth.

Prior to starting the loading phase, a period of 2.25 hours was allowed for the dissipation of pore-pressures created by installation. Loading then commenced by the application of tension via a cable connected to the servo-controlled hydraulic jack, which was aligned to apply the load at an inclination angle of 10° from vertical. To simulate undrained conditions, the loading was

applied relatively quickly, with the time to reach peak load typically being about two minutes. Load was applied until displacements corresponding to 15% to 30% of the caisson height were achieved. Displacement of the pile and pore-pressures in the pile cells and soil were monitored throughout the tests). Attempts were made to identify and map the main failure surface by using a colored spaghetti, which had been inserted into the soil.

The combined results from all four static tests are presented in Fig. 46 as curves of force versus displacement. With the exception of the centrifuge test performed on the Lysaker clay having the higher strength profile, the results displayed very good similarity. Also included in Fig. 46 are the results from the static model test performed by NGI at 1 g (scaled to the centrifuge units).

Pore-pressures were measured by Morrison and Clukey in the cells comprising the pile and in the soil at and below the tip of the pile. Measurements of changes in the pore-pressure in the cells during pull-out were categorized according to the cell location, and are presented in Fig. 47 as curves of changes of the pore-pressure versus average vertical displacement. With the exception of the higher suction pressure observed in the first test on Lysaker (and the questionable value observed on one transducer in the first test on Speswhite clay), the results show consistent trends and similar values.

The agreement observed between the force versus displacement relationships for three centrifuge tests having similar strength profiles and the results from the 1 g model test performed by NGI were felt to strengthen the credibility of using centrifuge modeling for this application. Additionally, initial evaluations also indicated that differences in behavior observed between the two types of clay tested were small.

Rao et al. (1997) tested model suction anchors of different L/D ratios (1.0 and 2.0 : 1.0) in a two phase testing program involving short term and sustained pull-out. Under the short term monotonic loading, pull-out tests were conducted to estimate the ultimate uplift capacity (P_u) of the suction anchor which also brought out the variation of suction pressures with the anchor movement at the top of the soil plug and at the anchor bottom.

In the sustained load tests, model anchors were subjected to different sustained loads (F) which were less than the short term ultimate uplift capacities (P_u) as obtained from the above short term load tests. These load tests were conducted for a sustained load level of (F/P_u) of 25%, 50% and 75%. The variations in anchor displacement, suction pressure at the top of the soil plug, and anchor base with time (t) for given sustained load levels (F/P_u) were brought out in these tests.

The typical pull-out load-displacement curves obtained from short-term pull-out load tests on model suction anchors of different L/D ratios are shown in Fig. 48. These curves were obtained from tests on anchors embedded in a clay bed. From these curves, three distinct phases in the pull-out behavior were observed. In phase 1, at the initial ranges of the deformations up to 2.0 mm, a steep rise was seen in the pull-out resistance, followed by phase 2 in which there was a gradual and slow increase in the pull-out resistance with deformation. However, in phase 2, the deformation was quite large. In phase 3, there was a reverse curve exhibiting a sudden increase in the pull-out resistance, followed by sudden pull-out of the anchor. A soil plug was noted inside the anchor, which increased the pull-out capacity.

From the load deformation curves presented in Fig. 48, a steep rise in the capacity is seen even at deformations less than 1.5 mm, indicating that the skin friction predominates in this phase. As the plug is formed, only the external skin friction is mobilized. Phase 1 is followed by a large deformation process (phase 2) which can be called suction induced reverse end bearing, and lasts to deformations of as much as 12 mm. Beyond this stage, the tensile strength of the soil at the anchor bottom mobilizes. When the pull-out force exceeds the load capacity of these three components, there can be a rupture in the soil mass at the base of the anchor and the anchor gets pulled out clear of the base. Results presented in Fig. 48, show that with an increase in L/D, there is an improvement in the ultimate anchor capacity.

Suction pressure showed a variation at the top of the soil plug. The variation in suction pressure at the top of the soil plug with anchor displacement is shown in Fig. 49, for the L/D ratios tested. These suction pressures are negative, and the transducers used in this set-up were

capable of measuring the negative pressures, i.e., pressures less than atmospheric pressure up to -100 kN/m^2. The curves show that the suction pressure increases with an increase in the anchor displacement but does not exhibit a clear peak value. This confirms that suction remains developed during the entire pull-out process and that the soil plug remains intact within the anchor.

Suction pressure showed a variation at the anchor bottom also. Fig. 50 shows the typical plot of the change in suction pressure at the anchor base with vertical displacement for various L/D ratios. At the anchor bottom, the suction pressure increases with displacement to reach a maximum value, unlike the pressure variation at the top of the soil plug. Peak pressure is mobilized at relatively low displacements after which it drops down to a constant value at larger displacements.

Sustained load tests were also performed on the piles for all the given L/D ratios varying the sustained load levels (F/P_u) in the range of 25%, 50% and 75%. In these tests, by keeping the static load constant, time dependent observations of anchor displacement and pore-pressure changes at the top of the plug and anchor base could be made. Fig. 51 shows the typical plot of the anchor displacement with time for the different F/P_u values corresponding to L/D of 2.0 . From this plot, Rao et al. observed that for any given sustained load levels (F/P_u), the anchor displacement increases initially with time and then it becomes more or less stable. Also, with the increase in sustained load levels, the corresponding displacement at which the anchor was stabilized also increased. This was felt to imply that for a given time, the magnitude of the anchor displacement increases with the increase in F/P_u. Further, as the sustained load level (F/P) increases, the rate of strain increases significantly before the movement was stabilized. Almost the same trend was observed for L/D of 2.0. In all the sustained load tests, it was observed by Rao et al. that even for the maximum sustained load level of 75%, the anchor failure in the form of complete pull-out did not occur within the observed time frame.

The change in pore-water-pressure at the top of the soil plug and at the anchor bottom with time for different sustained load levels are shown in Figs. 52 and 53, respectively. These

plots correspond to L/D of 1.0. From both plots, it is noted that the magnitude of suction pressures mobilized for a given F/P_u value stabilized after a slight decrease with time.

Based on the results of their model tests, several conclusions were drawn by Rao et al.: First, displacements corresponding to 16 % of the anchor diameter were necessary to mobilize the ultimate pull-out capacities in suction anchors under short term loading. This large deformation enables the mobilization of the skin friction, suction induced reversed end bearing, and the tensile strength of the soil at the anchor base.

Secondly, under the specific conditions of the testing program, the soil plug moved with the anchor up to the failure point and contributed to the break-out capacity. Adequate suction pressure remained developed at the anchor top to hold the soil plug in position.

Furthermore, under short term monotonic loading, the suction pressure at the top of the soil plug increased with the increase in the anchor displacement right up to the failure point and there was no well-defined peak in the suction pressure mobilized. However, at the anchor bottom, the suction pressure increased with displacement to reach a maximum value. The peak pressure value was mobilized at relatively low displacements and then it dropped down to a constant value at larger displacements.

Lastly, under sustained pull-out, even at a sustained load level (F/P_u) of 75%, the anchor failure in the form of complete pull-out did not occur within the observed time frame. In the sustained load tests, up to a sustained load level of 75%, the anchor movement became stabilized with time. However, the suction pressure developed at the top of soil plug and at the anchor base stabilized after a decrease with time.

Cyclic Loading

Concerns about cyclic loading on foundations of ocean structures was expressed as early as the 1970's (Clausen et al., 1975). The Ekofisk tank was first of a number of concrete gravity

structures that were placed in the North Sea (Clausen et al., 1975). The submerged weight of the structure was 190,000 metric tons, with wave action also causing large repetitive horizontal forces and overturning moments. The 100-year wave used for design was estimated at 24 m high. Model tests by Clausen et al. showed that the 100-year wave would exert a horizontal force at the seafloor of 78,600 tons and a moment of 2,800,000 ton-meters. Several thousand smaller waves that would occur during a maximum storm were also of concern to the researchers.

On the 19th of November, 1973 a storm with an estimated wave height of 21 m, corresponding to 90% of the 24 m high 100-year wave, was encountered at the Ekofisk site (Clausen et al., 1975). To interpret geotechnical data, it was essential to understand the wave forces acting on the tank. These forces were evaluated for given values of wave height and wave period. The tank was subjected to a 21 m high wave of period 15 seconds on the 19th of November 1973, subjecting the structure to the following forces:

Vertical force:	190,000	tons
Horizontal force:	69,000	tons
Overturning moment:	2,500,000	ton-meters

The problem of forces generated by cyclic loading of deep sea-based structures became even more acute as gravity-based oil production platforms increased in size. New technologies and ways of approaching the problem became necessary. Andersen and Lauritzen (1988) proposed a method for the design of piled foundations for deep sea platforms. Their procedure accounts for the redistribution of average stresses that occur during cyclic loading, determining if the failure mode will be large cyclic displacements, large average displacements, or a combination of both (Andersen et al., 1993).

In order to analyze better, the problem of cyclic loading, Andersen and Lauritzen first defined some material parameters. The average shear stress, τ_a, was composed of, (1) the initial shear stress within the soil prior to the installation of a platform, $\tau_0 = 0.5\ (1 - K_0)p_0'$, where $p_0' =$

the effective overburden stress; and K_o = the coefficient of lateral earth pressure at rest; and (2) an additional shear stress, $\Delta\tau_a$, which is induced by the submerged weight of the platform.

The initial shear stress τ_o was specified to be acting under drained conditions, and the soil would be consolidated under this stress. The shear stress due to the weight of the platform, $\Delta\tau_a$, first acted under undrained conditions, but as the soil consolidated under the weight of the platform, this shear stress also acted under drained conditions.

The cyclic wave loads would cause the cyclic shear stress, τ_{cy}. . Because storm wave heights and periods vary continuously from one wave to another, and the cyclic shear stress would also vary from cycle to cycle.

Andersen and Lauritzen (1988) presented examples of soil behavior during cyclic loading as shown in Figs. 55 (a) and (b). For the DSS test with symmetrical cyclic loading with $\tau_a = 0$, the cyclic shear strain, γ_y, increases with an increasing number of cycles, and the failure mode is large cyclic shear strains. The researchers also stated, however, that failure due to cyclic loading might not necessarily involve large cyclic shear strains. Andersen and Lauritzen provided an example of this in Fig. 55 (b), where the failure mode was by large average shear strains, and relatively modest cyclic shear strains.

The procedure defined by Andersen and Lauritzen for the calculation of failure is based on the assumption that the cyclic shear strength, $\tau_{f,cy}$, is the sum of the average and cyclic shear stresses that cause failure after a given number of cycles :

$$\tau_{f,cy} = (\tau_a + \tau_{cy})_f \qquad [64]$$

Figs. 56 (b) and (c) and 57 (b) and (c) show how the cyclic shear strength can be illustrated with fully drawn curves. The numbers along the curves indicate the average and cyclic shear strains at failure. Points with the same combination of cyclic and average shear strains at failure are connected by dotted curves.

The diagrams in Figs. 56 and 57 show that for a given type of soil, the cyclic shear

strength depends upon the stress path, OCR, τ_a , and the number of cycles in the applied load history. The diagrams are valid for situations where τ_{cy} is constant during the storm. A real storm is composed of waves with varying heights and periods, and the soil elements beneath a platform would be subjected to a cyclic shear stress that varies from one cycle to another .

Studies by Andersen and Lauritzen of clay under cyclic loading have shown that although the cyclic secant shear stiffness may be a function of a number of parameters, two parameters with the greatest importance are the current effective stress $p'_a = 1/2(\sigma'_1+\sigma'_3)$ and the cyclic shear stress, τ_{cy}. The "average" shear stress, τ_a, Fig. 58 (b) has little influence unless it is so high that the overlain cyclic shear stress brings the soil sample to failure repeatedly, i. e., $\tau_a + \tau_{cy}$ reaches the shear strength.

It is necessary to determine the equivalent number of load cycles with constant τ_{cy} that will produce the same effect as the real cyclic load history. The equivalent number of cycles, N_{eqv}, can be applied when determining the strength from diagrams like those in Figs. 56 and 57. According to Andersen and Lauritzen , N_{eqv} is dependent on τ_a and the type of test (triaxial versus DSS), therefore, one should determine N_{eqv} for both DSS and triaxial tests and for various values of τ_a. In their study, Andersen and Lauritzen determined N_{eqv} with a procedure utilizing contour diagrams of the type shown in Fig. 58.

The following is a synopsis of the steps needed to calculate failure criteria for gravity based platforms as proposed by Andersen and Lauritzen:

1. Assume a combination of γ_a and γ_{cy} at failure.

2. Determine the values of τ_a corresponding to the assumed γ_a and γ_a from the cyclic shear strength diagrams (Fig. 60). The values of τ_a should be determined from the triaxial compression, DSS, and triaxial extension loading.

3. Determine the location of potential failure surfaces that give equilibrium with the weight of the platform and the soil. This can be done by specifying the τ_a-values determined in step 2 as strengths in limiting equilibrium stability analyses with the weight of the platform and the soil as the driving force. The value of τ_a at each point can be determined by interpolation between τ_a for compression, DSS, and extension conditions, depending on the inclination of the potential failure surface at that point. (With the sign convention used in the laboratory tests and in the diagrams in this paper, the sign of the extension value of τ_a from the diagrams should be changed when used in this analysis). The location of surfaces that fulfill the equilibrium with the platform weight can, for example, be expressed by the location of the circle centers as shown in Fig. 61.

4. Determine the cyclic shear strengths $\tau_{f,cy}$ corresponding to the combination of γ_a and γ_{cy} assumed in step 1 from the cyclic shear strength diagrams (Fig. 60). The values of $\tau_{f,cy}$ should be determined for the triaxial compression, DSS, and triaxial extension loading.

5. Perform stability analyses with the cyclic shear strength obtained from step 4 and with cyclic wave forces and platform weight as driving forces. The value of $\tau_{f,cy}$ at each point can be determined by interpolation between $\tau_{f,cy}$ for compression, DSS, and extension loading, depending on the inclination of the potential failure surface at that point. The analyses should be made for the surfaces that were found to fulfill equilibrium with the weight of the platform and the soil in step 3. The critical surface is the one that gives the lowest material coefficient γ_m This is shown in Fig. 61.

6. Return to step 1 and repeat the calculations for another combination of γ_a and γ_{cy} This iteration should be continued until the combination of γ_a and γ_{cy} that gives the lowest calculated material coefficient in step 5 has been established.

Andersen and Lauritzen suggested that in practice the calculations are relatively simple and fast to perform, provided that the cyclic shear strength curves (Fig. 60) and a convenient limiting equilibrium stability computer program are available. Figs. 56, 57, and 59 present cyclic shear strength values of Drammen clay for various conditions. Andersen and Lauritzen mentioned the limiting equilibrium computer program CAP (Lauritzen and Schjetne 1976) as a good choice. The Norwegian Geotechnical Institute has extended the program to enable the analysis of different types of slip surfaces.

Although most of the work done involving cyclic loading of deep sea structures was centered on gravity based platforms, studies related to cyclic loading of TLP's were discussed as early as 1982. Hoeg (1982) undertook the study while working on the first TLP which was

anchored to the seabed using standard piling techniques, in the Hutton Field in the North Sea. With the use of piles to anchor a TLP, Hoeg suggested that one needs to consider both tension and compression loads as they relate to stress, strain, and cyclic degradation of soil properties. These effects are important when considering the capacity and long term pull-out behavior of piles for tension leg structures.

Hoeg considered a pile subjected to a sustained axial tension force P_{av} as well as a cyclic axial load P_{cy} as an example (Fig. 62). During a storm the cyclic load magnitude and frequency would vary. After pile installation, but prior to pile loading, a soil element close to the pile shaft would be subjected to effective stresses, which changed during reconsolidation after installation of the pile. The application of the sustained load, P_{av}, would introduce an additional shear stress, τ_{av}, in the soil element, which might or might not consolidate under the shear stress before the $\pm \tau_{cy}$ was introduced (Fig. 62). The laboratory simple shear test apparatus was deemed well suited for a study of soil elements subjected to such a stress history. The results were schematically presented in the normalized diagram illustrated in Fig. 63, where s_u denotes the undrained shear strength of the soil element when consolidated to the in-situ stresses and sheared to failure by monotonically increasing the shear stress. A boundary line is seen between the "stable" and "unstable" regions for a given number of cycles applied. Hoeg discerned that outside the boundary the imposed stress conditions led to a progressive accumulation of permanent (average) strains or a progressive increase in the cyclic strain amplitude before the given number of stress cycles was reached. Inside the boundary, the situation stabilized after the first few cycles. The position of the boundary between the "stable" and "unstable" regions was felt by Hoeg to be dependent on the number of cycles (or storm duration) the soil element would be called upon to endure.

The same reasoning applied to the individual soil element was also applied to the pile in Fig. 62. Hoeg assumed that the pile, when subjected to a monotonically increasing load, pulled out of the ground when the load was equal to P_{ult}, while the somewhat smaller load, P_{cr}, denoted the load level at which the rate of creep deformation exceeded a certain acceptable value (Fig. 64). The load P_{cr} would be used to normalize the average and cyclic pile loads in an interaction

diagram corresponding to the one shown in Fig. 63.

Hoeg stated that a very large number of cycles needed to be applied to ensure that a truly stable situation was reached (refer to Fig. 63) and not only a situation which seemed stable but actually deteriorated when the cycling was continued. Puech (1982) concluded that:

$$P_{max}/P_{cr} = (P_{av} + P_{cy}) / P_{cr} = 0.6 \quad [65]$$

where:

P_{av} = sustained axial tension force

P_{cr} = load level at which the rate of creep deformation exceeds acceptable value

P_{max} = maximum load level

P_{cy} = cyclic axial load

to avoid a progressive pull-out of the pile, and this criterion is discussed below.

Earlier efforts by Andersen et al. (1978) demonstrated that it is not P_{max} that governs the soil behavior during cyclic loading. This is shown on Fig. 65 which illustrates the results from three triaxial tests performed by Hoeg on identical soil samples subjected to the same τ_{max} but varying τ_{av}. The sample subjected to reversal in the direction of the resulting shear stresses deteriorated much more dramatically than the two others did. The reason why Puech (1982) found it adequate to define his criterion in terms of P_{max} might be due to the fact that he only performed tests for which P_{av}/P_{cr} varied within the limited range 0.3 to 0.4. For a tension leg platform (TLP), the tethers cannot take compression, so any reversal occurs in the direction of average shaft friction.

Further investigations undertaken by Clukey and Morrison (1993) described the problems faced by TLP foundations in more detail. Clukey and Morrison in Fig. 66 present a schematic of the various loads imposed on a TLP. The various environmental forces are wind, waves, and currents, all of which tend to cause overturning moments on the TLP hull. The TLP also has two

additional loads as a result of set-down and mispositioning. Mispositioning loads occur when the TLP is slightly offset from the desired location. Set-down results from the lateral displacement of the hull, which tends to lower the mean position of the hull.

Clukey and Morrison discussed cyclic loading as it related to the above parameters. Cyclic loads are those applied rapidly enough (seconds to minutes) to generate an undrained soil response, and are derived mostly from wave forces, although there is some contribution from the mispositioning and set-down loads. Reverse-end-bearing capacity induced by the passive suction at the bottom of the suction pile can generally be counted on to resist the cyclic loads.

Interest in the cyclic loading behavior of suction piles continued with a study by Andersen et al. (1994). In an effort to further his previous work on foundation loads of deep sea platforms, Andersen et al. modified the earlier procedure (Andersen and Lauritzsen, 1988) for determining the bearing capacity for gravity-based platforms. This modification was to allow the use of the procedure for calculating the pull-out capacity for anchors for TLP's. The only modification needed to adapt the procedure (described earlier in this section) to calculate the pull-out capacity for anchors is to use extension shear strengths instead of compression shear strengths in the soil beneath the structure, and compression shear strengths instead of extension shear strengths in the soil outside the platform (Fig. 67).

Andersen et al. also stated that the pull-out capacity should be calculated with limiting equilibrium analyses. It was also stipulated that various types of failure surfaces should be analyzed along with a search to find the location of the surface that produces the lowest bearing capacities. The critical type of failure surface depends on several factors, including the load inclination, the ratio between static and cyclic loads, the shear strength profile, and the embedment depth to diameter ratio of the anchor.

Andersen et al. performed the limiting equilibrium analyses with the cyclic shear strength of the soil. The cyclic shear strength was determined from cyclic triaxial and DSS laboratory tests consolidated to in-situ vertical and horizontal effective stresses. Tests were run to failure under conditions that simulated the stress conditions along the potential failure surface as closely as

possible (Fig. 67). The tests were run stress-controlled with various constant average (static) and cyclic shear stresses.

As presented by Andersen et al., a soil element subjected to a combination of average and cyclic shear stresses would respond as indicated in Fig.68. The soil element in Fig. 68 was consolidated under a shear stress, τ_0. The shear stress is increased by $\Delta\tau_a$ to τ_a under undrained conditions, and then a cyclic shear stress τ_{cy}, was applied. The permanent and the cyclic shear strains, γ_p and γ_{cy}, would increase with the number of cycles, and after a certain number of cycles, the shear strains would be large leading to failure. The failure might occur either as large cyclic shear strains, large permanent shear strains, or as a combination of the two, depending on the values of τ_a and τ_{cy}. Andersen et al. stated that the cyclic shear strength, $\tau_{f,cy}$, would be:

$$\tau_{f,cy} = (\tau_a + \tau_{cy})_f \qquad [66]$$

The researchers noted that the cyclic shear strength was not a material constant, but depended on the cyclic load history (e.g. the number of cycles), τ_a, and the stress path (e.g. triaxial vs. DSS type of loading).

The actual cyclic load history was in the calculations represented by an equivalent number of cycles, N_{eqv}, at a constant cyclic load that produces the same effect as the actual cyclic load history.

According to Andersen et al., the combinations of τ_a and τ_{cy} that caused cyclic failure for a given number of cycles and the failure mode could be determined from the triaxial and DSS laboratory tests and plotted as functions of τ_a and τ_{cy} in Fig. 70. Each point represents one test, and the numbers written beside the point identify the number of cycles to failure as well as the failure mode.

The cyclic shear strength, defined above as $\tau_{f,cy} = (\tau_a + \tau_{cy})_f$, can be established by replotting the data in Fig. 70. The result is shown by Andersen et al. in Fig. 71, which demonstrates that the cyclic shear strength and the failure mode depend on τ_a, the number of cycles, and the type of test.

The procedure to calculate the pull-out capacity of an anchor subjected to a combination of static and cyclic loads is explained by means of the simplified example in Fig.72. The normalized cyclic shear strength diagrams are valid for the upper 0.77 m of the soil profile at the site for the model tests. Similar diagrams have been established by Andersen et al. (1994) and used for the clay beneath 0.77 m.

With the τ_a distribution that exists in the soil prior to cyclic loading, the cyclic shear strengths of the four elements are indicated by Andersen et al. in the cyclic shear strength diagrams as points 1A, 2A, 3A and 4A in Fig. 72. From the location of the four points on the curves, the researchers noted that the different elements along the potential failure surface would have different failure modes and tend to fail in different ways. This will not satisfy strain compatibility along the potential failure surface and therefore cannot occur. According to the researchers, the average stresses must therefore redistribute in such a way that the failure mode (i.e. the combination of γ_p and γ_{cy} at failure) is approximately the same in all the elements along the potential failure surface. An example presented by Andersen et al. of the stress redistribution, which fulfills strain compatibility, is shown in Fig. 72 by points 1B, 2B, 3B and 4B.

It was also noted that in order to determine the stress redistribution and the values of τ_a at failure, the following requirements must be included in addition to the standard requirements for limiting equilibrium analysis (Andersen et al., 1994):

* Strain compatibility along the failure surface both for average shear strains and for cyclic shear strains

* Equilibrium between the static loads and the average shear stresses along the failure surface.

According to Andersen et al., with these two conditions, the distribution of τ_a, the cyclic shear along the potential failure surface, and the factor of safety can be determined. An iteration process similar to that seen earlier in this section is needed to determine the critical failure mode

and the minimum safety factor. The calculation proposed by Andersen et al. includes the following steps:

1) Assume a combination of γ_p and γ_{cy} at failure (e.g. points 1B, 2B, 3B and 4B with $\gamma_p \pm \gamma_{cy} = 15 \pm 3\%$ in Fig. 72).

2) Read off the values of τ_a corresponding to the assumed γ_p and γ_{cy} from the cyclic shear strength diagrams (Fig. 72). The values of τ_a should be determined for triaxial compression, DSS and triaxial extension type of loading.

3) Determine the location of potential failure surfaces that give equilibrium with the weight of the platform. This can be done by specifying the τ_a values determined in Step 2 as strengths in limiting equilibrium stability analyses with the static load as the driving force. The value of τ_a at each point can be determined by interpolation between τ_a for compression, DSS and extension conditions, depending on the inclination of the potential failure surface at that point. (With the sign convention used in the laboratory tests and in the diagrams in this chapter, the sign of the extension values of τ_a from the diagrams should be changed when used in this analysis). The location of surfaces that fulfill equilibrium with the static load (i.e. a safety factor of 1.0) can be expressed by the location of the circle center, as illustrated in Fig. 73.

4) Determine the cyclic shear strengths, $\tau_{f,cy}$ corresponding to the combination of γ_p and γ_{cy} in Step 1 from the cyclic shear strength diagrams (Fig. 72). The values of $\tau_{f,cy}$ should be determined for triaxial compression, DSS and triaxial extension types of loading.

5) Perform stability analyses with the cyclic shear strengths from Step 4 and with static load and cyclic wave loads as driving forces. The values of $\tau_{f,cy}$ at each point can be determined by interpolation between $\tau_{f,cy}$ for compression, DSS and extension types of loading, depending on the inclination of the potential failure surface at that point. The analyses should be made for the surfaces, which were found to fulfill equilibrium with the static load in Step 3. The critical surface is the one, which gives the lowest safety factor. This is illustrated in Fig. 73.

6) Return to Step 1 and repeat the calculations for another combination of γ_p and γ_{cy} This iteration should be continued until the combination of γ_p and γ_{cy} which gives the lowest calculated safety factor in Step 5 has been established.

The results of the bearing capacity analyses include:

1) failure load

2) type and location of critical failure surface

3) failure mode (i.e. whether the failure will occur as large cyclic displacements, large permanent displacements, or a combination of the two. This can be deduced from the relative value of γ_p and γ_{cy} for the critical failure mode determined in Step 6.)

Further investigations were conducted by Clukey and Morrison (1995) to simulate field loading conditions of a suction pile system. To that end, a series of sever cyclic tests were performed. The types of loads applied during these tests are summarized in Fig. 74. The researchers performed three tests where the angle of loading was constant throughout the test. Two of these tests were performed with only vertical cyclic loading (Fig. 74 (a)) while one test was performed with the loading angle inclined at 6° from horizontal (Fig. 74 (b)).

Clukey and Morrison performed another four tests with a variable loading angle. Two of these tests were performed by varying the load angle about a mean inclination of 6° (Fig. 74 (c)). The loading angle varied ± 1° in one of these tests and ± 2° in the other. These tests are referred to by the researchers as combined loading tests.

Two tests were started by varying the inclination angle ± 2° about a mean angle of 6°. The mean loading was then changed and further cyclic loading was performed. Clukey and Morrison chose this type of test to determine the potential cyclic degradation as a result of sequential storms approaching from different directions. In one of these tests the loading angle was rotated back to vertical while in the other test the mean inclination was changed ± 6° These tests are referred to by Clukey and Morrison as combined-sequential loading tests (Fig.74 (d)).

Cyclic loading tests were performed in multiple steps. Five-hundred cycles of loading were applied by the researchers in each step except for one case, each level of cyclic loading was

investigated with 500 cycles applied at a loading frequency of 5 Hz, followed by 500 cycles applied at 1 Hz. In one test several of the steps used a loading frequency of 2.5 Hz. Variable loading frequencies were used to investigate the possible effects of pore-pressure dissipation on the results.

After 1,000 cycles of loading, the loading level was increased and the process repeated. If large deformations were not noted by Clukey and Morrison after the cyclic loading, a static pull-out test was performed.

For four of the tests reported, static pull-out tests were performed following cyclic loading. In all the tests the post cyclic capacity was greater than the predicted capacities (Table 9). The static capacities were based on the monotonically loaded centrifuge tests performed as part of the overall program. The increase in the static uplift capacity was found to vary from about 5% to 35% with an average value of 15%. The greatest increases corresponded to the tests that experienced the greatest cyclic load ratios.

The increase in the post cyclic capacity was felt to be attributable to consolidation effects around the pile. According to Clukey and Morrison, consolidation would result from the generation and dissipation of pore-pressures during cyclic loading. It was suggested that if sufficient time is allowed for consolidation between the storms, the suction pile foundation would not have a permanent reduction in capacity from the cyclic loading. The foundation should therefore be capable of withstanding the impact of multiple design storms.

Lateral Loading of Piles

Lateral loading of suction piles is considered similar to the case of driven pile systems (Grande and Nordal, 1979). A statically admissible stress field is described in front of the pile as a modified Prandtl stress field, based on a constant mobilized friction, $\tan\rho$, throughout the field. (A similar stress field with $\tan\rho = \tan\phi$ is assumed for failure condition.) A simple "settlement"

calculation is then performed, Fig.75, as for a strip footing.

The incremental lateral displacement, dv, may be expressed as:

$$dv = \int_0^H \varepsilon_y \, dy = B \, dq'_n / M_q \, S_y \qquad [67]$$

where:

M_q = the extended compression modulus at current stress state

S_y = the dimensionless lateral deformation number given in Fig. 76, as a result of the integration of Eqn. 68.

dq'_n = net lateral load

B = pile width

The conventional lateral soil reaction coefficient can then be expressed as:

$$k_y = dp'_r / dv = Bdq'_n / dv = M_q / S_y \qquad [68]$$

where:

dp'_r = line load

According to Hoeg et al. (1982), the p-y method of lateral load analysis for piles used to predict lateral deflections, rotations and bending moments, must consider: 1) boundary conditions imposed on the pile by the superstructure, 2) varying moment of inertia of the pile, 3) soil layers of different stiffness, 4) non-linear stress-strain behavior of the soil and 5) the group effects . Hoeg et al. stated that the pile should be treated as a beam supported on discrete springs, which act independently of each other. At different positions along the pile, Hoeg et al. suggested the

assumption of a relationship between the lateral soil pressure, p, and the lateral pile displacement, y. Using this method, it was found that the lateral loads at mudline affected only the upper pile length of 10 to 15 diameters of a driven pile. The magnitudes of the computed bending moments in the pile are felt to be relatively insensitive to variations in the assumed p-y curves along the pile, but the lateral displacements and rotations are affected.

Relating the single pile theory to groups of piles subjected to the same lateral load, a pile in a group is expected to deflect much more than the same isolated pile. The pile group behavior can be analyzed by means of an incremental superposition of the non-linear single pile behavior based on the p-y analysis and the interaction from the other piles in the group based on an elastic continuum analysis.

The semi-empirical p-y curves described by Hoeg et al. can be adjusted to take into account the effects of repetitive cyclic loading. Superimposed cyclic axial loads reduce the lateral stiffness for flexible piles. Additionally, the p-y curves differ, for piles in tension and compression. The lateral stiffness for a pile in tension is less than for one in compression due to the direction of the shaft friction along the pile, and hence the smaller normal stresses in the surrounding soil.

Hoeg et al. noted that the soil element behavior, strain accumulation and build-up and dissipation of excess pore-pressures around the pile must be analyzed by means of finite element or finite difference continuum analyses.

Most prior work done on driven piles included piles of small diameter and great length (Hogervorst, 1980). A pile installed by suction, however, is generally of large diameter (D) and of short length (H), i. e. $1 \leq H/D \leq 3$ (Hogervorst, 1980). The bending stiffness of such piles will usually be very high. Hogervorst characterized this stiffness in an elastic foundation with the quantity βH^5. He stated that β included both the flexibility of the pile (EI) and the stiffness of the supporting soil (k) and is expressed in the formula

$$\beta H = [k/4EI]^{1/4} \qquad [69]$$

where:

k = stiffness of the supporting soil

H = the embedded length of the pile

It is further noted by Hogervorst that if $\beta H < 0.6$, then the deflection of the pile due to bending would usually be negligibly small compared with the setting of the soil. Piles that satisfy this condition would therefore be regarded as stiff, moving in the soil as a rigid body.

According to Hogervorst, several analytical approaches can be found for calculating the ultimate pile resistance for this condition. All known theories are based on equilibrium conditions of moments and lateral forces. The equilibrium condition with respect to point A, as shown in Fig. 77, is expressed:

$$M = -\int p\, z\, dz \qquad [70]$$

and

$$Q = \int p\, dz \qquad [71]$$

where

p = lateral soil pressure on pile

z = depth below the seabed

In general, the lateral soil pressure is given by depth-dependent p-y curves or

$$p = p(y,z) \qquad [72]$$

where y is the lateral deflection. If M=0, then the resistance Q can be calculated as a function of

the top deflection y_0:

$$Q = Q(y_0) \qquad [73]$$

When the anchor pile is installed in sand, the maximum allowable soil pressure according to Rankine's earth pressure theory is equal to

$$p = \gamma' z K_p \qquad [74]$$

where

γ' = underwater unit weight onf sand

K_p = coefficient of passive earth pressure according to Rankine.

According to Broms (1964), the maximum allowable lateral pile load could be in this case

$$Q = [\gamma' D H^3 \tan^2(45° - \phi/2)]/[2(a+H)] \qquad [75]$$

where:

ϕ = angle of internal friction of sand

a = distance from pulling point to sand surface

To compare the results with the those of the tests, it was necessary for Hogervorst to define a point on the load-deflection curves (Fig. 78) of the pile load tests corresponding to a threshold working load which could be taken as the allowable lateral force. To accomplish this, the Osterberg procedure for evaluating pile load tests was followed. In this procedure the load-deflection data are plotted on a log-log form as shown in Fig. 78 (b). Then two straight lines of

different slope can be drawn and their intersection can be defined as the load at which the soil starts to collapse. The load corresponding to this intersection is known as the yield point in the curve, and will be taken as the maximum allowable lateral load of the suction pile.

Lateral loading is somewhat different in clays. For static lateral loads, the ultimate unit lateral bearing capacity of soft clay p_u has been found to vary between 8 and 12 times the soil cohesion, except at shallow depths where failure occurs in a different mode due to minimum overburden pressure. Cyclic loads cause deterioration of lateral bearing capacity below that for static loads. In the absence of more definitive criteria, the following is recommended by API RP2A:

p_u increases from 3 to 9 times the soil cohesion as X increases from 0 to X_R according to:

$$p_u = 3c+\gamma X+J\,cX/D \qquad [76]$$

and

$$p_u = 9c \text{ for } X \geq X_R \qquad [77]$$

where:

p_u = ultimate resistance, psi (kPa)

c = undrained shear strength for undisturbed clay soil samples, psi (kPa)

D = pile diameter, in. (mm)

γ = effective unit weight of soil, lb/in^2 (MN/m^2)

J = dimensionless empirical constant with values ranging from 0.25 to 0.5 having been determined by field testing.

X = depth below soil surface, in. (mm)

X_R = depth below soil surface to bottom of reduced resistance zone in. (mm). For a condition of constant strength with depth, Eqns. 76 and 77 are solved simultaneously to give: $X_R = 6D/[(\gamma D/c) + J]$

According to API RP2A, when the strength varies with depth, plotting the two equations, i.e., p_u vs. depth, may solve Eqns. 76 and 77. The point of first intersection of the two equations is taken to be X_R. These empirical relationships may not apply where strength variations are erratic. In general, minimum values of X_R should be about 2.5 times the pile diameter.

Lateral soil resistance-deflection relationships for piles in soft clay are generally non-linear. The p-y curves for the short-term static load case may be generated from the following table (API RP2A):

p/p_u	y/y_c
0	0
0.5	1.0
0.72	3.0
1.00	8.0
1.00	8

where:

p = actual lateral resistance, psi (kPa)

y = actual lateral deflection, in. (mm)

y_c = $2.5\ e_c\ D$, in. (mm)

ε_c = strain which occurs at one-half the maximum stress on laboratory undrained compression tests of undisturbed soil samples.

For the case where equilibrium has been reached under cyclic loading, the p-y curves may be generated from the following table (API RP2A):

$X > X_R$		$X < X_R$	
p/p_u	y/y_c	p/p_u	y/y_c
0	0	0	0
0.5	1.0	0.5	1.0
0.72	3.0	0.72	3.0
0.72	8	$0.72X/X_R$	15.0
		$0.72X/X_R$	8

For static lateral loads the ultimate bearing capacity p_u of stiff clay (c > 1 tsf or 96 kPa)and would vary between 8 and 12 times the soil cohesion). Due to rapid deterioration under cyclic loadings the ultimate resistance will be reduced to a value considerably less and should be so considered in cyclic design.

While stiff clays also have non-linear stress-strain relationships, they are generally more brittle than soft clays. In developing stress-strain curves and subsequent p-y curves for cyclic loads, it is suggested by API RP2A that good judgment should reflect the rapid deterioration of the load capacity at large deflections for stiff clays.

According to API RP2A, the ultimate lateral bearing capacity for sand has been found to vary from a value at shallow depths determined by Eq. 79 to a value at deep depths determined by Eq. 80. At a given depth the equation giving the smaller value of p_u should be used as the ultimate bearing capacity (API RP2A).

$$p_{us} = (C_1 * H + C_2 * D) * \gamma * H \qquad [78]$$

$$p_{ud} = C_3 * D * \gamma * H \qquad [79]$$

where:

p_u = ultimate resistance (force/unit length), lbs/in. (kN/m) (s = shallow, d = deep)

γ = effective soil weight, Ib/in.^{2} (KN/m^2)

H = depth, in. (m)

ϕ' = angle of internal friction of sand, deg.

C_1, C_2, C_3 = Coefficients determined from Fig. 79 as function of ϕ'.

D = average pile diameter from surface to depth, in. (m)

API RP2A also notes that the lateral soil resistance-deflection (p-y) relationships for sand are also non-linear and in the absence of more definitive information may be approximated at any specific depth H, by the following expression:

$$P = A * p_u * \tanh * [(k * H)/A * p_u) * y] \quad [80]$$

where:

A = factor to account for cyclic or static loading condition. Evaluated by:

p_u = ultimate bearing capacity at depth H, Ibs/in. (kN/m)

k = initial modulus of subgrade reaction. lb/in.^{3} (kN/m^2). Determine from Fig. 80 as function of angle of internal friction, ϕ'.

y = lateral deflection, inches (m)

H = depth, inches (m)

For piles with the same pile head fixity conditions and embedded in either cohesive or cohesionless soils, the pile group would normally experience greater lateral deflection than that of a single pile under the average pile load of the corresponding group according to API RP2A. API RP2A also states that the major factors influencing the group deflections and load distribution among the piles are the pile spacing, the ratio of pile penetration to the diameter, the pile flexibility relative to the soil, the dimensions of the group, and the variations in the shear strength

and stiffness modulus of the soil with depth.

Other methods that have been used in designing group pile foundations for given loading conditions include advanced methods, such as the Focht-Koch (1973) method as modified by Reese et al. (1984) for defining group deflections and average maximum pile moments for design loads. Deflections are probably underpredicted at loads giving deflections of 20 percent or more of the diameter of the individual piles in the group.

Attachment Point

Varying the attachment point of the mooring lines can increase the lateral capacity of the pile in sand as well as clay. Attachment points were varied in experiments by Keaveny et al. (1994). It was found that lowering the point of attachment between the tether and anchor from the mudline to midway between mudline and skirt tips approximately doubled the capacity for both static and cyclic cases. Cycling the model reduced the capacity by about 10% for the midway loading.

It was suggested by Keaveny et al. that lowering the attachment point forces the model into a horizontal translation mode of failure rather than a rotational failure by minimizing the moments about the skirt tip.

Conclusion

Much mental and physical effort has been exerted to turn suction pile technology from an idea into a reality. Although the concept of a pile driven by hydrostatic pressure differences dates

back to at least the 1950's, design and analysis of the structures is still relatively imprecise. Much progress has gained through the use of driven pile theory modified to meet the needs of suction emplacement. This is particularly true of installation and lateral loading parameters. Still, many assumptions have been made out of necessity.

Assumptions exist for most parameters involved, but are especially prevalent in the areas of static loading, dynamic loading, and pore pressures within the soil associated with the pile. In some cases an exact answer is probably not even possible. In these cases, it is necessary to rely on empirical data to adjust and improve design techniques.

One of the most important parameters that govern the behavior of the suction pile is the development of pore water pressures, since it directly affects the soil effective shear strength. Many studies have indicated that such effect is rather significant in influencing the behavior of suction piles during installation, particularly in permeable soils such as sands. It is therefore imperative to better understand the effect of the pore water pressure developed within the soil and include such effect in the analysis of suction pile installation. Both hydrostatic and hydrodynamic pore water pressures need to be considered, since there will definitely be a water flow from the outside soil surface of the pile toward the inside soil surface due to the applied suction pressure. A steady state confined water flow problem may be considered for this purpose. In less permeable soils, i.e., silts and clays, the effect of hydrodynamic pore water pressures may not be as significant, since the time period for suction pile installation is rather short to establish a complete water flow. It however needs to be studied in depth.

One of the primary concerns associated with the use of suction piles to moor the Mobile Offshore Bases is to study the feasibility of utilizing very large suction piles that may be necessary to provide adequate resistance against the large magnitude of load anticipated from the Mobile

Offshore Bases. The installation of very large suction piles has not been studied in the past and therefore needs to be investigated for its feasibility. Inclusion of the hydrodynamic pore water pressures outside and within the suction pile is expected to allow a much more accurate simulation of the suction pile installation in the field.

In cohesionless soils, the upward flow of water not only induces hydrodynamic pore water pressures within the soil but also loosens the soil inside the pile, which in turn alters the soil shear strength characteristic. For given soil and pile geometric and material conditions, the change in soil shear strength and the pore water pressure development are considered primarily responsible for the response behavior of suction piles. The change in soil shear strength may take place near the tip and inside the pile. A series of carefully planned laboratory and field experiments need to be conducted to identify and quantify this change in soil shear strength characteristic due to the water flow caused by the suction pressure application.

The effect of water flow on the change in soil shear strength characteristic in cohesive soils has not been studied at all. Again, well-planned experimental tests need to be performed for identifying any such effect on cohesive soils.

The lateral resistance capacity of suction piles is typically estimated based on the conventional pile lateral bearing capacity equations, most of which utilize two-dimensional plane strain concept with a modification for the three-dimensional effects. For large diameter suction piles, it is however felt necessary to directly simulate the three-dimensional behaviors of the soil and the suction pile for more accurate analysis and design. Detailed study of the pile-soil interaction along the pile circumference and at the pile tip, considering the three-dimensional soil failure wedge, therefore must be conducted.

The cost information associated with the construction, transportation, installation, and removal of suction piles is critical for the wider use of suction piles. However, such information has been treated as proprietary by many manufacturers and installers, and subsequently they are not available in the literature. Additional attempts should be made to establish general guidelines on the cost of utilizing suction piles.

The technology of suction piles which drives piles into ocean floor through the application of suction pressure is still new. Much has been learned, but there is still much more to assess. With continued research, the suction pile system of seabed mooring should only become safer, easier, and more economical.

Acknowledgments

The authors would like to gratefully acknowledge the technical and financial support provided by the Office of Naval Research and the Naval Facilities Engineering Service Center.

Literature Cited

1 Aas, P, and Andersen, KH, (1992) Skirted Foundations for Offshore Structures. *Offshore South East Asia* OSEA paper no. 92145, pp. 305-312.

2 Albert, LF, Holtz, SRI, and Magris, E, (1987) The Superpile System: A Feasible Alternate Foundation for TLP in Deep Water. *Offshore Technology Conference* OTC Paper no. 5392. pp. 307-314

3 Andersen, KH, (1983) Strength and Deformation Properties of Clay Subjected to Cyclic Loading. *Rep. 52412-8, Norwegian Geotechnical Institute,* Oslo, Norway

4 Andersen, KH, Kleven, A, and Heien, D (1988) Cyclic Soil Data for Design of Gravity Structures. *J. Geotech. Engrg., ASCE*, 114(5).

5 Andersen, KH, Dyvik, R, and Schroder, K, (1992) Pullout Capacity Analysis of Suction Anchors for Tension Leg Platforms. *Boss-92*, 2, 1311-1322.

6 Andeasson, B, Christophersen, HP, and Kvalstad, TJ, (1988) Field Model Test and Analyses of Suction Installed Long-Skirted Foundations. *BOSS'88*, Trondheim, 243-257.

7 API RP2A-WSD-93, (1993) American Petroleum Institute, Planning, Designing, and Constructing Fixed Offshore Platforms--Working Stress Design. *American Petroleum Institute.*

8 Baird, JA, and Nacci, VA, (1972) The Shear Strength Parameters for Hydrostatic Anchoring. *Offshore technology Conference* OTC paper no. pp. 533-543.

9 Bezuijen, A, Hjortnaes-Pedersen, AGI and Luger, D, (1992) Study of Offshore Skirt Penetration Using Geo-Centrifuge. *24th OTC conf. , Houston*, May.

10 Briaud, JL and Tucker, LM, (1988) Measured and Predicted Axial Response of 98 Piles. *J. Geotech. Eng. Div. , ASCE* 114(9) pp. 984-1002.

11 Broms, BB, (1964). Lateral Resistance of Piles in Cohesionless Soils. *Journal of the Soil Mechanics and Foundations Division. SM3*

12 Brown, GA, and Nacci, VA. (1971) Performance of Hydrostatic Anchors in Granular Soils. *Offshore Technology Conference,* OTC Paper no. 1472.

13 Burgess, IW, Hird, CC, and Cuckson, J, (1981) Sinking Tests on Caisson Anchors in Clay. *In Offshore Structures: The Use of Physical Models in their Design* . eds. GST Arrner and Garas, Construction Press, pp. 289-298.

14 Burgess, IW, and Hird, CC, (1983), Stability of Installation of Marine Caisson Anchors in Clay. *Can. Geotech. Journ.* 20, pp. 385-393.

15 Burland, JB, (1973) Shaft Friction of Piles in Clay-- A Simple Fundamental Approach. *Ground Engng.* 6(3) 30-42.

16 By, T, and Skomedal, E, (1992) Soil Parameters for Foundation Design, Troll Platform *BOSS-92* , pp.909-920.

17 Bye, A, Ebrich, C, Rognlien, B, and Tjelta, TI, (1995) Geotechnical Design of Bucket Foundations. *Offshore Technology Conference* OTC paper no. 7793 pp. 869-863.

18 Chandler, RJ, (1968) The Shaft Friction of Piles in Cohesive Soil in Terms of Effective Stress. *Civ. Enng. Pub. Wrks. Rev.* 63 48-51.

19 Christophersen, HP (1992) The Non-Piled Foundation System of the Snorre Field. *Proc. Offshore Site Investigation and Foundation Behaviour, SUT, London*, Sept. 1992 pp. 433-447.

20 Clausen, CJF, DiBiagio, E, Duncan, JM, and Andersen, KH, (1975) Observed Behavior of the Ekofisk Oil Storage Tank Foundation . *Proc. of the 7th annual Offshore Technology Conference, Houston, Tex.* 1975.

21 Clukey, E, (1991) Suction Caissons, *Presented at the Design of Floating Production Systems, The University of Texas of Austin College of Engineering.*, Oct. 1991.

22 Clukey, EC, and Morrison, MJ, (1993) A Centrifuge and Analytical Study to Evaluate Suction Caissons for TLP Applications in the Gulf of Mexico. *(ASCE) Design and Performance of Deep Foundations: Piles and Piers in Soil and Soft Rock, Geotechnical Special Publication No. 38*, (eds Nelson, Smith, and Clukey) pp. 141-156.

23 Clukey, EC, and Morrison, MJ, (1995) The Response of Suction Caissons in Normally Consolidated Clays to Cyclic TLP Loading Conditions. *Offshore Technology Conference* OTC paper no. 7796, pp. 909-918.

24 Cuckson, J, (1981) The Suction Pile Finds its Place. *Offshore Engineer,* (Apr.) pp 80-81.

25 Dyvik, R, Andersen, KH, Madshus, C, and Amundsen, T, (1989) Model Tests of Gravity Platforms I: Description. *J. Geotech. Engrg., ASCE*, 115(11), 1532-1549

26 Dyvik, R, Andersen, KH, Hansen, SB, and Christophersen, HP, (1993) Field Tests of Anchors in Clay, I: Description. *J. Geotech. Engrg., ASCE*, 119(10), 1515-1531

27 Fines, S, Stove, OJ, and Guldberg, F (1991) Snorre TLP Tethers and Foundation. *Offshore Technology Conference* OTC paper no. 6623, pp. 587-597.

28 Focht-Koch (1973) Rational Analysis of the Lateral Performance of Offshore Pile Groups, *OTC 1896*

29 Fuglsang, LD, and Steensen-Bach, JO, (1991) Breakout Resistance of Suction Piles in Clay. *Proc. Int. Conf.: Centrifuge 91*, H -Yko and FG Mclead eds., A.A. Balkema Rotterdam, The Netherlands, 153-159.

30 Goodman, LJ, Lee, CN, and walker, FJ, (1961) The Feasibility of Vacuum Anchorage in Soils. *Geotechnique, London, England,* 1(3), 356-359.

31 Guttormsen, TR, and Wikdal, JA, (1994) Foundation of the Tordis Submudline Silo. *BOSS-94* , pp. 189-203.

32 Hansteen, OE, and Hoeg, K, (1994) Soil-Structure Interaction Analysis of Embedded Caisson Anchor Under Tension Load. *BOSS-94,* pp. 49-62.

32 Helfrich, SC, Brazil, RL, and Richards, AF, (1976) Pullout Characteristics of a Suction Anchor in Sand. *Offshore Technology Conference*, OTC Paper no. 2469. v. 1 pp. 501-506.

34 Hjortnaes-Pedersen, AGI, and Bezuijen, A (1992) Offshore Skirt Penetration in Clay in the Geo-Centrifuge. *BOSS-92* pp. 528-542.

35 Hoeg, K, (1982) Geotechnical Issues in Offshore Engineering. State of the Art Lecture at the Third Int. Conf. on Behavior of Offshore Structures, *BOSS' 82*, MIT, Cambridge, Mass., USA

36 Hogervorst, JR (1980) Field Trials with Large Diameter Suction Piles. *Offshore Technology Conference*, OTC Paper no. 3817. pp. 217-223

32 Iskander, MG, Olsen, RE, and Pavlicek, RW, (1993) Behavior of Suction Piles in Sand. *(ASCE) Design and Performance of Deep Foundations: Piles and Piers in Soil and Soft Rock, Geotechnical Special Publication No. 38*, (eds Nelson, Smith, and Clukey), pp. 157-171.

37 Jardine, RJ, and Christoulas, S. (1991) Recent Developments in Defining and Measuring Static Piling Parameters. *Gen. Report, Int. Conf. on Deep Foundations. Paris, Presse de l'Ecole de Ponts et Chaussees.* pp. 713-746,

38 Jardine, RJ, Lehane, BM, and Ebverton, SJ, (1993) Friction Coefficients for Piles in Sands and Silts. *Offshore Site Investigation and Foundation Behaviour.* pp. 661-677

39 Jones, WC, Iskander, MG, Olsen, RE, and Goldberg, AD, (1994) Axial Capacity of Suction Piles in Sand. *BOSS-94* , pp. 63-75.

40 Jostad, HP, Andersen, KH, and Tjelta, TI, (1997) Analyses of Skirted Foundations and Anchors in Sand Subjected to Cyclic Loading. *In Press*

41 Keaveny, JM, Hansen, SB, Madshus, C, and Dyvik, R, (1994) Horizontal Capacity of Large Scale Model Anchors. *Proceedings of the XIII International Conference of Soil Mechanics and Foundation Engineering, New Delhi, India*, June (accepted for publication).

42 Larsen, P, (1989) Suction Anchors as an Anchoring System for Floating Offshore Structures." *Offshore Technology Conference*, OTC Paper no. 6029. pp. 535-540

43 Mackereth, FJH, (1958) A Portable Core Sampler for Lake Deposits. *Limnology and Oceanography*, 3, pp. 181-191.

44 Morrison, MJ, and Clukey, EC, (1994) Behavior of Suction Caissons Under Static Uplift Loading. *Centrifuge94*, Leung, Lee, and Tan (eds.) Rotterdam. pp. 823-828

45 Pavlicek, (1993) Axial Tensile Load Capacity of Suction Piles. *M.Sc. Thesis, The University of Texas at Austin.*

46 Potyondy, JG, (1961) Skin Friction Between Various Soils and Construction Materials. *Geotechnique* bf 11(4) pp. 229-353.

47 Poulos, HG, (1989) Pile Behavior - Theory and Application., Rankine Lecture. *Geotechnique*, 34(2) pp. 365-415.

48 Puech, AA (1982) Basic Data for the Design of Tension Piles in Silty Soils. International Conference on the Behaviour of Off-Shore Structures, 3. *BOSS' 82* Cambridge, Mass. Proceedings. 1 pp. 141-157.

49 Rao, SN, Ravi, R, and Ganapathy, C, (1997), Pullout Behavior of Model Suction Anchors in Soft Marine Clays. *Proc. 7th. IOPE Conf. Honolulu, USA*, 1997.

50 Reese, LC et al. (1984) "Analysis of a Pile Group Under Lateral Loading," Laterally Loaded Deep Foundations: Analysis and Performance, *ASTM, STP 835.* pp. 56-71

51 Renzi, R, Maggioni, W, and Smits, F, (1991) A Centrifugal Study on the Behavior of Suction Piles. *Proc. Int. Conf. Centrifuge91*, pp. 169-176.

52 Renzi, R, and Maggioni, W, (1994) Modeling the Behavior of Skirt Piles. *BOSS-94* , pp. 77-85.

53 Sahota, BS, and Wilson, Q (1982) Breakout Behavior of Suction Anchors Embedded in Submerged Sands. *Offshore Technology Conference. OTC Paper no. 4206.* pp. 117-132

54 Steensen-Bach, JO, (1992) Recent Model Tests with Suction Piles in Clay and Sand. *Offshore Technology Conference,* OTC paper no. 6844 1, pp. 323-330

55 Schofield, AN, (1974) Suction Anchors Could Eliminate Pile Driving. *Offshore Services,* 7(3), 37-39.

56 Senpere, D, and Auvergne, GA, (1982) Suction Anchor Piles - A Proven Alternative to Driving or Drilling. *Offshore Technology Conference,* OTC Paper no. 4206. pp. 483-493

57 Svano, G, Lango, H, Madshus, C, and Skomedal, E, (1992) Effective Stress Concept for Dynamic Stiffness of Clay. *BOSS-92,* pp.951-968.

58 Tjelta, TI, Guttormsen, TR, and Hermstad, J, (1986) Large Scale Penetration Test at a Deepwater Site. *Offshore Technology Conference,* OTC Paper no. 5103. pp. 483-493

59 Tjelta, TI Aas, PM, Hermstad, J, and Naes, E (1990) The Skirt Piled Gulfaks C Platform Installation. *Proceedings 22th Offshore Technology Conference (OTC), Houston, Tex. Paper No. OTC 6473.*

60 Tjelta, TI (1994) Geotechnical Aspects of the Bucket Foundations Replacing Piles for the Europipe 16/11-E Jacket *Offshore Technology Conference OTC paper no. 7379, Houston*

61 Wang, MC Nacci, VA, and Demars, (1975) Behavior of Underwater Suction Anchor in Soil . *Ocean Eng.*, 3 47-62.

62 Wang, MC, Demars, KR, and Nacci, VA, (1978) Application of Suction Anchors in Offshore Technology. *Offshore Technology Conference,* OTC Paper no. 3203. pp. 1311-1320

63 Wilson Q, and Sahota, BS. (1977) Trials with Suction Anchors. *Ocean Industry,* Aug. 1977 pp. 55-56.

64 Wilson Q, and Sahota, BS. (1978) Suction Anchors. *European Offshore Petro. Conf. and Exh. in London EUR* 16, 1978.

65 Wilson Q, and Sahota, BS. (1980) Pullout Parameters for Buried Suction Anchors. *Offshore Technology Conference*, OTC Paper no. 3816

Appendix 1

Figures and Tables

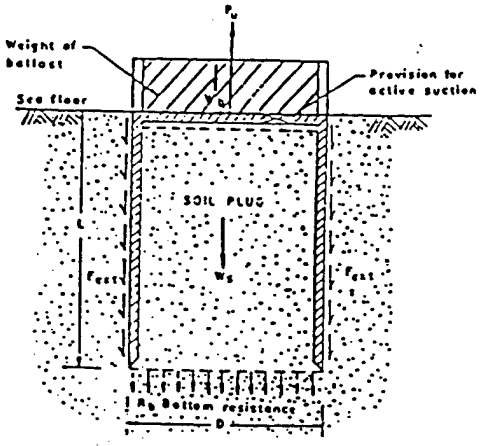

Fig. 1. Typical suction anchor (after Rao et al., 1997)

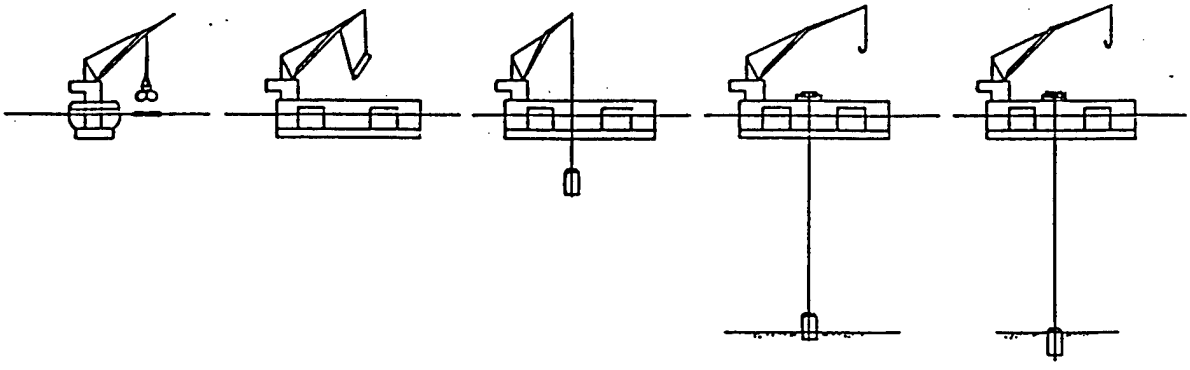

Fig. 2. Installation procedures for suction piles. (after Tjelta et al., 1986)

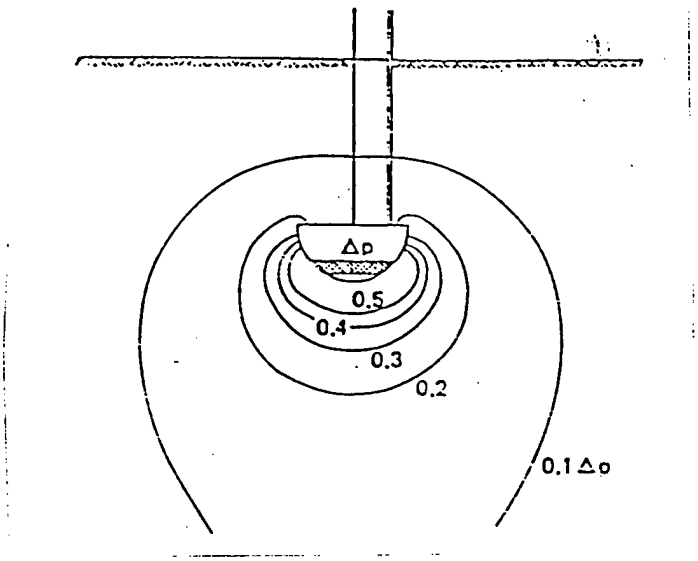

Fig. 3. Typical pore pressure field around a buried suction anchor (after Wilson and Sahota., 1980)

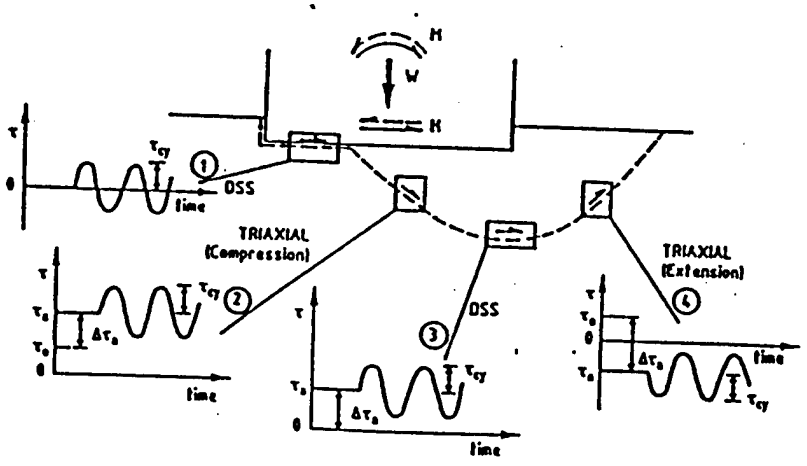

Fig. 4. Simplified load conditions for some elements along potential failure surface. (after Andersen et al., 1988)

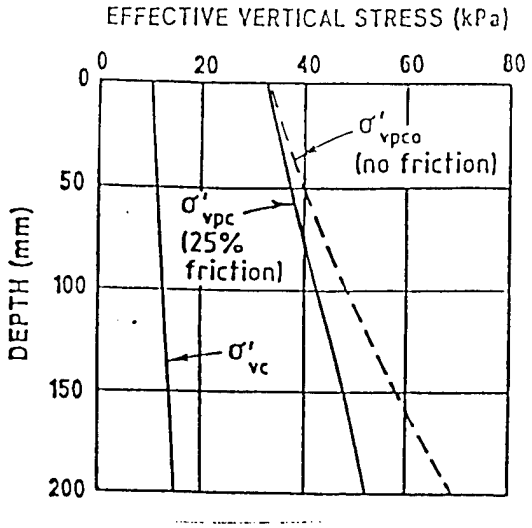

Fig. 5. Maximum and final effective vertical stress profiles for model clay. (after Dyvik et al., 1989)

Model test number (1)	Final sample height (mm) (2)	$\Delta H/H_o$ (%) (3)	Average measured water content (%) (4)
1	231	34.0	—
2	234	33.1	42.1
3	233	33.4	40.1
4	232	33.7	43.0
5	231	34.0	40.5

Table 1. Final sample heights and water contents for five model bins. (after Dyvik et al., 1989)

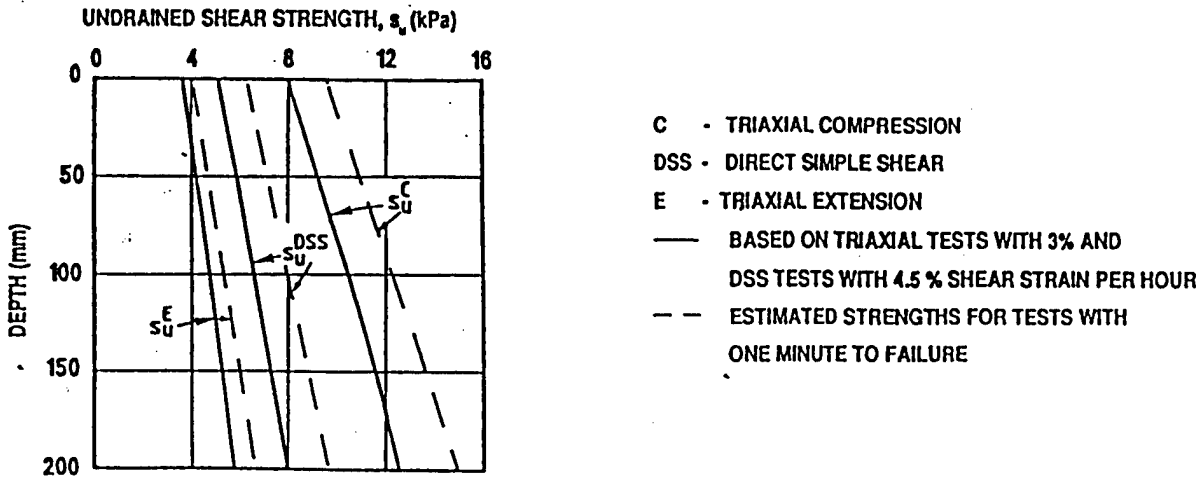

Fig. 6. Undrained shear strengths with depth for model clay (after Dyvik et al., 1989)

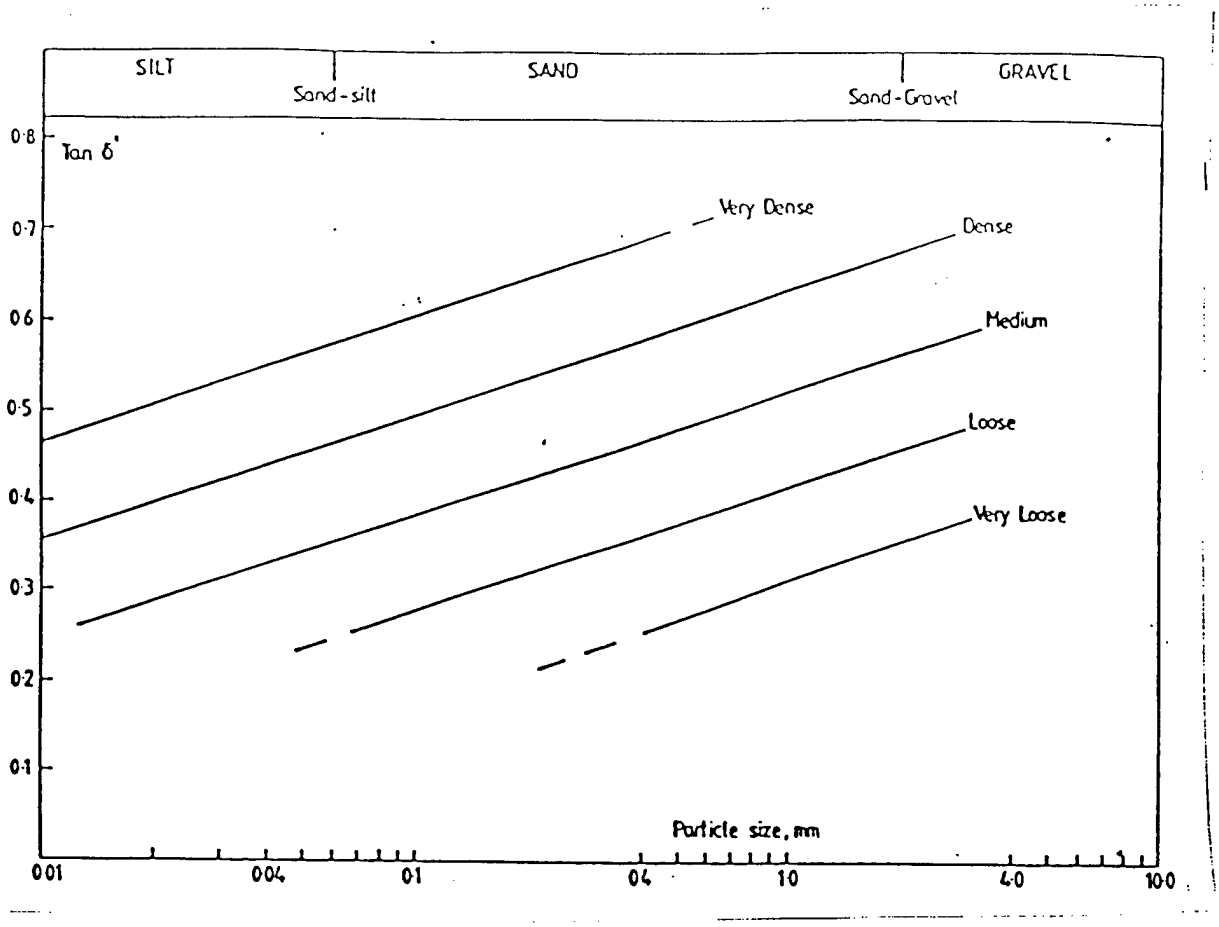

Fig. 7. Graphical interpretation of API recommended δ' values in granular soils (after Jardine et al.., 1993)

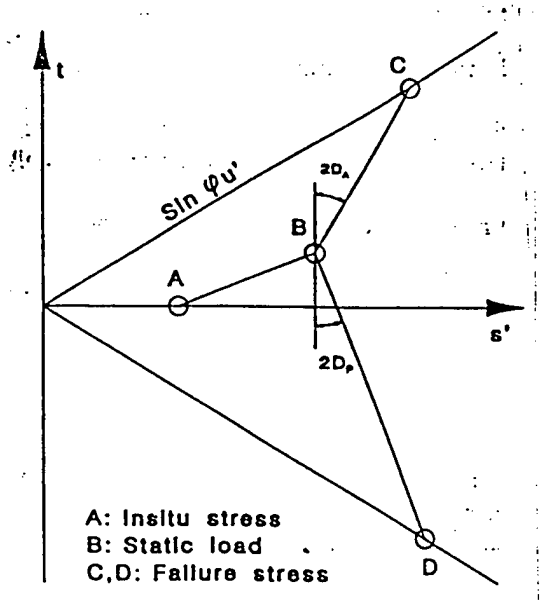

Fig. 8. Principles of undrained shear strength. (after Bye et al., 1995)

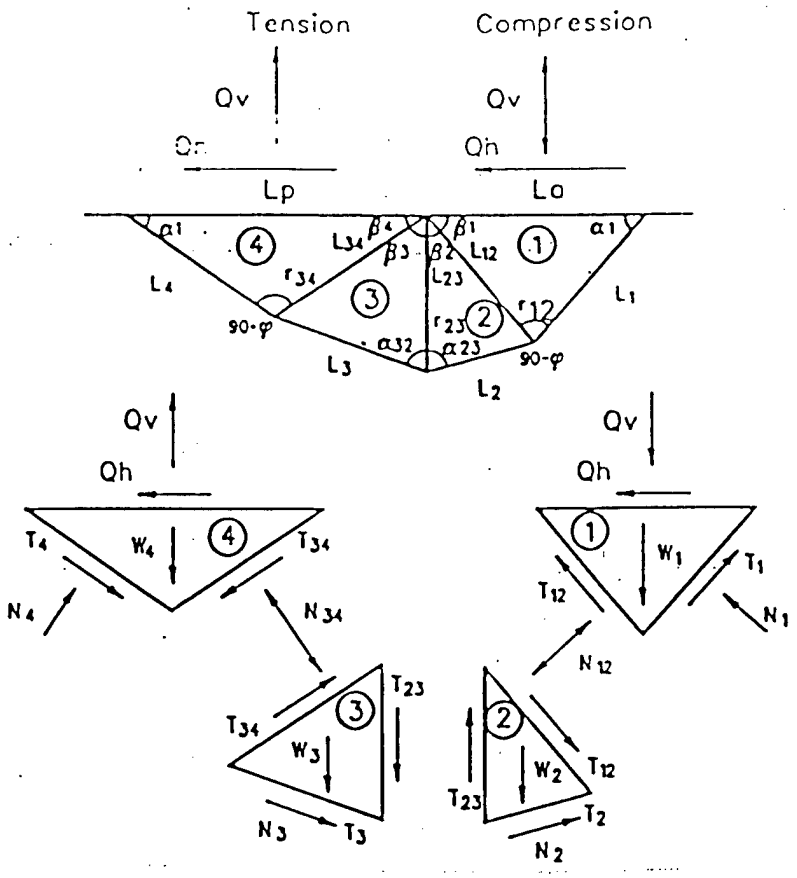

Fig. 9. Slip surface geometry and forces. (after Bye et al., 1995)

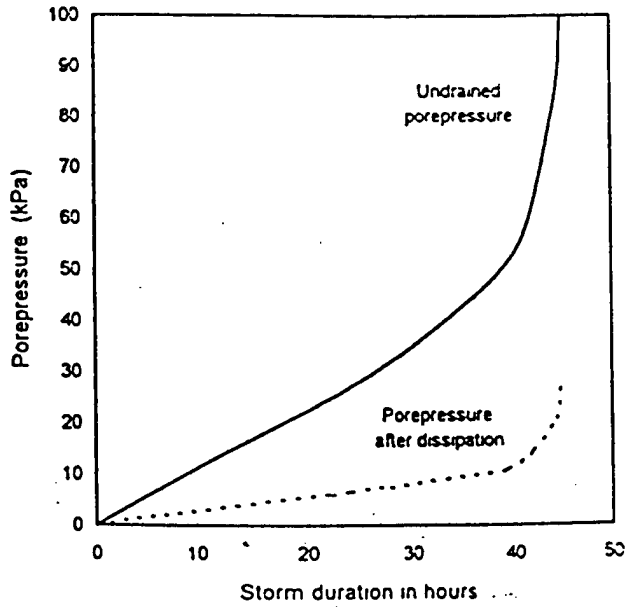

Fig. 10. Dissipation of pore pressures. (after Bye et al., 1995)

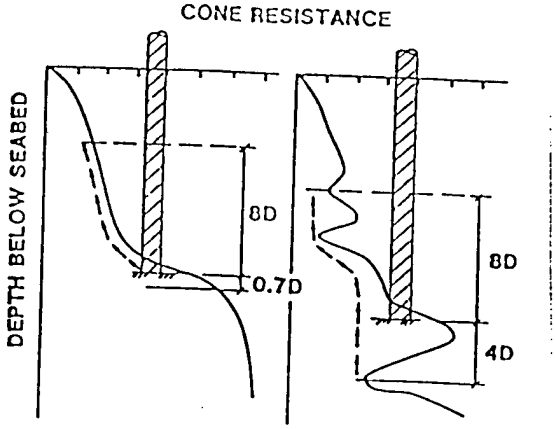

$$q_p = \frac{(I+II)/2+III}{2}$$

KEY

D : Diameter of the pile

I : Average cone resistance below the tip of the pile over a depth which may vary between 0.7D and 4D.

II : Minimum cone resistance recorded below the pile tip over the same depth of 0.7D to 4D.

III : Average of the envelope of minimum cone resistances recorded above the pile tip over a height which vary between 6D and 8D. In determining this envelope, values above the minimum value selected under II are to be disregarded.

q_p : Ultimate unit point resistance of the pile.

NOTE

To account for geometry D = 0.5 used in predictions.

Fig. 11. Empirical method applied for prediction of tip penetration resistance. (after Tjelta et al., 1986)

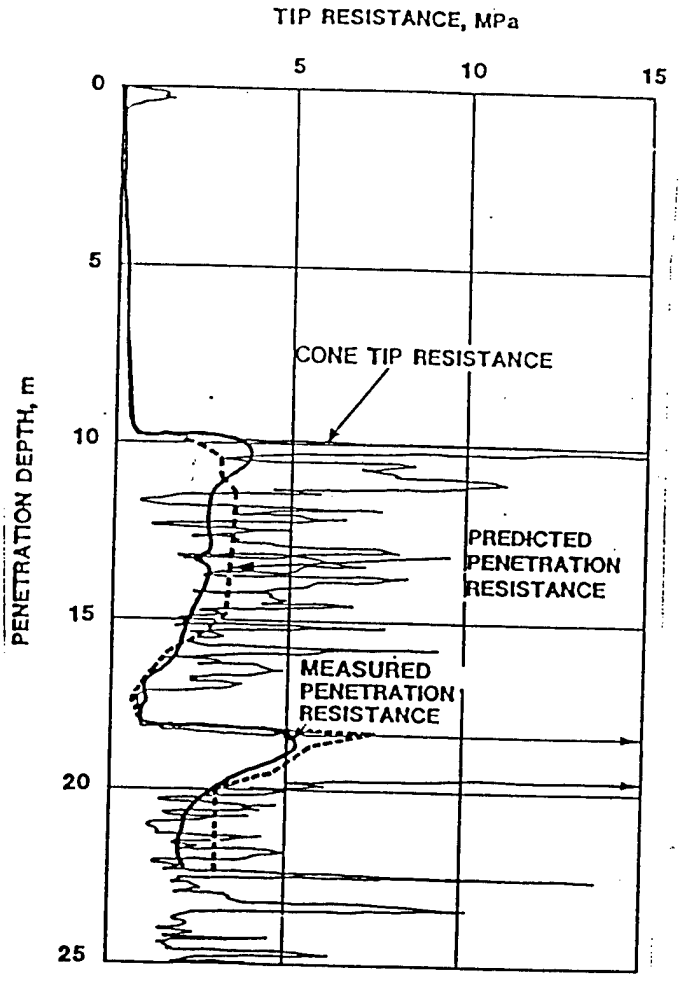

Fig 12. Measured and predicted tip resistance on concrete element compared with in-situ cone penetration test results. (after Tjelta et al., 1986)

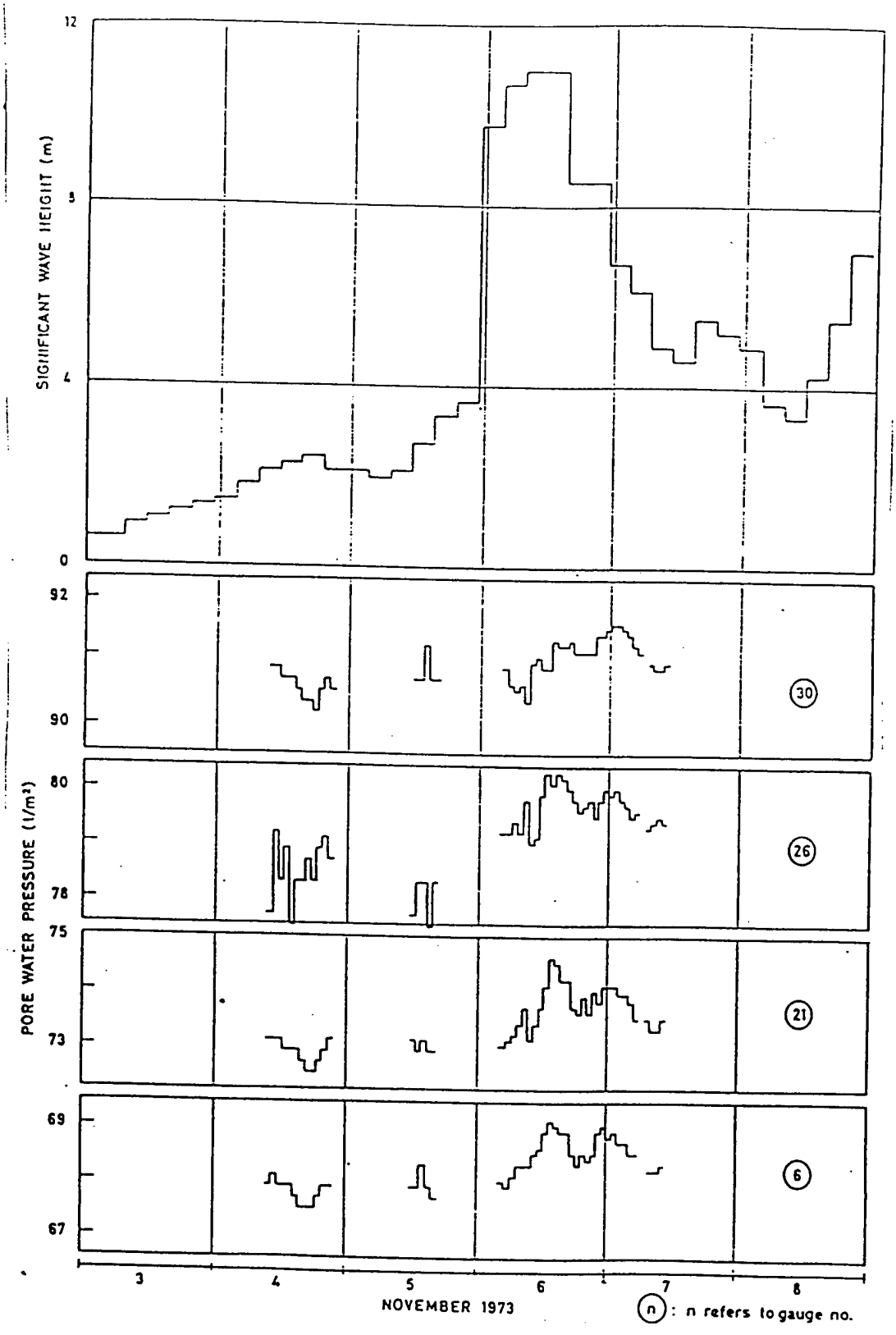

Fig. 13. Pore water pressure and wave height versus time. (after Clausen et al., 1975)

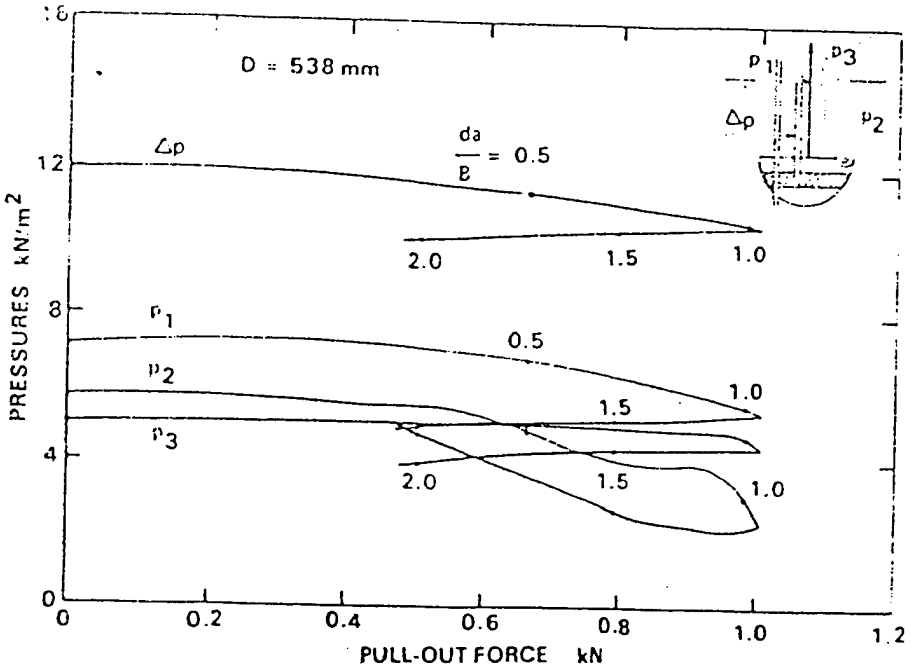

Fig. 14. Various pressures versus pull-out force, anchor displacement ration for the 102 mm anchor. (after Sahota and Wilson, 1982)

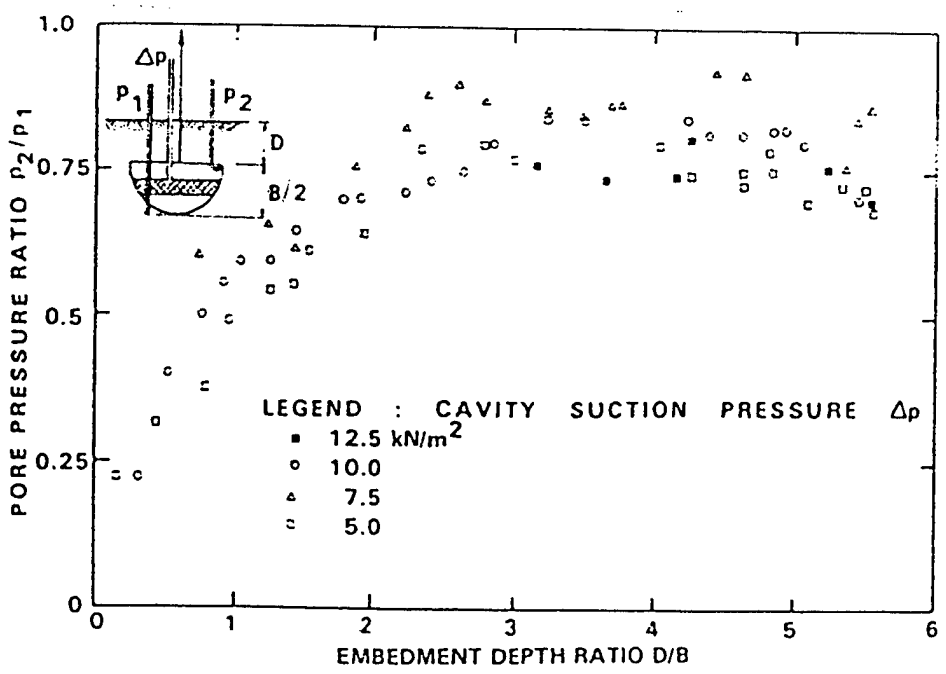

Fig. 15. Pore pressure ratio versus embedment depth ratio for the 102 mm anchor. (after Sahota and Wilson, 1982)

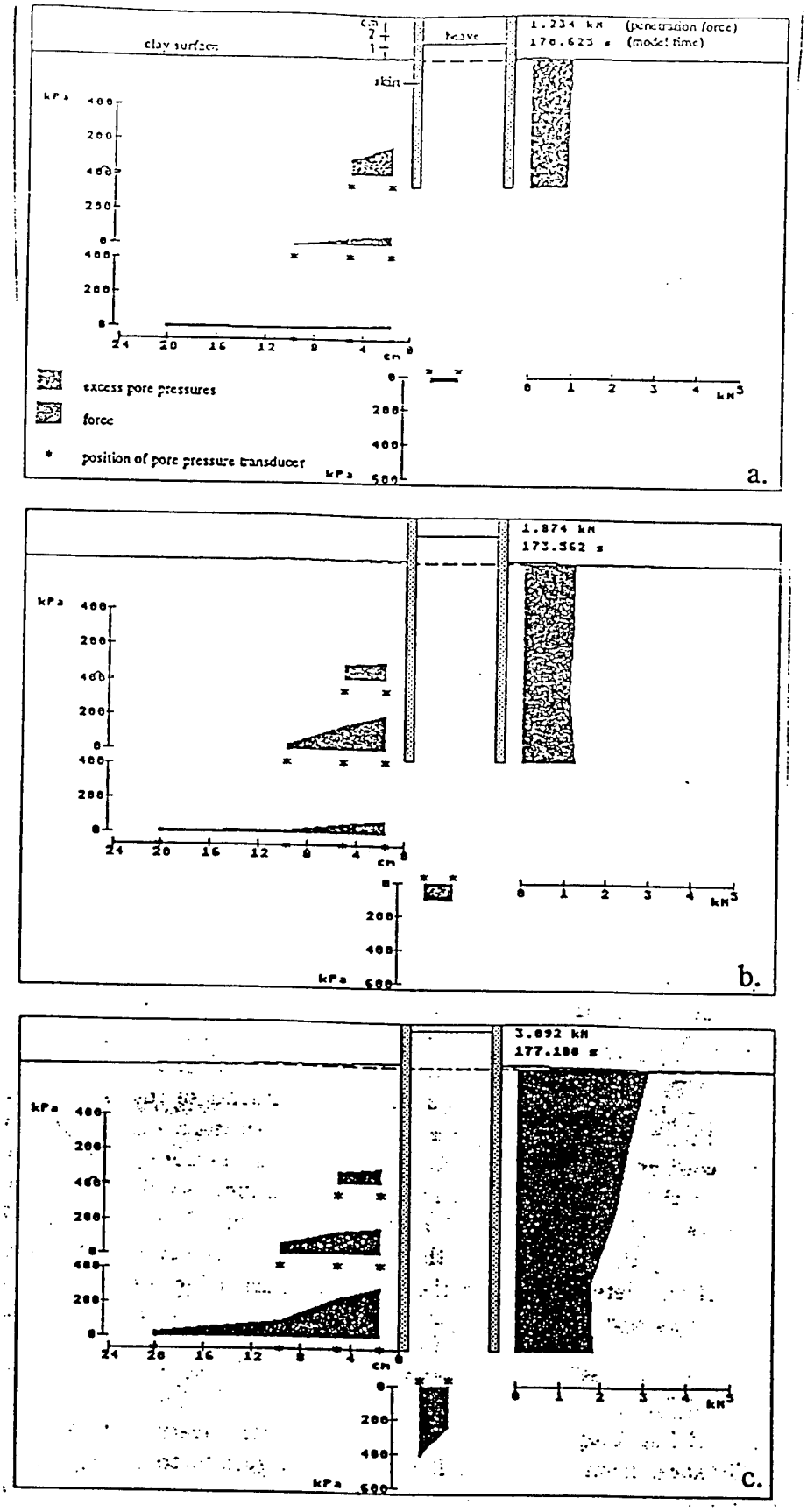

Fig. 16. Excess pore pressure, heave, and force measured during penetration of clay (a) half of the penetration, (b) two-thirds of the penetration, (c) full penetration of the skirt. (after Hjortnaes-Petersen and Bezuijen, 1992)

v mm/s	c_{um} kPa	c_{ub} kPa	F N	u kPa	N_1	N_2	σ_t kPa
			65 mm dia. piles				
1.0	6.0	11.0	299	-66	7.1	7.4	74
1.0	3.4	7.0	266	-50	10.4	9.8	69
1.0	5.0	7.0	234	-57	8.6	10.0	56
1.0	6.3	8.5	250	-62	7.4	9.2	59
1.0	5.8	8.3	239	-60	7.2	9.0	56
0.1	2.6	6.0	208	-44	9.4	8.5	52
0.1	2.6	6.0	220	-50	10.0	9.5	56
0.1	8.0	10.5	300	-63	7.2	7.8	72
0.1	4.3	7.8	214	-49	7.1	7.7	51
1.0	6.0	8.5	515	- 9	8.1*	11.3*	-88*
0.1	4.7	7.0	440	+ 7	8.5*	10.9*	-98*
			80 mm dia. piles				
1.0	17.0	20.0	810	-95	5.9	6.9	114
1.0	16.4	20.5	695	-94	4.7	6.5	92
1.0	15.5	18.5	713	-96	7.5	10.1	99
0.1	15.4	17.0	814	-93	7.1	8.0	117
0.1	15.0	18.0	680	-86	5.1	7.0	88
0.1	15.5	16.0	844	-98	8.1	8.6	126
1.0	14.0	17.5	1100	-103	6.5*	10.3*	-33*
0.1	18.7	24.5	-	-98	-	7.6*	-

*Centrifuge test at 40 g.

Table 2. Results of tests with suction piles. (after Fuglsang and Steensen-Bach, 1991)

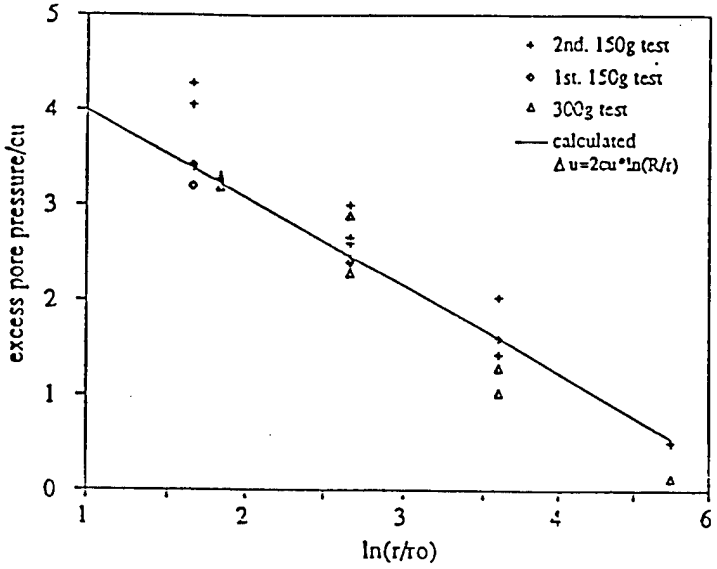

Fig. 17. Measured and calculated excess pore pressure as a function of the relative radius. (after Hjortnaes-Petersen and Bezuijen, 1992)

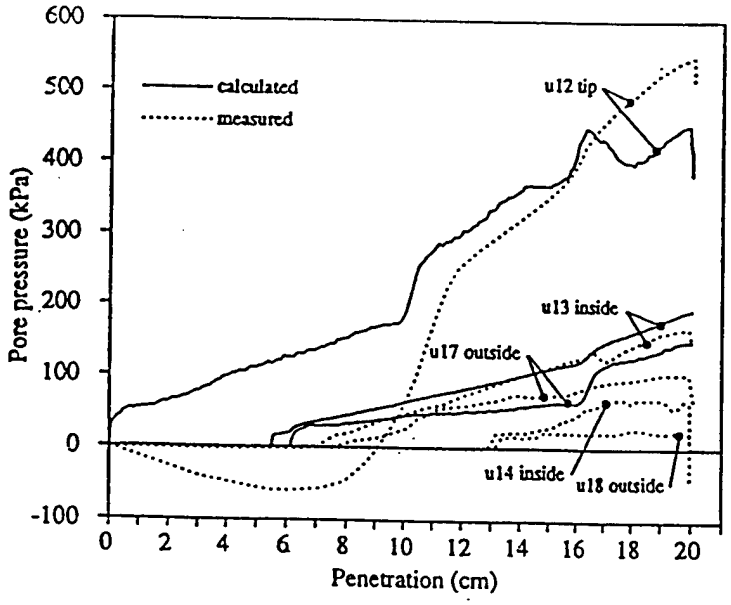

Fig. 18. Excess pore pressures measured with transducers in skirt, and compared with calculations. (after Hjortnaes-Petersen and Bezuijen, 1992)

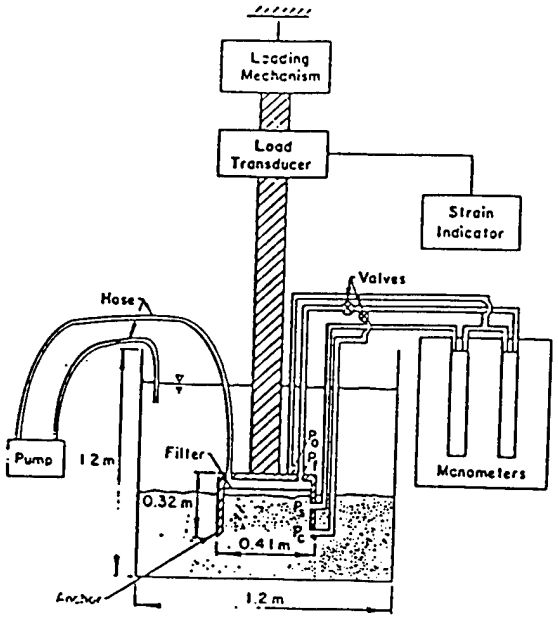

Fig. 19. Schematic diagram (not to scale) of test tank, loading mechanism, pump, and suction anchor. p_0 = ambient water pressure above anchor, p_f = pressure above filter, p_s = pressure below filter, p_c = pressure at cutting edge of anchor. (after Helfrich et al., 1976)

Series	Test	Max. pullout force, kN	P_o-P_c, kPa	P_o-P_s, kPa	Flowrate, $\mu m^3/s$	Wt. of sand pulled out, kN
I	1	1.907	19.4	-	1.47	0.439
	2	1.989	34.4	-	1.67	0.446
	3	1.913	32.2	-	1.53	0.466
	4	1.298	17.3	-	0.72	0.328
	5	2.208	37.1	-	1.76	0.491
	6	1.922	18.9	-	0.96	0.326
	7	1.635	6.7	-	1.22	0.437
II	8	2.085	37.9	11.9	1.65	0.450
	9	1.971	35.0	11.4	1.62	0.455
	10	2.061	36.9	11.8	1.68	0.468
III	11	0.390	1.1	-	-	0
	12	0.370	1.3	-	-	0

Table 3. Laboratory test results. (after Helfrich et al., 1976)

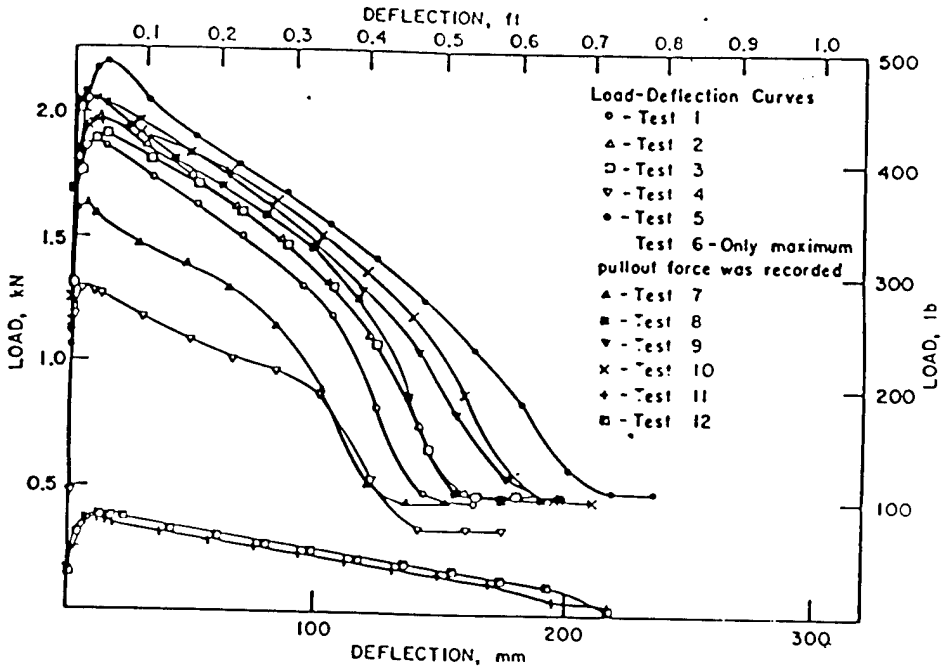

Fig. 20. Force or load on the test suction anchor related to the vertical movement, or deflection, for 12 laboratory tests in medium to fine sand. (after Helfrich et al., 1976)

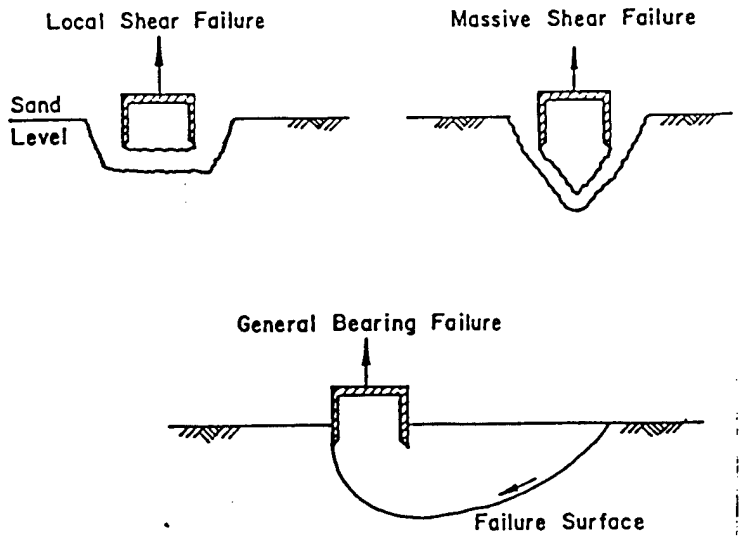

Fig. 21. Three modes of shear failure below suction anchors: local shear, conical shear, and general bearing failure. (after Helfrich et al., 1976)

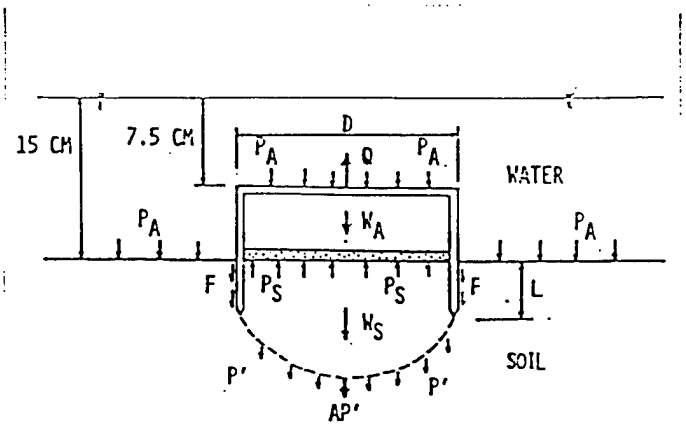

Fig. 22.Force components on an anchor. (after Wang et al., 1976)

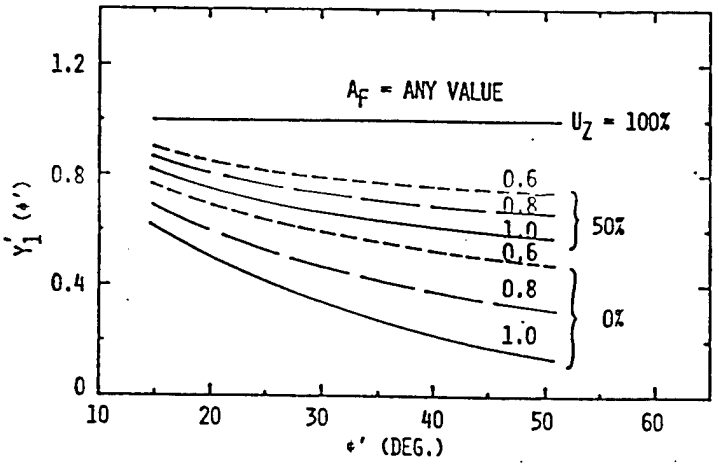

Fig. 23. Curves for function $Y_1'(\phi')$. (after Wang et al., 1976)

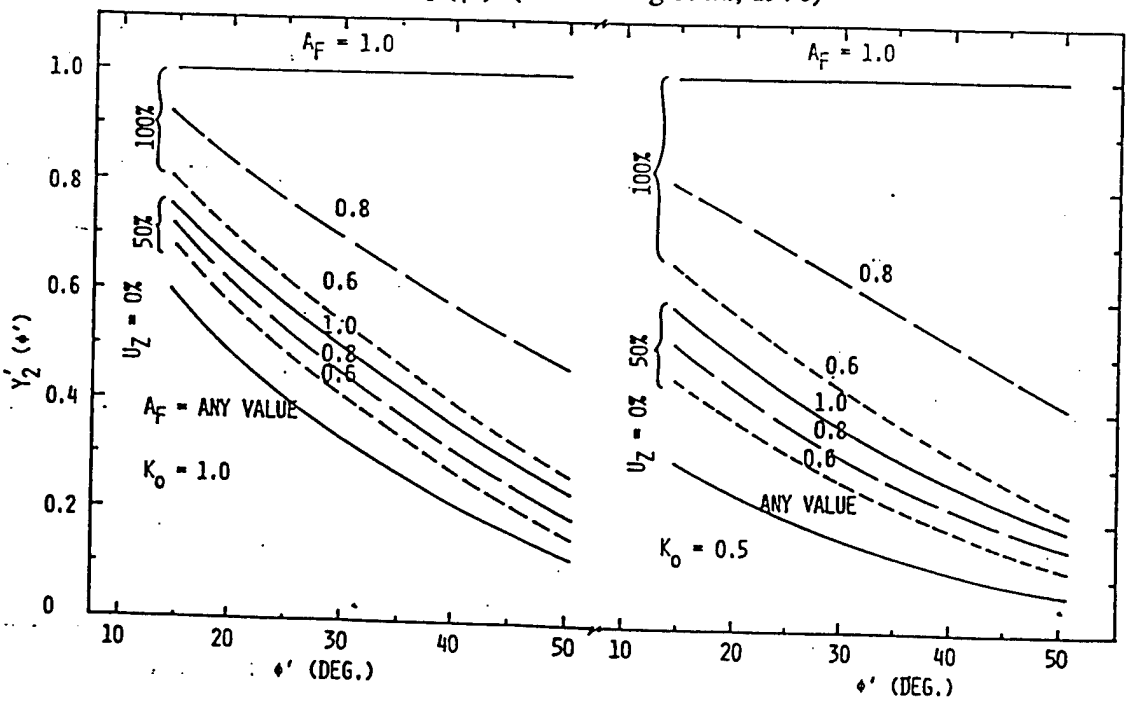

Fig. 24. Curves for function $Y_2'(\phi')$ (after Wang et al., 1976)

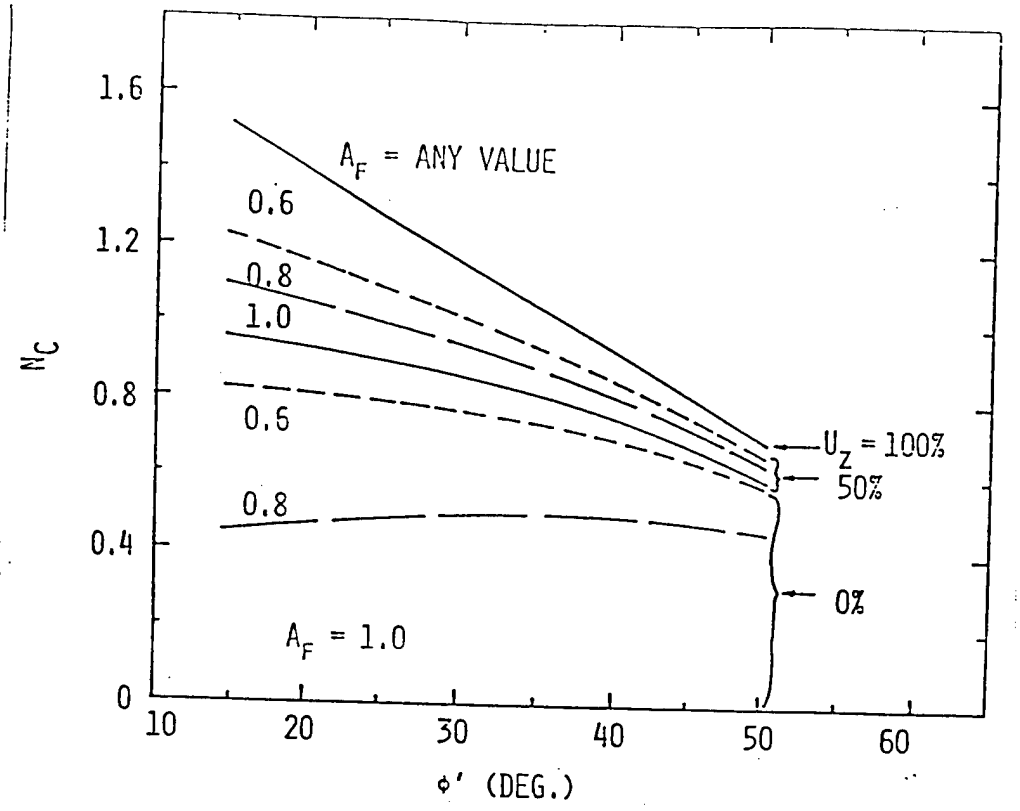

Fig. 25. Relation between N_c and ϕ'. (after Wang et al., 1976)

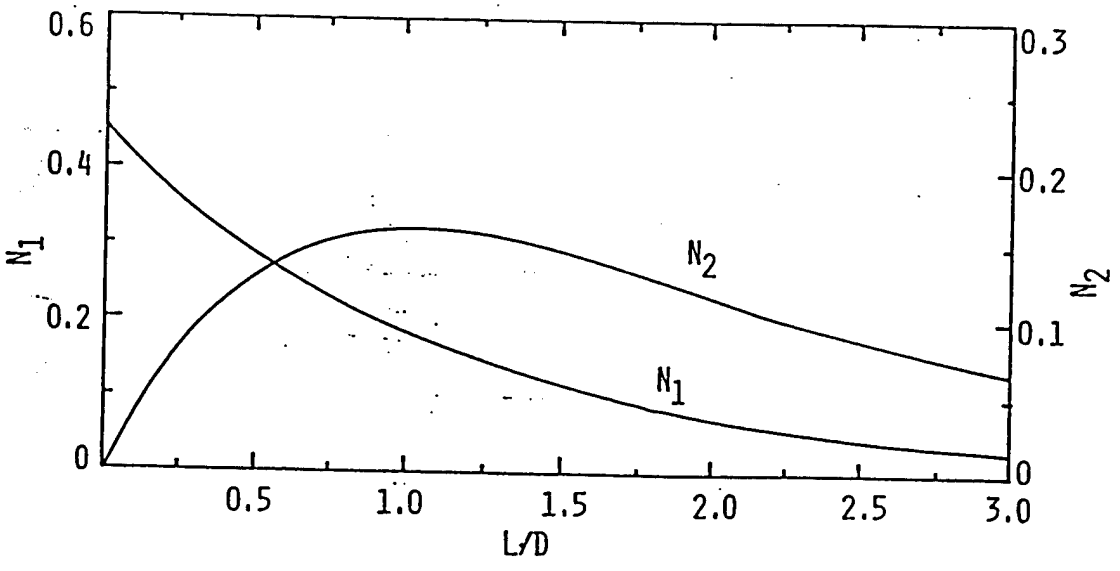

Fig. 26. N_1 and N_2 as a function of L/D, respectively. (after Wang et al., 1976)

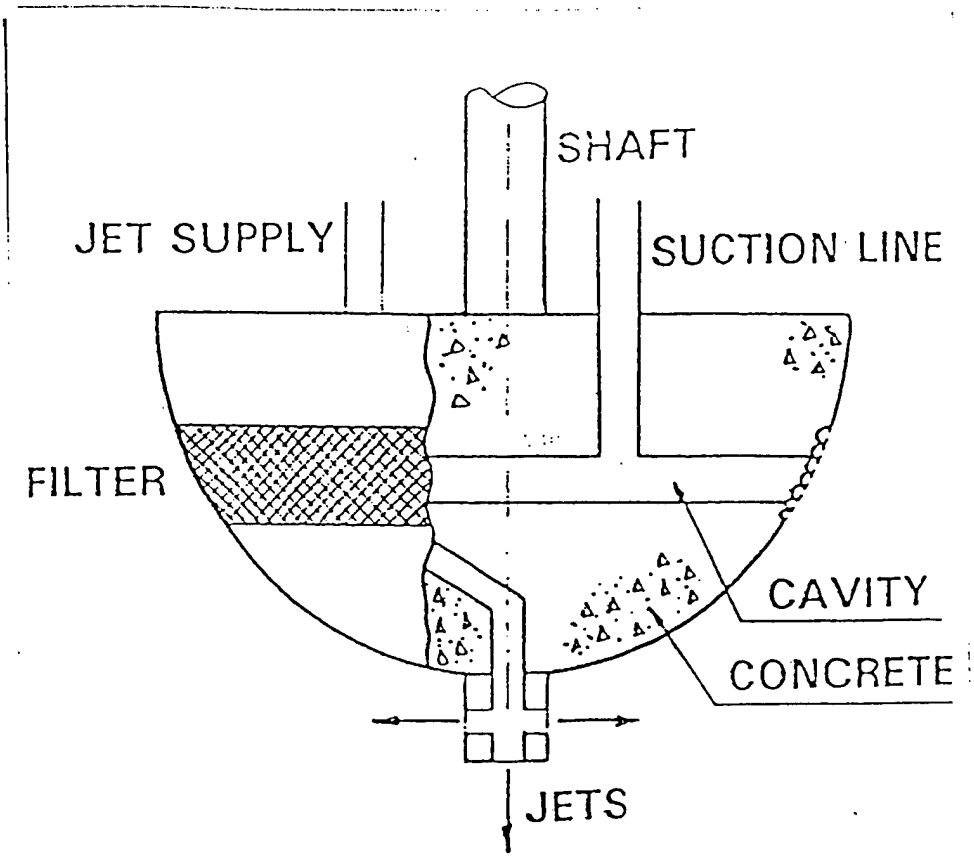

Fig. 27. Typical suction anchor. (after Sahota and Wilson, 1982)

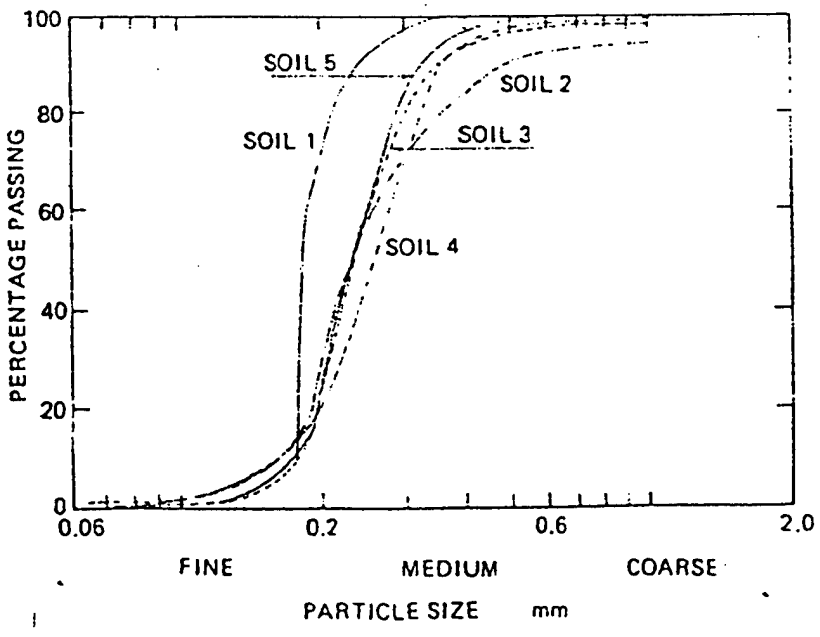

Fig. 28. Particle size distribution curves for the test soils. (after Sahota and Wilson, 1982)

Properties of the test soils

	Model tests	Sea trials (average)
Specific gravity	2.67	2.64
Submerged density (Unit buoyant weight) kN/m^3	9.32 (fresh water)	8.94 (salt water)
Maximum dry density kN/m^3	16.01	15.93
Minimum dry density	13.74	13.50
Relative density	0.557	0.555
Internal angle of friction ϕ (loose state, dry)	29°	32°
Internal angle of friction ϕ (dense state, dry)	37°	37°
Internal angle of friction ϕ (loose state, wet)	-	30°
Internal angle of friction ϕ (dense state, wet)	-	39°
Moisture content at dense state ϕ in %	-	25%

Table 4. Properties of test soils. (after Sahota and Wilson, 1982)

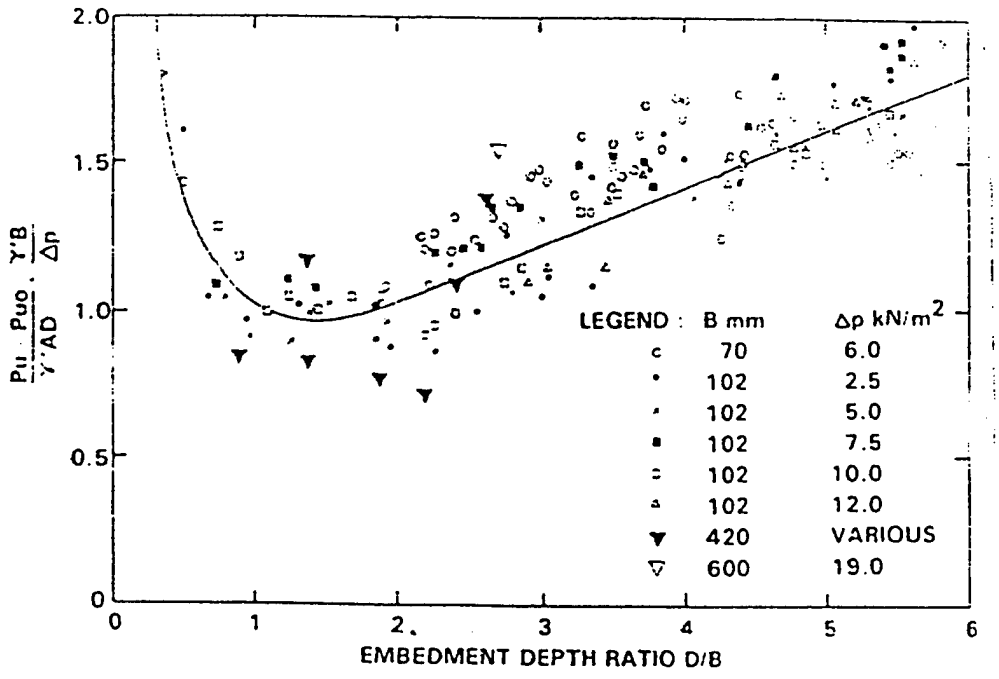

Fig. 29. Collapsed non-dimensional presentation of break-out force data for various anchors . (after Sahota and Wilson, 1982)

	Pile Diameter, D (m)						
	6	7	8	9	10	11	12
W_{pile} (kN)	1060	1255	1440	1640	1880	2040	2250
$W_{soil\ plug}$ (kN)	4090	5560	7270	9200	11360	13740	16350
P_{int} (kN)	4610	5370	6140	6910	7680	8840	9210
P_f (after scour) kN) Cyclic tension	2650	3080	3520	3950	4390	4825	5270
P_f (after scour) (kN) API - static tension	4510	5260	6000	6750	7490	8240	8930
Operating (1-year storm):							
No. of piles	4*	3*	3	2*	2	2	2
Factor of safety	2.79	2.68	3.35	2.72	3.26	3.64	4.47
100-yr storm:							
No. of piles	5	4*	3*	3	2*	2	2
Factor of safety	2.26	2.32	2.17	2.64	2.11	2.49	2.90
* probably the most economical							

Table 5. Submerged weights of piles and soil plugs, internal and external soil skin friction resistances and calculated factors of safety for piles of various diameters. (after Albert et al., 1987)

Item	Evaluation	B
1.Reliability of loads	good	1
2.Uncertainties in soil-pile behaviour	limited, if we use α=0.5 for skin friction	1
3.Inspection and repair	very poor	1.5
4.Consequences of foundation failure	relatively severe	1.3
5.Difficulty of installation	average	1.25
6.Quality of soil	poor	1.4
7.Residual strength of soil-pile system	very poor	1.5
8.Load redistribution capabilities	average	1.2

Table 6. Evaluation of the B coefficient for various aspects of the Superpile foundation. (after Albert et al., 1987)

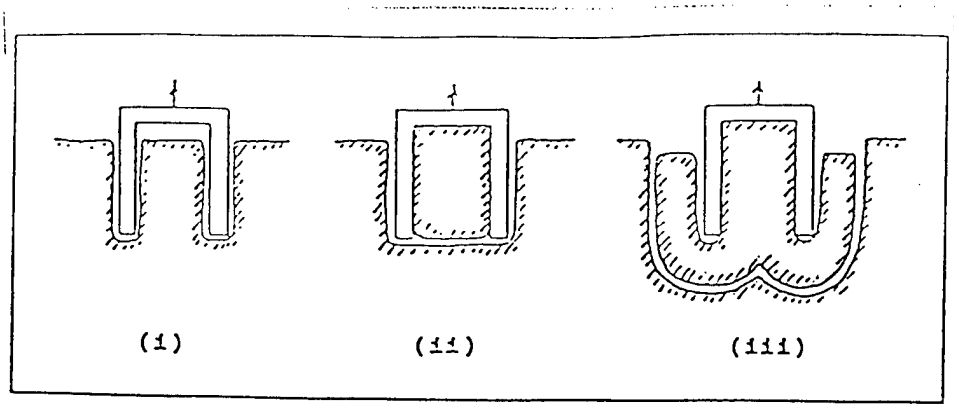

Fig. 30. Observed failure mechanisms (i) local shear failure, (ii) local tension failure, (iii) general shear failure. (after Steensen-Bach, 1992)

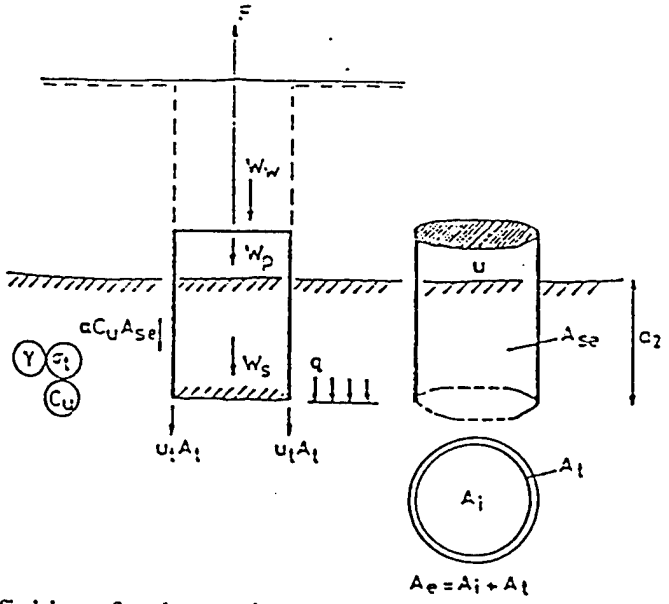

Fig. 31. Definitions for the suction pile. (after Steensen-Bach, 1992)

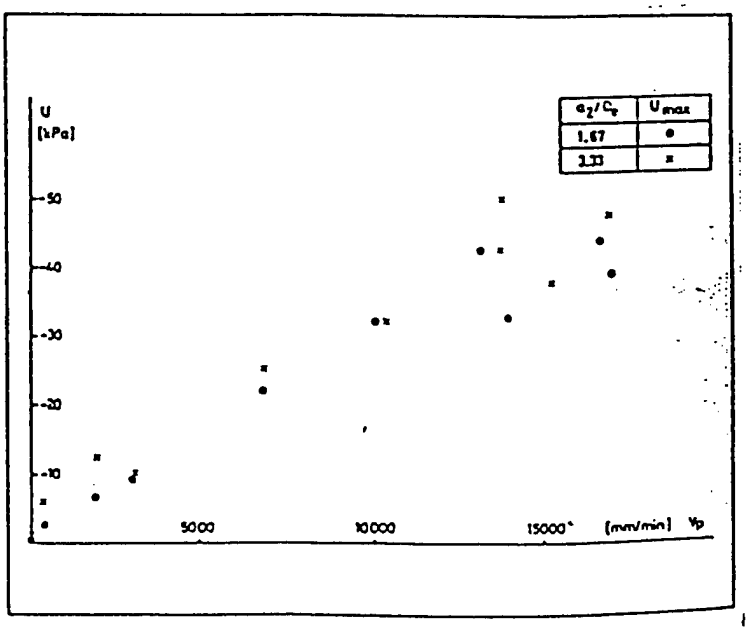

Fig. 32. Maximum suction in monotonic break-out tests in G12 sand. (after Steensen-Bach, 1992)

Test Type				Caisson Embed-ment	Measured Soil-Uplift	Measured Suction at Caisson Head at Peak Load	Calc. External Skin Frict.	Calc. Suction at Bottom of Caisson	Suction[5] Efficiency
Rate[1]	Install.[2]	Load[3]	Config.[4]	(Ft)	(Kips)	(Kips)	(Kips)	(Kips)	(%)
R	Suct.	Vert.	SC	102.6	20,724	11,438	5,778	16,187	92.3
S	Suct.	Vert.	MC	109.2	15,116	7,803	7,317	14,030	55.6
R	Suct.	Vert.	MC	108.1	17,506	5,852	6,156	16.044	70.7
S	Suct.	Vert.	SC	106.3	20,073	12,837	6,941	19,898	66.0
R	Suct.	Vert.	SC	105.7	22,014	13,044	6,494	19,764	78.5

Note: 1 Ft. = 0.305m, 1 Kip = 4.45 kN, 1 ksf = 47.9 kPa

(1) Relative rate of loading, R-Rapid, S-Slow.
(2) Installation, No Suction, Suction.
(3) Load Orientation, Inclined, Vertical.
(4) Caisson Configuration, Single Cell, Multi-Cell.
(5) Suction efficiency is ratio of (measured soil uplift-calc. external skin frict.) / calc. suction bottom of caisson

Table 7. Summary of static centrifuge tests. (after Clukey and Morrison, 1993)

Test series	Method of installation	Pressure differential across top kPa (psi)	Pen. force‡ N (lb)	Pen. distance cm (in)	Pen. rate cm/min (in/min)	Height of excess soil plug cm (in)
1	Maximum vacuum	4.75 (0.69)	50.3 (11.3)	13.8 (5.4)	15.2 (6.0)	5.9 (2.33)
2	Maximum vacuum	4.07 (0.59)	44.5 (10)	14.5 (5.7)	13.7 (5.4)	5.2 (2.05)
3	Pushing	N/A	445† (100)	17.8 cm (7.0)	53.3 (21.0)	1.7 (0.67)
4	Minimum vacuum	2.83 (0.41)	34.2 (7.7)	15 (5.9)	1.65 (0.65)	4.7 (1.85)

‡ Penetration force = pressure differential * Area + submerged pile weight
† from load cell measurement

Table 8. Summary of data for tension tests. (after Iskander et al., 1997)

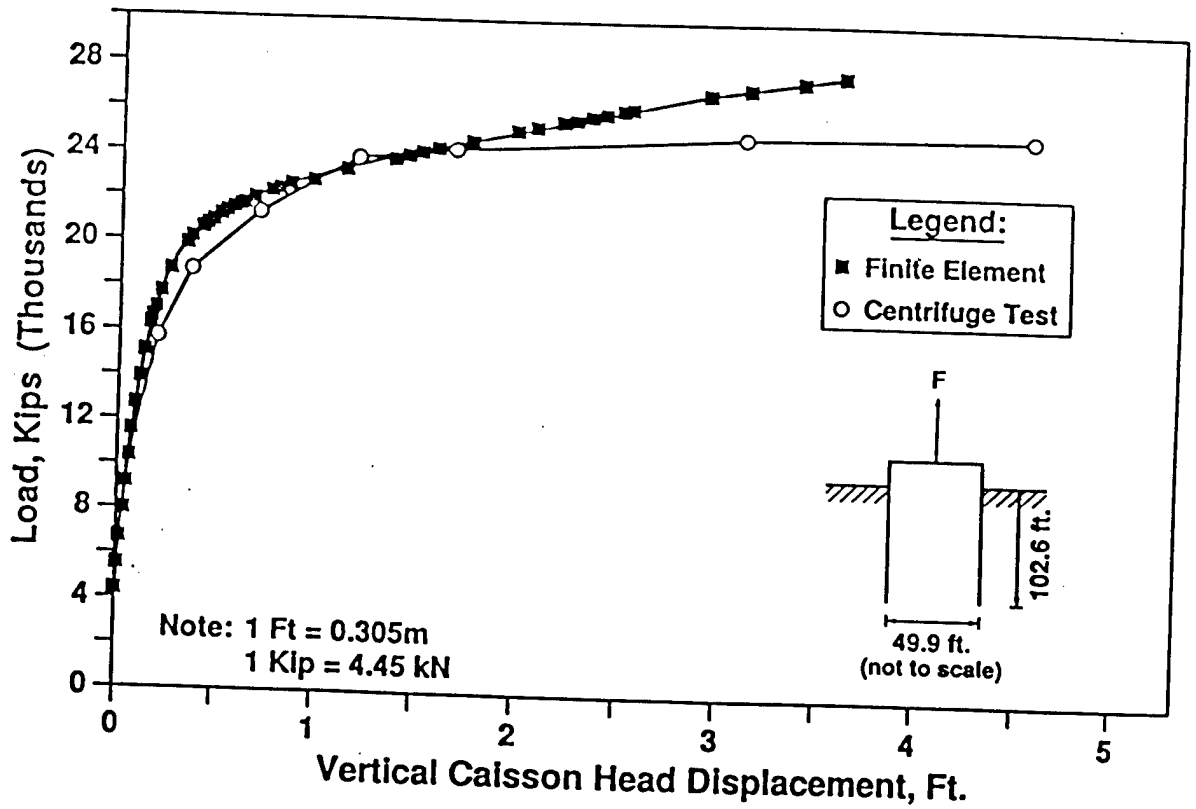

Figure 33. Comparison of centrifuge results and finite element analysis of suction caisson foundation. (after Clukey and Morrison, 1993)

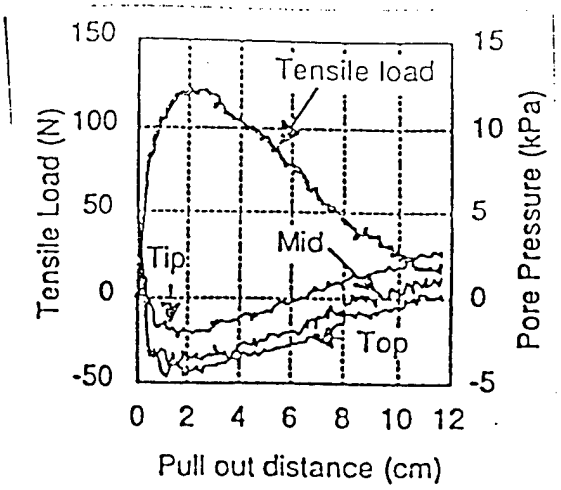

Fig. 34. Pull-out of suction pile (test series 1). (after Iskander et al., 1993)

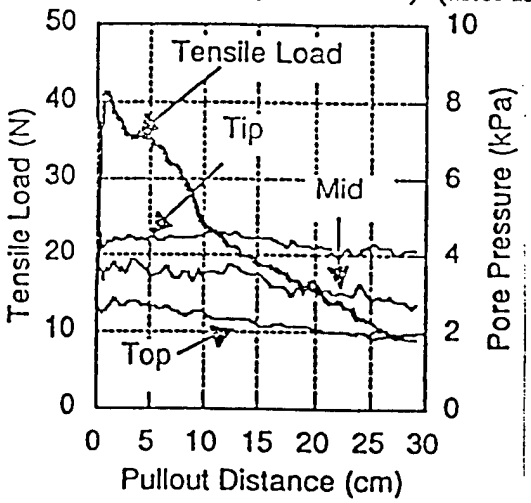

Fig. 35. Pull-out of suction pile (test series 2). (after Iskander et al., 1993)

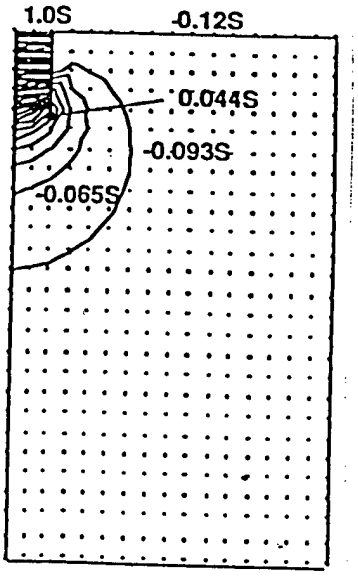

Fig. 36. Pore pressure distribution (steady state). (after Iskander et al., 1993)

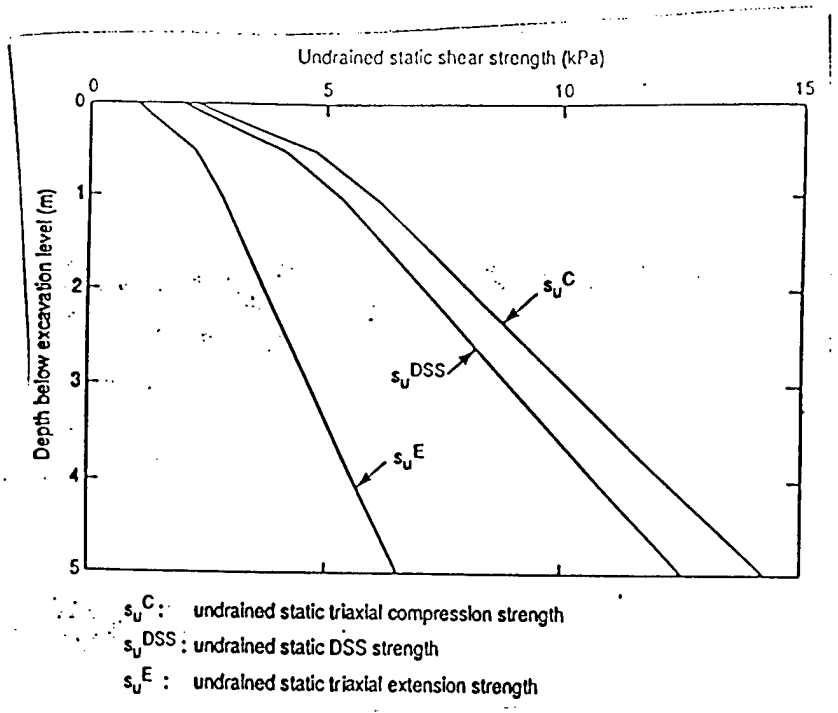

Fig. 37. Undrained static shear strength. (after Andersen et al., 1993)

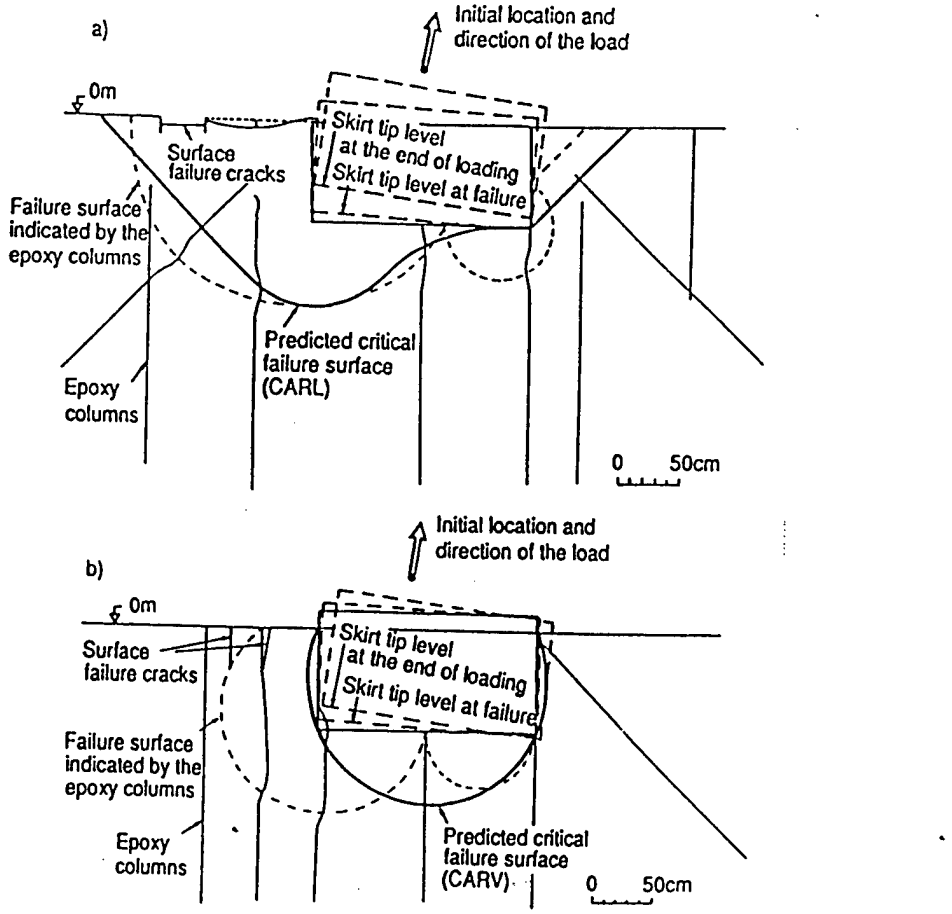

Fig. 38. Failure surfaces and observed displacements: (a) model test 1, (b) model test 4. (after Andersen et al., 1993)

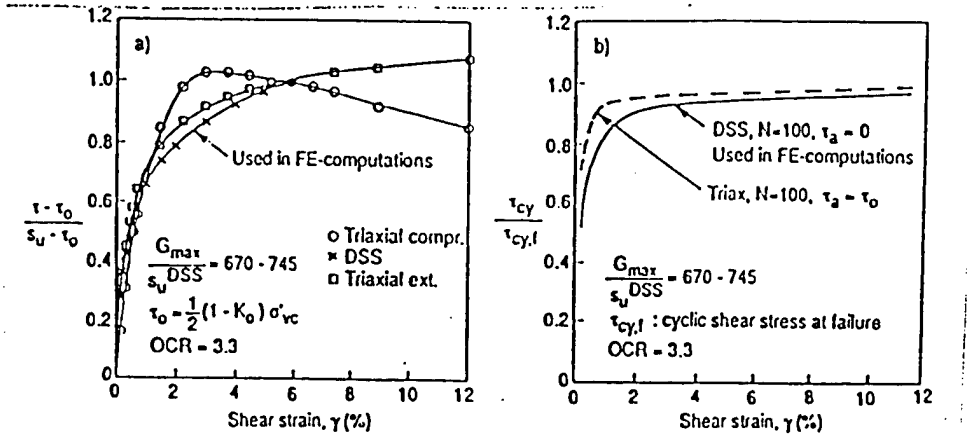

Fig. 39. Normalized stress-strain curves from laboratory tests: (a) static, (b) cyclic. (after Andersen et al., 1993)

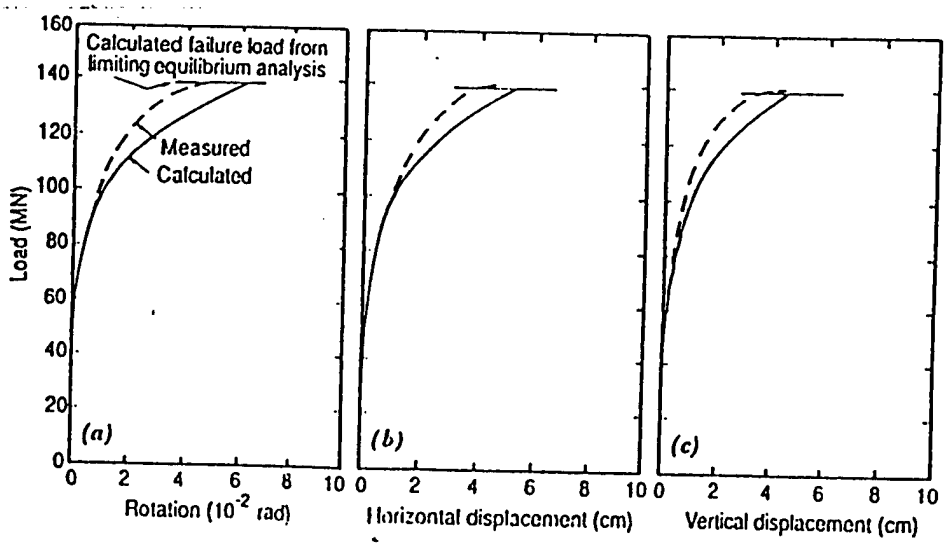

Fig. 40. Predicted and measured displacements at ground surface level in model test 1 (static): (a) rotational, (b) horizontal, (c) vertical. (after Andersen et al., 1993)

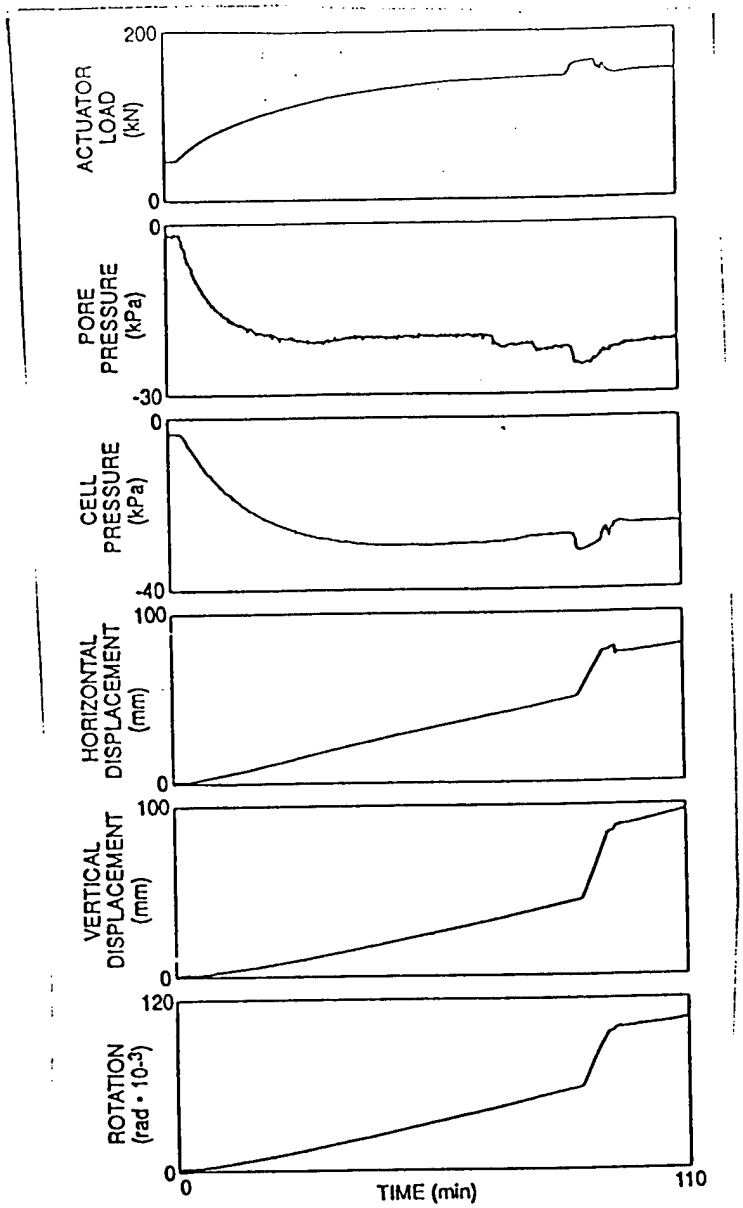

FIG. 5. Selected Results from Static Model Test 1

Fig. 41. Selected results from model test 1. (after Dyvik et al., 1993)

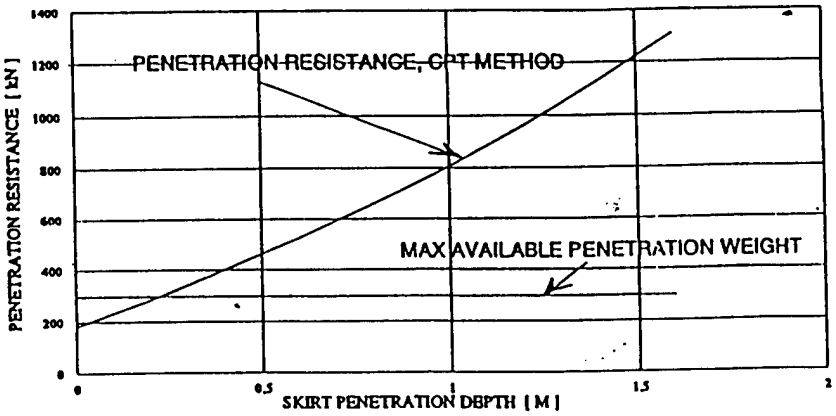

Fig. 42. Predicted penetration resistance, dense sand. (after Tjelta and Haaland, 1993)

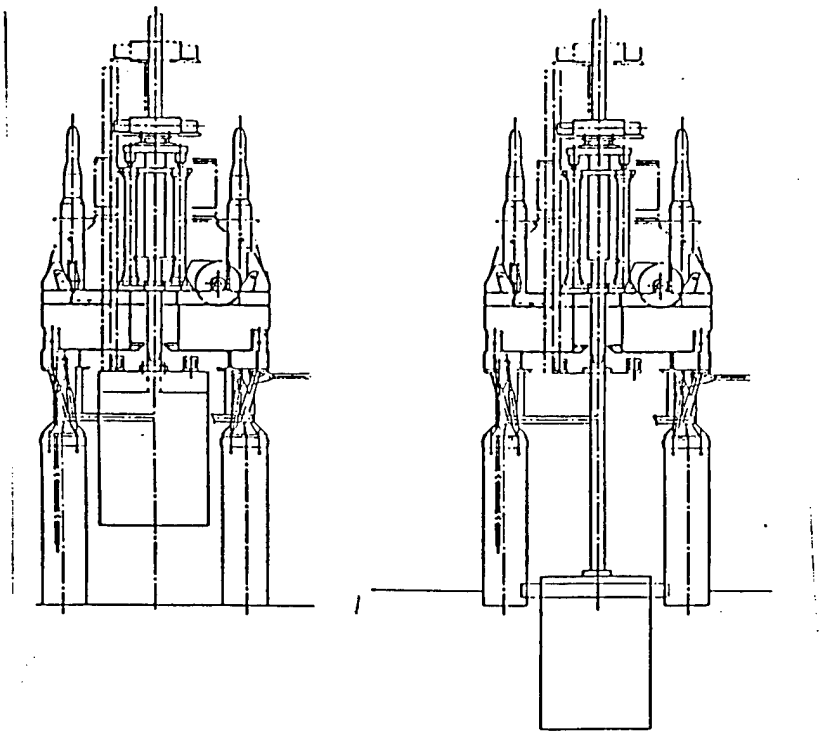

Fig. 43. Field test rig. (after Tjelta and Haaland, 1993)

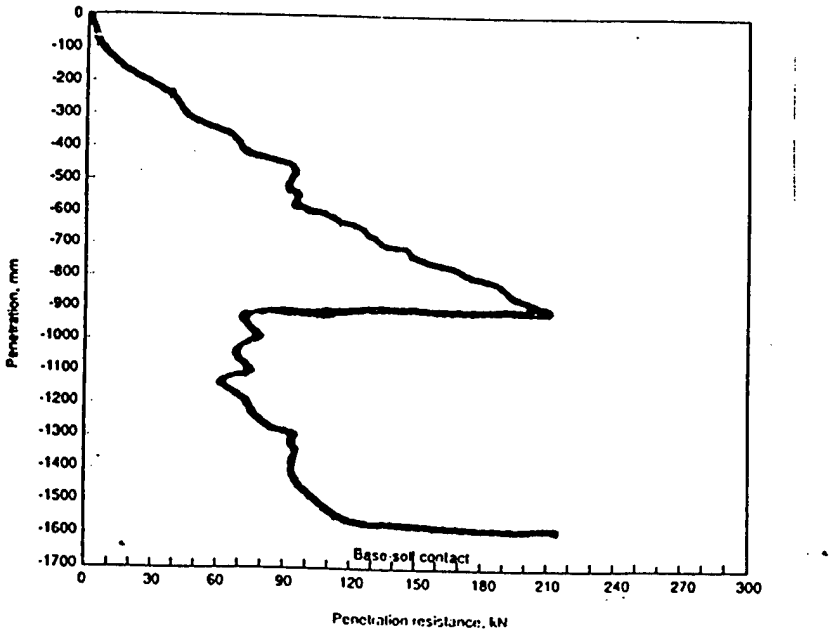

Fig. 44. Penetration results. (after Tjelta and Haaland, 1993)

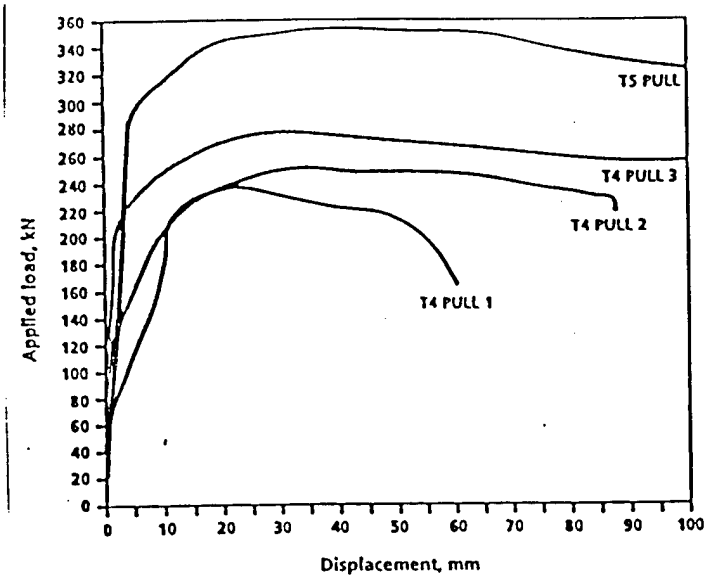

Fig. 45. Static pull-out tests. (after Tjelta and Haaland, 1993)

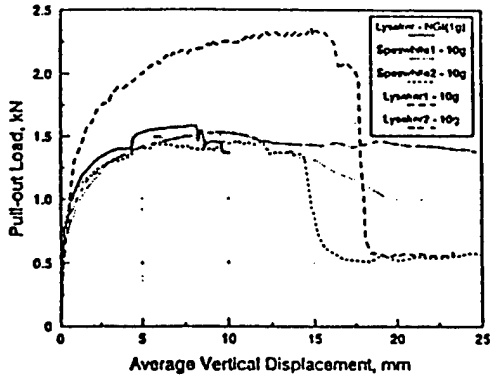

Fig. 46. Results of static pull-out tests. (after Morrison and Clukey, 1994)

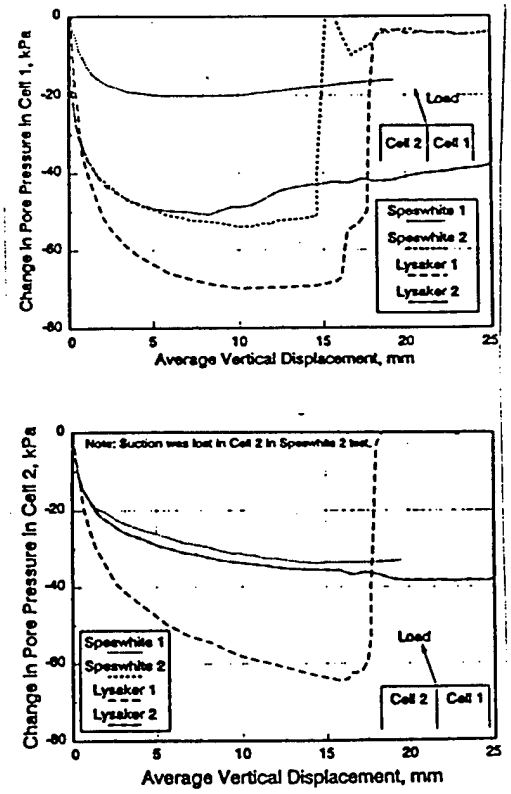

Fig 47. Pore pressure changes. (after Morrison and Clukey, 1994))

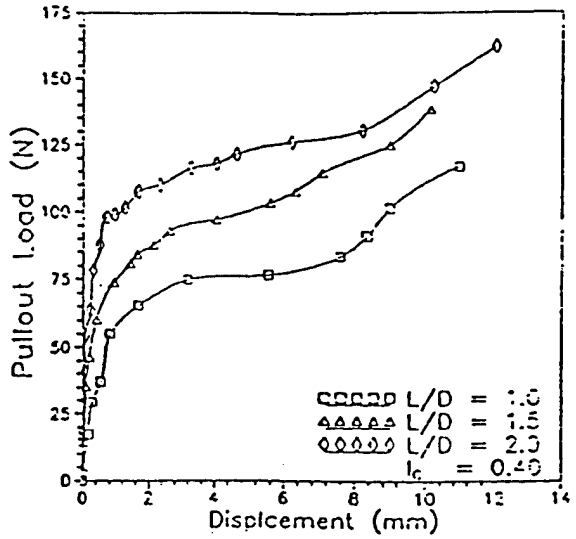

Fig. 48. Pull-out load-displacement curves of suction anchor ($I_c = 0.4$). (after Rao et al., 1997)

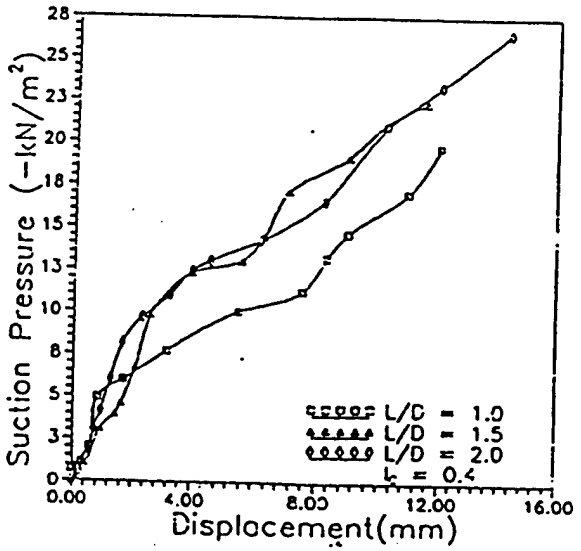

Fig. 49. Suction pressure variation of plug top with anchor displacement (Ic = 0.4). (after Rao et al., 1997)

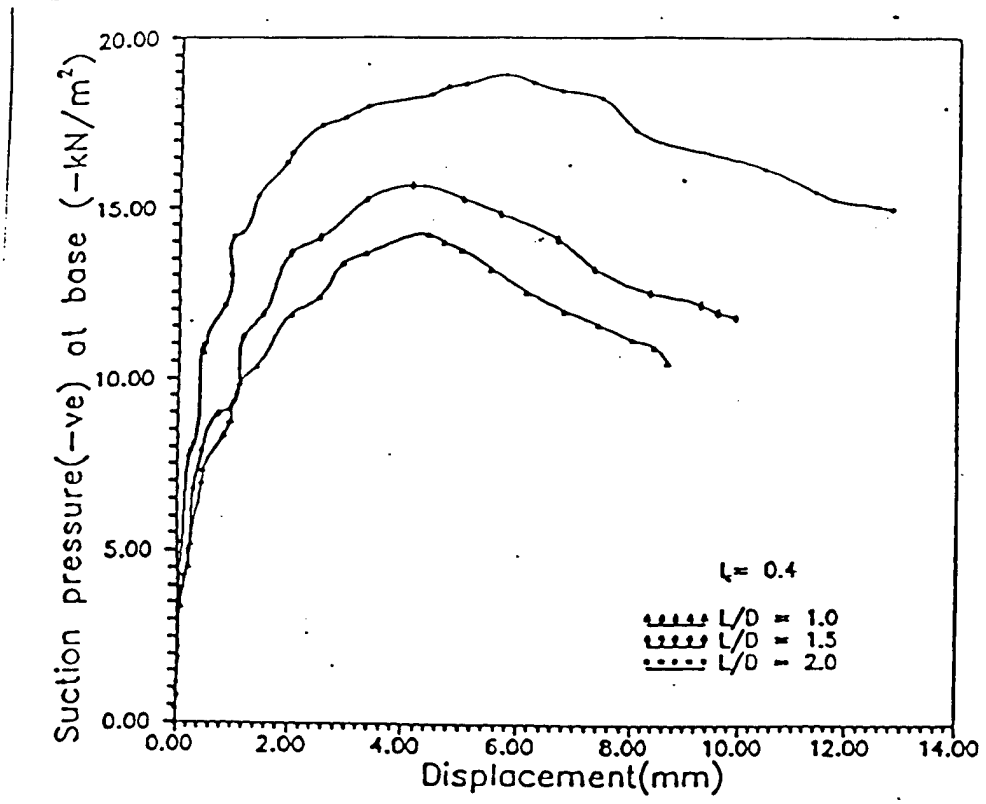

Fig. 50. Suction pressure (-ve) variation at anchor base with upward displacement ($I_c = 0.4$). (after Rao et al., 1997)

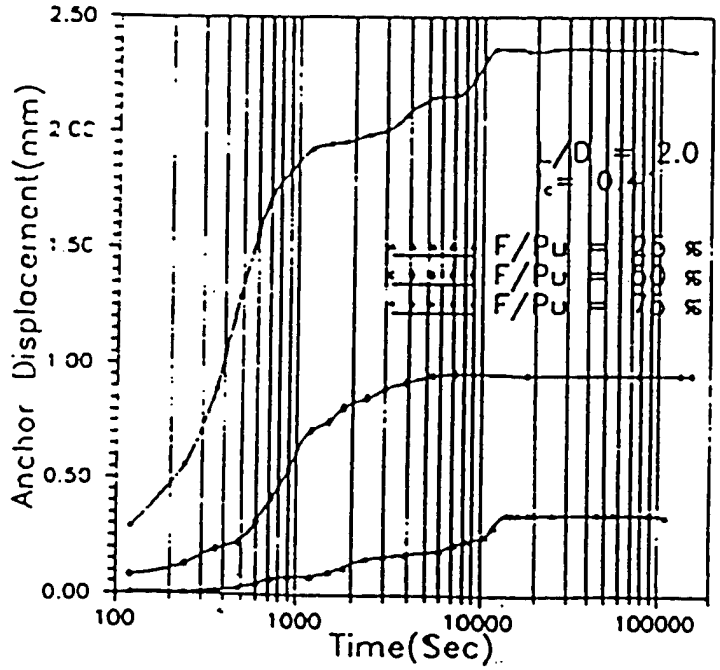

Fig. 51. Anchor displacement versus time for different sustained load levels (L/D = 2.0). (after Rao et al., 1997)

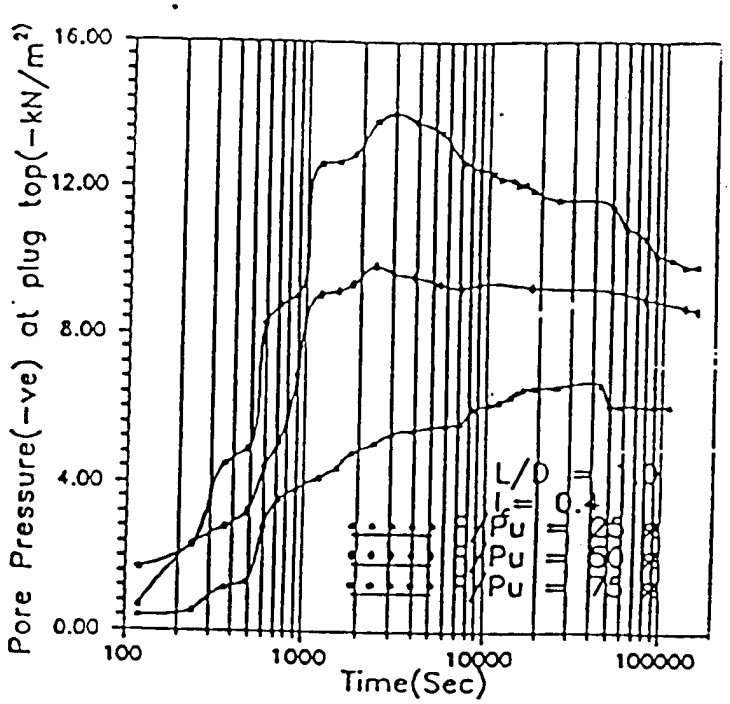

Fig. 52. Variation of suction pressure (-ve) at top of soil plug with time under different F/P_u. (after Rao et al., 1997)

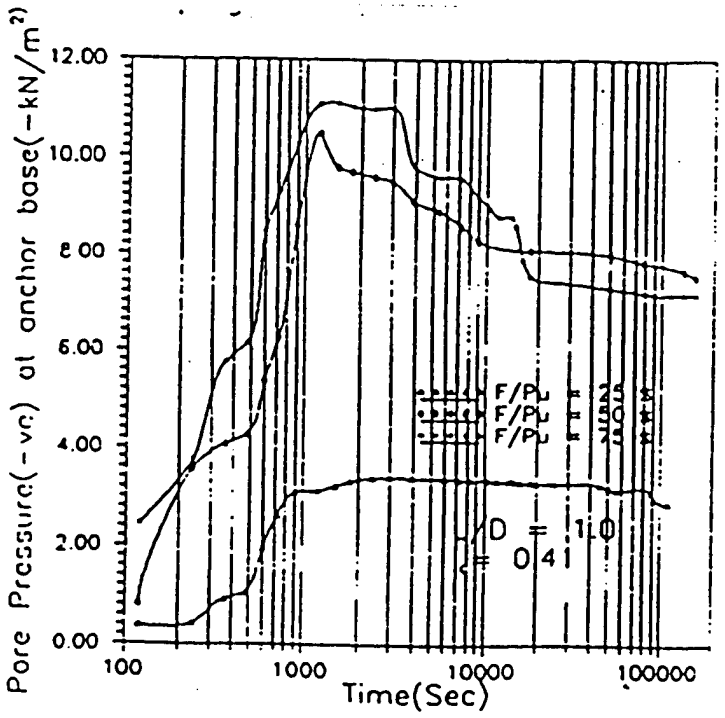

Fig. 53. Variation of suction pressure (-ve) at anchor base with time under different F/P_u. (after Rao et al., 1997)

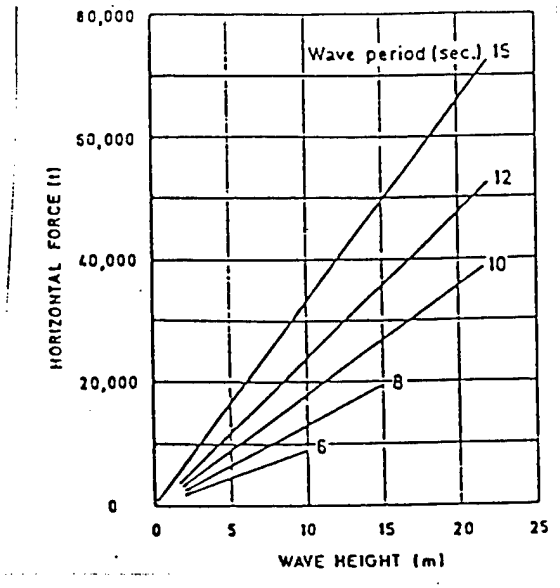

Fig. 54. Horizontal force versus wave height. (after Clausen et al., 1975)

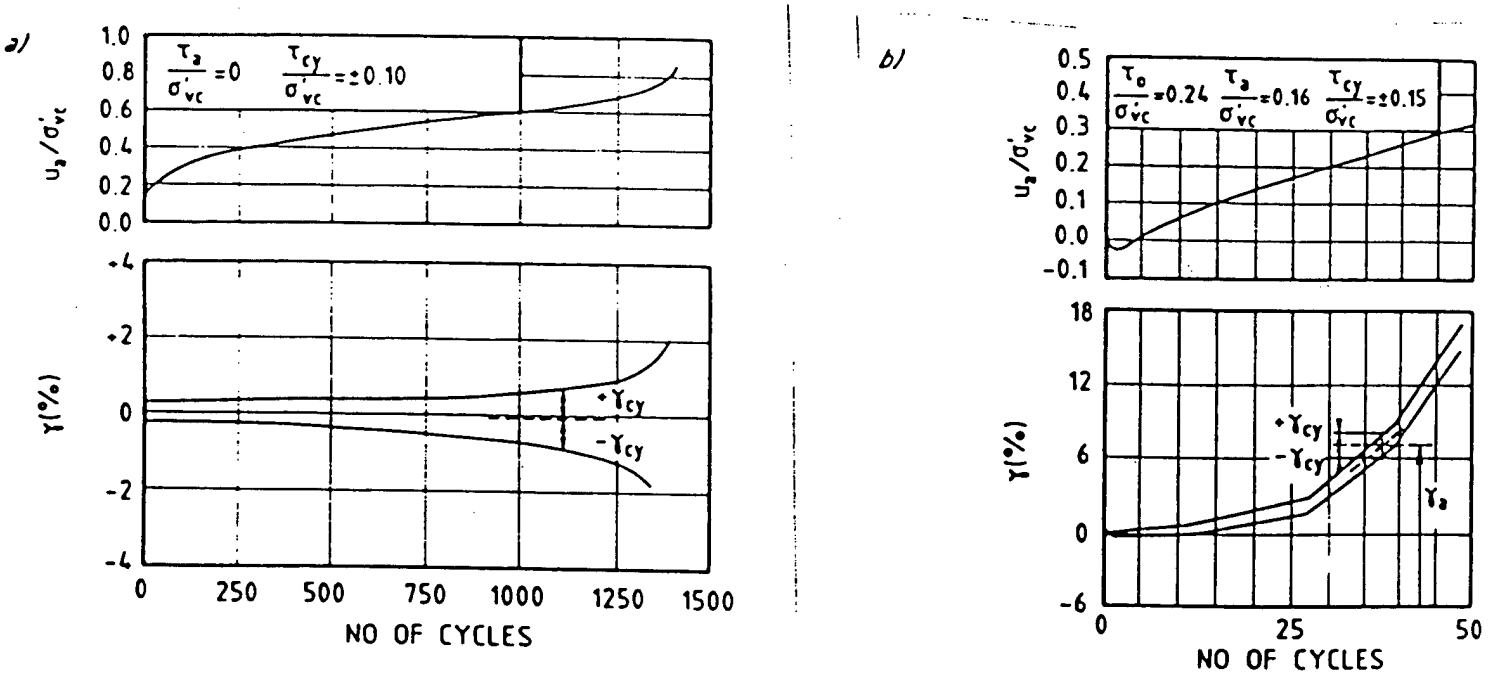

Fig. 55. Development of pore pressure and shear strains with number of cycles; Examples with normally consolidated Drammen clay: (a) DSS tests; (b) triaxial tests. (after Andersen and Lauritzen., 1988)

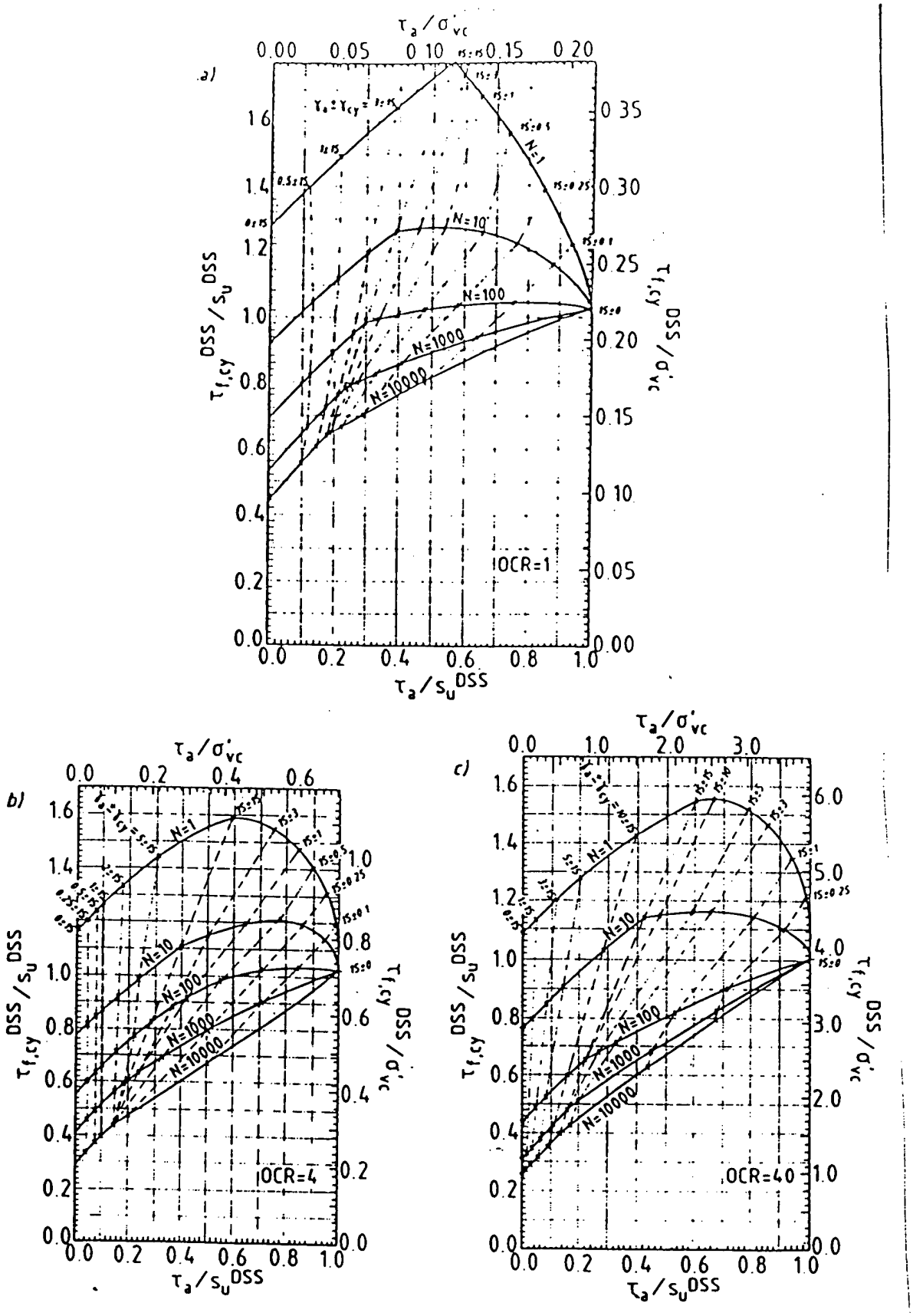

Fig. 56. Cyclic shear strength in DSS test on Drammen clay as a function of τ_a and number of cycles: (a) OCR = 1, (b) OCR = 4, (c) OCR = 40. (after Andersen and Lauritzen., 1988)

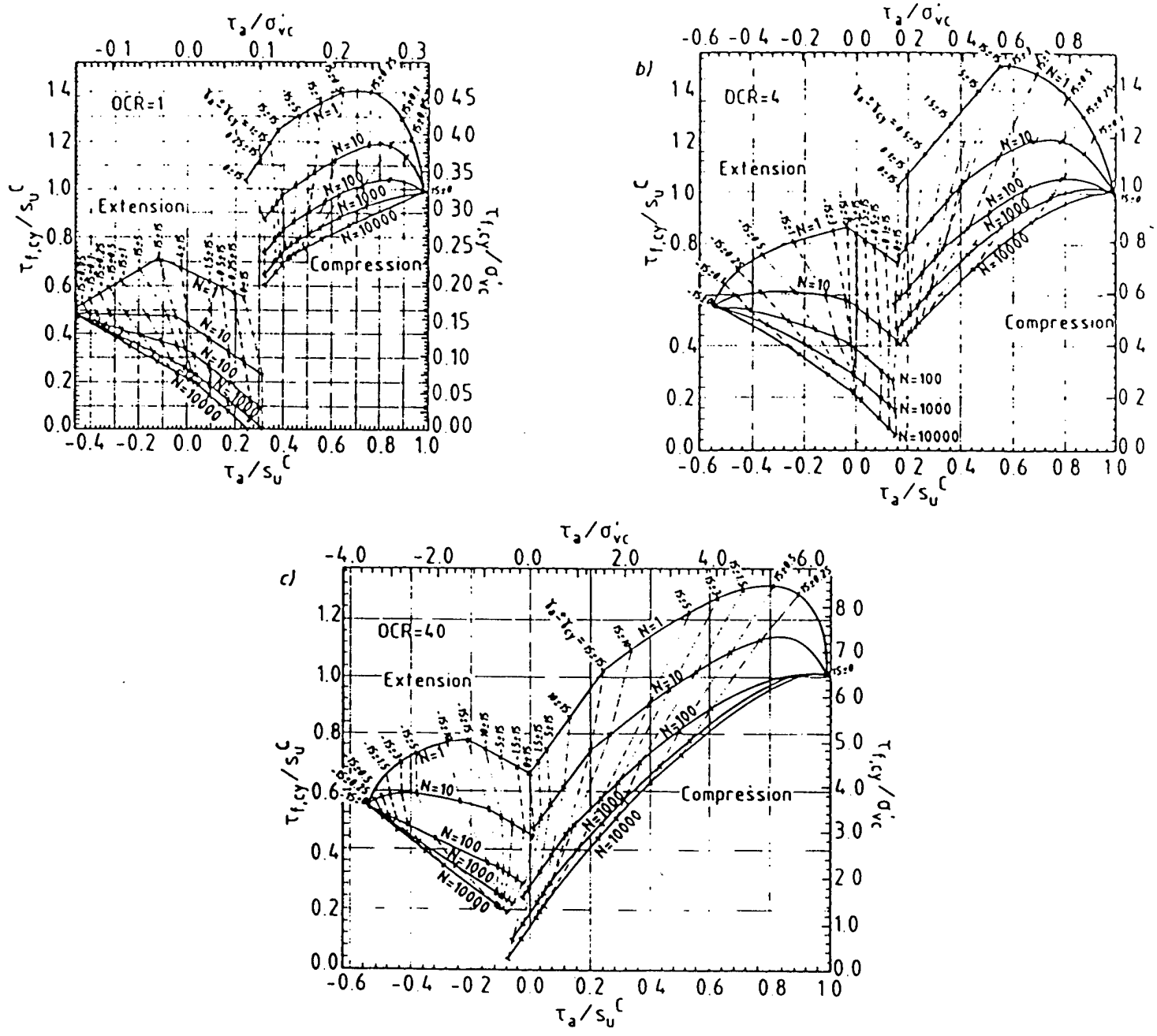

Fig. 57. Cyclic shear strength in triaxial test on Drammen clay as a function of τ_a and number of cycles: (a) OCR = 1, (b) OCR = 4, (c) OCR = 40. (after Andersen and Lauritzen., 1988)

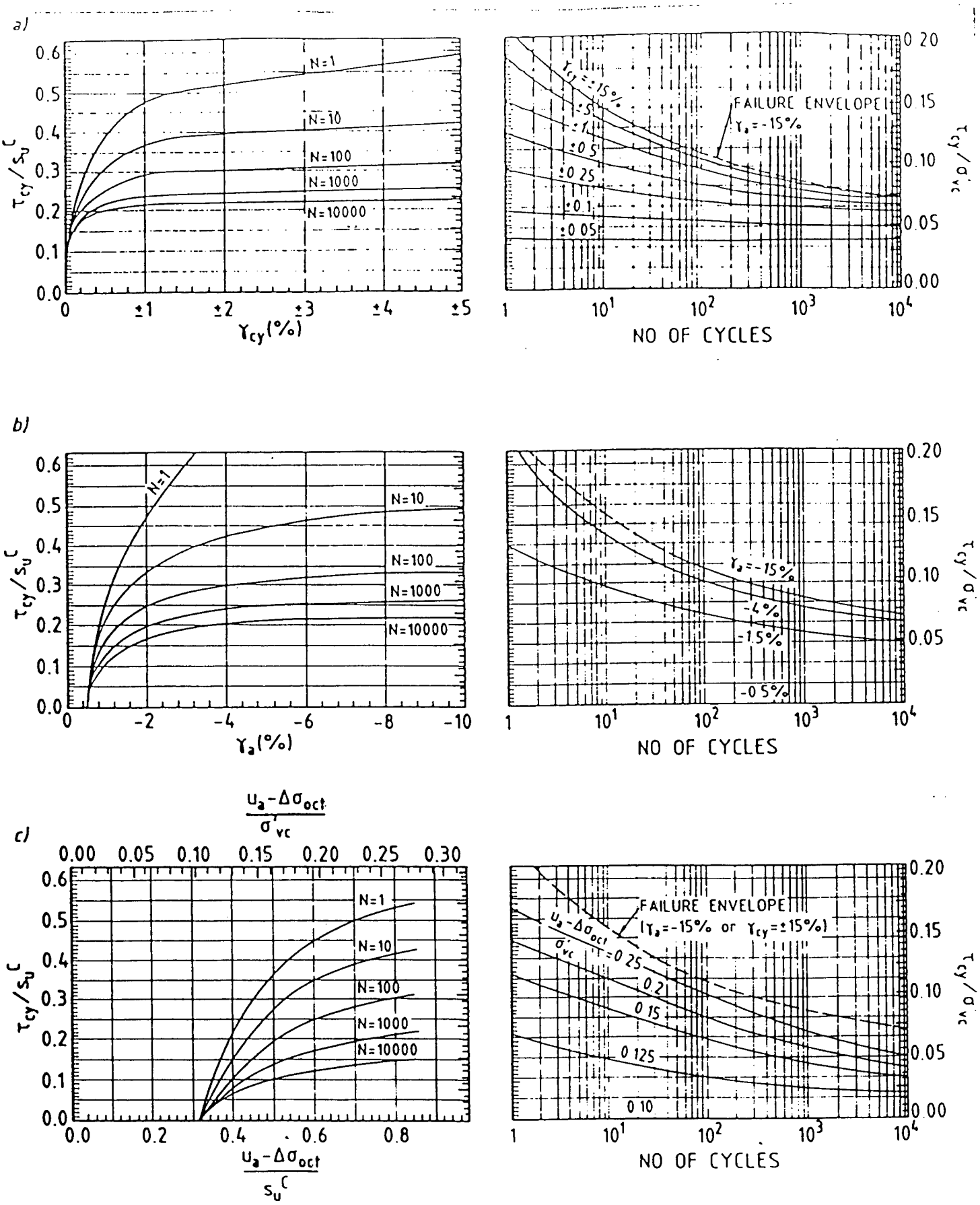

Figure 58. Contour diagram for triaxial tests with $\tau_a = 0$ on Drammen clay with OCR = 1: (a) cyclic shear strains, (b) average shear strains, (c) average pore pressures. (after Andersen and Lauritzen, 1988)

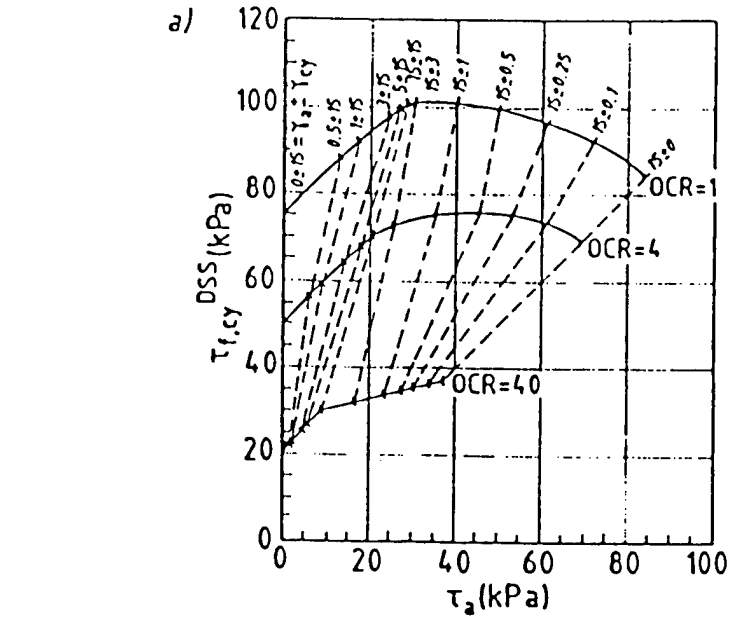

OCR	σ'_{vc} (kPa)	s_u^{DSS} (kPa)
1	390	84
4	98	69
40	9.7	37

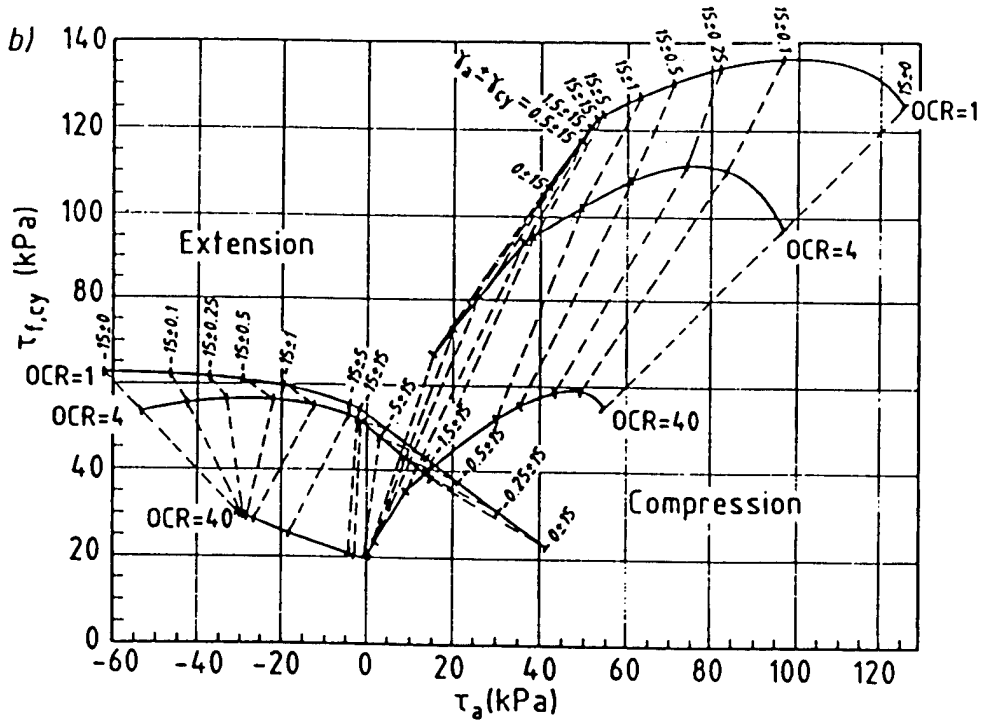

OCR	σ'_{vc} (kPa)	s_u^{C} (kPa)
1	390	126.5
4	98	96
40	8.5	55

Fig. 59. Cyclic shear strength of Drammen clay as a function of τ_a and OCR for a six-hour storm: (a) DSS, (b) triaxial. (after Andersen and Lauritzen., 1988)

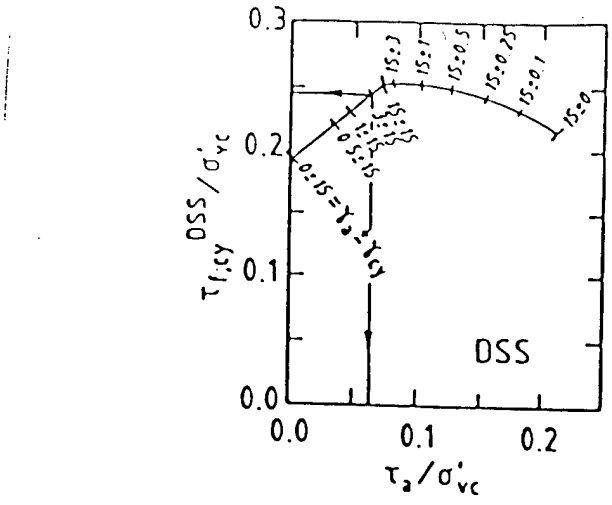

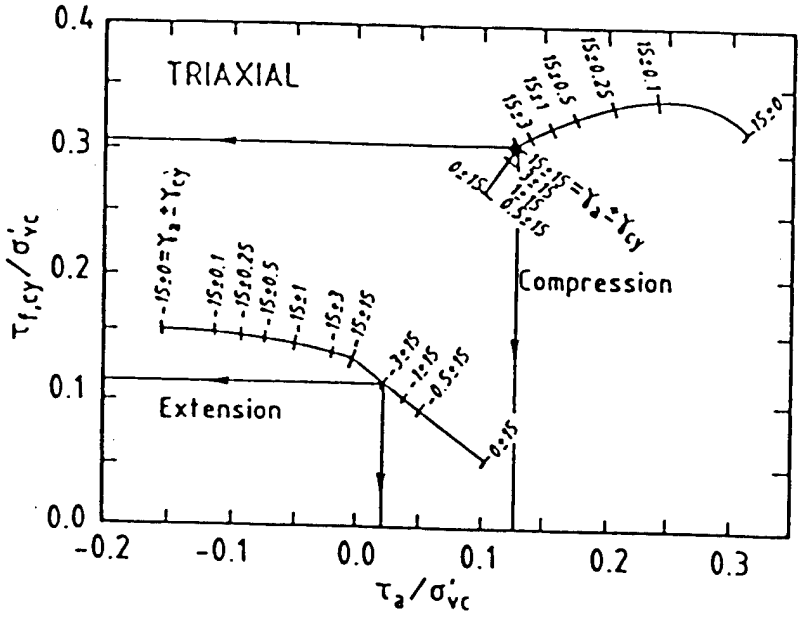

	$\frac{\tau_a}{\sigma'_{vc}}$ (Step 2)	$\frac{\tau_{f,cy}}{\sigma'_{vc}}$ (Step 4)
Compr.	0.424	0.304
DSS	0.064	0.241
Ext.	-0.021	0.115

For $\gamma_a \pm \gamma_{cy} = 3 \pm 15\%$

Figure 60. Example of determination of τ_a and $\tau_{f,cy}$ for assumed shear strain combination of $\gamma_a \pm \gamma_{cy} = 15\% \pm 3\%$ (Steps 2 and 4 described in iteration procedure). (after Andersen and Lauritzen, 1988)

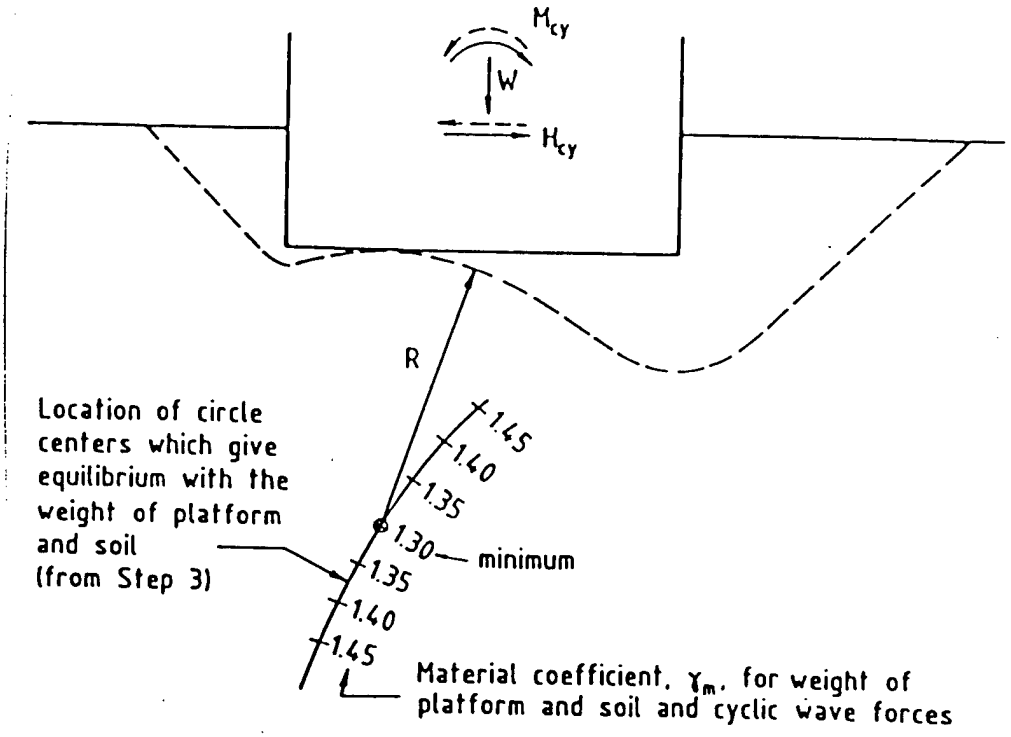

Figure 61. Determination of cyclic bearing capacity; Schematic for one combination of γ_a and γ_{cy}. (after Andersen and Lauritzen, 1988)

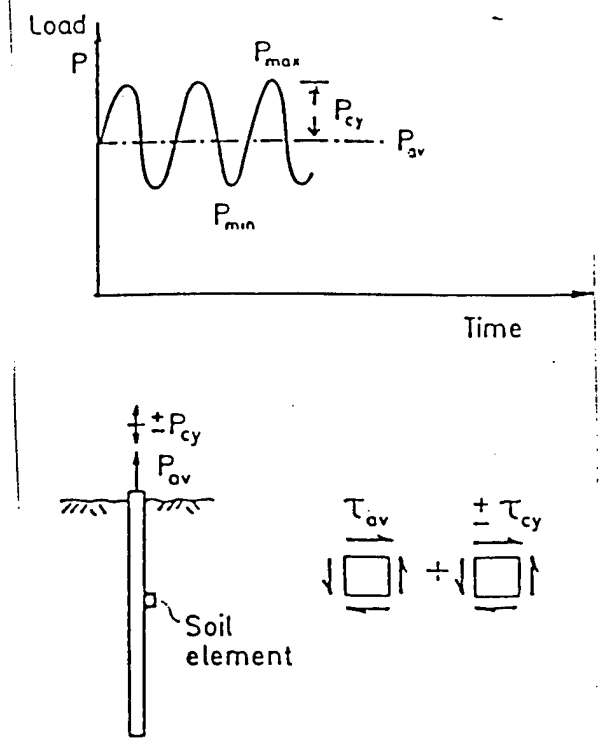

Fig. 62. Pile subjected to sustained and cyclic tension loads. (after Hoeg, 1982)

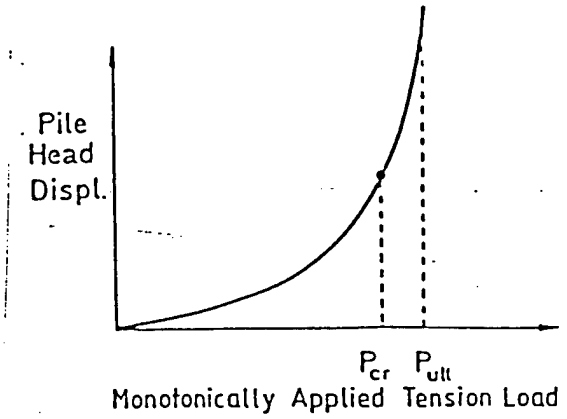

Fig. 64. Pile subjected to monotonically increasing tension load. (after Hoeg, 1982)

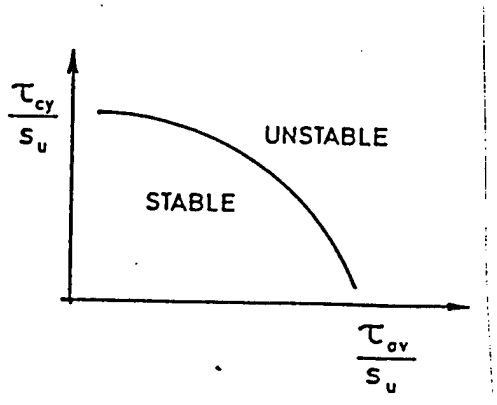

Fig. 63. Behavior of soil element shown in figure 62. (after Hoeg, 1982)

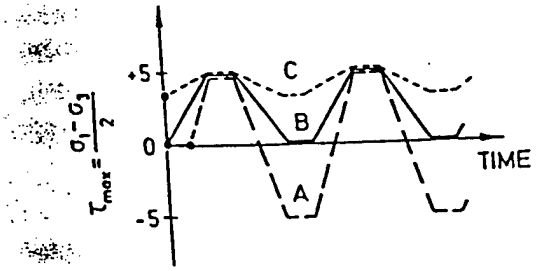

Fig 65. Effects of different types of load cycles. (after Hoeg, 1982)

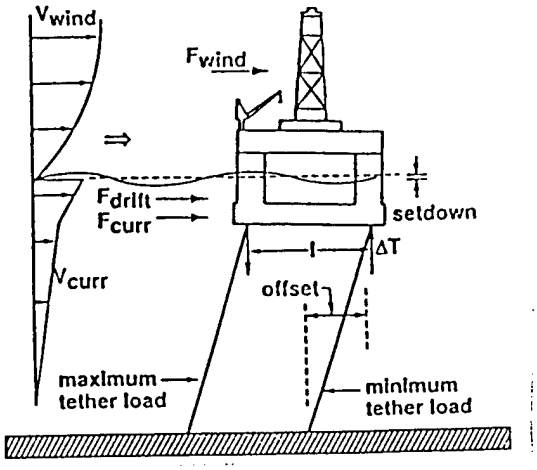

Fig. 66. Schematic of loading condition of TLP. (after Clukey and Morrison., 1993)

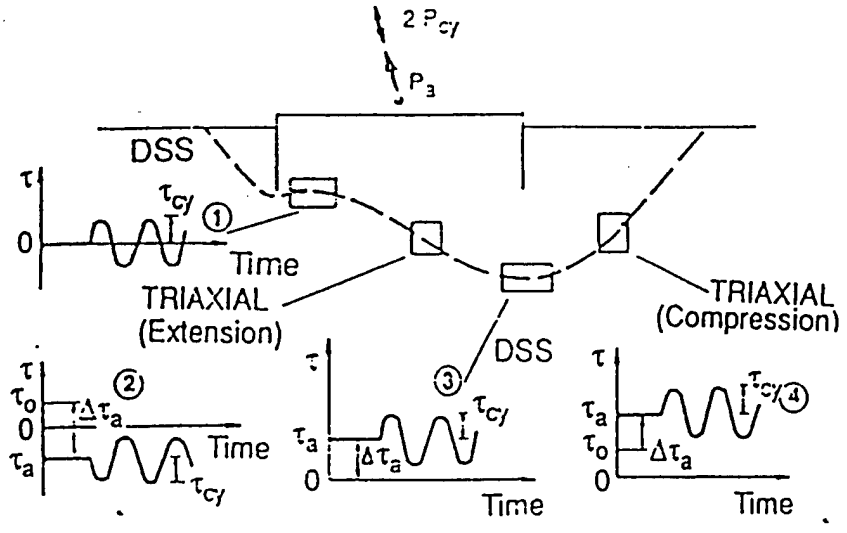

Fig. 67. Simplified stress condition for some elements along a potential failure surface in the soil . (after Andersen et al., 1994)

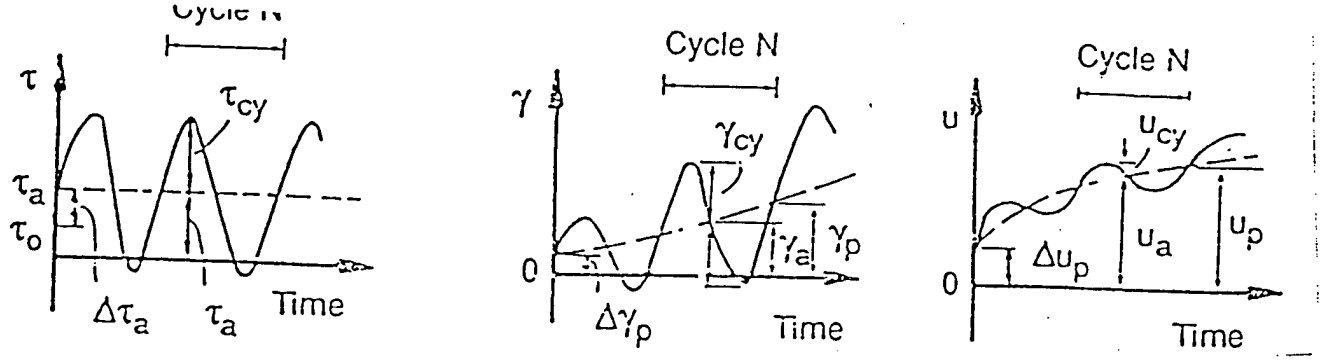

Fig. 68. Time histories of shear stress and pore pressure for a soil element subjected to cyclic loading. (after Andersen et al., 1994)

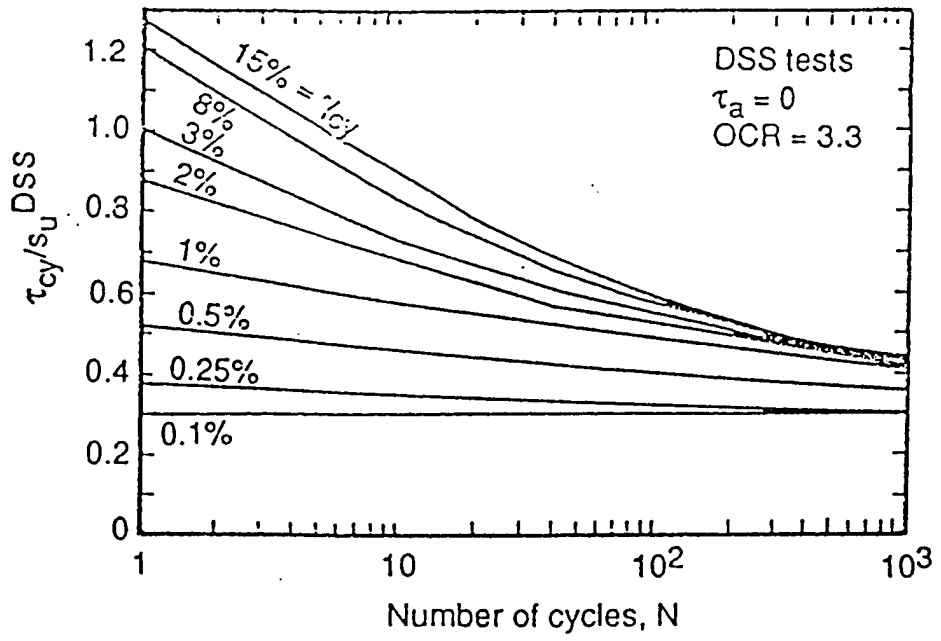

Fig. 69. Cyclic shear strain contour diagram for DSS tests on clay beneath 0.77 m. (after Andersen et al., 1994)

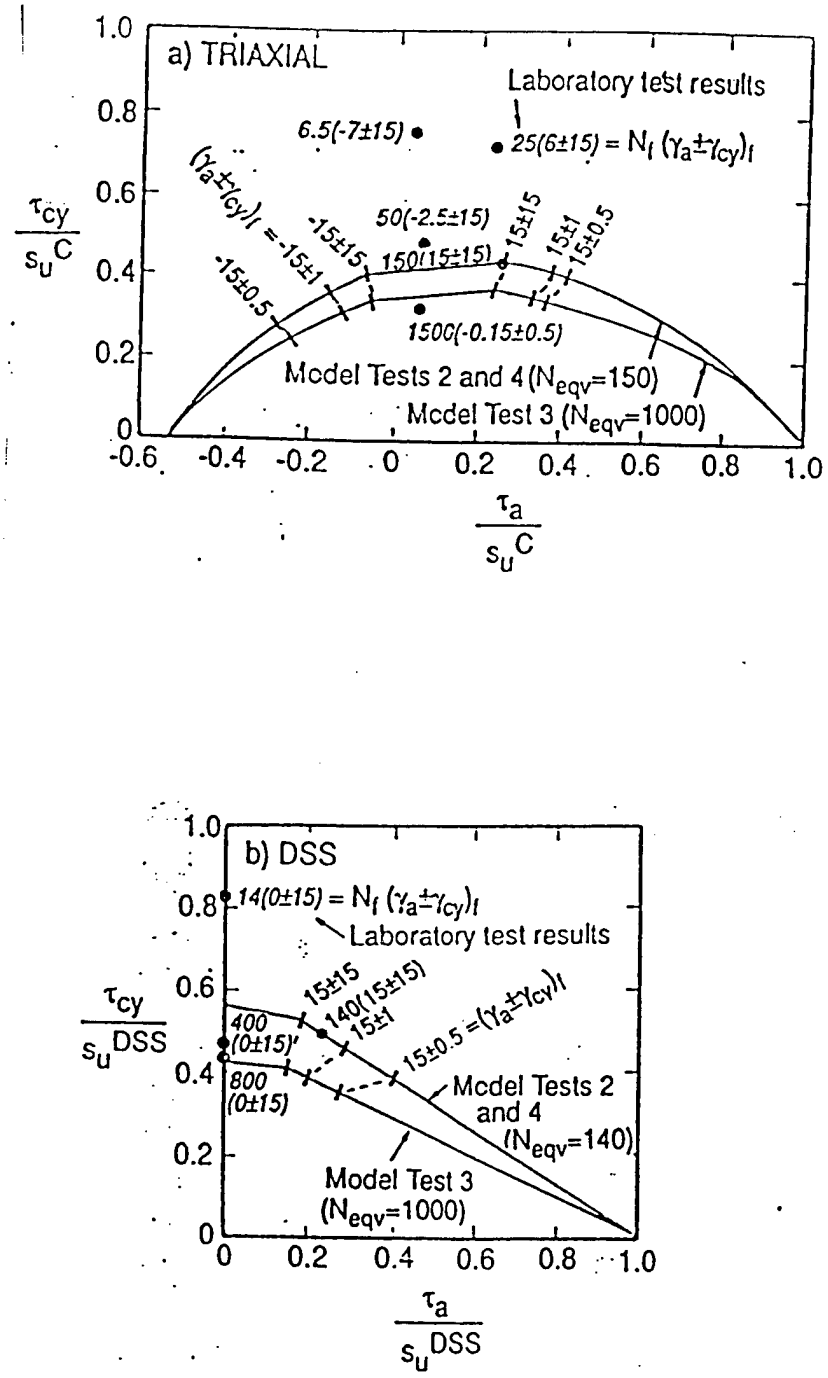

Fig. 70. Number of cycles to failure and failure mode (i.e. $\gamma_p = \gamma_{cy}$) as a function of τ_a and τ_{cy}. (after Andersen et al., 1994)

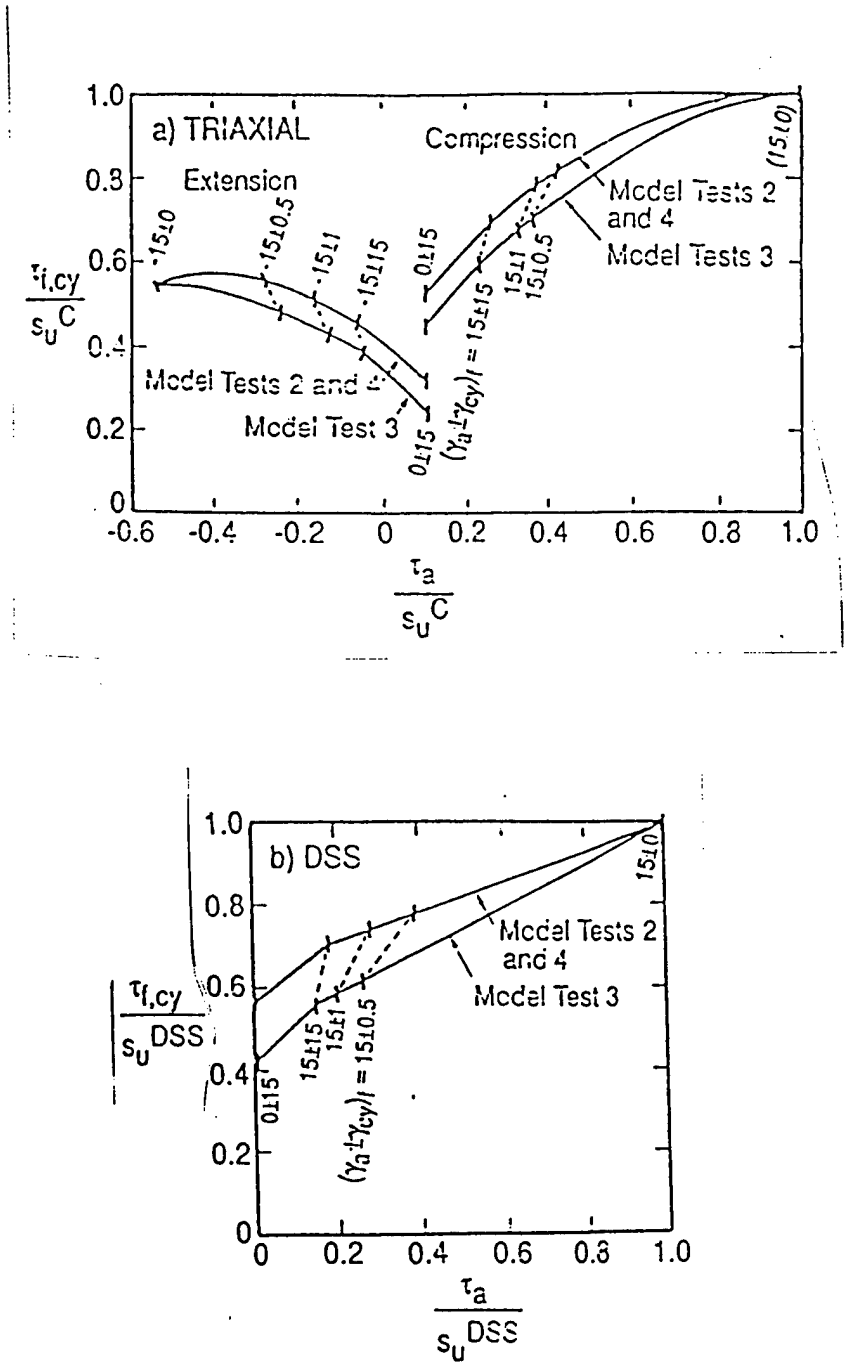

Fig. 71. Cyclic shear strength for model test 2 and 4 (N_{eqv} = 140 - 175) and model test 3 (N_{eqv} = 1000) (after Andersen et al., 1994)

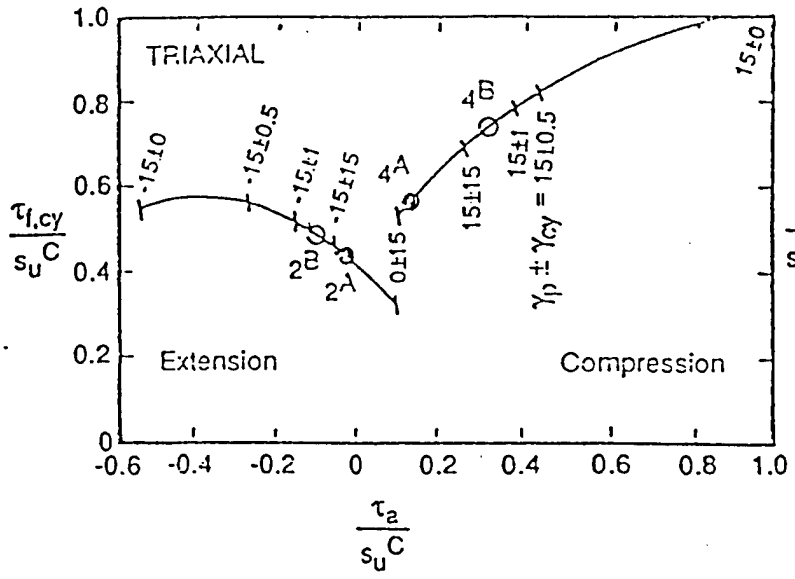

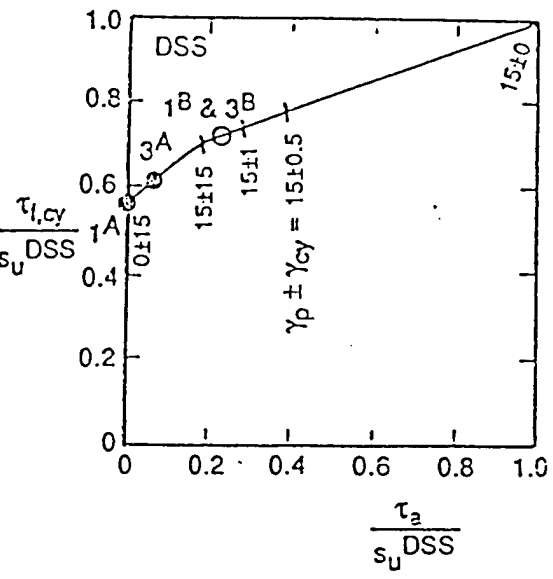

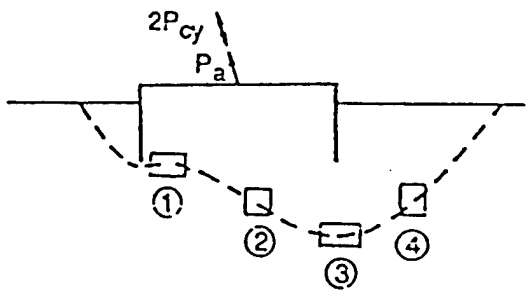

	$\frac{\tau_a}{s_u}$ (Step (2))*	$\frac{\tau_{f,cy}}{s_u}$ (Step (4))*
Compr.	0.30	0.74
DSS	0.23	0.73
Ext.	0.10	0.49

For $\gamma_p \pm \gamma_{cy}$ = 15±3 %

* Refers to iteration steps described in text

Fig. 72. Simplified general calculation example. Cyclic shear strengths before and after redistribution of τ_a due to cyclic loading assuming a shear strain combination $\gamma_p \pm \gamma_{cy}$ = 15 ± 3%(after Andersen et al., 1994)

Test No./ Phase	Test Type	Caisson Embed. ft.	Load Offset, kips	Static Offset Ratio, %	Cyclic Load, kips	Cyclic Load Ratio, %	No of Equiv. Cycles	Freq (Hz)	No. of Applied Cycles	Perm. Displ., in	Calc. Static Capacity, kips	Meas. Static Capacity, kips
1/II	Vert.	113.2	4724	1.9	±2923	±13.6	-	5	500	0.2	21417	-
"	"	"	"	"	"	"	-	1	"	0.1	"	-
"	"	"	6745	11.3	±5845	±27.3	-	5	"	0.9	"	-
"	"	"	"	"	"	"	1045	1	"	0.4	"	22546
2/II	Incl.	104.7	4721	2.0	±3372	±17.1	-	5	500	0.2	19775	-
"	"	"	"	"	"	"	-	1	"	0.2	"	-
"	"	"	6745	12.3	±5845	±29.6	-	5	"	0.9	"	-
"	"	"	"	"	"	"	1065	1	"	0.4	"	20739
3/III	Comb. ±2°	96.3	4721	2.0	+3372	+19.0	-	5	500	0.1	17776	-
				"	−4496	−25.3	-	"				-
"	"	"	"	12.3	±3372	±19.0	-	1	500	0.1	"	-
"	"	"	6745	"	±5845	±32.9	378	5	"	2(165)[1] 4(250)[1]	"	Failed
4/II	Vert.	100.5	4960	4.1	±3934	±25.3	-	5	350	0.4	15559	-
"	"	"	"	"	"	"	-	1	375	0.2	"	-
"	"	"	7644	21.4	±6746	±43.4	191	5	375	4(125)[1]	"	Failed
5/III	Comb.-Seq. ±2°	100.8	4621	1.9	±3148	±20.2	-	5	500	0.2	15593	-
"		"	"	"	"	"	-	1	"	0.2	"	-
"	Vert.	"	"	"	±4046	±25.9	-	5	"	0.1	"	-
"	Vert.	"	6296	12.7	±5620	±36.0	689	5	"	0.4	"	21107
6/III	Comb. ±1°	108.6	4721	2.4	±4027	±23.9	-	2.5	500	0.4	16830	-
"	"	"	5171	5.1	±4721	±28.1	-	2.5	"	0.2	"	-
"	"	"	5845	9.1	±5396	±32.1	-	2.5	"	0.4	"	-
"	"	"	6745	14.4	±6295	±37.4	-	1	"	2	"	-
"	"	"	6745	14.4	±6295	±37.4	805	5	"	1	"	Failed
"	"	"	7644	19.8	±7194	±42.7	-	1	"	2(100)[1], 4(250)[1]	"	20073
7/III	Comb.-Seq. ±2°	101.9	4631	2.0	±2248	±14.3	-	5	500	0.4	16830	-
"		"	"	"	±3372	±21.4	-	1	"	0.8	"	-
"	Chg. Dir.	"	"	"	±2248	±14.3	-	5	"	0.3	"	-
"	"	"	"	"	±3372	±21.4	-	1	"	0.3	"	-
"	"	"	5058	4.7	±4496	±37.4	-	5	"	0.6	"	-
"	"	"	7307	19.0	±6070	±38.6	275	1	"	2(60)[1], 4(110)[1]	"	Failed

Submerged unit weight of caisson and associated loading equipment = 4320 kips

[1] Number of Cycles

Table 9. (after Clukey and Morrison, 1995)

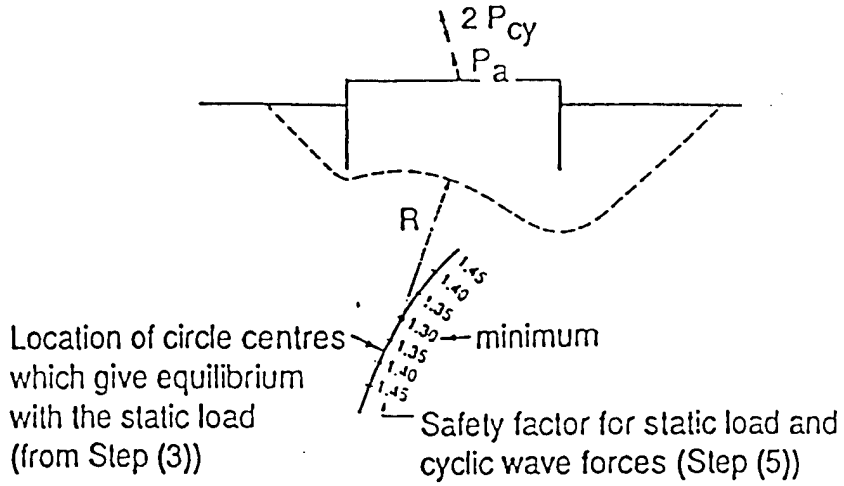

Fig. 73. Determination of critical failure surface and minimum safety factor for one combination of $\gamma_p \pm \gamma_{cy}$. (after Andersen et al., 1994)

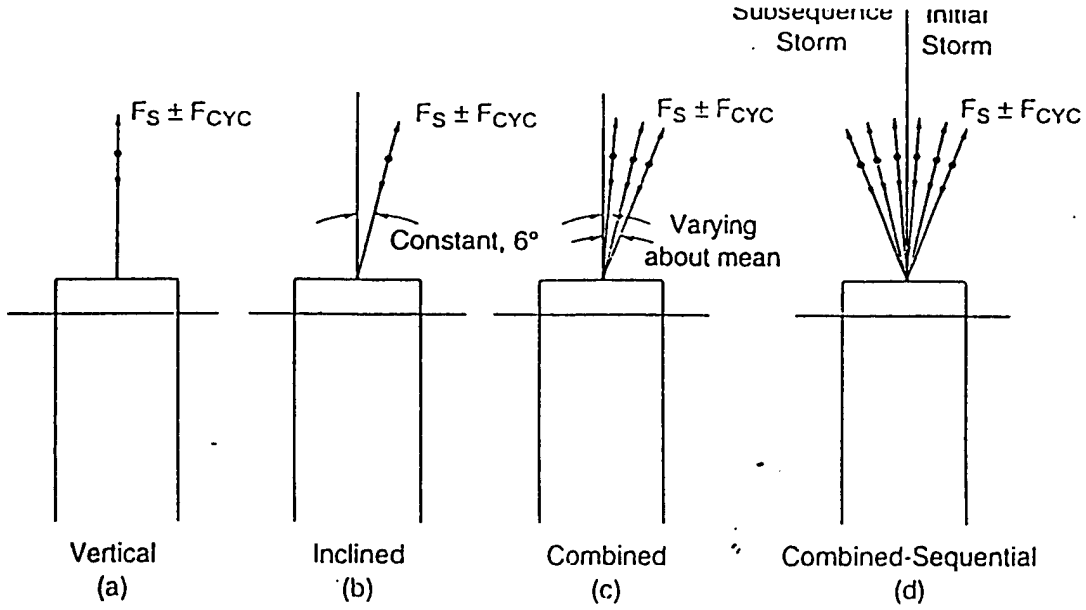

Fig. 74. Types of cyclic centrifuge tests. (after Clukey and Morrison, 1995)

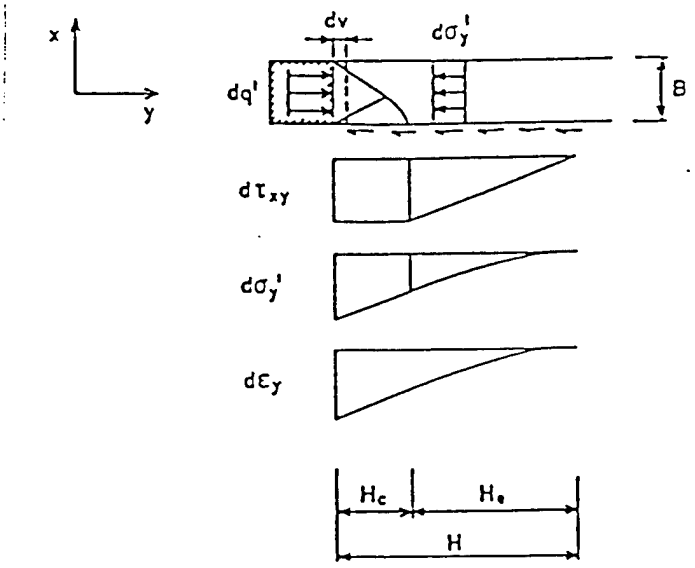

Fig. 75. Simplified deformation pattern. (after Grande and Nordal, 1979)

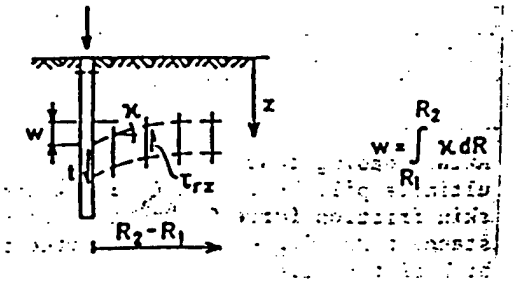

Fig. 76. Simplified deformation pattern. (after Grande and Nordal, 1979)

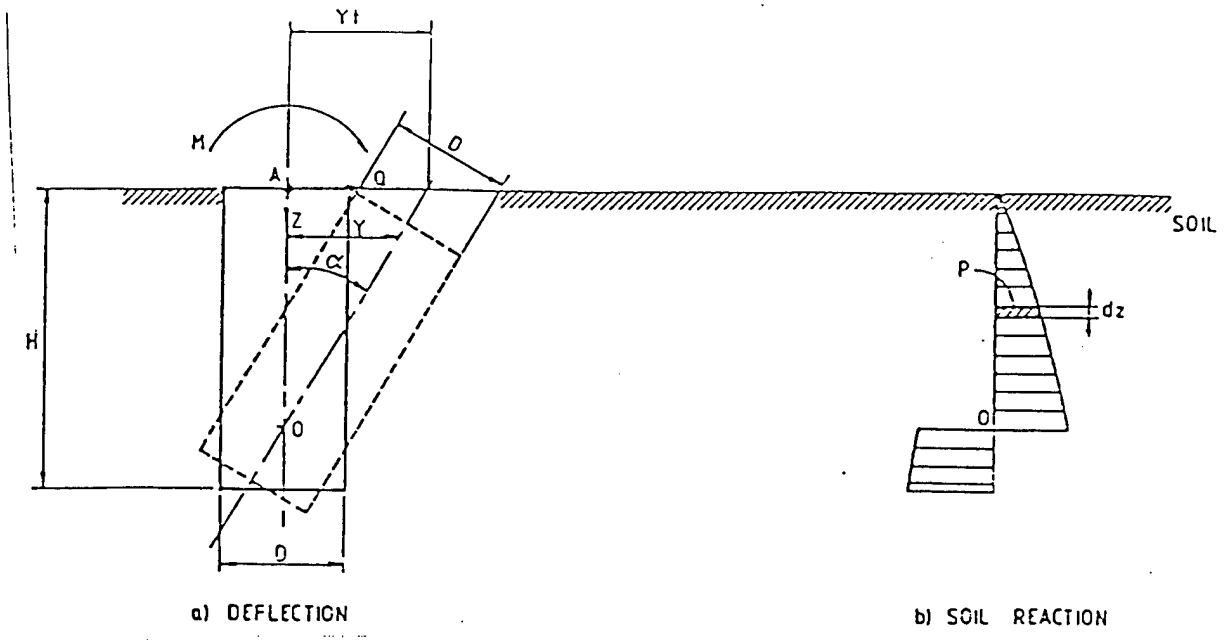

Fig. 77. A short laterally loaded rigid pile. (after Hogervorst, 1980)

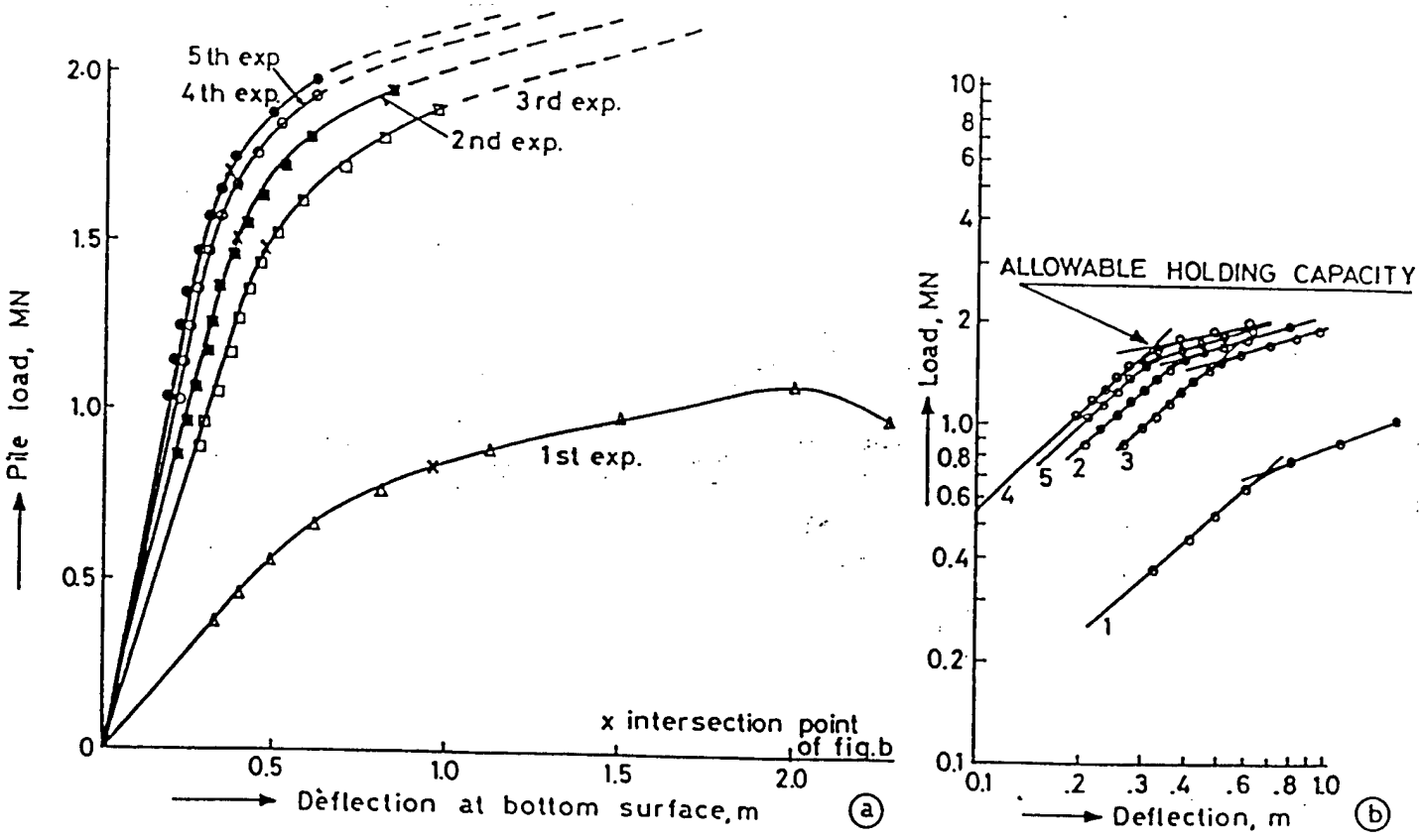

Fig. 78. Load-deflection diagram. (after Hogervorst, 1980)

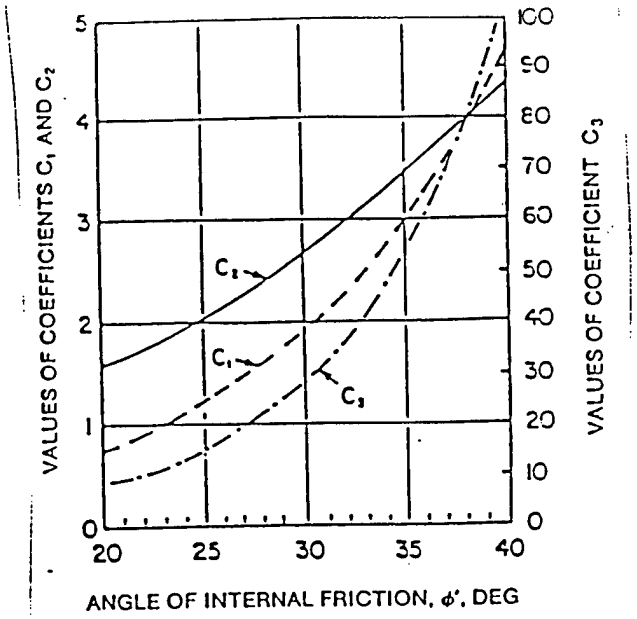

Fig. 79. Coefficients and function of ϕ'. (after API RP2A, 1993)

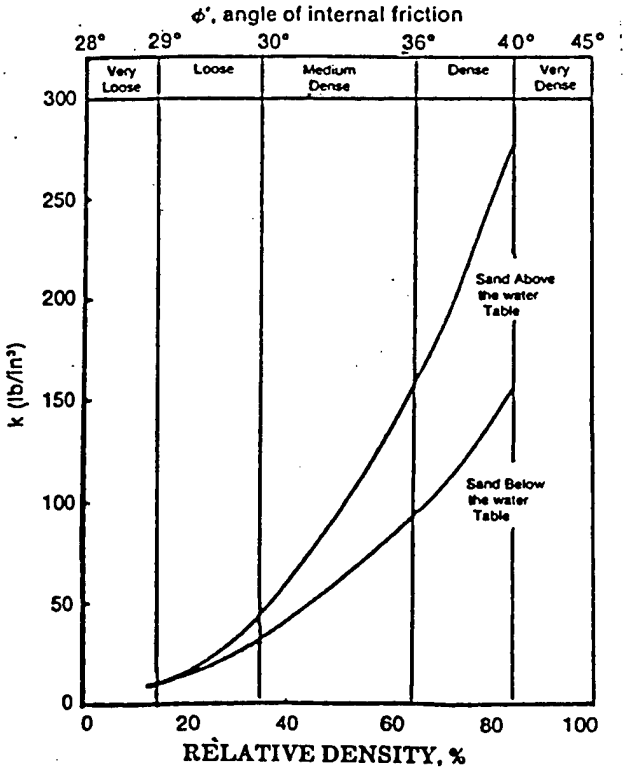

Fig. 80. Relative density, %. (after API RP2A, 1993)

Quarterly Progress Report (Jan. 1 - Mar. 31, 1998)

Title: Use of Suction Piles for Mooring of Mobile Offshore Bases
ONR Grant No. N00014-97-1-0887

Principal Investigator: Sangchul Bang
Department of Civil and Environmental Engineering
South Dakota School of Mines and Technology
Rapid City, South Dakota

Date: Mar. 25, 1998

Activities completed during the current quarter and planned for the next quarter

1. Literature Study

The draft task completion report on literature study was reviewed by the NFESC staff and their review results were received. The draft report is currently being modified to reflect the comments provided by NFESC. Comments from SDSM&T on the NFESC review have been submitted for further review. The final task completion report on literature study will be submitted after the review process is completed.

2. Performance Study of Suction Piles

The suction pile performance study using linear elastic soil material properties has been completed. Detailed description of the results of the analysis as well as the pile geometry and material properties is included in Appendix – A in this report. Briefly, eight different cross-sections of suction piles were selected and their performances analyzed by ABAQUS finite element method of analysis software and FEMAP pre- and post-processor. The selected cross-sections include; circle, hexagon, triangle, rectangle, Y-shape, cross-shape, clover-shape with either 3 or 4 leaves, clustered circles with either 3 or 4 sub-circles. Dimensions of each cross section have been determined based on the same circumferential length, i.e., the contact areas between the piles with various cross-sectional shapes and the soil remain the same. This in essence keeps the total amount of pile material the same for all cross-sections.

Suction piles with various cross-sections were loaded with either a horizontal or vertical concentrated force of 300,000 lbs at the geometric center of the pile top cover.

Their responses were analyzed in terms of various pile and soil displacements and stresses.

The results indicate that the circular shape is the most effective cross-section with respect to the overall soil and pile behaviors under both horizontal and vertical loads. There was however no general consensus for the next most effective cross-sectional shape. Either Y-shape or clustered circles or cross-shape was identified as the next most effective when various responses of the soil and pile were analyzed and compared.

Since the linear elastic analysis can only be viewed as qualitative analysis, three cross-sections have been chosen for the next step of the analysis which utilizes the plasticity soil properties. Those selected cross-sections are; circle, Y-shape, and triangle. Currently, suction piles with these three cross-sections embedded in sandy soil are being studied, in which the soil behaviors are modeled by the linear elastic soil properties up to yield and then by the Extended Drucker-Prager plasticity parameters. These plasticity parameters have been quoted from the NFESC report provided by Ted Shugar. This sandy soil has a friction angle of 46.2 degrees with no cohesion and the dilation angle of 21.6 degrees.

3. Analysis and Design Method of Suction Piles

An analytical solution previously developed by the principal investigator for the analysis of laterally loaded piles and subsequently modified for suction piles has been used to study the behaviors of suction piles under lateral loads and to identify the effect of the location of mooring line attachment under various conditions. Six different soil types so far have been investigated. They include; sands with friction angles of 30, 35 and 40 degrees and clays with average cohesions along the entire length of the pile of 100, 250, and 500 psf. The pile diameters studied vary from 10 ft. to 50 ft. with the length to diameter ratio varying from 1 to 4.

From the results of the analysis with sands, it was found that the ratio between the depth to the mooring line attachment point and the pile length (H"/L) that corresponded to the ultimate pile lateral resistance (P_{ult}) increased with the pile length to diameter ratio (L/D) but with a decreasing rate. The H"/L ratio at P_{ult} also varied only with the ratio L/D and remained almost independent of the soil friction angle and the pile diameter. The ratio between the depth to the pile rotation point and the pile length at P_{ult} was about 0.45 to 0.6 in all cases.

For clay soils with relatively low cohesion values, the H"/L ratio decreased as the L/D ratio increased with a faster rate for larger pile diameters. With high cohesion, the H"/L ratio increased as the L/D ratio increased with a faster rate for smaller diameter piles. The ratio between the depth to the pile rotation point and the pile length at P_{ult} generally increased as the ratio L/D increased, resulting in 0.94 – 0.965 in almost all cases.

During the next reporting period, it is planned to continue this study, considering additional soil types including clay soils whose strengths are depth-dependent, e.g., 10 psf/ft and 20 psf/ft. The effect of the flange at the top of the suction pile will also be studied. The detailed results of the study will be summarily included in future reports.

4. Model Testing

The newly constructed model apparatus has been used to test four series of suction piles in sand. Each series consists of four to five almost identical tests (except a slight variation in initial pile penetration depth) in order to minimize any potential error. The main variables in these series of tests were the suction pile initial penetration depth and the amount of surcharge applied at the top of the pile as shown below in Table – 1.

Series	Initial Pile Penetration (ft.)	Surcharge (lbs)
1	1.0	48.8
2	1.0	61.0
3	1.0	73.2
4	3.0	73.2

Table – 1 Details of Suction Pile Tests

Please note that the surcharge of 48.8 lbs is an additional weight on top of the plastic model pile to produce the equivalent weight of the steel pile with equal dimensions. Appendix – B of this report includes the complete measurements of the first three series model tests. The measurements include the pile penetration history as a function of the applied suction pressure inside the pile. The results of the series 4 have not been processed yet. They will be included in the future report with additional test results.

During the next reporting period, it is planned to continue the model suction pile tests in sand with various surcharge (48.8, 61.0, and 73.2 lbs) and initial pile penetration depths (1, 2, and 3 ft.). A total of nine series of model tests with each series having a minimum of five tests will be completed for this model suction pile. Soon after, a larger diameter model pile will be tested under the same conditions to identify the effect of the pile diameter to length ratio.

An analytical solution method has also been developed to simulate the suction pile installation procedure. It describes and establishes the relationship between the

suction pressure inside the pile and the pile penetration depth under given material and geometric conditions. A brief description of the analytical solution was included in the previous quarterly report (Dec., 1997).

Appendix – C of this report includes the calibration of the mobilized soil friction angle parameter, alpha, from the results of series 1 through 3 model tests. The parameter (alpha) describes the average mobilized effective soil friction angle at the tip and inside the pile where the soil friction values may be lower than that of the outside surface of the pile due to the water flow caused by the suction pressure application. In Appendix – C, the alpha values are plotted as a function of the total head gradient between the tip of the pile and the inside soil surface within the pile. The results indicate that the values of alpha mostly lie within a band between 0.75 and 1.10 with a slight decrease in its value as the total head gradient increases. These are in agreement with generally expected soil behaviors influenced by the flow of water.

5. Verification of Cable Mooring Line Centrifuge Tests

The results of the centrifuge model tests on mooring cables have been visited again to identify the effect of the chasing wires and to provide necessary validation of the analytical solution. Four chasing wires were connected to the cable mooring line during the tests for the purpose of identifying the geometries of the mooring cable. However, the details of the centrifuge tests are not available, other than the technical report and photos provided by the University of Colorado, Boulder, who was contracted to conduct the tests.

Appendix – D of this report provides the details of the centrifuge test validation procedures and the results. It is noted that numerous assumptions had to be introduced due to a lack of sufficient information on test details. Interpolation and extrapolation were also used to interpret the test results.

Although general conclusions are provided in Appendix – 4, the validation steps need to be repeated as new information on test details become available. The number of assumptions introduced must be reduced before this validation can be accepted with high level of confidence. Dr. Law, who was in charge of the centrifuge model tests, is currently being contacted for any additional test details.

cc: Bob Taylor, Jim Forrest, Mike Blmenburg

APPENDIX – A FINITE ELEMENT ANALYSIS OF SUCTION PILES WITH LINEAR ELASTIC SOIL PROPERTIES

FINITE ELEMENT ANALYSIS OF SUCTION PILES WITH LINEAR ELASTIC SOIL PROPERTIES

1. DESCRIPTION

The purpose of this study is to identify a set of the most efficient cross-sectional shapes of the suction pile in terms of lateral and vertical resistance prior to the detailed analysis with plastic soil properties. It was assumed that the length and thickness of the pile and the contact area between the pile and the soil remained the same for all shapes in order to maintain the same amount of pile material. A circular pile with 30 feet in diameter and 30 feet in length was selected as the control. Eleven additional cross-sections were selected according to the above assumptions and their behaviors analyzed.

The objective of this study is to qualitatively compare the responses of various pile cross-sections under lateral and vertical loads using linear elastic soil properties. This is to limit the number of cross-sections to be considered in the detailed quantitative analysis with plastic soil properties. AISI 4340 steel which is being used most commonly in manufacturing industry was chosen as the material of suction piles. ABAQUS software, written by Hibbit, Karlsson & Sorensen, Inc. and one of the most widely used finite element analysis computer programs for research and design purposes, was utilized for the detailed analysis. Additionally, FEAMAP software was used for the easy performance of pre- and post-processing of input and output such as three dimensional mesh generation and graphical display of output, etc.

The study included eleven different cross-sections. This resulted in thirty different modes due to different directions of the horizontal loads and aspect ratios, i.e., the ratio between the width and length of their branches or cells. The selected pile cross sections are the ones that have been widely used in conventional piling. They include; circular, triangular, square, Y-shaped, cross-shaped, clover shaped with three or four leaves, and clusters of three or four circles. The cross-sectional profiles selected for the study are shown in Figure-1.

For the detailed finite element analysis, the selected cross-sections were expanded into three-dimensional columns to simulate the suction piles of uniform cross-sections. Figure-2 shows the three dimensional finite element grid used for the analysis of a suction pile with a circular cross-section.

2. MATERIAL AND LOADING PARAMETERS

It was assumed that the soil was homogeneous and isotropic and its behaviors could be described completely by two parameters, Young's modulus (E) and Poisson's ratio (ν), i.e., linear elastic. The following soil parameters were selected to represent typical seafloor soil properties.

$E = 5{,}000$ psf

$\nu = 0.499$

AISI 4340 steel was chosen for the pile material. The detailed parameters are

Figure-1 Selected Cross-sectional Shapes of Pile

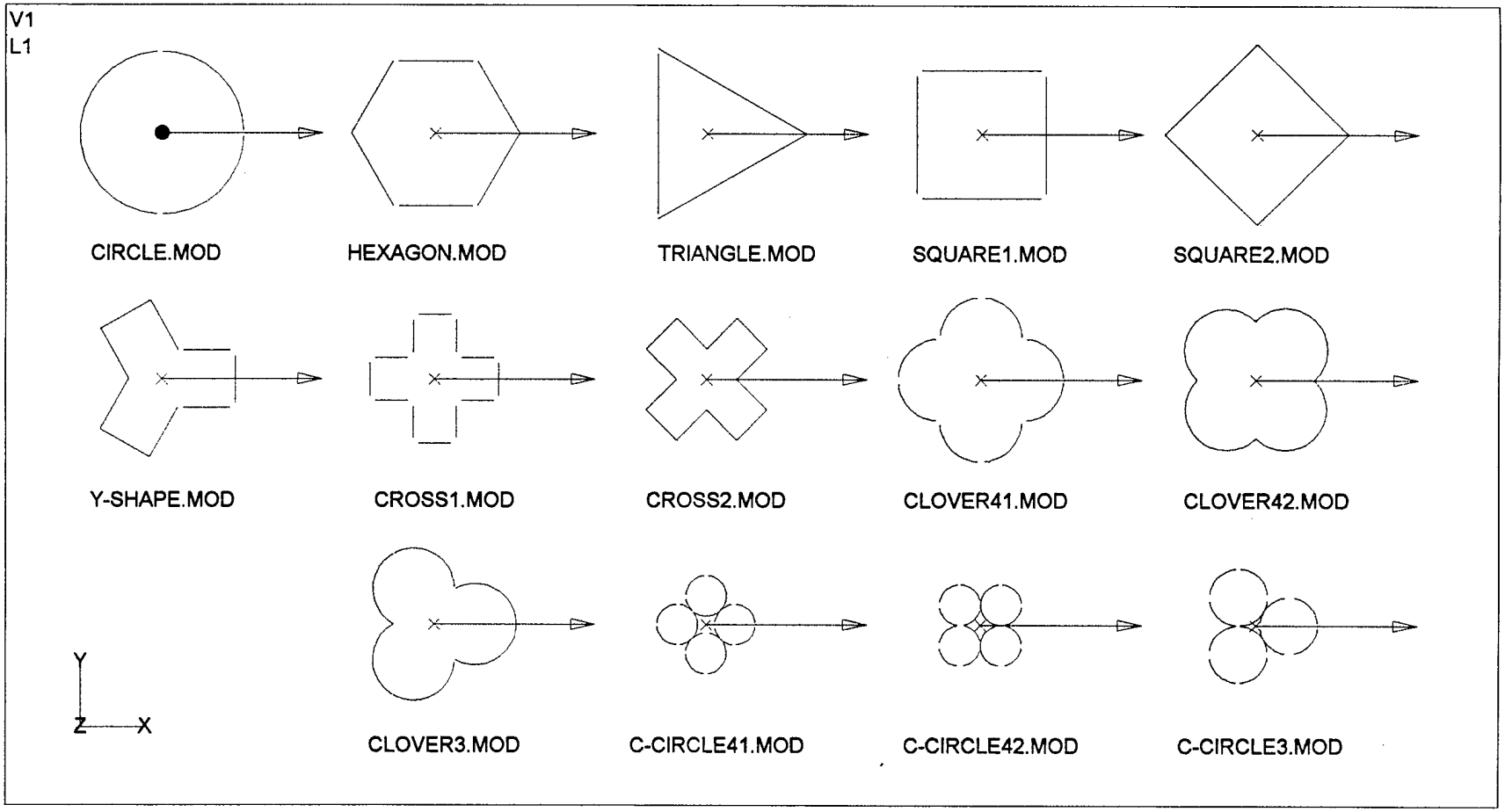

Figure-2 Nodal Arrangement of Circular Pile

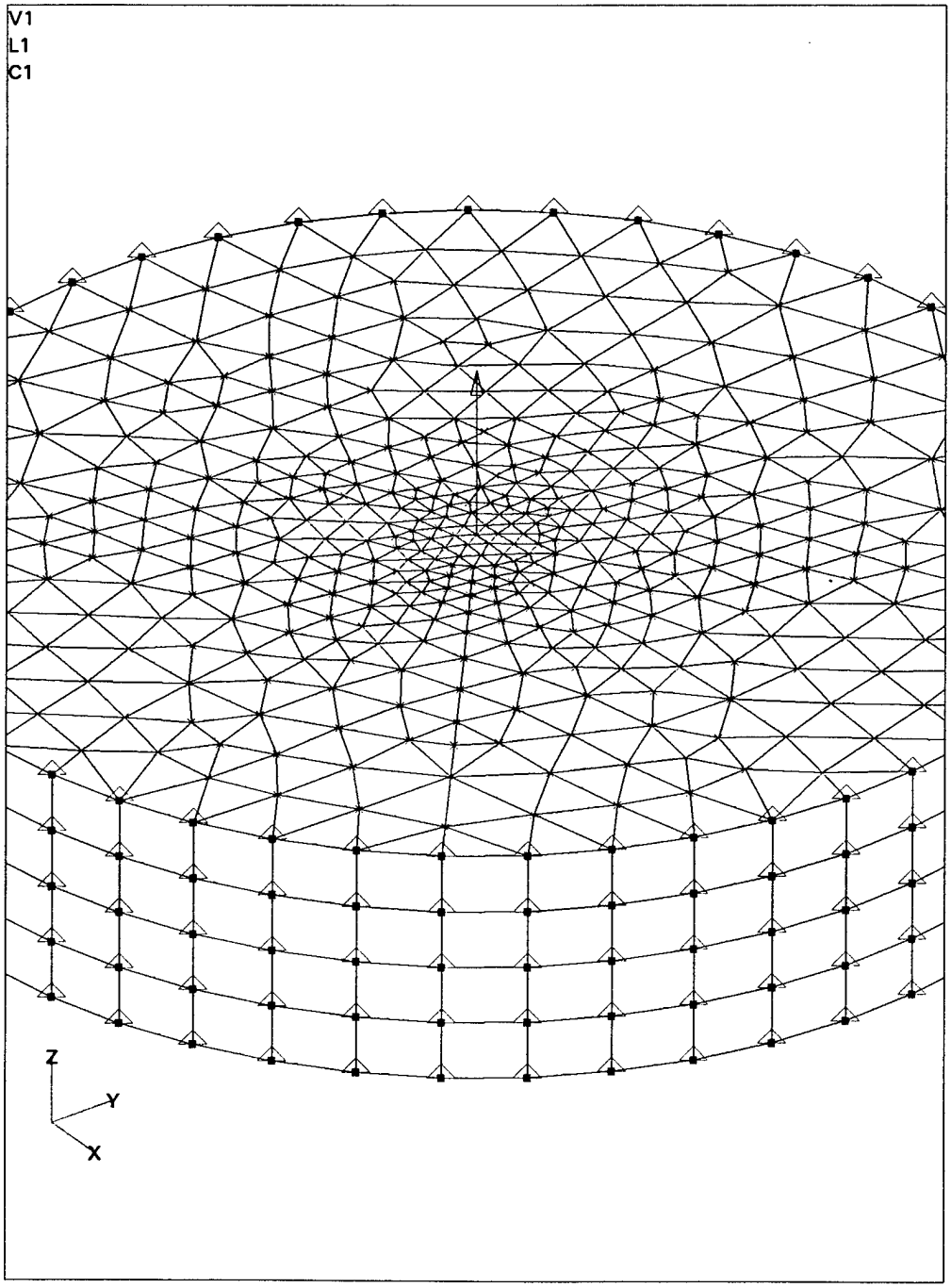

summarized below. G represents the shear modulus and σ_y indicates the stress limit or the yield stress.

E = 29,000,000 psi

G = 11,000,000 psi

ν = 0.32

σ_y = 215,000 psi for tension

240,000 psi for compression

156,000 psi for shear

The loads were applied at the center of the pile cap along with the horizontal or vertical direction. The horizontal load was applied to study the suction pile behavior associated with the lateral resistance, and the vertical loads for the pull-out behavior. The applied load remained as 300,000lbs for either horizontal or vertical direction.

3. DESCRIPTION OF SELECTED PILE CROSS-SECTIONS

The detailed dimensions of each pile cross-section were determined based on the constant pile-soil contact area. In addition, the length of the pile was fixed as 30 feet. A circular pile of 30 feet in diameter and 30 feet in length was selected as the standard pile. The contact area of this circular pile with the soil is 900.0π ft^2. A total of 23 cross-sectional shapes were selected as shown in Table-1. As can be seen from the table, the cross-sections with Y-shape, cross-shape, clover shape, and clustered circles were further

divided into subshapes with various cell or branch dimensions. The detailed dimensions of the pile cells are defined in Figure 3 and listed in Table-1. It should be noted that the ratio inside the parenthesis in Table-1 indicates the ratio between the larger and shorter lengths of rectangular branches of Y-shaped or cross-shaped pile cross-sections.

Figure-3 Definition of Pile Cross-Section Dimensions

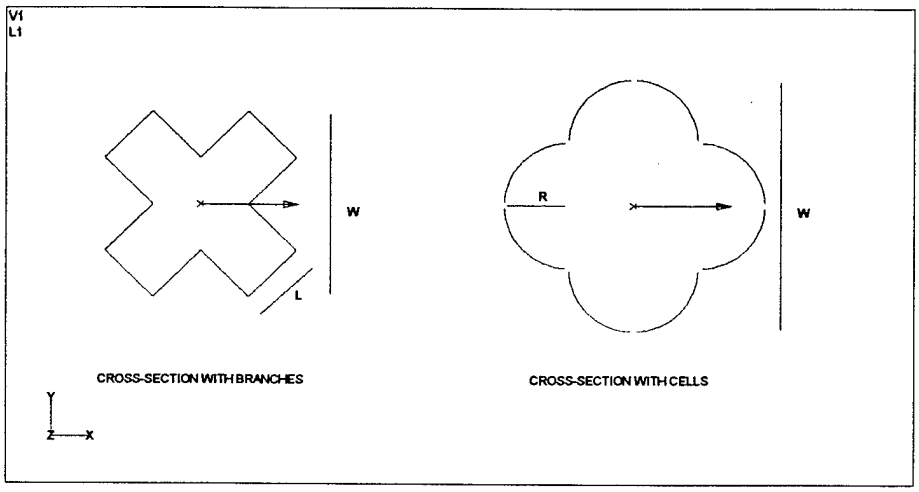

Note;

1. L = constant width of the pile cell
2. W = face width or largest width of the pile
3. R = radius of circular cell

As shown in Table-1, pile cross-sections with more cells or branches tend to have smaller value of w due to the imposed condition of constant contact area between the soil and pile. It is noted that as the ratio of the longer and shorter lengths of rectangular

Table-1 Dimensions of Pile Cells

Types of Pile	Dimension (R or L, ft)	Face Width (W, ft)	Types of Pile	Dimension (R or L, ft)	Face Width (W, ft)
Circle	R = 15.00	30.00	Cross2 (1:2)	L = 4.71	19.99
Hexagon	L = 15.38	26.64	Cross1 (1:3)	L = 3.37	23.56
Triangle	L = 31.42	31.42	Cross2 (1:3)	L = 3.37	19.04
Square1	L = 23.56	23.56	Cross1 (1:4)	L = 2.62	23.56
Square2	L = 23.56	33.32	Cross2 (1:4)	L = 2.62	18.51
Y-shape (1:1)	L = 10.47	28.60	Clover41	R = 7.50	30.00
Y-shape (1:2)	L = 6.28	28.05	Clover42	R = 7.50	25.61
Y-shape (1:3)	L = 4.49	27.81	Clover3	R = 7.50	27.99
Y-shape (1:4)	L = 3.49	27.68	C-circle41	R = 3.75	18.11
Cross1 (1:1)	L = 7.85	23.55	C-circle42	R = 3.75	21.21
Cross2 (1:1)	L = 7.85	22.20	C-circle3	R = 5.24	20.94
Cross1 (1:2)	L = 4.71	23.56			

Note;

1. C-circle indicates cross-section width clustered circles
2. Clover-shaped cross-sections with four leaves consist of half-circles.
3. Clover-shaped cross-section with three leaves consists of circles with circumference of 0.75 times the full circle.
4. Cross1 indicates the cross-shaped cross section with the horizontal load applied along the centerline of its branch (Figure-1)
5. Cross2 indicates the cross-shaped cross section with the horizontal load applied between the branches (Figure-1)
6. Clover41 indicates the clover-shaped cross-section with the horizontal load applied through the centerline of its cell.
7. Clover42 indicates the clover-shaped cross-section with the horizontal load applied between the cells.
8. C-circle41 indicates the clustered circles cross-section with the horizontal load applied through the centerline of its cell.
9. C-circle42 indicates the clustered circles cross-section with the horizontal load applied between cells.

branches of cross- and Y-shaped cross-sections changes, the face width of the pile does not change much. Consequently, piles with slender rectangular branches do not necessarily yield better results. It was observed that the face width of the pile more or less governs the pile resistance.

4. DISCUSSION OF RESULTS

4.1 Behaviors Under Horizontal Load

To investigate the behaviors of piles with various cross-sections under horizontal load, the maximum lateral displacements from the output of the finite element analysis were compared, since piles experiencing smaller lateral displacements under same conditions were believed to be more efficient. In addition, the maximum horizontal normal compressive and minor principal stresses of the soil and the maximum horizontal normal tensile and major principal stresses within the pile top were also compared to study the performance of piles with various cross-sections.

The sizes of the soil elements near the pile or the pile elements near the point of loading were tried to be kept the same for all cross-sections considered in order to minimize the element size effect when generating the finite element mesh (discretization or griding). However, it was not entirely possible to maintain the element sizes exactly the same. As a result, the comparisons described below may include certain inherent errors. This is more evident for the stress comparisons, since the stresses are calculated at the

geometric centers of the elements. The results are summarized in Table-2.

1) Pile Horizontal Displacements

The maximum horizontal displacement due to the horizontal point load applied at the center of the pile cap occurred always at the top of the pile toward the loading direction, whereas the minimum displacement occurred at the bottom of the pile as shown in Figure-4. The difference in pile movements along the vertical direction indicates that the pile was experiencing a rotational movement. Because of the relatively high stiffness of the pile material, no difference in horizontal displacements on any given horizontal pile cross-section was observed (Figure-5).

As shown in Table-2, the circular cross-section yielded the smallest maximum horizontal displacement of 0.463 feet. The horizontal displacement of 0.478 feet for Y-shape cross section with aspect ratio of 1:1 was the next smallest. Hexagon and triangle cross-sections produced the same displacements of 0.539 feet. The remaining cross-sections underwent much higher horizontal displacements. The five best cross-sections in terms of the smallest horizontal displacement are listed in Table-3 in order of increasing magnitude.

The maximum horizontal displacement is more or less related with the face width (W) of the pile. As shown in Figure-6, the maximum horizontal displacement generally decrease with the increases in the face width of the pile.

Table-2. Pile Responses due to Horizontal Load

No	Cross-section	Load, P_x (lbs)	$\delta_{horizon}$ (ft)	Soil		Pile	
				$\sigma_{x\text{-normal}}$ (psf)	$\sigma_{1\text{-principal}}$ (psf)	$\sigma_{x\text{-normal}}$ (psf)	$\sigma_{3\text{-principal}}$ (psf)
1	Circle	30,0000	0.463	-1,234.1	-1,271.9	213,362.2	251,974.1
2	Hexagon	"	0.539	-769.0	-795.4	290,178.7	228,297.2
3	Triangle	"	0.539	-1,321.7	-1,347.5	176,514.6	222,626.7
4		-300,000	0.539	-949.0	-992.9	290,069.4	319,693.9
5	Square1	300,000	0.511	-1,016.5	-1,057.6	197,061.7	225,329.4
6	Square2	"	0.480	-1,483.5	-1,511.8	265,100.4	299,000.6
7	Y-shape (1:1)	"	0.478	-777.2	-792.1	114,214.0	209,738.3
8		-300,000	0.478	-692.8	-713.0	136,891.4	315,212.2
9	Y-shape (1:2)	300,000	0.535	-1,497.7	-1,510.6	986,449.4	991,839.4
10		-300,000	0.535	-1,377.7	-1,400.3	283,259.7	539,419.2
11	Y-shape (1:3)	300,000	0.759	-1,408.0	-1,461.3	1,566,514.0	1,577,371.0
12		-300,000	0.759	-1,604.7	-1,638.1	467,600.3	988,001.2
13	Y-shape (1:4)	300,000	0.905	-2,214.6	-2,233.1	2,219,640.0	2,241,384.0
14		-300,000	0.905	-2,179.0	-2,182.2	757,703.6	1,473,907.0
15	Cross1 (1:1)	300,000	0.604	-1,346.6	-1,374.6	137,658.0	308,256.0
16	Cross2 (1:1)	"	0.568	-997.6	-1,017.6	133,674.5	410,489.4
17	Cross1 (1:2)	"	0.759	-1,201.4	-1,272.9	528,851.4	738,552.4
18	Cross2 (1:2)	"	0.724	-1,038.5	-1,061.2	240,806.1	600,118.5
19	Cross1 (1:3)	"	0.994	-2,351.6	-2,416.1	825,200.9	1,113,784.0
20	Cross2 (1:3)	"	0.988	-2,632.4	-2,634.4	600,587.3	1,146,139.0
21	Cross1 (1:4)	"	0.969	-1,997.9	-2,145.5	991,921.8	1,967,976.0
22	Cross2 (1:4)	"	0.979	-1,989.2	-2,101.4	834,382.8	1,662,154.0
23	Clover41	"	0.799	-1,945.5	-1,979.4	346,083.9	401,336.8
24	Clover42	"	0.598	-2,280.5	-2,284.3	412,957.7	481,922.6
25	Clover3	"	0.623	-2,407.9	-2,475.9	463,357.1	463.358.0
26		-300,000	0.623	-2,129.2	-2,166.2	658,110.3	658,112.7
27	C-circle41	300,000	1.290	-3,311.8	-3,595.0	803,725.9	1,009,618.0
28	C-circle42	"	1.293	-3,910.1	-3,936.5	1,292,378.0	1,292,402.0
29	C-circle3	"	1.094	-2,233.2	-2,262.2	245,431.6	540,225.5
30		-300,000	1.094	-1,860.2	-1983.2	985,818.2	985,890.3

Note:

1. $\sigma_{1\text{-principal}}$ is the minimum soil minor principal stress
2. $\sigma_{3\text{-principal}}$ is the maximum pile major principal stress

Figure-4 X-Directional Displacements of Soil for Circular Pile

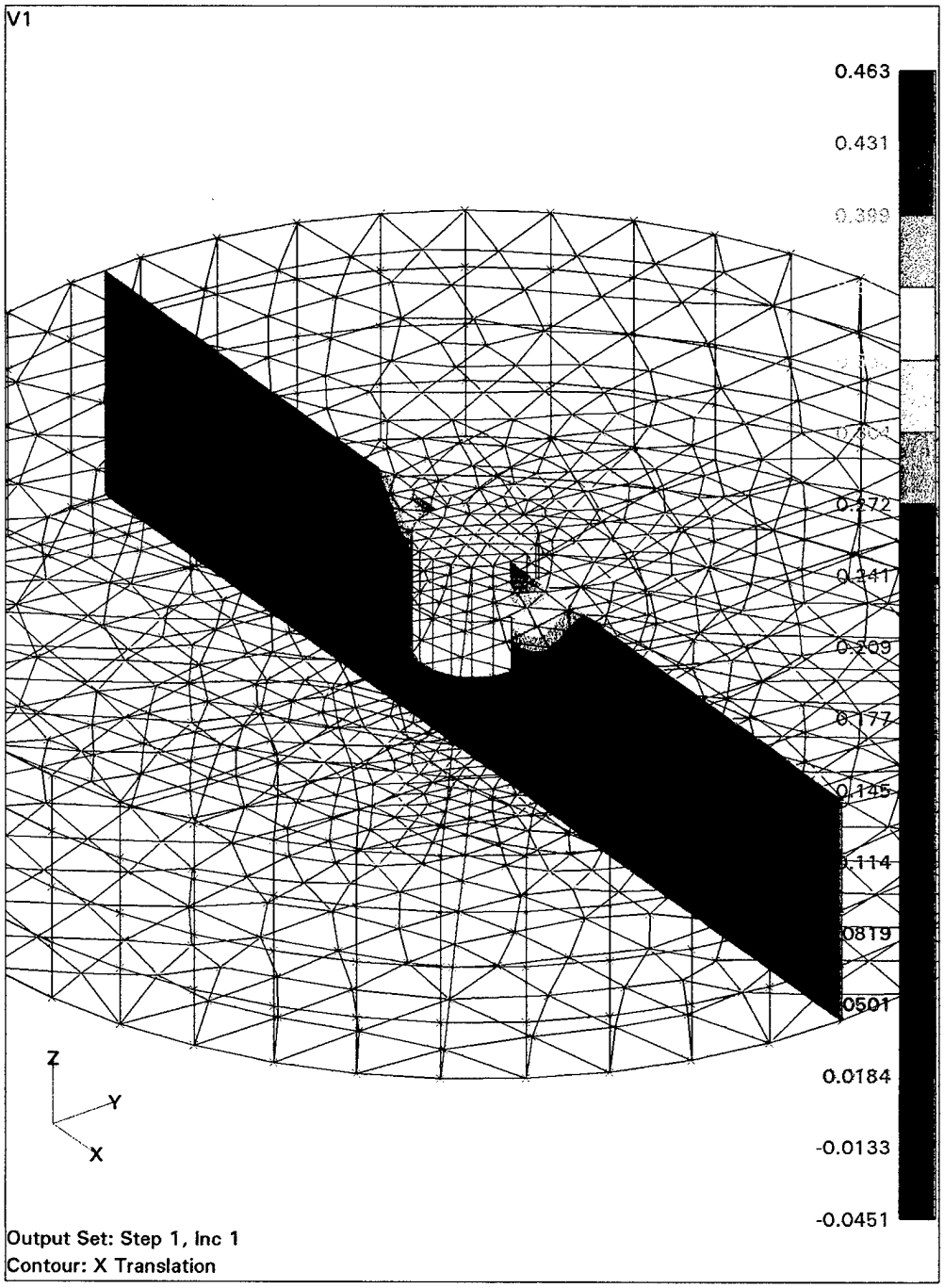

Figure-5 X-Directional Displacements of Pile for Circular Pile

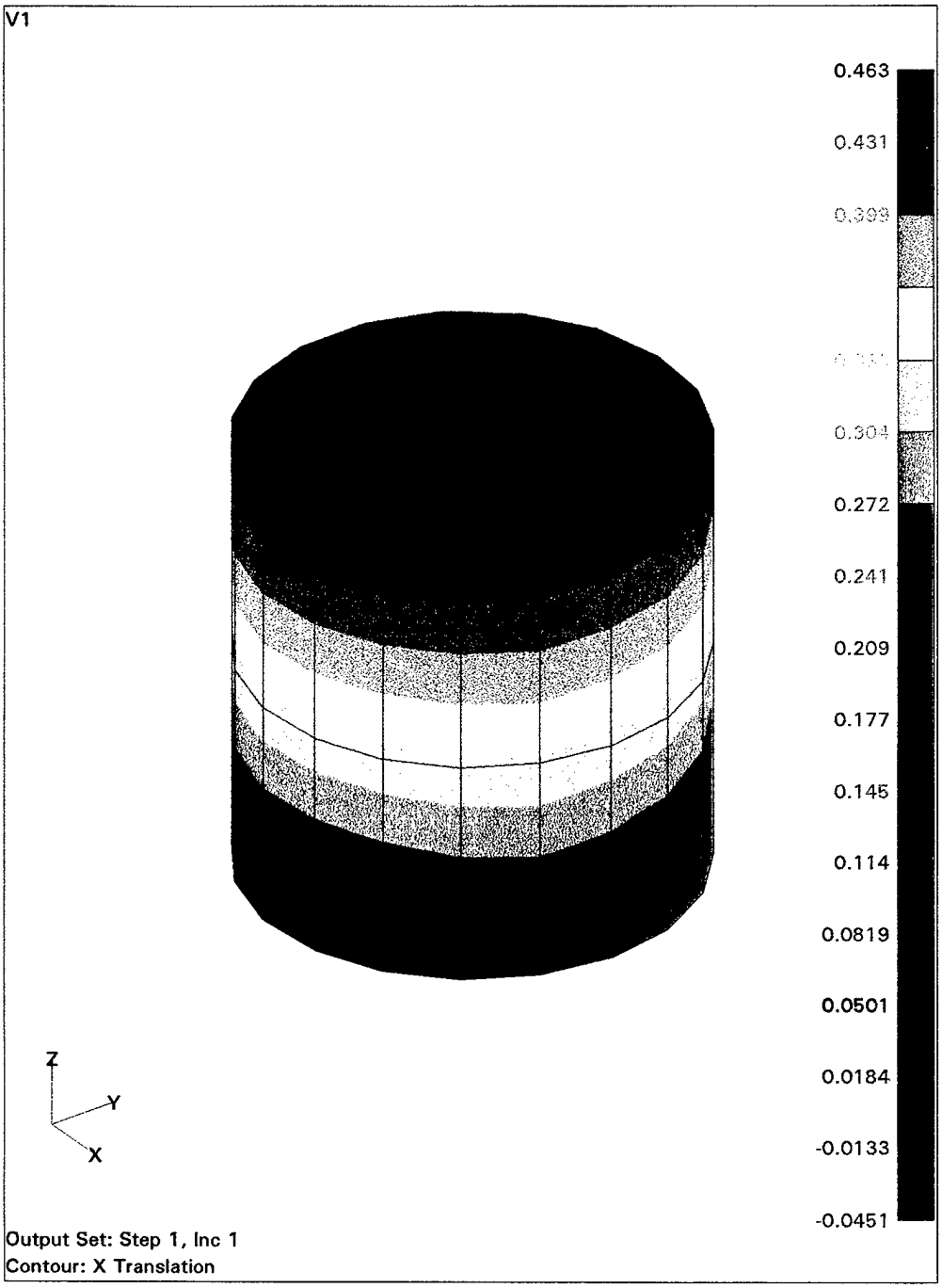

Table-3 Five Cross-Sections with Smallest Maximum Horizontal Displacements

Order	Cross-Section	Maximum Displacement (ft)
1	Circle	0.463
2	Y-shape (1:1)	0.478
3	Square	0.511
4	Y-shape (1:2)	0.535
5	Triangle or Hexagon	0.539

Figure-6. Face Width of Pile vs. Maximum Horizontal Displacement

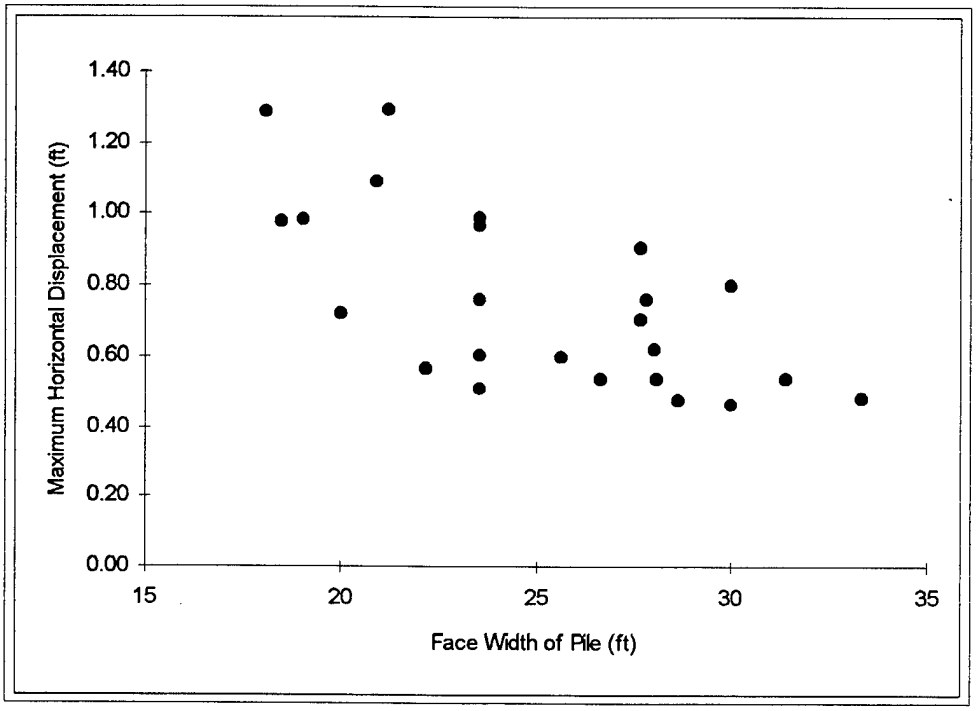

2) Horizontal Normal Soil Stresses

Since the compressive stress developed within the soil is directly related with the soil failure and thus the lateral resistance of the pile, the horizontal normal soil

compressive stresses resulting from the horizontal point load applied at the center of the pile cap were selected for comparison. As indicated previously, the comparison of stresses may include certain errors due to the fact that stresses are evaluated at the centers of elements in the finite element method of analysis.

The maximum horizontal normal soil compressive stress was always generated at the top of the advancing side of the pile. On the other hand, the receding side of the pile experienced tensile stresses due to the nature of the elastic analysis. This may be unrealistic, since the soil tends to separate from the pile or develop virtually no stress near the receding side of the pile.

The smallest horizontal normal soil compressive stress was generated with the hexagonal cross-section as shown in Table-2. The five best cross sections in terms of the maximum horizontal normal soil compressive stress due to a horizontal load are listed in Table-4. It is noted that the maximum stress values were selected considering the directions of the horizontal load, i.e., the worse condition. For instance, the cross (1:2) cross-section experienced the maximum horizontal normal soil compressive stress of -1,038.5 psf when the load was applied between the branches (indicated as cross2 (1:2) in Table-2), whereas the stress of -1,201.4 psf was resulted when the load was applied along the centerline of the branch (indicated as cross1 (1:2) in Table-2). -1,201.4 was selected as the maximum horizontal normal soil compressive stress associated with the cross (1:2) section.

Figure-7 shows the scatter plot between the maximum horizontal normal soil compressive stress and the maximum horizontal soil displacement. As can be seen, the

Table-4 Five Cross-sections with Smallest Maximum Horizontal Normal Soil Compressive Stresses

Order	Cross-Section	Maximum horizontal normal compressive stresses (psf)
1	Hexagon	-769.0
2	Y-shape (1:1)	-777.2
3	Cross (1:2)	-1,201.4
4	Circle	-1,234.1
5	Triangle	-1,321.7

stresses is linearly proportional to the displacement.

Figure-7 Maximum Horizontal Normal Soil Compressive Stress vs. Maximum Horizontal Soil Displacement

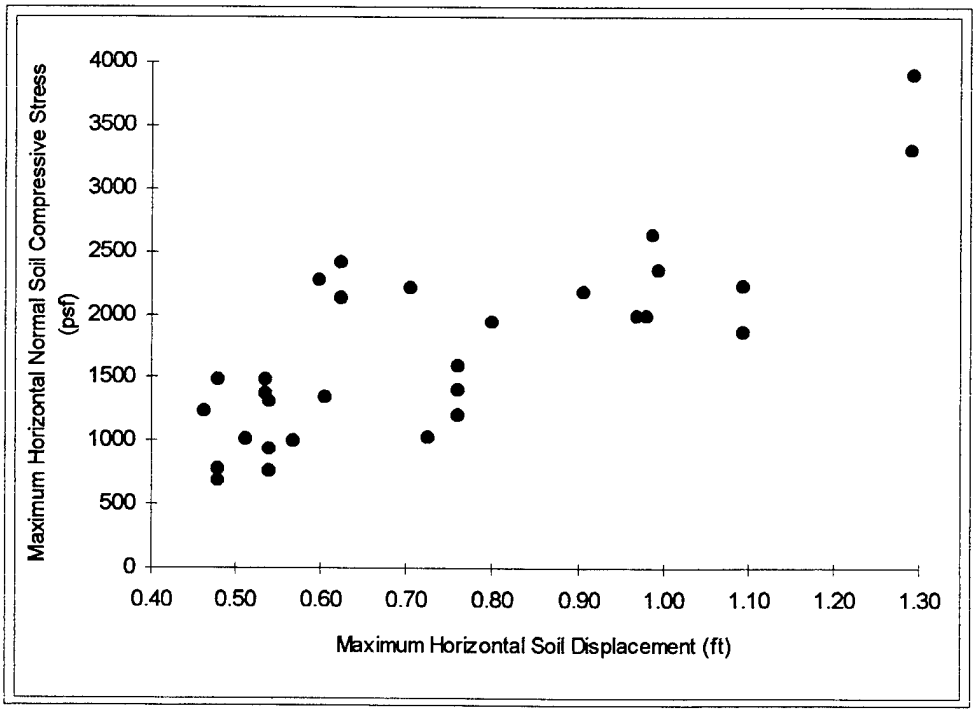

3) Minimum Soil Minor Principal Stresses

The minimum minor principal stress of the soil was selected for additional comparison, since this describes the absolute maximum soil compressive stress. The complete results are included in Table-2. They are similar to those of the maximum horizontal normal soil compressive stresses. The five best cross-sections with respect to the minimum soil minor principal stress are listed in Table-5.

The relationship between the maximum displacement and the minimum soil minor principal stress also shows a similar pattern with the maximum soil horizontal normal stress, i.e., the stress increases as the displacement increases (Figure-8).

Table-5 Five Cross-Sections with Smallest Minimum Soil Minor Principal Stress

Order	Cross-Section	Minimum soil minor principal stress (psf)
1	Y-shape (1:1)	-792.1
2	Hexagon	-795.4
3	Circle	-1,271.9
4	Cross (1:2)	-1,272.9
5	Triangle	-1,347.5

4) Maximum Horizontal Normal Pile Tensile Stresses

In general, the steel material fails due to tensile stress under most circumstances. Therefore, the maximum horizontal normal pile tensile stress was considered for

Figure-8 Minimum Soil Minor Principal Stress vs. Maximum Horizontal Soil Displacement

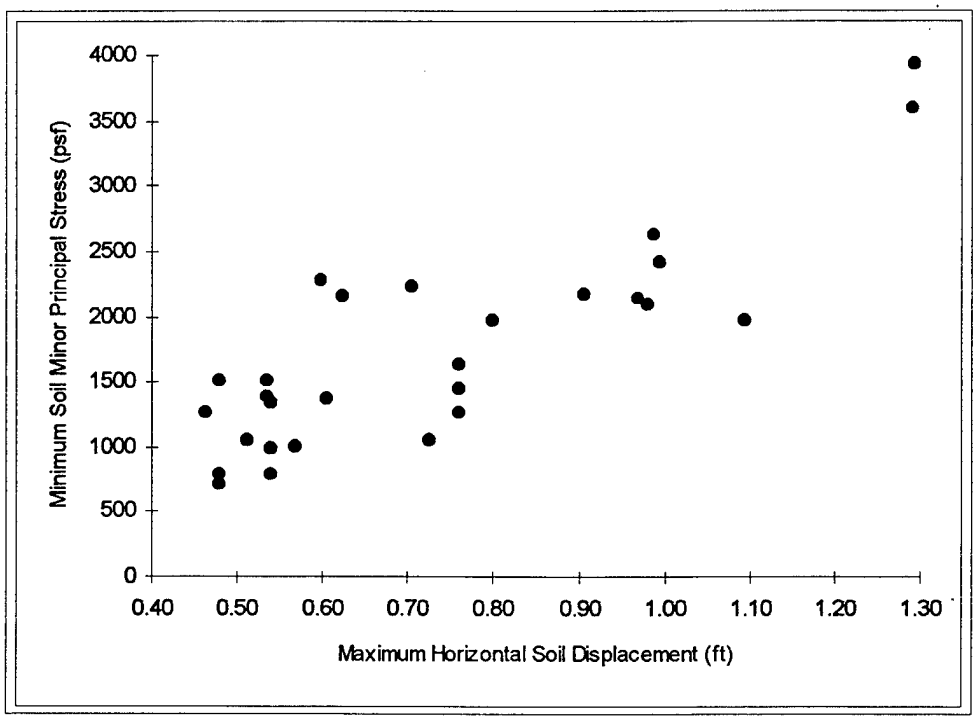

comparison. Please note that the cylindrical outer surface of the pile was modeled by either shell elements in case of curved surfaces or plate elements in case of plane surfaces. The stresses typically used for the comparison were along the top and bottom of the plate/shell elements. However, the maximum horizontal normal pile tensile stresses on the outside surface of the pile were greater than those on the inside surface of the pile in almost all cases. Therefore, only the maximum horizontal normal pile tensile stresses developed on the outside surface of the pile were compared.

The maximum horizontal normal pile tensile stresses on the outside surface of the pile always developed near the point of load application at the pile cap. The five best

cross-sections in terms of the smallest maximum horizontal normal pile tensile stress are listed in Table-6.

Table-6 Five Cross-Sections with Smallest Maximum Horizontal Normal Pile Tensile Stress

Order	Types of Pile	Maximum horizontal normal pile tensile stress (psf)
1	Y-shape (1:1)	136,891.4
2	Cross (1:1)	137,658.0
3	Circle	213,362.2
4	Square	265,100.4
5	Triangle	290,069.4

The relationship between the maximum horizontal normal pile tensile stress on the outside surface of the pile and the maximum horizontal pile displacement is shown in Figure-9. Though some scatter in data points is evident, generally the maximum horizontal pile tensile stress is proportional to the maximum pile horizontal displacement.

5) Maximum Pile Major Principal Stresses

The maximum pile major principal stresses developed on the outside surface of the pile was additionally compared, since this describes the absolute maximum tensile stress within the pile. Table-2 indicates the magnitude of such stress for all cross-sections considered.

Figure - 9 Maximum Horizontal Normal Pile Tensile Stresses vs. Maximum Horizontal Pile Displacement

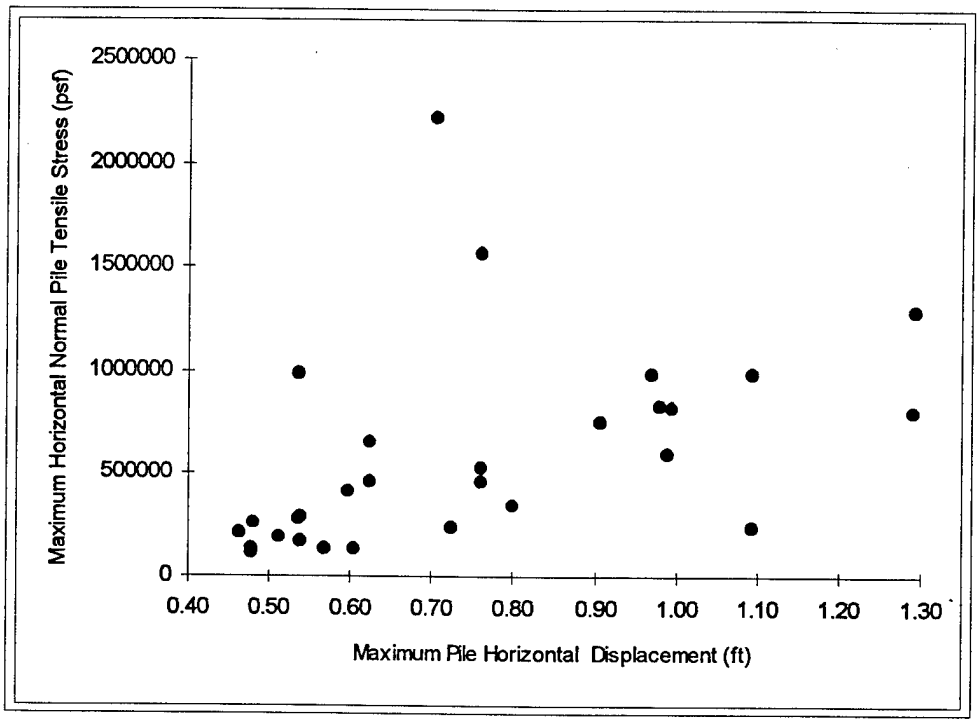

The five best cross-sections with respect to the smallest maximum pile major principal stress are shown in Table-7.

Table-7 Five Cross-Sections with Smallest Maximum Pile Major Principal Stress

Order	Cross-section	Maximum pile major principal stress (psf)
1	Hexagon	228,297.2
2	Circle	251,974.1
3	Square	299,000.6
4	Y-shape (1:1)	315,212.2
5	Triangle	319,693.6

The maximum pile major principal stress generally increases with the increase in the maximum pile horizontal displacement as shown in Figure 10.

Figure - 10 Maximum Pile Major Principal Stress vs. Maximum Pile Horizontal Displacement

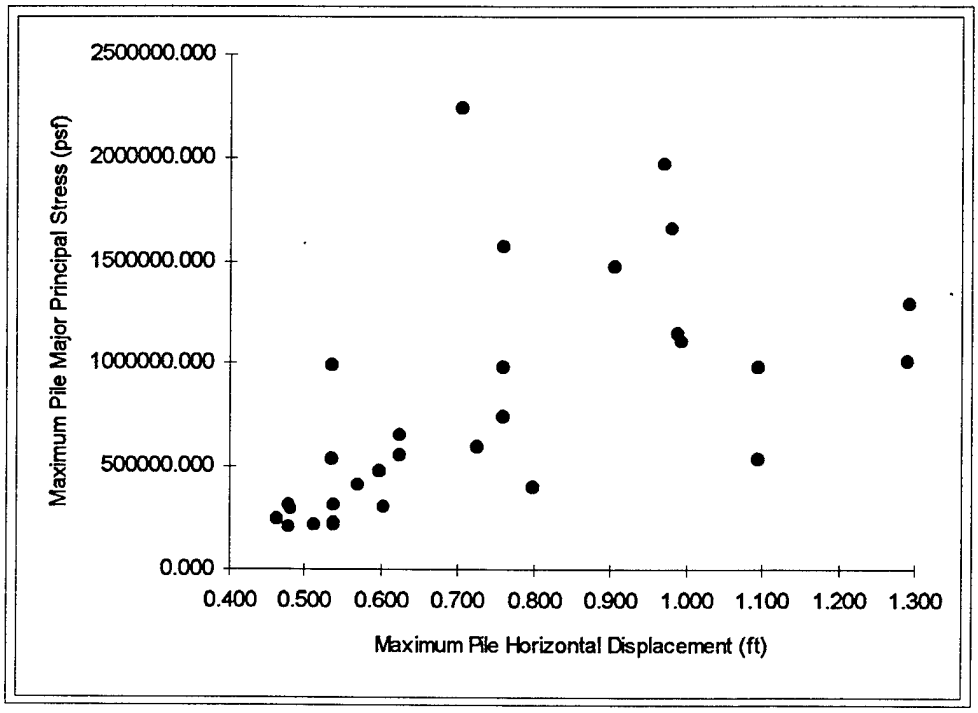

6) Relationship between Soil Stresses and Pile Stresses

The maximum horizontal normal soil compressive stresses generally increases with the increase in the maximum horizontal normal pile tensile stress as shown in Figures-11.

It is noted that the data points near the coordinate origin are those with no branches or cells, while the data points further away from the origin are those with branches or cells.

Figure - 11 Maximum Horizontal Pile Tensile Stress vs. Maximum Horizontal Normal Soil Compressive Stress

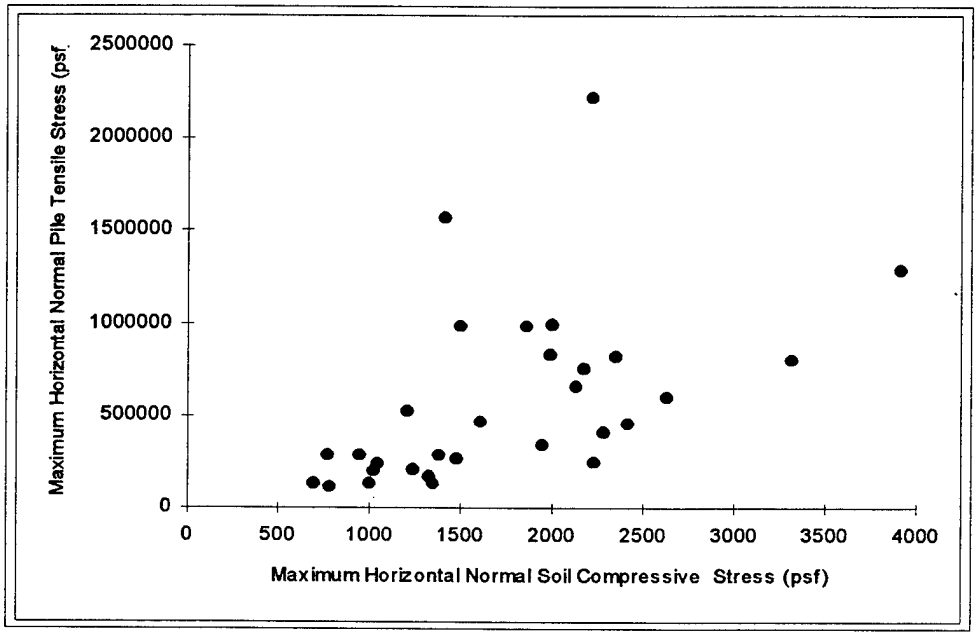

The relationship between the maximum pile major principal stress and the minimum soil minor principal stress also shows a similar pattern with that between the maximum horizontal normal pile tensile stress and the maximum horizontal normal soil compressive stress as shown in Figure-12.

4.2 Behaviors Under Vertical Load

Figure - 12 Maximum Pile Major Principal Stress vs. Minimum Soil Minor Principal Stress

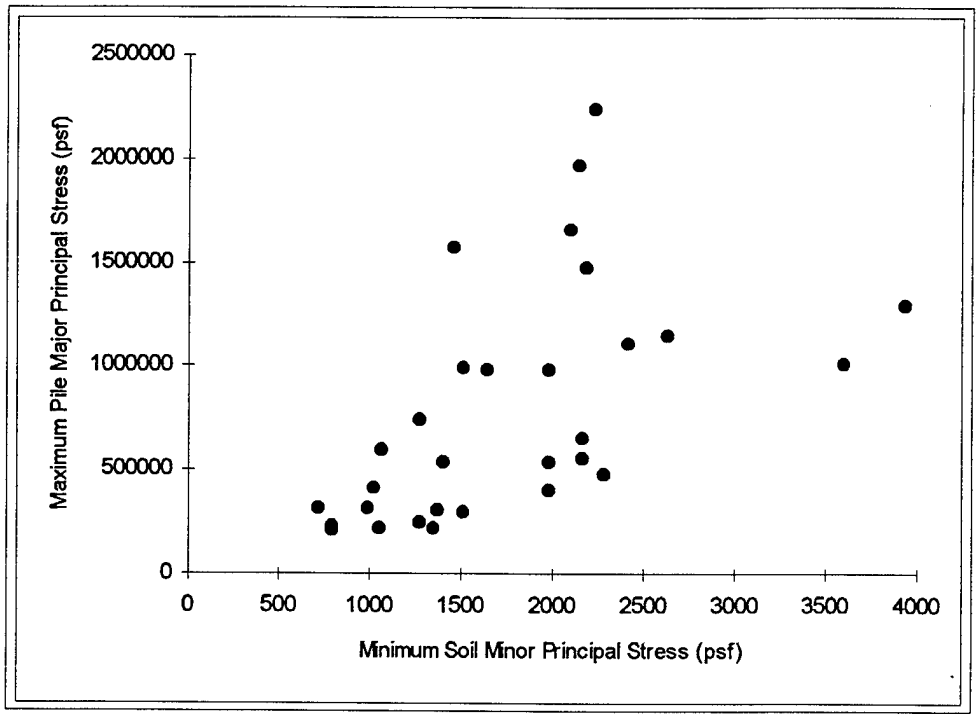

To investigate the behaviors of suction piles with various cross-sectional shapes under a vertical load applied at the center of the pile cap, sixteen different modes were examined. As was the case of the horizontal load, the displacements were the primary factor considered as the comparison. Other parameters considered for additional comparisons include; the maximum pile major principal stress and the minimum soil minor principal stress.

The elements and nodal configurations used for the study of the pile behavior under the horizontal load were used without change for studying the effects of the vertical load except the direction of the load. The results of the analysis are summarized in Table-8

Table-8. Pile Responses due to Vertical Load

No.	Type of Pile	Max. $\delta_{vertical}$ (ft)	Soil	Pile
			$\sigma_{1\text{-principal}}$ (psf)	$\sigma_{3\text{-principal}}$ (psf)
1	Circle	1.220	-714.0	1,235,627.0
2	Hexagon	1.408	-1,533.7	12,694,291.0
3	Triangle	1.575	-1,064.4	13,605,085.0
4	Square	1.469	-2,824.1	13,559,383.0
5	Y-shape (1:1)	0.514	-879.2	2,494,272.0
6	Y-shape (1:2)	0.733	-1,797.6	16,801,791.0
7	Y-shape (1:3)	0.536	-1,310.4	17,704,726.0
8	Y-shape (1:4)	0.510	-1,147.2	16,565,421.0
9	Cross (1:1)	0.470	-1,091.4	2,340,180.0
10	Cross (1:2)	0.585	-1,826.1	11,746,705.0
11	Cross (1:3)	0.535	-1,436.6	4,5089,08.0
12	Cross (1:4)	0.469	-1,852.0	12,620,515.0
13	Clover4	1.711	-2,080.2	24,602,413.0
14	Clover3	1.475	-1,722.8	25,767,137.0
15	C-circle4	0.482	-1,222.2	13,017,584.0
16	C-circle3	0.684	-860.9	12,153,883.0

Note:

1 $\sigma_{1\text{-principal}}$ is the minimum soil minor principal stress

2 $\sigma_{3\text{-principal}}$ is the maximum pile major principal stress

1) Maximum Pile Vertical Displacements

The maximum pile vertical displacement due to the applied vertical point load at the center of the pile cap was always observed at the point of loading as expected. Figure-13 shows the distribution of the pile vertical displacements due to 300,000lbs of tension applied at the center of the pile top. As shown in Table-8, smaller pile vertical

Figure 13. Vertical Displacements of Pile for CIRCLE.MOD

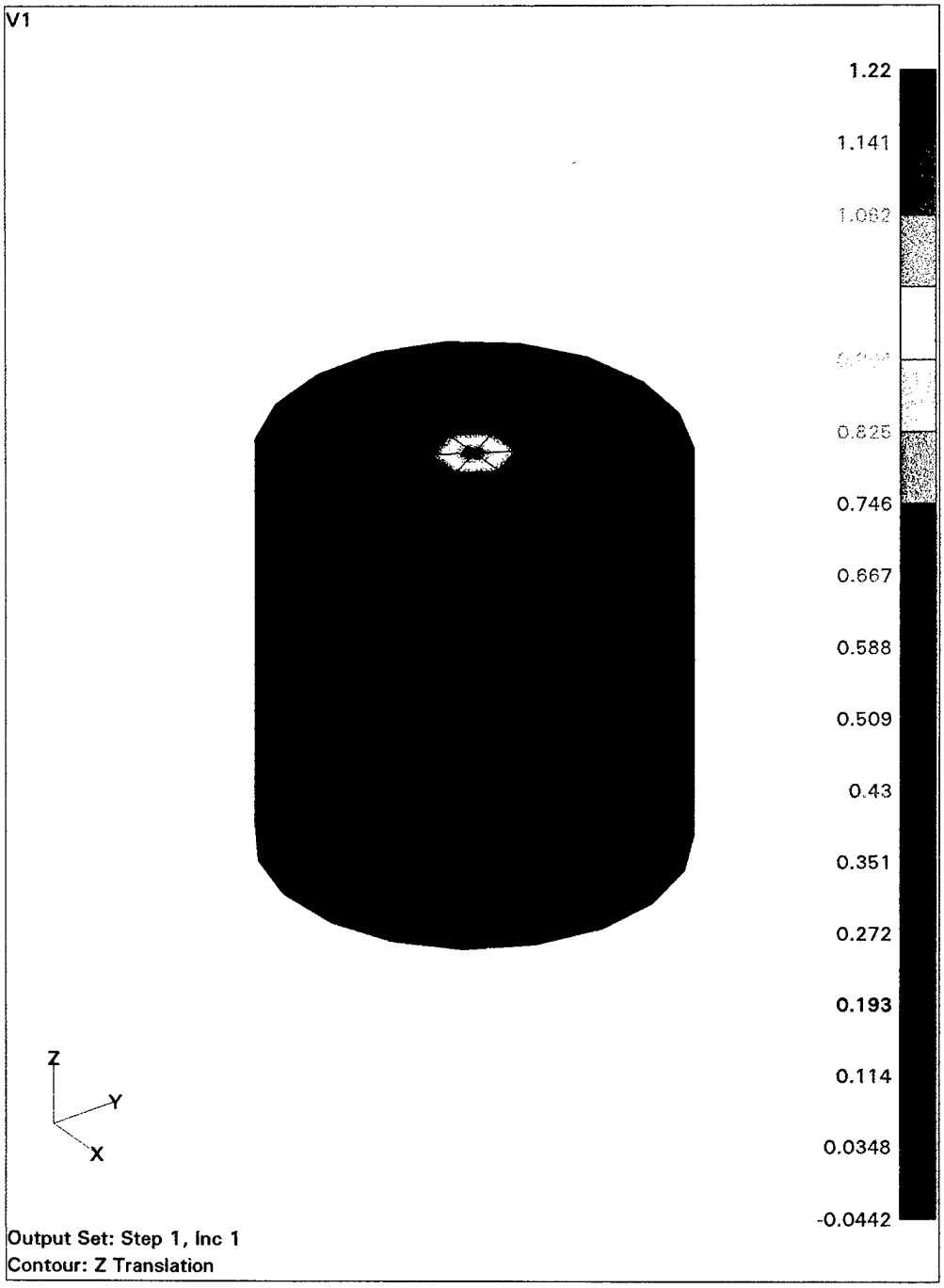

Table-8. Pile Responses due to Vertical Load

No.	Type of Pile	Max. $\delta_{vertical}$ (ft)	Soil	Pile
			$\sigma_{1\text{-principal}}$ (psf)	$\sigma_{3\text{-principal}}$ (psf)
1	Circle	1.220	-714.0	1,235,627.0
2	Hexagon	1.408	-1,533.7	12,694,291.0
3	Triangle	1.575	-1,064.4	13,605,085.0
4	Square	1.469	-2,824.1	13,559,383.0
5	Y-shape (1:1)	0.514	-879.2	2,494,272.0
6	Y-shape (1:2)	0.733	-1,797.6	16,801,791.0
7	Y-shape (1:3)	0.536	-1,310.4	17,704,726.0
8	Y-shape (1:4)	0.510	-1,147.2	16,565,421.0
9	Cross (1:1)	0.470	-1,091.4	2,340,180.0
10	Cross (1:2)	0.585	-1,826.1	11,746,705.0
11	Cross (1:3)	0.535	-1,436.6	4,5089,08.0
12	Cross (1:4)	0.469	-1,852.0	12,620,515.0
13	Clover4	1.711	-2,080.2	24,602,413.0
14	Clover3	1.475	-1,722.8	25,767,137.0
15	C-circle4	0.482	-1,222.2	13,017,584.0
16	C-circle3	0.684	-860.9	12,153,883.0

Note:

1 $\sigma_{1\text{-principal}}$ is the minimum soil minor principal stress

2 $\sigma_{3\text{-principal}}$ is the maximum pile major principal stress

1) Maximum Pile Vertical Displacements

The maximum pile vertical displacement due to the applied vertical point load at the center of the pile cap was always observed at the point of loading as expected. Figure-13 shows the distribution of the pile vertical displacements due to 300,000lbs of tension applied at the center of the pile top. As shown in Table-8, smaller pile vertical

The five best cross-sections in terms of the smallest maximum pile major principal stresses are listed in Table-10.

Table-10 Five Cross-Sections with Smallest Maximum Pile Major Principal Stress

Order	Cross-section	Maximum pile major principal stress (psf)
1	Circle	1,235,627.0
2	Cross (1:1)	2,340,180.0
3	Y-shape (1:1)	2,494,272.9
4	Cross (1:3)	4,508,908.0
5	Cross (1:2)	11,746,883.0

4.3 Results from Various Cross-Sections

Appendix-1 includes some of the results from the analysis with circular, Y-shape, clover shape with three leaves, and clustered circle with four cells under a horizontal load of 300,000lbs. The results include; (1) horizontal displacements, (2) horizontal displacements on a vertical plane along the horizontal load direction, (3) horizontal normal stresses of the pile on the pile surface, (4) horizontal normal stresses of the soil on the pile surface, (5) major principal stresses of the pile on the pile surface, and (6) minor principal stresses of the soil on the pile surface.

5. SUMMARY AND CONCLUSIONS

Based on the results of comparisons, the cross-sectional shape of the pile has a significant effect on the performance of the pile. There also exists a general trend in terms of the overall behavior of the pile with given cross-sectional shape. In general, the horizontal pile displacement due to the horizontal point load at the center of the pile cap decreases with the increase in the face width of the pile. All stresses of the soil or pile increase with the increase in the horizontal displacement. The critical response of the pile under the vertical point load at the center of the pile cap is concentrated near the point of loading and therefore the soil vertical displacement does not dictate the overall maximum vertical displacement.

Behaviors of soil under horizontal load

Circle, Y-shape (1:1), square, Y-shape (1:2), triangle, and hexagon cross-sections have been identified to be the most effective shapes of the pile in terms of the maximum horizontal pile displacement. Hexagon, Y-shape (1:1), cross (1:2), circle, and triangular sections have been shown as the most effective cross-sectional shapes in terms of the soil stresses.

Behaviors of pile under horizontal load

Circle, Y-shape (1:1), square, triangle, and hexagon cross-sections have been shown as the most effective in terms of the pile stresses.

Behaviors of soil under vertical load

Circle, C-circle3, Y-shape (1:1), triangle, and cross (1:1) cross-sections are the five best shapes in terms of the soil stresses.

Behaviors of pile under vertical load

Circle , cross (1:1), Y-shape(1:1), cross (1:3), and cross (1:2) cross-sections are the five best shapes in terms of the pile stresses.

Based on the findings described above, it may be concluded that circle, Y-shape (1:1), hexagon, and triangle cross-sections are the most effective in terms of providing resistance against both horizontal and vertical loads. Therefore, the further detailed study of the behaviors of the pile with plastic soil properties will be carried out with the circle, triangle, and Y-shape (1:1) cross-sections.

APPENDIX-1. RESULTS OF ANALYSIS

TABLE OF FIGURES

Figure-A1 Horizontal Displacements (Circular Section)

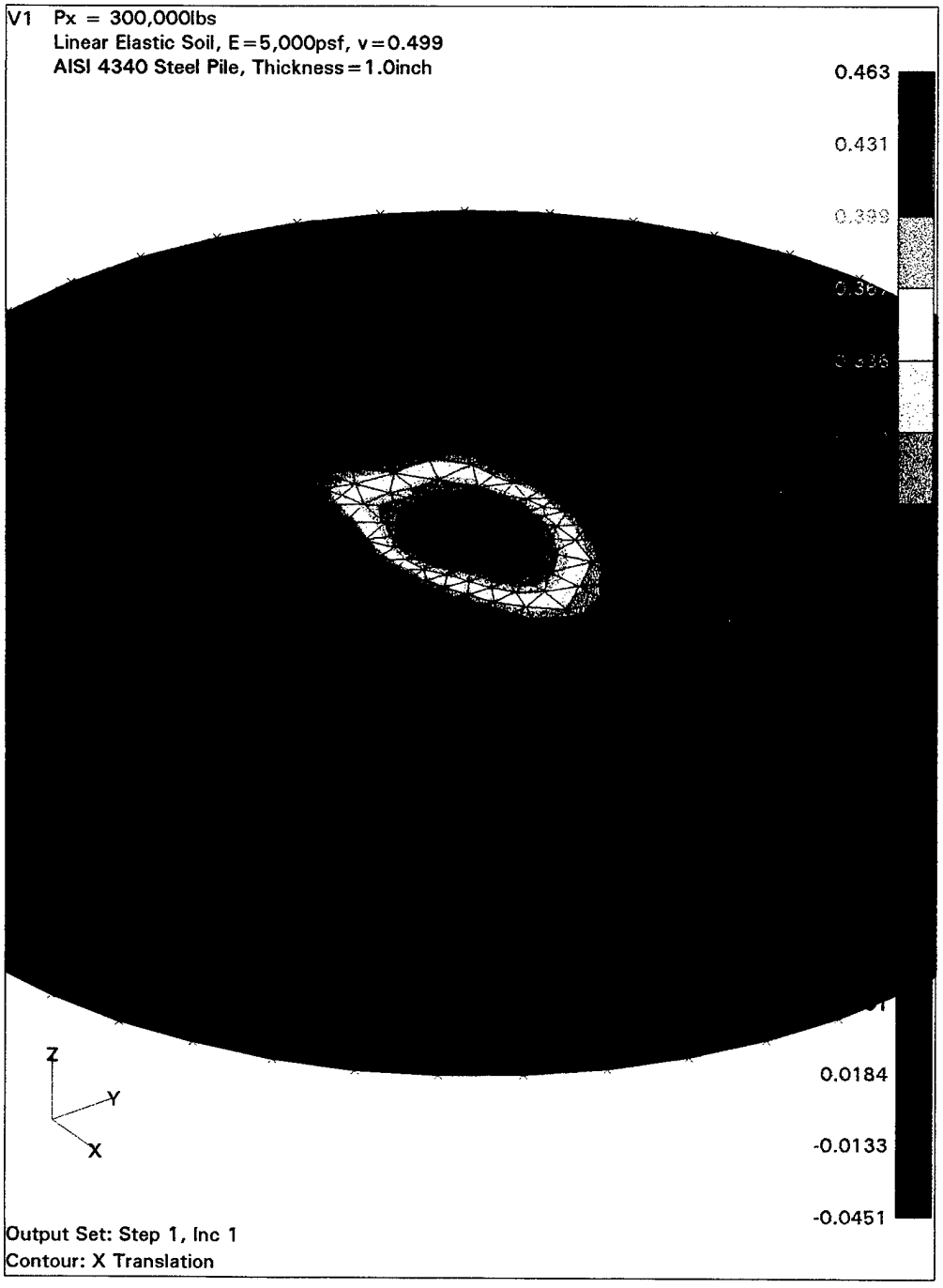

Figure-A2 Hor. Displ. on a Vert. Plane along the Hor. Load Direction (Circular Section)

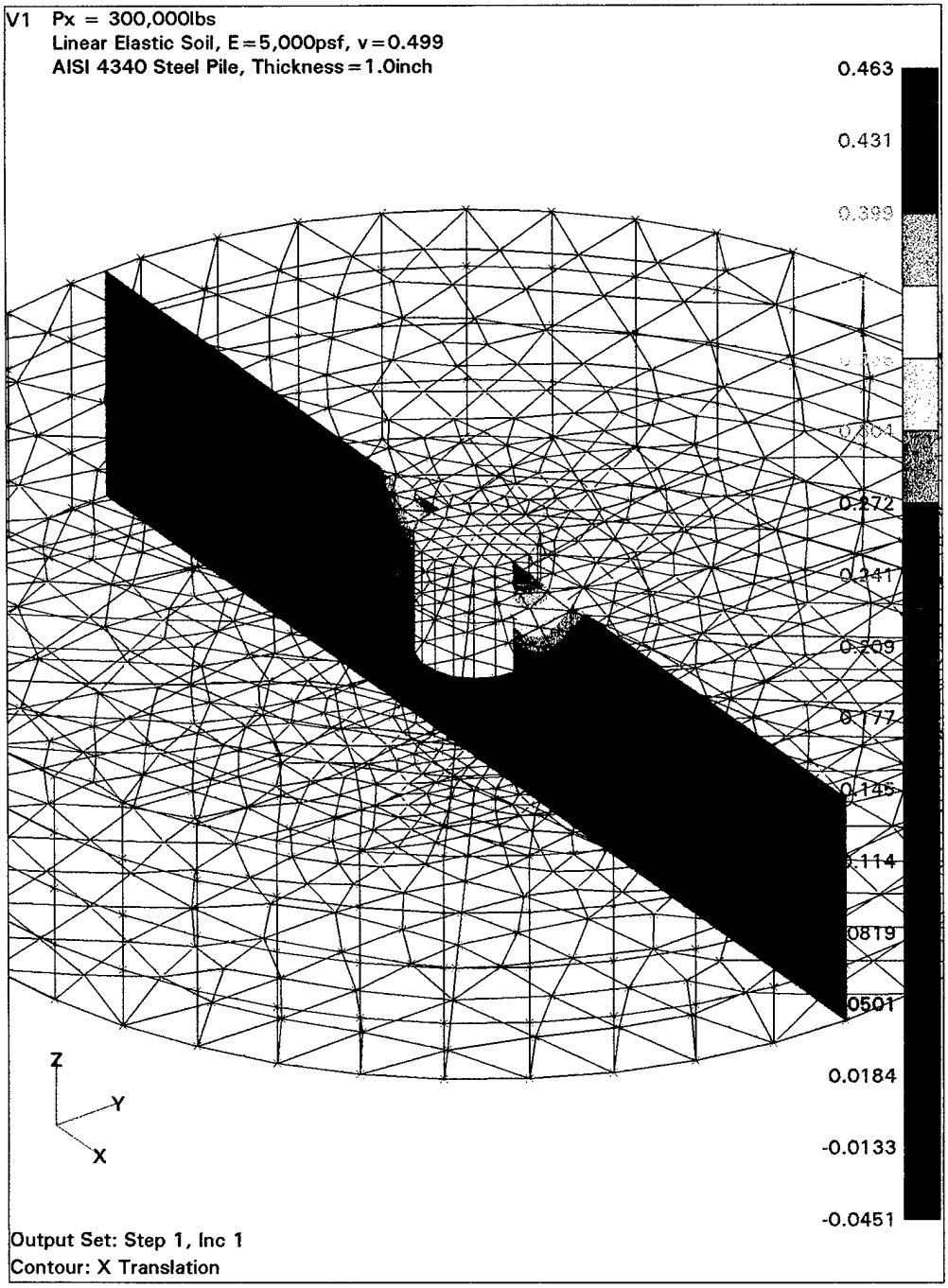

Figure-A3 Hor. Normal Pile Stresses on the Pile Surface (Circular Section)

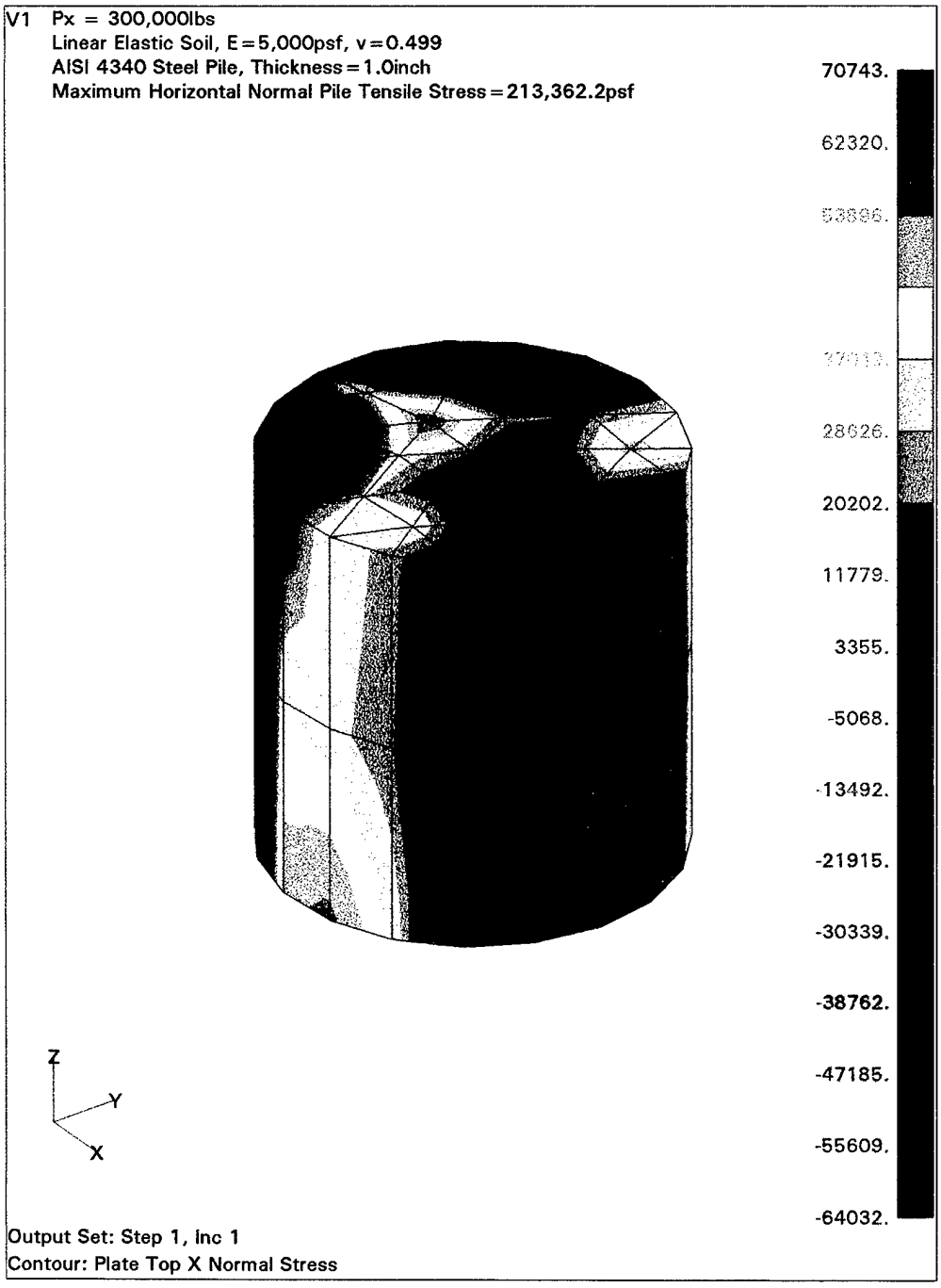

Figure-A4 Hor. Normal Soil Stresses on the Pile Surface (Circular Section)

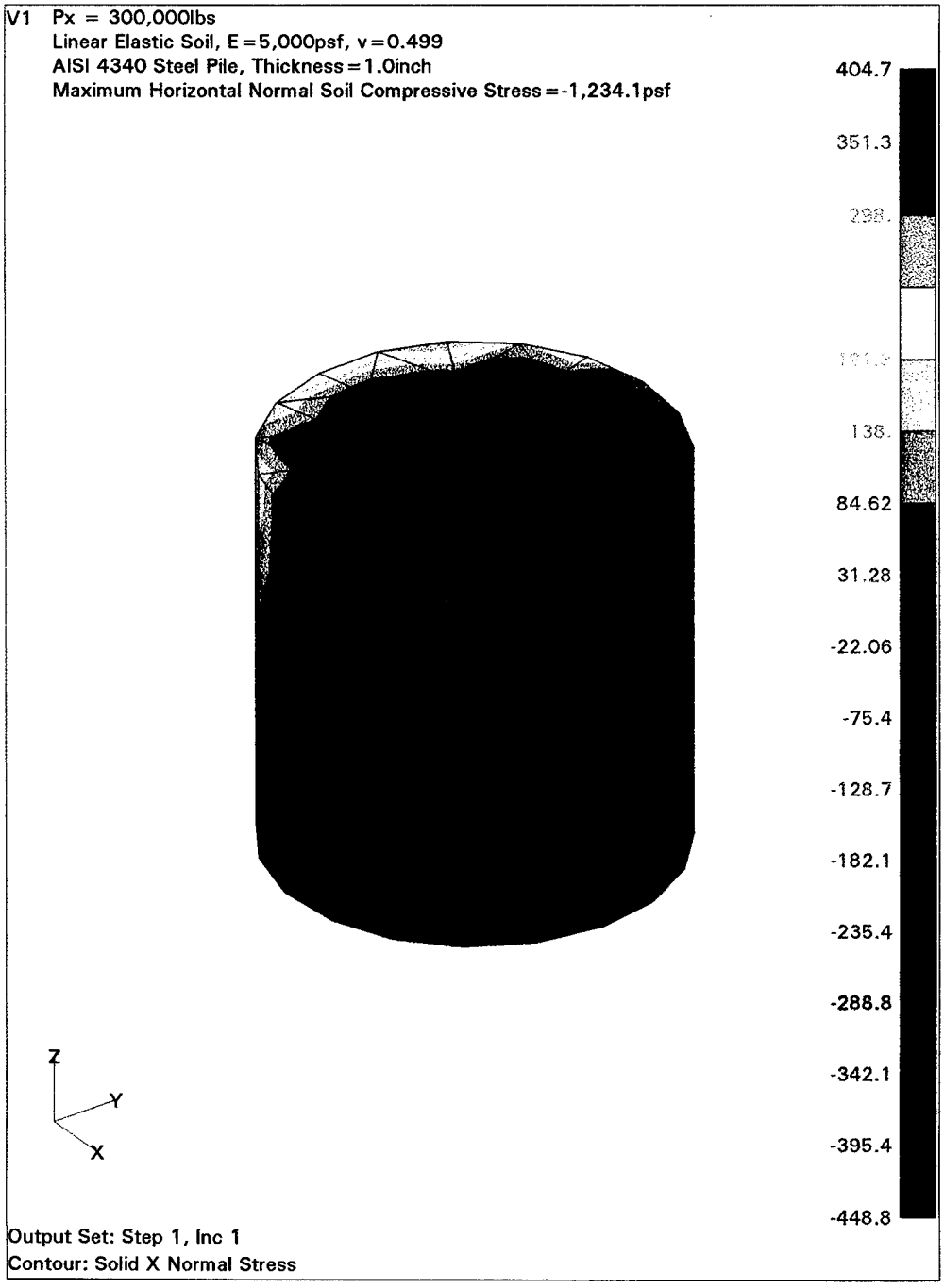

Figure-A5 Pile Major Principal Stresses on the Pile Surface (Circular Section)

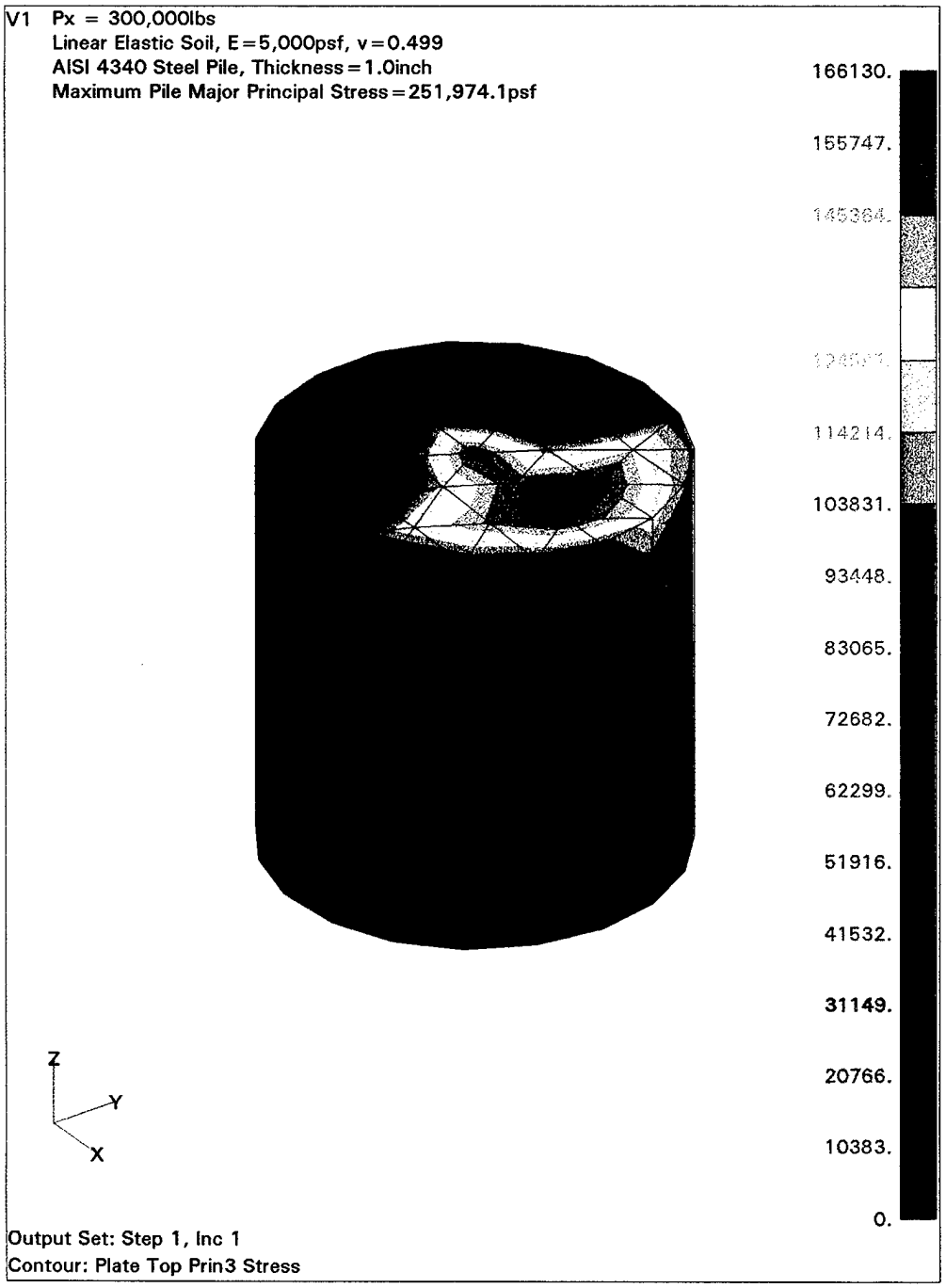

Figure-A6 Soil Minor Principal Stresses on the Pile Surface (Circular Section)

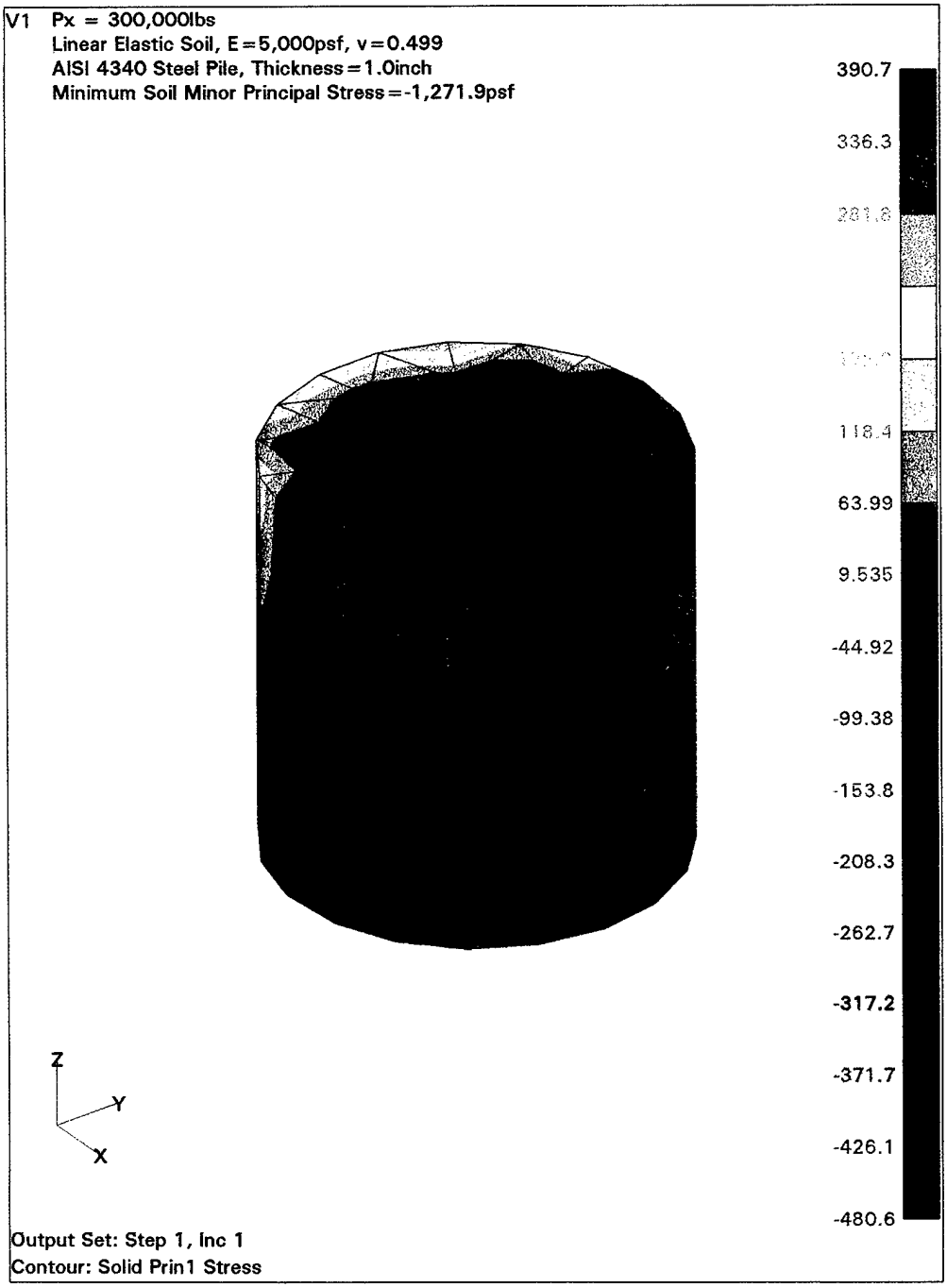

Figure-A7 Horizontal Displacements (Y-shape)

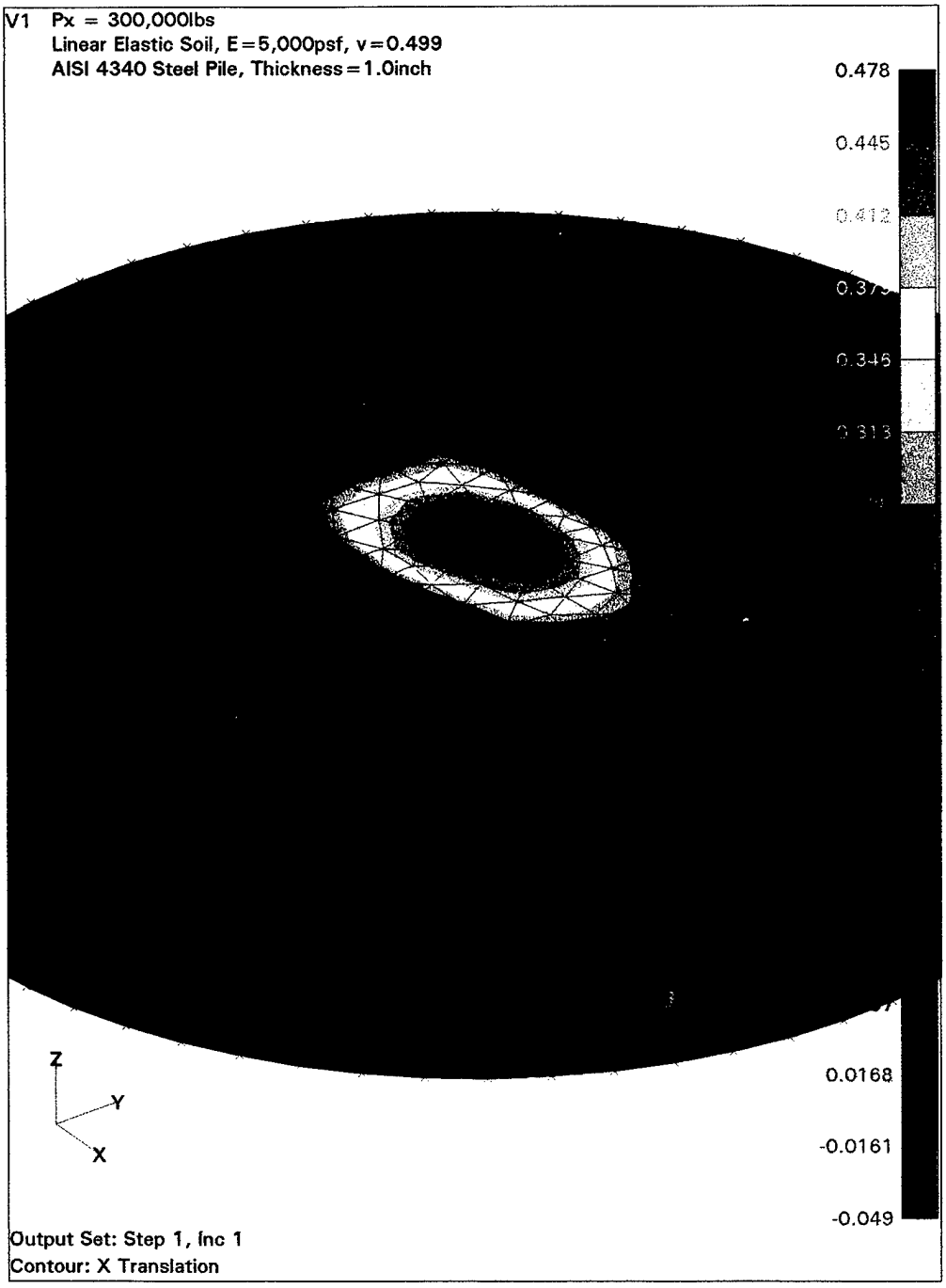

Figure-A8 Hor. Displ. on a Vert. Plane along the Hor. Load Direction (Y-shape)

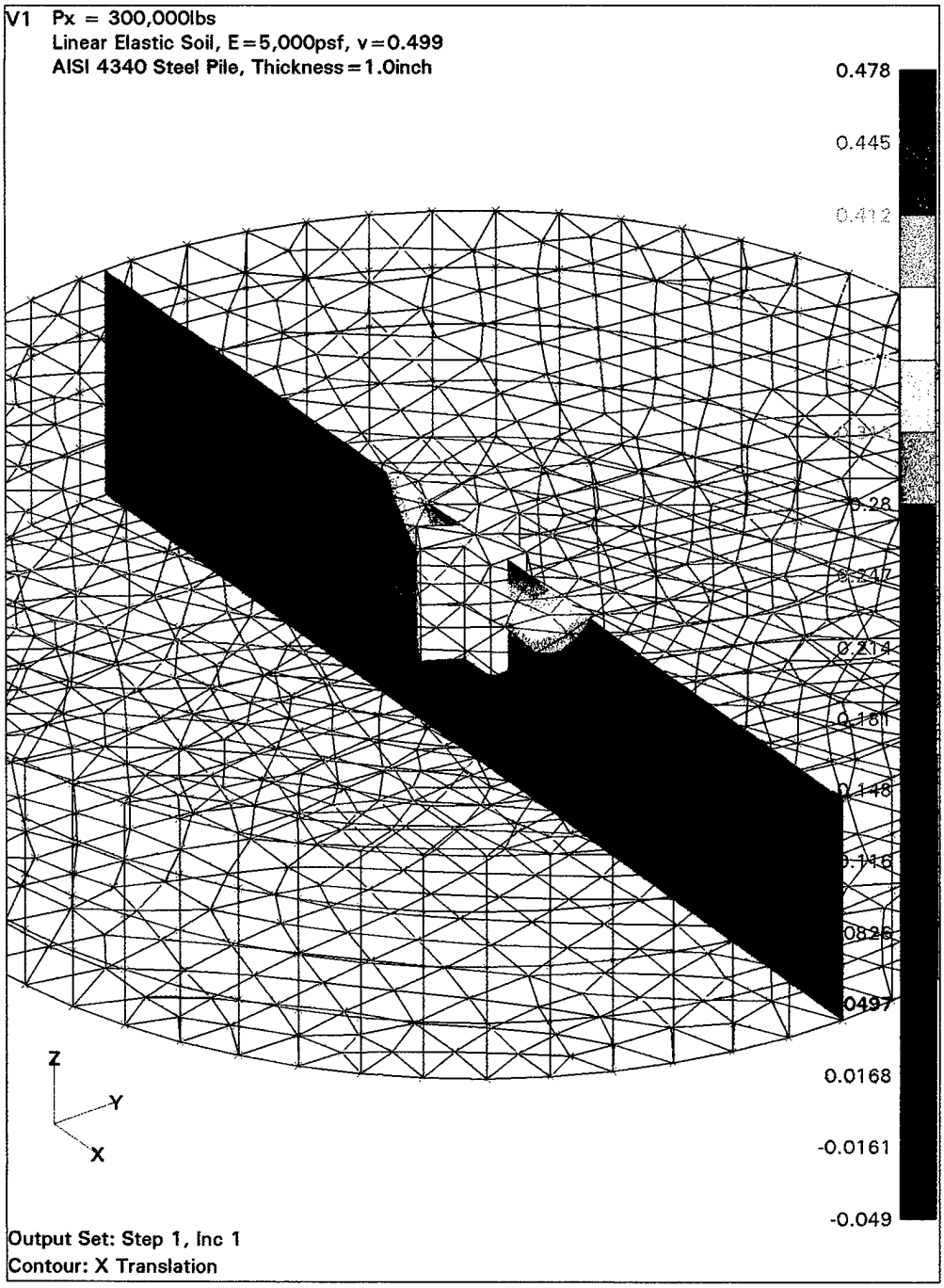

Figure-A9 Hor. Normal Pile Stresses on the Pile Surface (Y-shape)

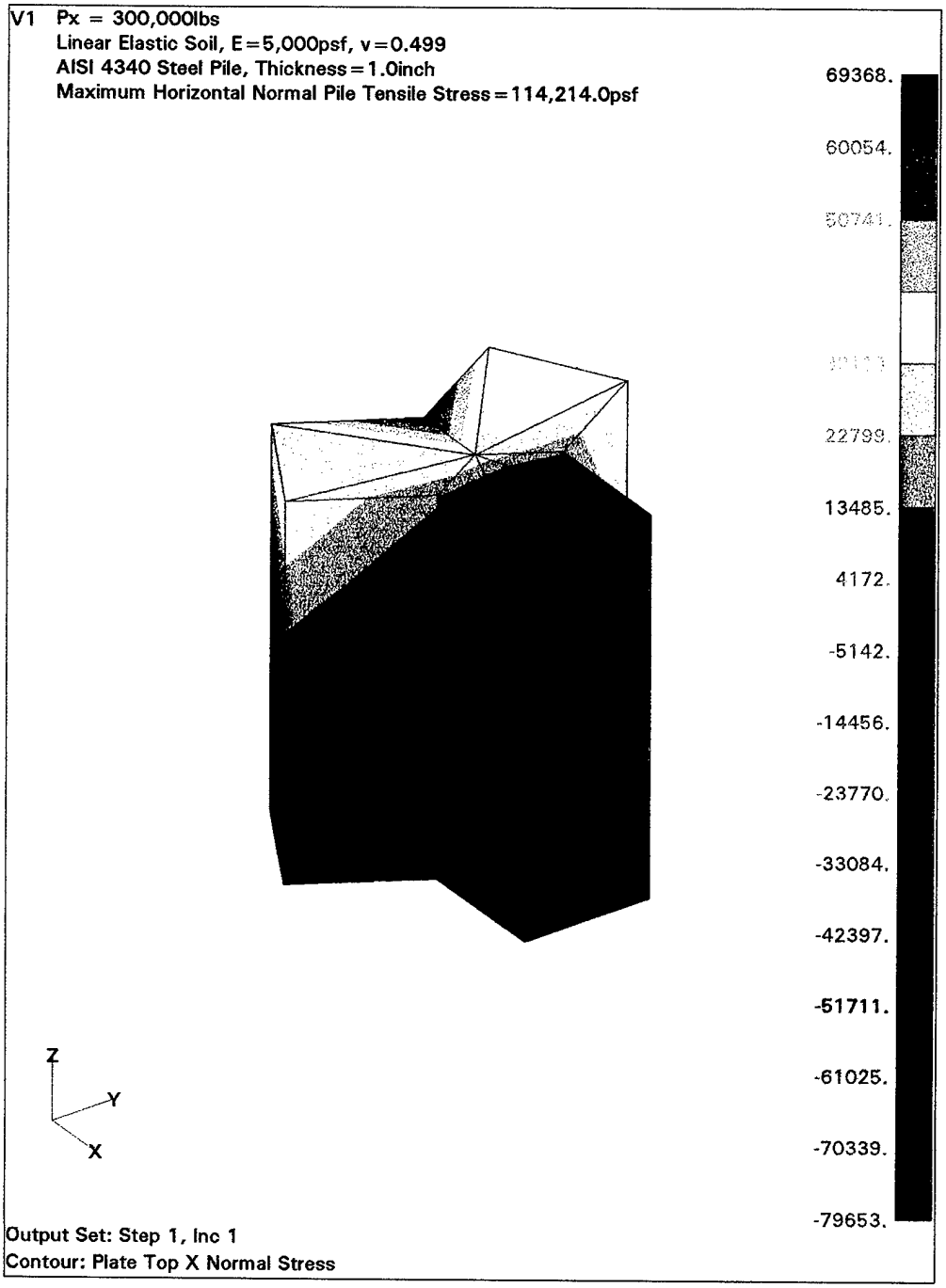

Figure-A10 Hor. Normal Soil Stresses on the Pile Surface (Y-shape)

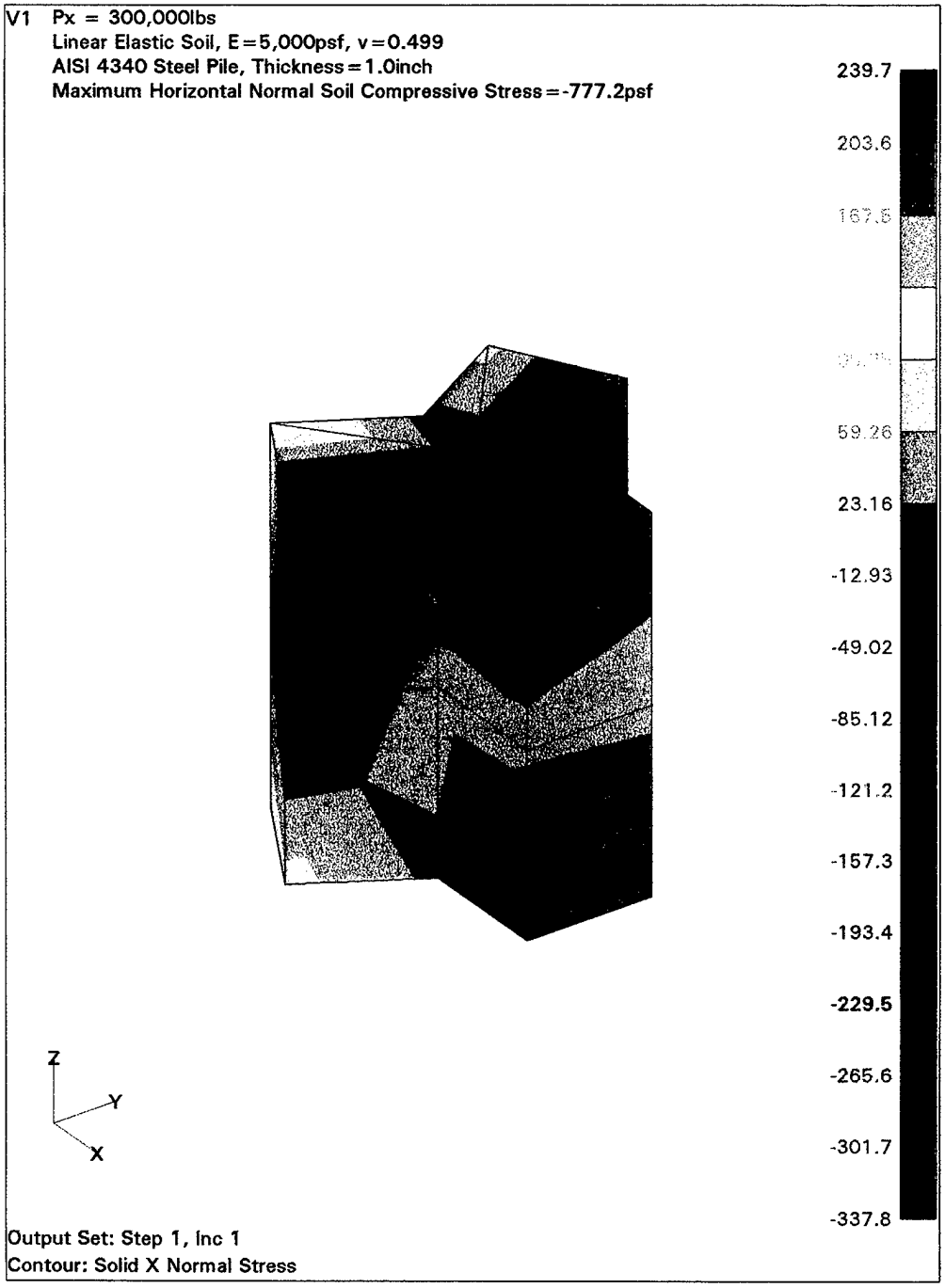

Figure-A11 Pile Major Principal Stresses on the Pile Surface (Y-shape)

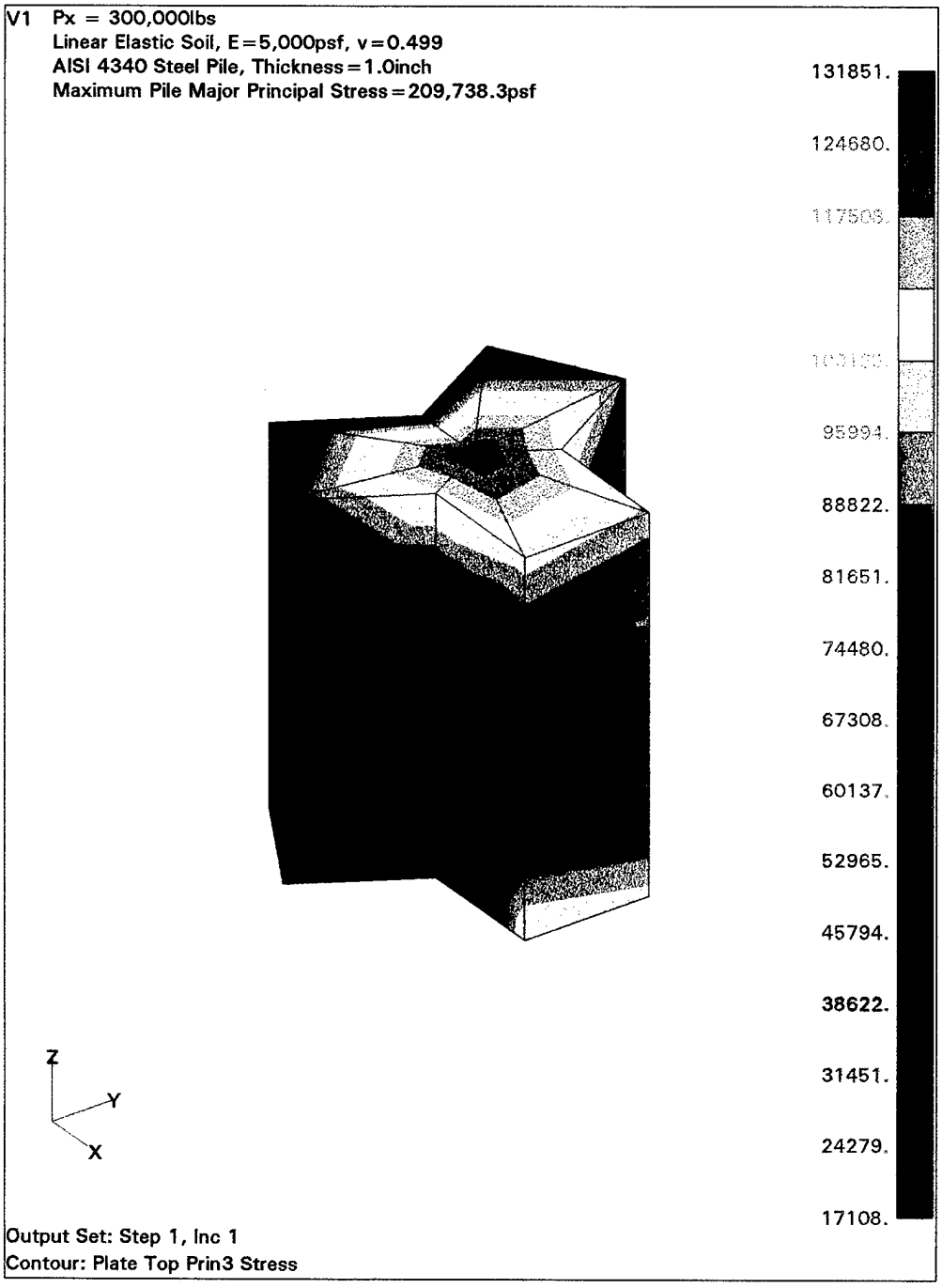

Figure-A12 Soil Minor Principal Stresses on the Pile Surface (Y-shape)

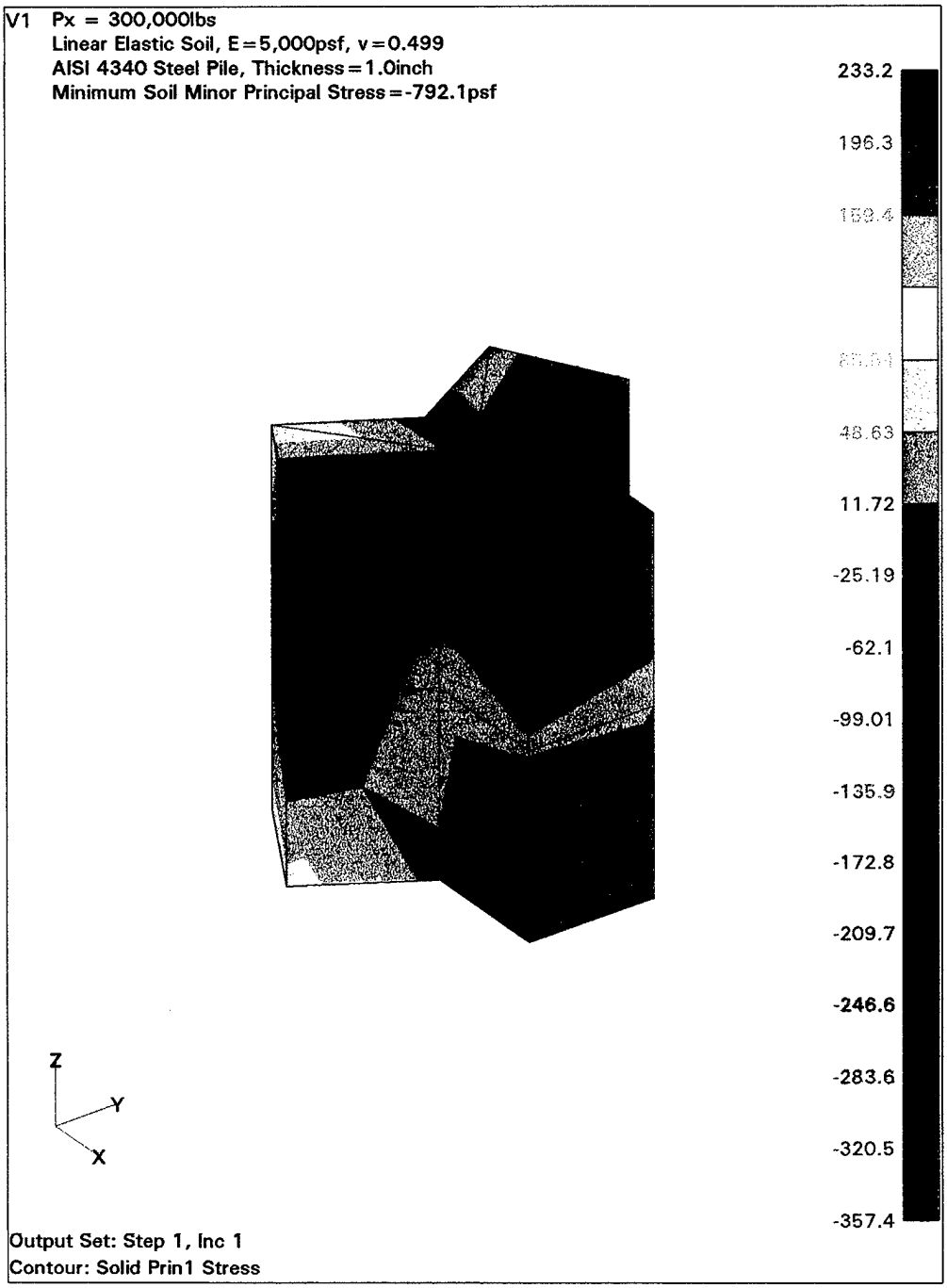

Figure-A13 Horizontal Displacements (Clover-shape with Three Leaves)

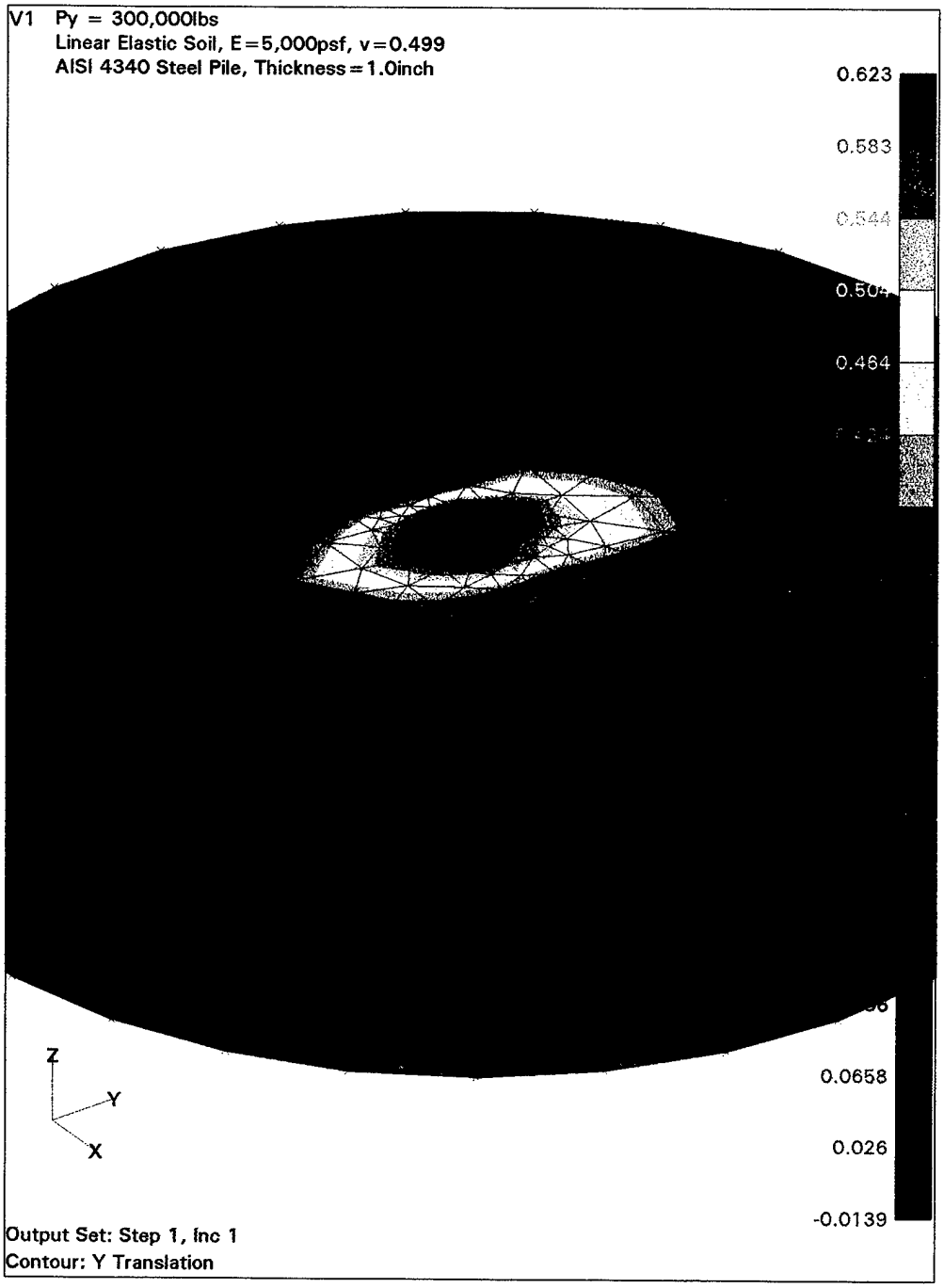

Figure-A14 Hor. Displ. on a Vert. Plane along the Hor. Load Direction (Clover-shape with Three Leaves)

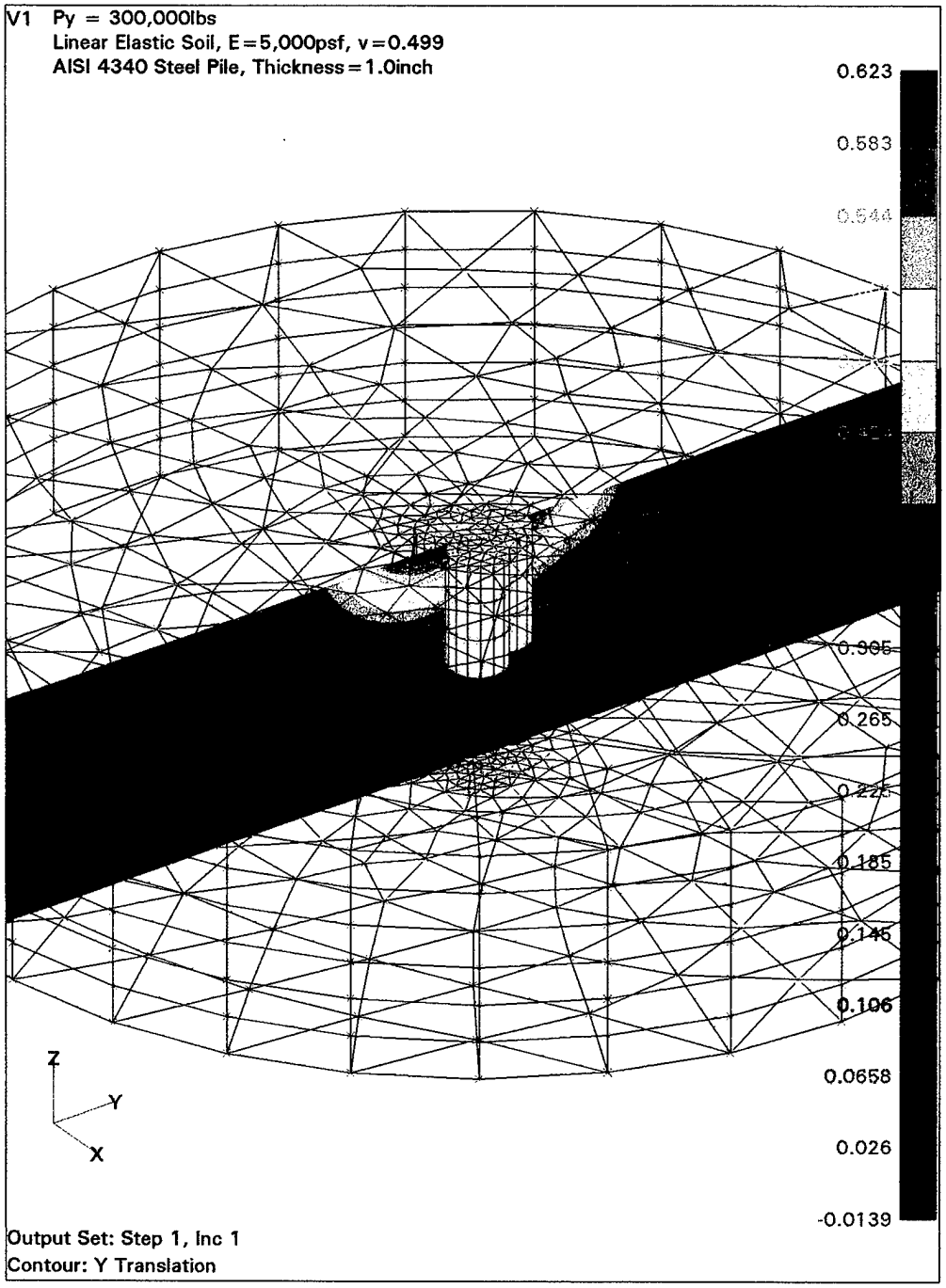

Figure-A15 Hor. Normal Pile Stresses on the Pile Surface (Clover-shape with Three Leaves)

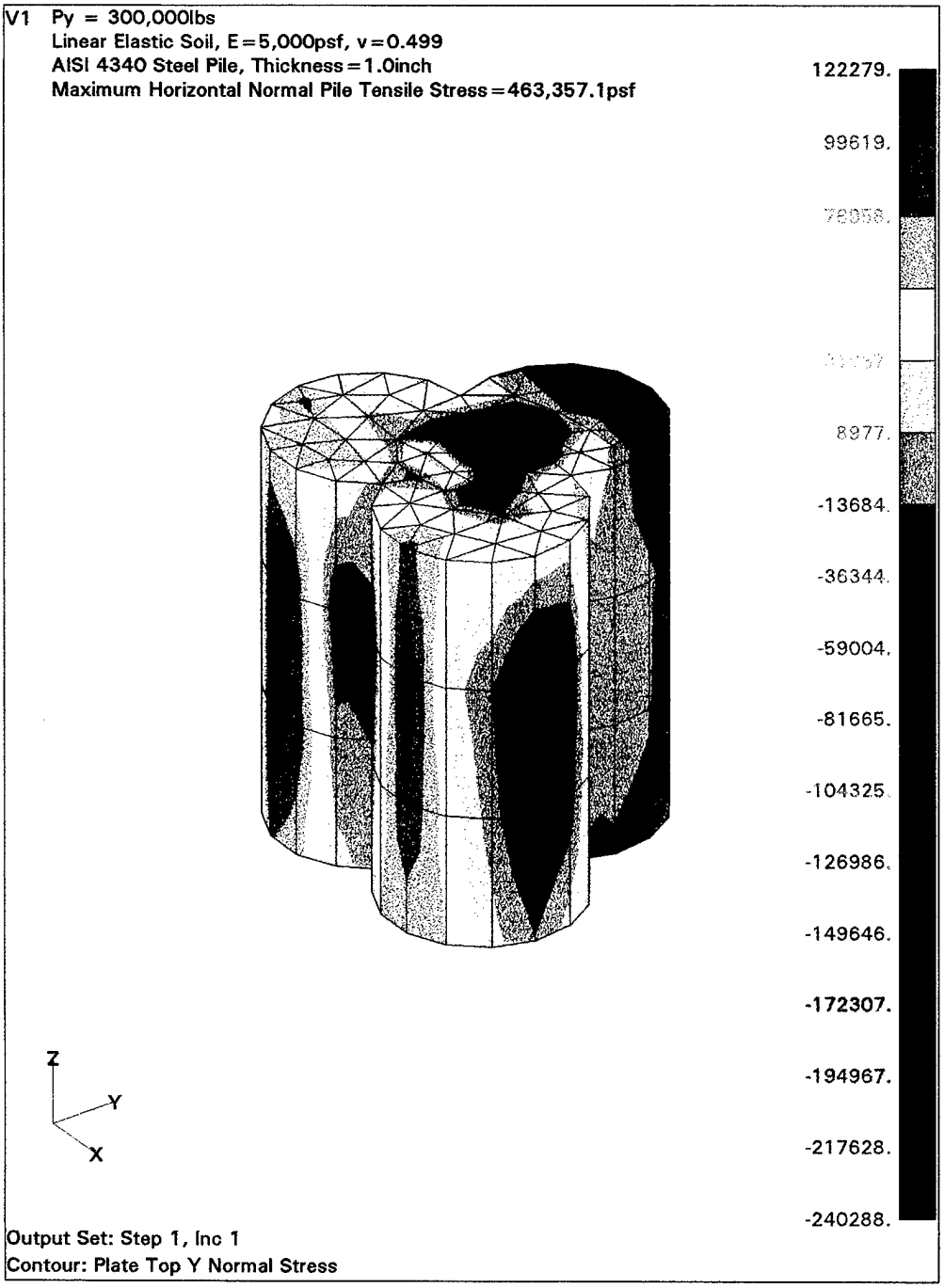

Figure-A16 Hor. Normal Soil Stresses on the Pile Surface (Clover-shape with Three Leaves)

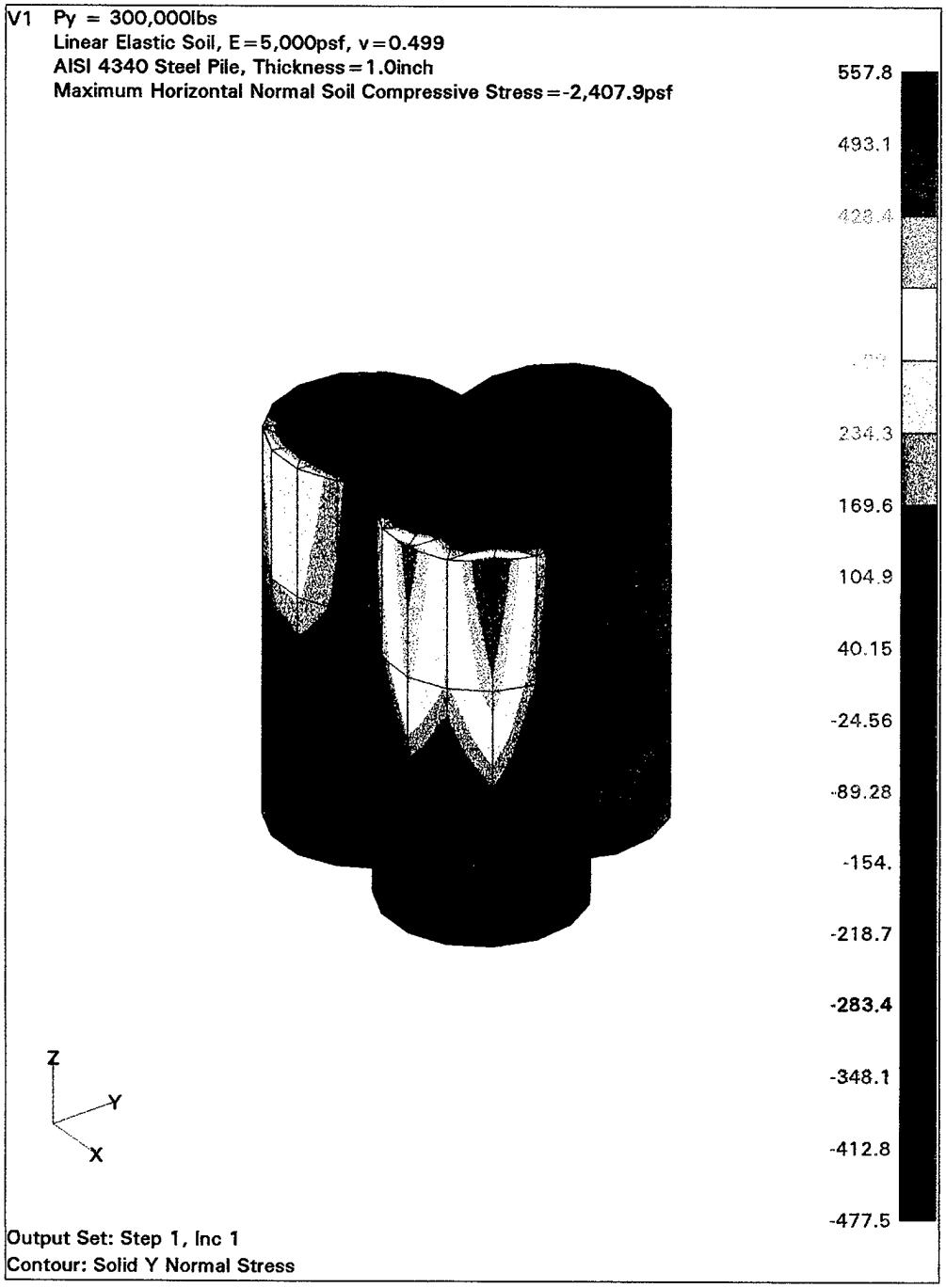

Figure-A17 Pile Major Principal Stresses on the Pile Surface (Clover-shape with Three Leaves)

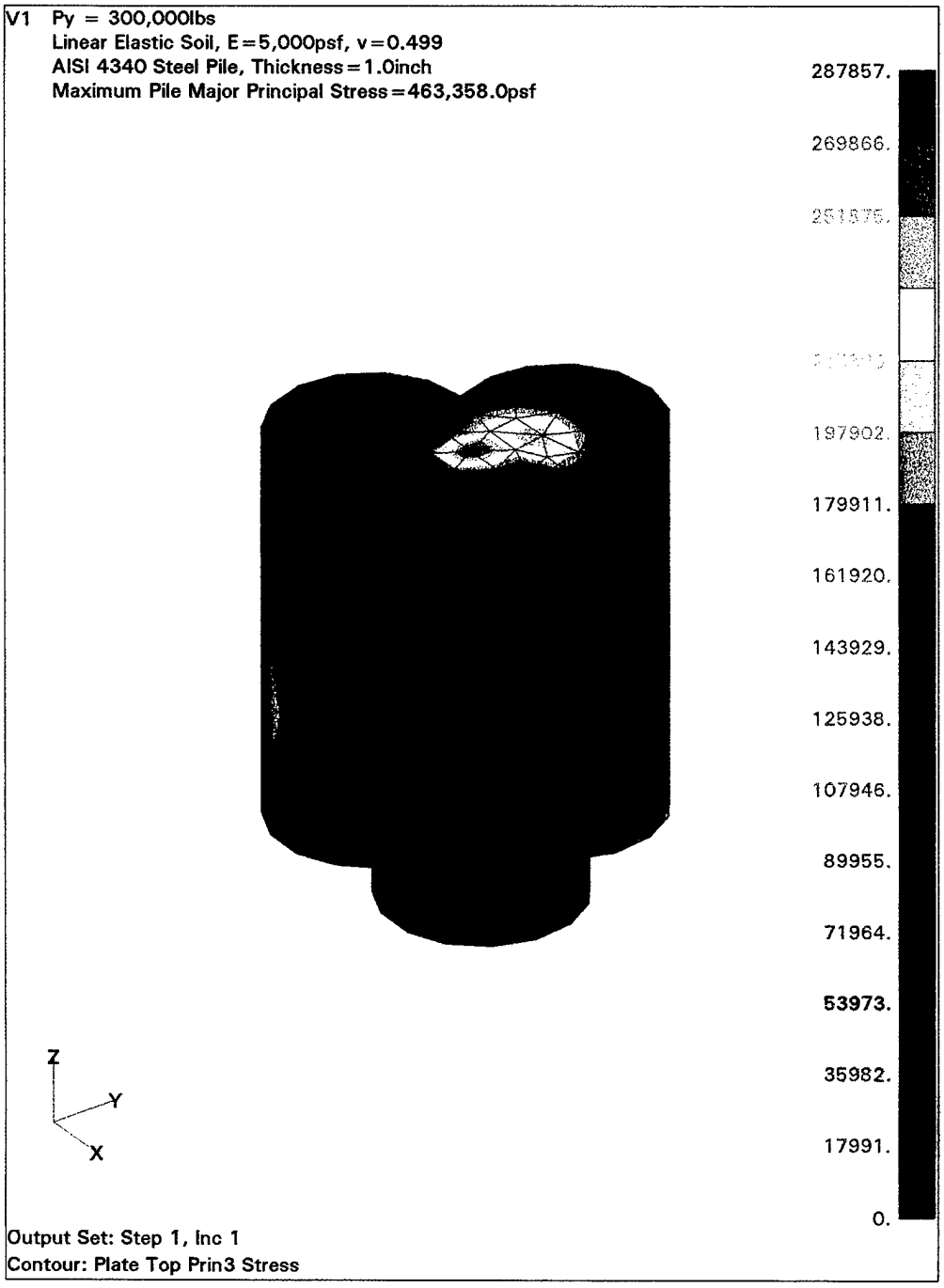

Figure-A18 Soil Minor Principal Stresses on the Pile Surface (Clover-shape with Three Leaves)

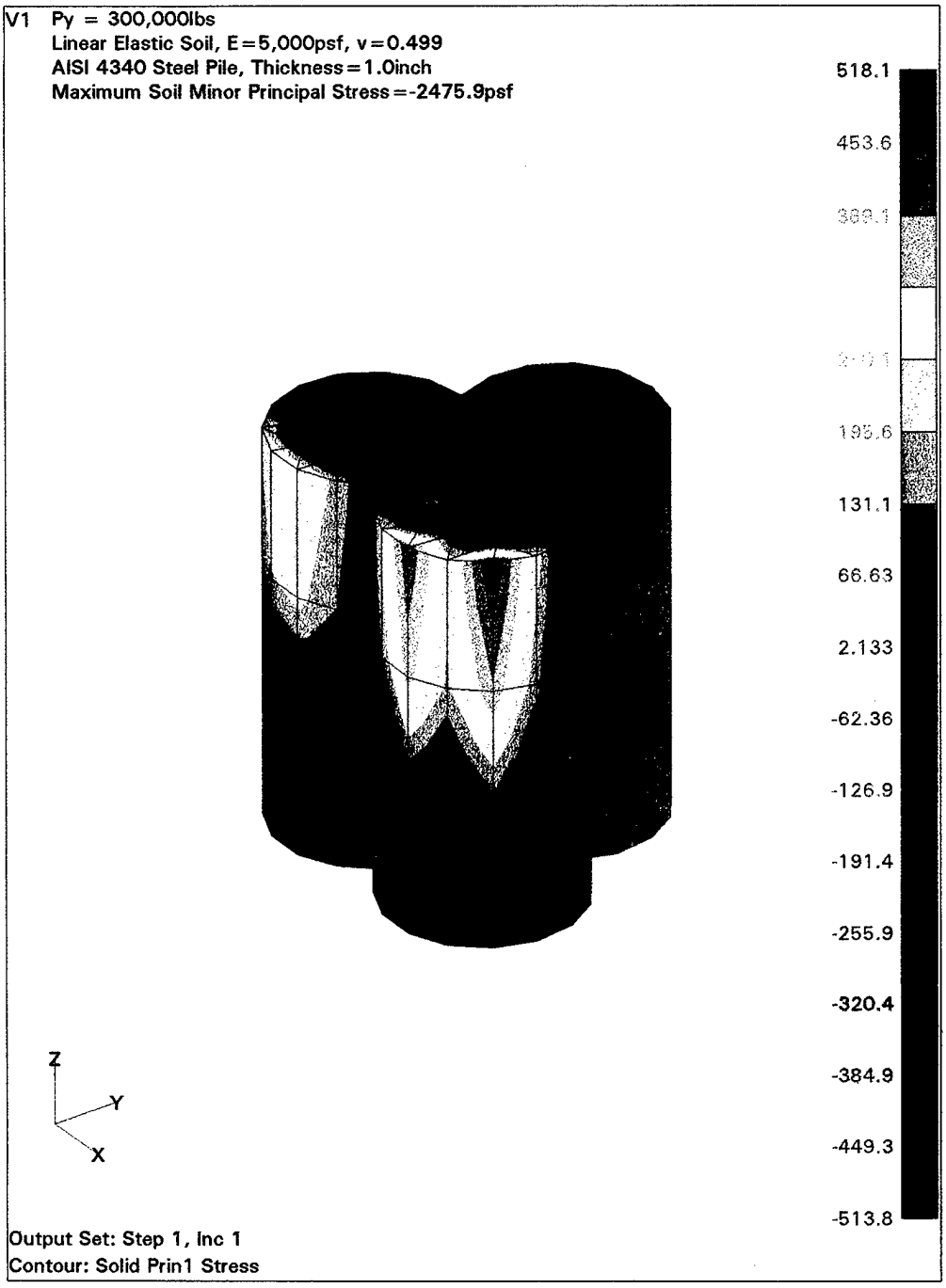

Figure-A19 Horizontal Displacements (Clustered circle with four cells)

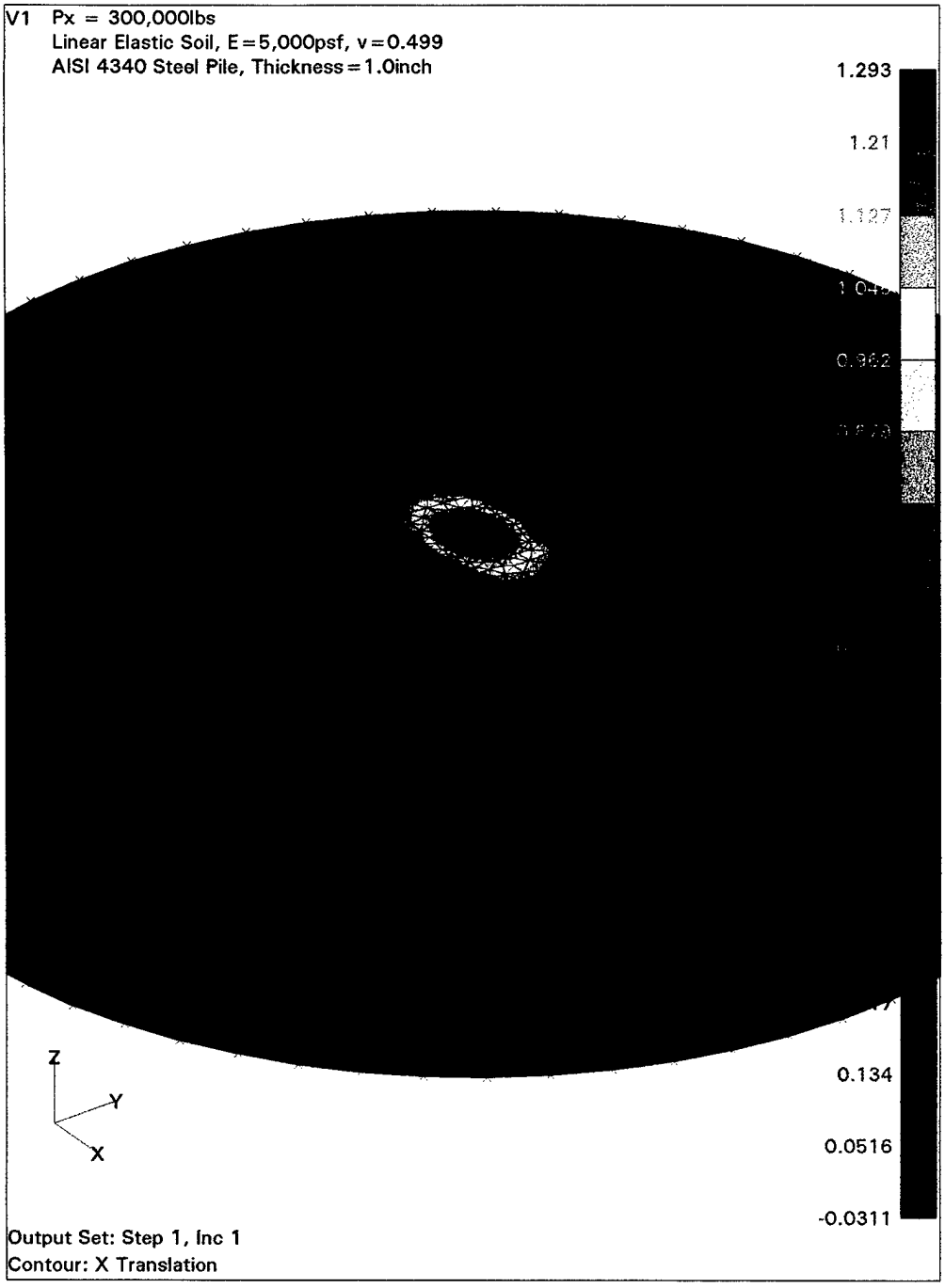

Figure-A20 Hor. Displ. on a Vert. Plane along Hor. Load D. (Clustered circle with four cells)

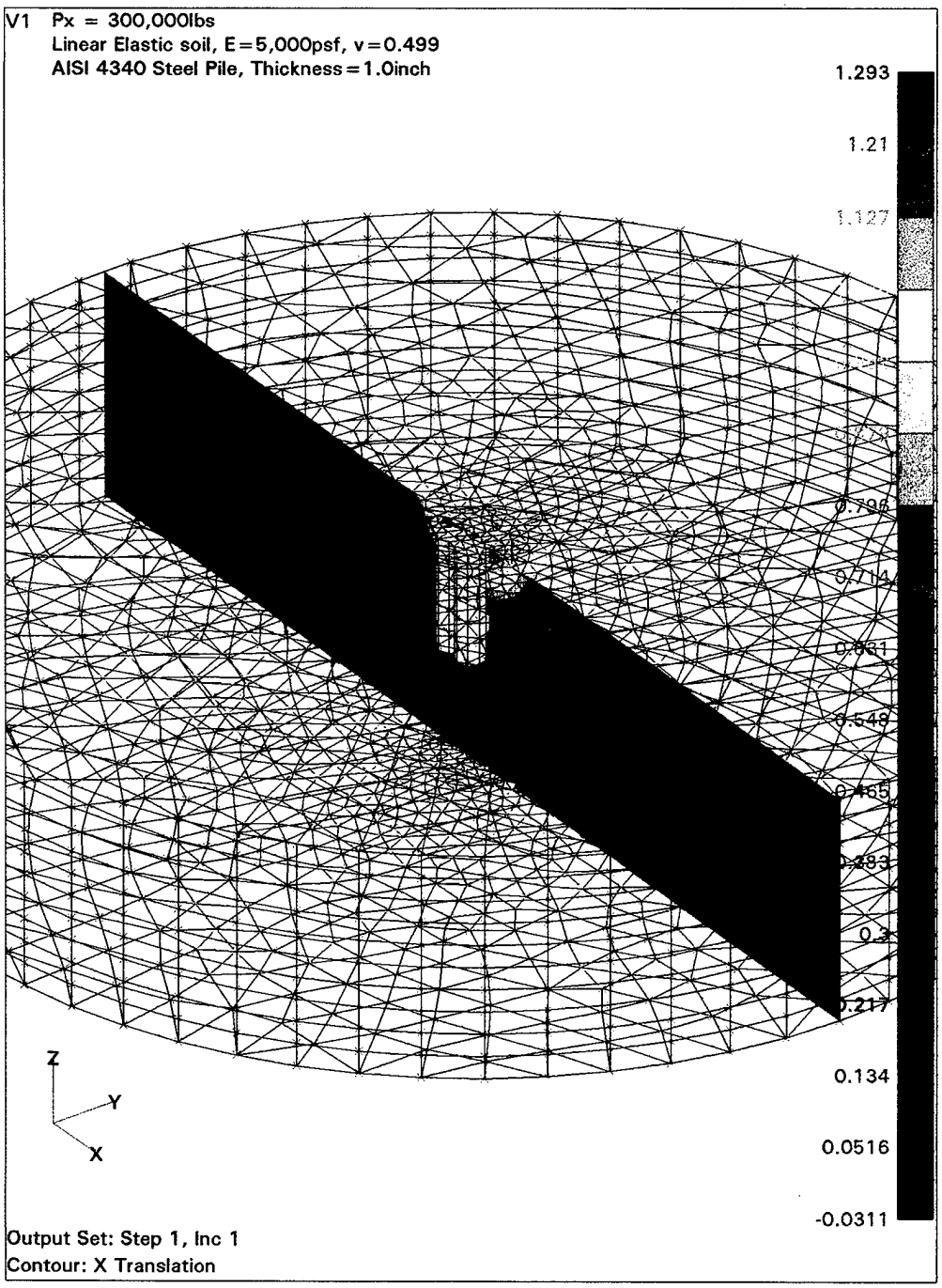

Figure-A21 Hor. Nor. Pile Stresses on the Pile Surface (Clustered circle with four cells)

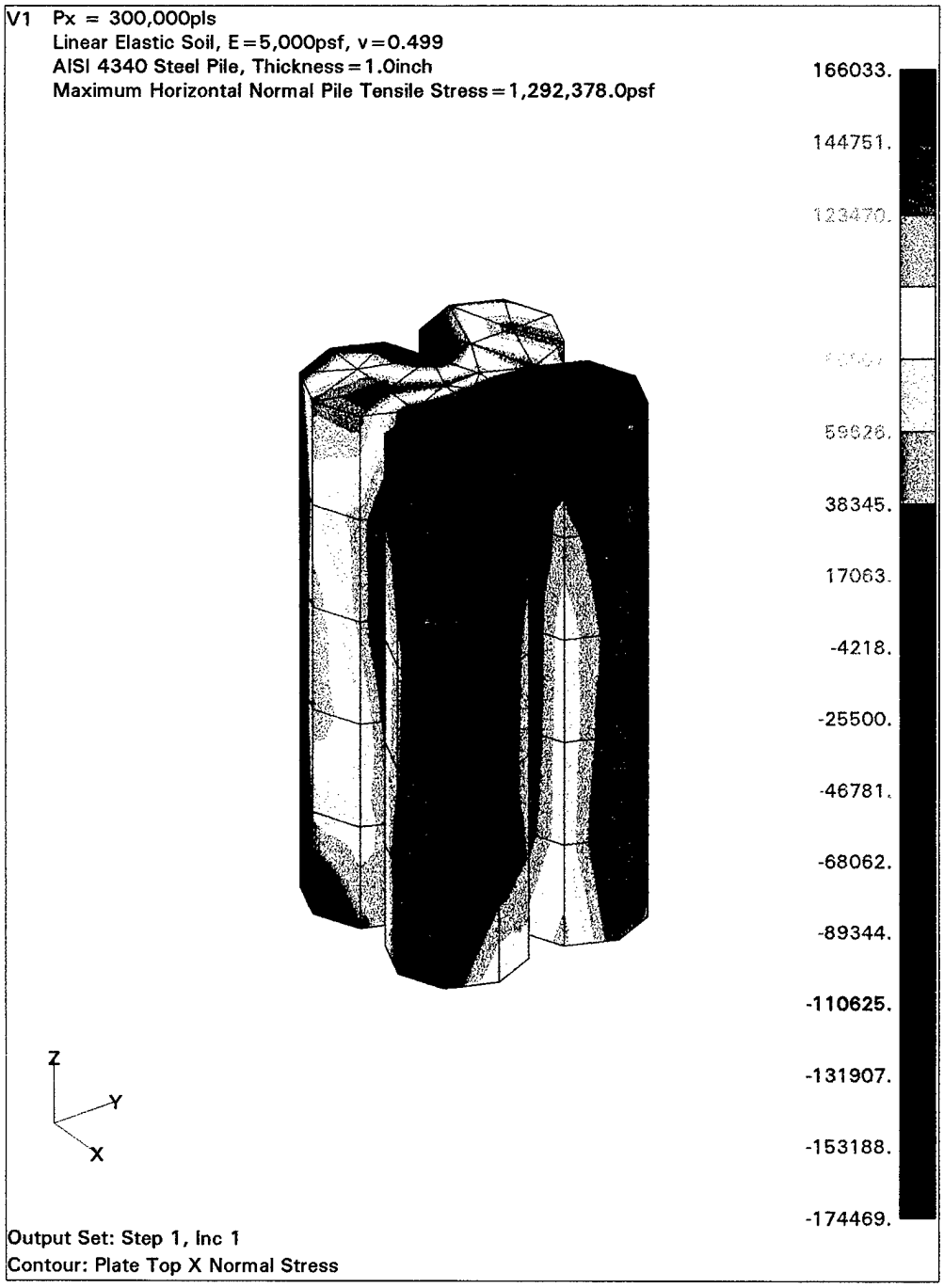

Figure-A22 Hor. Nor. Soil Stresses on the Pile Surface (Clustered circle with four cells)

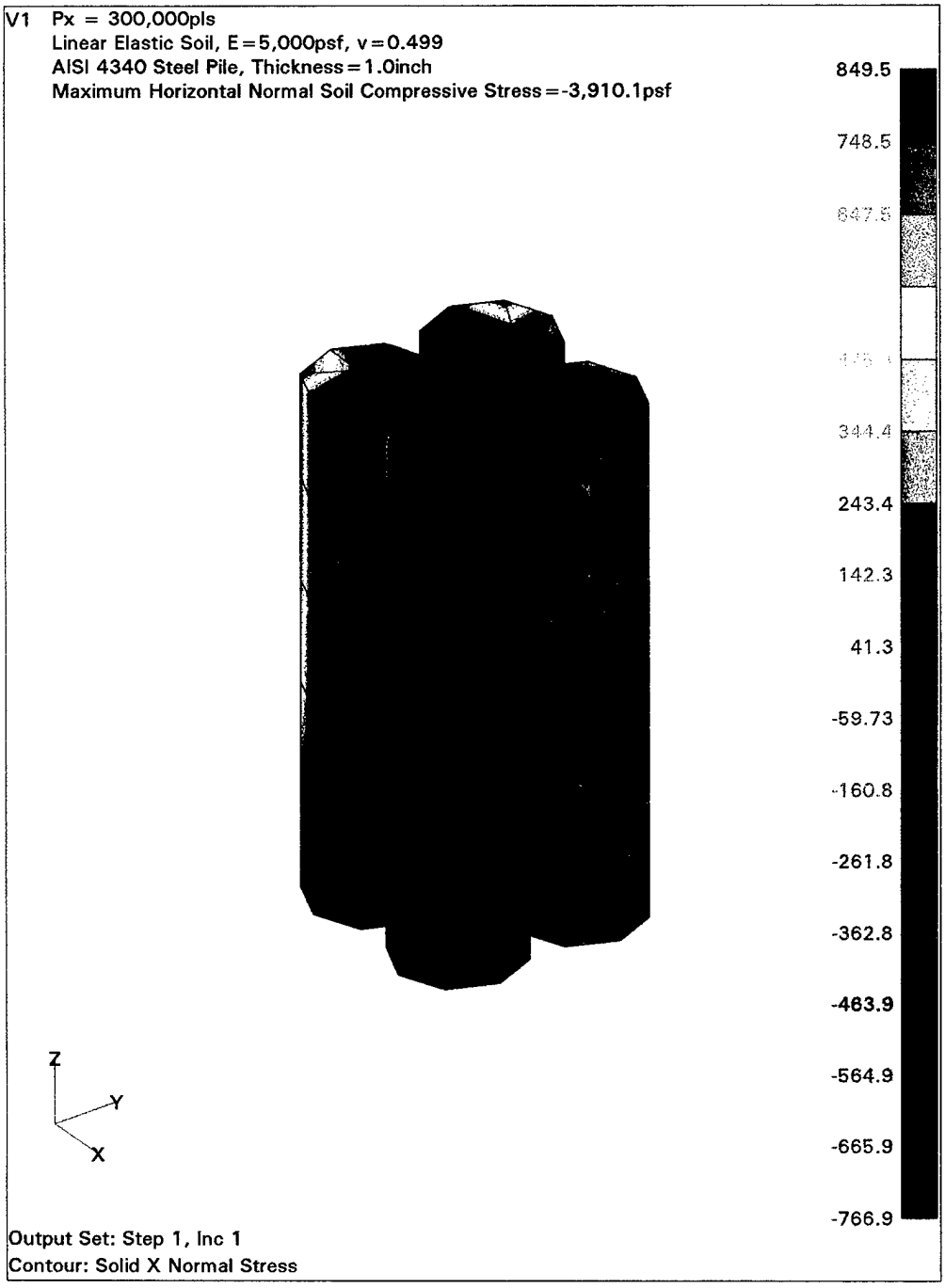

Figure-A23 Pile Major Principal Stresses on the Pile Surface (Clustered circle with four cells)

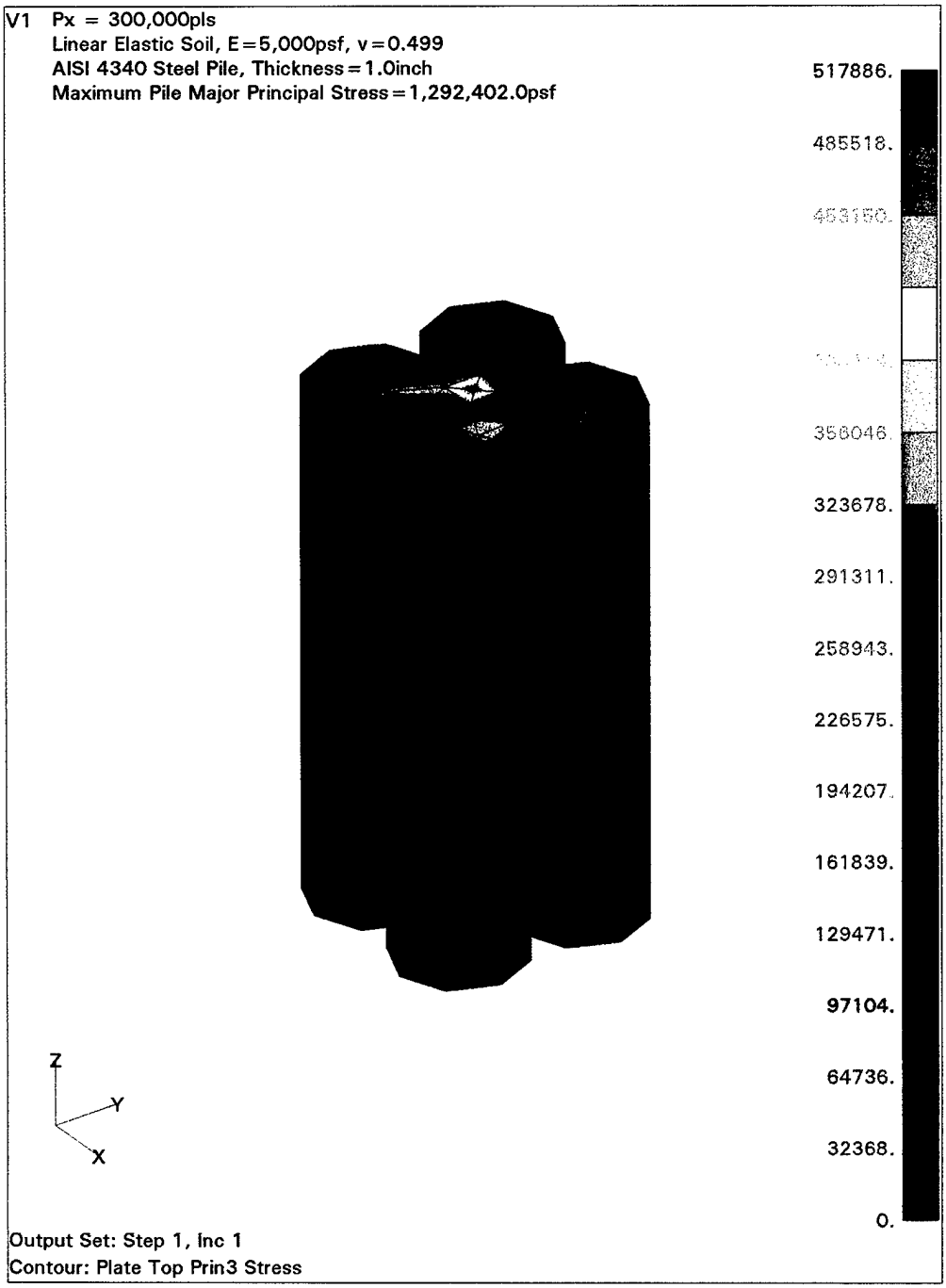

Figure-A24 Soil Minor Principal Stresses on the Pile Surface (Clustered circle with four cells)

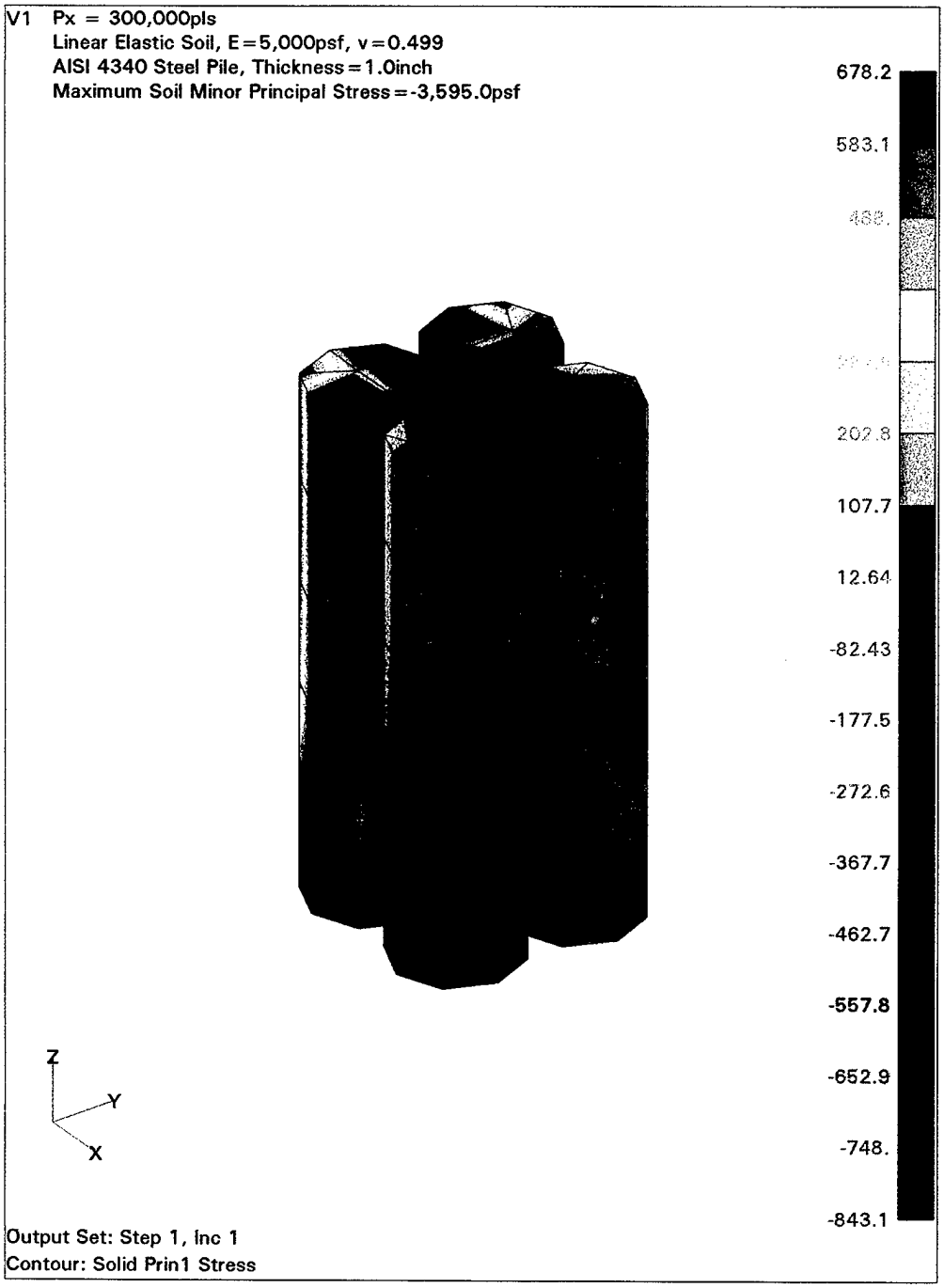

APPENDIX – B EXPERIMENTAL MODEL TEST RESULTS

Test 1A	1/30/98					
Pile	pile wt. (lbs	9.6	Surcharge wt. (lb	39.2		
	Length	Inner dia.	Outer dia.	Wall thickness	hamber heigh	Chamber dia.
(inches)	60.00	4.45	4.98	0.23	68.00	23.30
(feet)	5.00	0.37	0.42	0.02	5.67	1.94
Penetration		Stop pressure				
inches	feet	psi	psf			
1	0.08	0.91	131.04			
2	0.17	1.25	180.00			
3	0.25	1.26	181.44			
4	0.33	1.48	213.12			
5	0.42	1.71	246.24			
6	0.50	2.00	288.00			

Test 1B	2/3/98					
Pile	pile wt. (lbs)	9.6	Surcharge wt	39.2	Water Depth (ft	0.17
	γ_{water} (pcf)	62.4		γ_{sat} (pcf)	120	
	Length	Inner dia.	Outer dia.	Wall thicknes	hamber height	Chamber dia.
(inches)	60.00	4.45	4.98	0.23	68.00	23.30
(feet)	5.00	0.37	0.42	0.02	5.67	1.94
Penetration		Pressure		Stop	Water Column Height	
inches	feet	psi	psf		inches	feet
0.25	0.02	1.43	205.92		18.00	1.50
0.50	0.04	1.43	205.92			0.00
0.75	0.06	1.43	205.92		18.50	1.54
1.00	0.08	1.49	214.56			0.00
1.25	0.10	1.49	214.56			0.00
1.50	0.13	1.49	214.56		22.00	1.83
1.75	0.15	1.72	247.68			0.00
2.00	0.17	1.77	254.88			0.00
2.25	0.19	1.77	254.88			0.00
2.50	0.21	1.77	254.88			0.00
2.75	0.23	1.77	254.88			0.00
3.00	0.25	1.83	263.52			0.00
3.25	0.27	1.83	263.52		24.00	2.00
3.50	0.29	1.83	263.52			0.00
3.75	0.31	1.89	272.16			0.00
4.00	0.33	1.89	272.16			0.00
4.25	0.35	1.89	272.16			0.00
4.50	0.38	1.89	272.16		25.50	2.13
4.75	0.40	1.89	272.16			0.00
5.00	0.42	1.95	280.80		26.00	2.17
5.25	0.44	1.95	280.80			0.00
5.50	0.46	1.95	280.80			0.00
5.75	0.48	1.95	280.80		27.00	2.25
6.00	0.50	2.00	288.00			0.00
6.25	0.52	2.29	329.76			0.00
6.50	0.54	2.35	338.40			0.00
6.75	0.56	2.35	338.40			0.00
7.00	0.58	2.40	345.60			0.00
7.25	0.60	2.40	345.60			0.00
7.50	0.63	2.40	345.60		35.00	2.92
7.75	0.65	2.46	354.24			0.00
8.00	0.67	2.46	354.24			0.00
8.25	0.69	2.46	354.24		top	
8.50	0.71	2.46	354.24			
8.75	0.73	2.52	362.88			
9.00	0.75	2.52	362.88			
9.25	0.77	2.52	362.88			
9.50	0.79	2.58	371.52			
9.75	0.81		0.00			
10.00	0.83		0.00			

Test 1C	2/3/98					
Pile	pile wt. (lbs)	9.6	Surcharge wt	39.2	Water Depth	0.17
	γ_{water} (pcf)	62.4		γ_{sat} (pcf)	120	
	Length	Inner dia.	Outer dia.	Wall thicknes	hamber heigh	Chamber dia.
(inches)	60.00	4.45	4.98	0.23	68.00	23.30
(feet)	5.00	0.37	0.42	0.02	5.67	1.94
Penetration		Pressure		Stop	Water Column Height	
inches	feet	psi	psf	psf	inches	feet
0.25	0.02	0.97	139.68		7.75	0.65
0.50	0.04	0.75	108.00		8.00	0.67
0.75	0.06	1.03	148.32		8.25	0.69
1.00	0.08	1.03	148.32		8.50	0.71
1.25	0.10	1.03	148.32		9.00	0.75
1.50	0.13	1.03	148.32	156.96	9.00	0.75
1.75	0.15	1.26	181.44		13.50	1.13
2.00	0.17	1.32	190.08		13.50	1.13
2.25	0.19	1.32	190.08		13.75	1.15
2.50	0.21	1.32	190.08		14.00	1.17
2.75	0.23	1.32	190.08		14.25	1.19
3.00	0.25	1.38	198.72		14.50	1.21
3.25	0.27	1.38	198.72		14.75	1.23
3.50	0.29	1.38	198.72		15.00	1.25
3.75	0.31	1.43	205.92	205.92	20.60	1.72
4.00	0.33	1.66	239.04		23.00	1.92
4.25	0.35	1.72	247.68		23.25	1.94
4.50	0.38	1.78	256.32		23.50	1.96
4.75	0.40	1.78	256.32		23.75	1.98
5.00	0.42	1.78	256.32		24.00	2.00
5.25	0.44	1.78	256.32		24.50	2.04
5.50	0.46	1.83	263.52		24.75	2.06
5.75	0.48	1.83	263.52		25.00	2.08
6.00	0.50	1.83	263.52		25.25	2.10
6.25	0.52	1.89	272.16		25.75	2.15
6.50	0.54	1.89	272.16	280.80	26.00	2.17
6.75	0.56	2.18	313.92		32.75	2.73
7.00	0.58	2.23	321.12		33.00	2.75
7.25	0.60	2.23	321.12		33.25	2.77
7.50	0.63	2.29	329.76		33.50	2.79
7.75	0.65	2.29	329.76		33.75	2.81
8.00	0.67	2.29	329.76		34.00	2.83
8.25	0.69	2.29	329.76		34.25	2.85
8.50	0.71	2.35	338.40		34.50	2.88
8.75	0.73	2.35	338.40		25.00	2.08
9.00	0.75	2.41	347.04		35.25	2.94
9.25	0.77	2.41	347.04		36.00	3.00
9.50	0.79	2.41	347.04	387.36	26.75	2.23
9.75	0.81		0.00			0.00
10.00	0.83		0.00			0.00

Test 1D	2/4/98					
Pile	pile wt. (lbs)	9.6	Surcharge wt	39.2	Water Depth	0.17
	γ_{water} (pcf)	62.4	γ_{sat} (pcf)	120	Initial Penetration	1.00
	Length	Inner dia.	Outer dia.	Wall thicknes	Chamber height	Chamber dia.
(inches)	60.00	4.45	4.98	0.23	68.00	23.30
(feet)	5.00	0.37	0.42	0.02	5.67	1.94
Penetration		Pressure		Stop	Water Column Height	
inches	feet	psi	psf	psf	inches	feet
0.25	0.02	0.57	82.08		-1.50	-0.13
0.50	0.04	0.75	108.00			0.00
0.75	0.06	0.75	108.00			0.00
1.00	0.08	0.75	108.00	108.00	1.00	0.08
1.25	0.10	0.80	115.20		5.00	0.42
1.50	0.13	0.86	123.84	123.84	5.50	0.46
1.75	0.15	0.92	132.48		7.00	0.58
2.00	0.17	0.97	139.68		7.00	0.58
2.25	0.19	0.97	139.68		7.00	0.58
2.50	0.21	0.97	139.68	139.68	7.50	0.63
2.75	0.23	1.09	156.96		9.00	0.75
3.00	0.25	1.09	156.96		9.25	0.77
3.25	0.27	1.09	156.96	165.60	9.50	0.79
3.50	0.29	1.20	172.80	172.80	12.00	1.00
3.75	0.31	1.26	181.44		12.25	1.02
4.00	0.33	1.26	181.44		12.50	1.04
4.25	0.35	1.26	181.44		12.75	1.06
4.50	0.38	1.32	190.08		13.00	1.08
4.75	0.40	1.32	190.08	205.92	13.25	1.10
5.00	0.42	1.43	205.92		15.00	1.25
5.25	0.44	1.43	205.92		15.25	1.27
5.50	0.46	1.49	214.56		15.00	1.25
5.75	0.48	1.49	214.56		15.50	1.29
6.00	0.50	1.49	214.56		15.75	1.31
6.25	0.52	1.49	214.56		15.75	1.31
6.50	0.54	1.49	214.56		16.25	1.35
6.75	0.56	1.55	223.20		16.25	1.35
7.00	0.58	1.55	223.20		16.50	1.38
7.25	0.60	1.55	223.20		16.75	1.40
7.50	0.63	1.55	223.20		17.00	1.42
7.75	0.65	1.55	223.20	230.40	18.00	1.50
8.00	0.67	1.60	230.40	230.40	19.75	1.65
8.25	0.69	1.72	247.68		20.00	1.67
8.50	0.71	1.72	247.68		20.25	1.69
8.75	0.73	1.72	247.68		20.50	1.71
9.00	0.75	1.78	256.32		20.75	1.73
9.25	0.77	1.78	256.32		21.50	1.79
9.50	0.79		0.00			0.00
9.75	0.81		0.00			0.00
10.00	0.83		0.00			0.00

Test 1E	2/4/98						
Pile	pile wt. (lbs)	9.6	Surcharge wt.	39.2	Water Depth	0.17	
	γ_{water} (pcf)	62.4	γ_{sat} (pcf)	120	nitial Penetratio	1.00	
	Length	Inner dia.	Outer dia.	Wall thicknes	Chamber height	Chamber dia.	
(inches)	60.00	4.45	4.98	0.23	68.00	23.30	
(feet)	5.00	0.37	0.42	0.02	5.67	1.94	
Penetration		Pressure		Stop	Movement	Water Column Height	
inches	feet	psi	psf	psf	psf	inches	feet
0.25	1.02	0.92	132.48		132.48		
0.50	1.04	0.97	139.68			8.50	0.71
0.75	1.06	0.97	139.68			8.50	0.71
1.00	1.08	1.03	148.32			8.75	0.73
1.25	1.10	1.03	148.32	156.96		9.25	0.77
1.50	1.13	1.26	181.44		181.44	13.50	1.13
1.75	1.15	1.37	197.28			13.75	1.15
2.00	1.17	1.37	197.28				
2.25	1.19					14.00	1.17
2.50	1.21	1.38	198.72			14.00	1.17
2.75	1.23	1.38	198.72			14.50	1.21
3.00	1.25	1.38	198.72			14.75	1.23
3.25	1.27	1.38	198.72			14.75	1.23
3.50	1.29	1.38	198.72			15.00	1.25
3.75	1.31	1.38	198.72			15.25	1.27
4.00	1.33	1.43	205.92			15.50	1.29
4.25	1.35	1.43	205.92			15.75	1.31
4.50	1.38	1.43	205.92			16.00	1.33
4.75	1.40	1.43	205.92			16.25	1.35
5.00	1.42	1.43	205.92			16.50	1.38
5.25	1.44	1.49	214.56	223.20		17.25	1.44
5.50	1.46	1.60	230.40		230.40	19.75	1.65
5.75	1.48	1.60	230.40			20.00	1.67
6.00	1.50	1.66	239.04			20.25	1.69
6.25	1.52	1.72	247.68			20.50	1.71
6.50	1.54	1.72	247.68			20.75	1.73
6.75	1.56	1.72	247.68			21.00	1.75
7.00	1.58	1.72	247.68			21.25	1.77
7.25	1.60	1.78	256.32			21.75	1.81
7.50	1.63	1.78	256.32	263.52		22.25	1.85
7.75	1.65	1.89	272.16	272.16		24.00	2.00
8.00	1.67	1.89	272.16			24.50	2.04
8.25	1.69	1.89	272.16			24.50	2.04
8.50	1.71	1.95	280.80			24.75	2.06
8.75	1.73	1.95	280.80			25.00	2.08
9.00	1.75	1.95	280.80			25.25	2.10
9.25	1.77	1.95	280.80			25.50	2.13
9.50	1.79	2.01	289.44			25.50	2.13
9.75	1.81	2.01	289.44			26.00	2.17
10.00	1.83	2.06	296.64			26.00	2.17
10.25	1.85	2.06	296.64			26.25	2.19
10.50	1.88	2.06	296.64			26.50	2.21
10.75	1.90	2.06	296.64			27.00	2.25
11.00	1.92	2.12	305.28	313.92	313.92	28.00	2.33
11.25	1.94	2.23	321.12			31.00	2.58
11.50	1.96	2.23	321.12			31.25	2.60
11.75	1.98	2.35	338.40			32.00	2.67
12.00	2.00	2.35	338.40				
12.25	2.02	2.35	338.40			32.25	2.69
12.50	2.04	2.41	347.04			32.50	2.71
12.75	2.06	2.41	347.04			32.50	2.71
13.00	2.08	2.41	347.04			32.75	2.73
13.25	2.10	2.41	347.04			32.75	2.73
13.50	2.13	2.41	347.04			33.00	2.75
13.75	2.15	2.41	347.04			33.00	2.75
14.00	2.17	2.41	347.04			33.25	2.77
14.25	2.19	2.46	354.24	420.48		33.25	2.77

Test 2A	2/11/98							
Pile	pile wt. (lbs)	9.6	Surcharge wt.	51.4	Water Depth	0.17		
	γ_{water} (pcf)	62.4	γ_{sat} (pcf)	120	nitial Penetratio	1.04		
	Length	Inner dia.	Outer dia.	Wall thicknes	Chamber height	Chamber dia.		
(inches)	60.00	4.45	4.98	0.23	68.00	23.30		
(feet)	5.00	0.37	0.42	0.02	5.67	1.94		
Penetration		Pressure		Stop	Movement	Water Column Height		Corrected
inches	feet	psi	psf	psf	psf	inches	feet	feet
0.25	1.06							
0.50	1.08							
0.75	1.10				57.60			
1.00	1.13	0.52	74.88	82.08	74.88	5.15	0.43	0.26
1.25	1.15	0.63	90.72					
1.50	1.17	0.63	90.72	99.36	108.00	8.50	0.71	0.54
1.75	1.19	0.75	108.00					
2.00	1.21	0.80	115.20					
2.25	1.23	0.80	115.20			13.00	1.08	0.91
2.50	1.25	0.86	123.84	123.84	132.48			
2.75	1.27	0.92	132.48	139.68	148.32	16.50	1.38	1.21
3.00	1.29	1.15	165.60		165.60			
3.25	1.31	1.20	172.80					
3.50	1.33	1.20	172.80					
3.75	1.35	1.26	181.44	181.44	190.08	23.50	1.96	1.79
4.00	1.38	1.32	190.08					
4.25	1.40	1.32	190.08					
4.50	1.42	1.32	190.08					
4.75	1.44	1.38	198.72					
5.00	1.46	1.38	198.72					
5.25	1.48	1.38	198.72					
5.50	1.50	1.40	201.60					
5.75	1.52	1.43	205.92			26.00	2.17	2.00
6.00	1.54	1.49	214.56			29.00	2.42	2.25
6.25	1.56	1.49	214.56	214.56	230.40			
6.50	1.58	1.60	230.40			30.50	2.54	2.37
6.75	1.60	1.66	239.04					
7.00	1.63	1.66	239.04			30.75	2.56	2.39
7.25	1.65	1.66	239.04	247.68	256.32	32.25	2.69	2.52
7.50	1.67							
7.75	1.69	1.78	256.32					
8.00	1.71	1.78	256.32					
8.25	1.73	1.78	256.32					
8.50	1.75	1.78	256.32					
8.75	1.77	1.80	259.20					
9.00	1.79	1.83	263.52					
9.25	1.81	1.83	263.52					
9.50	1.83	1.89	272.16					
9.75	1.85	1.89	272.16					
10.00	1.88	1.92	276.48					
10.25	1.90	1.92	276.48					
10.50	1.92	1.92	276.48					
10.75	1.94	1.92	276.48					
11.00	1.96	1.95	280.80					
11.25	1.98	2.01	289.44			35	2.92	2.75
11.50	2.00	2.03	292.32					
11.75	2.02	2.06	296.64					
12.00	2.04	3.32	478.08					
12.25	2.06	3.38	486.72		354.24			
12.50	2.08	3.44	495.36					
12.75	2.10	3.44	495.36					
13.00	2.13	3.90	561.60					
13.25	2.15	3.15	453.60	462.24	511.2			
13.50	2.17	3.95	568.80	586.08	652.32			
13.75	2.19	4.58	659.52	685.44	866.88			
14.00	2.21	6.42	924.48					
14.25	2.23	6.47	931.68		1196.64			

Test 2B	2/11/98							
Pile	pile wt. (lbs)	9.6	Surcharge wt	51.4	Water Depth	0.17		
	γ_{water} (pcf)	62.4	γ_{sat} (pcf)	120	nitial Penetratio	1.13		
	Length	Inner dia.	Outer dia.	all thicknes	Chamber height	Chamber dia.		
(inches)	60.00	4.45	4.98	0.23	68.00	23.30		
(feet)	5.00	0.37	0.42	0.02	5.67	1.94		
Penetration		Pressure		Stop	Movement	Water Column Height		Corrected
inches	feet	psi	psf	psf	psf	inches	feet	feet
0.25	1.15							
0.50	1.17							
0.75	1.19							
1.00	1.21							
1.25	1.23							
1.50	1.25							
1.75	1.27				74.88			
2.00	1.29	0.52	74.88		90.72	6.00	0.50	0.33
2.25	1.31	0.75	108.00		123.84			
2.50	1.33	0.86	123.84					
2.75	1.35	0.86	123.84					
3.00	1.38	0.92	132.48			10.50	0.88	0.71
3.25	1.40	0.92	132.48					
3.50	1.42	0.97	139.68	139.68	148.32	13.00	1.08	0.91
3.75	1.44	1.03	148.32					
4.00	1.46	1.09	156.96	156.96	165.60	15.00	1.25	1.08
4.25	1.48	1.15	165.60					
4.50	1.50	1.15	165.60			17.00	1.42	1.25
4.75	1.52	1.26	181.44					
5.00	1.54	1.29	185.76					
5.25	1.56	1.32	190.08					
5.50	1.58	1.32	190.08					
5.75	1.60	1.32	190.08					
6.00	1.63	1.38	198.72					
6.25	1.65	1.38	198.72					
6.50	1.67	1.43	205.92					
6.75	1.69	1.43	205.92	205.92				
7.00	1.71	1.43	205.92					
7.25	1.73	1.49	214.56					
7.50	1.75	1.49	214.56			21.50	1.79	1.62
7.75	1.77	1.55	223.20	223.20		24.00	2.00	1.83
8.00	1.79	1.60	230.40					
8.25	1.81	1.66	239.04					
8.50	1.83	1.66	239.04					
8.75	1.85	1.72	247.68					
9.00	1.88	1.72	247.68					
9.25	1.90	1.72	247.68	256.32		26.00	2.17	2.00
9.50	1.92	1.83	263.52					
9.75	1.94	1.83	263.52					
10.00	1.96	1.83	263.52					
10.25	1.98	1.83	263.52					
10.50	2.00	1.89	272.16					
10.75	2.02	1.89	272.16					
11.00	2.04	1.89	272.16					
11.25	2.06	1.89	272.16					
11.50	2.08	1.95	280.80					
11.75	2.10	1.95	280.80					
12.00	2.13	2.01	289.44					
12.25	2.15	2.01	289.44					
12.50	2.17	2.01	289.44					
12.75	2.19	2.06	296.64					
13.00	2.21	2.06	296.64					
13.25	2.23	2.12	305.28					
13.50	2.25	2.12	305.28			30	2.50	2.33
13.75	2.27	2.18	313.92	321.12		33	2.75	2.58
14.00	2.29	2.23	321.12					

14.25	2.31	2.24	322.56	
14.50	2.33	2.29	329.76	
14.75	2.35	2.29	329.76	
15.00	2.38	2.29	329.76	
15.25	2.40	2.29	329.76	
15.50	2.42	4.97	715.68	
15.75	2.44	6.42	924.48	1113.12

Test 2C	2/11/98							
Pile	pile wt. (lbs)	9.6	Surcharge wt	51.4	Water Depth	0.17		
	γ_{water} (pcf)	62.4	γ_{sat} (pcf)	120	nitial Penetratio	1.00		
	Length	Inner dia.	Outer dia.	Wall thicknes	Chamber height	Chamber dia.		
(inches)	60.00	4.45	4.98	0.23	68.00	23.30		
(feet)	5.00	0.37	0.42	0.02	5.67	1.94		
Penetration		Pressure		Stop	Movement	Water Column Height		Corrected
inches	feet	psi	psf	psf	psf	inches	feet	feet
0.25	1.02	0.40	57.60	66.24	57.60	5.00	0.42	0.25
0.50	1.04	0.51	73.44		73.44	7.50	0.63	0.46
0.75	1.06	0.51	73.44	82.08				
1.00	1.08	0.57	82.08					
1.25	1.10	0.63	90.72	90.72	99.36	9.00	0.75	0.58
1.50	1.13	0.69	99.36	99.36	106.56	11.00	0.92	0.75
1.75	1.15	0.74	106.56					
2.00	1.17	0.74	106.56					
2.25	1.19	0.80	115.20			13.00	1.08	0.91
2.50	1.21	0.80	115.20					
2.75	1.23	0.86	123.84					
3.00	1.25	0.91	131.04					
3.25	1.27	0.91	131.04			16.00	1.33	1.16
3.50	1.29	0.97	139.68	148.32				
3.75	1.31	0.97	139.68					
4.00	1.33	1.03	148.32					
4.25	1.35	1.03	148.32					
4.50	1.38	1.09	156.96					
4.75	1.40	1.09	156.96					
5.00	1.42	1.12	161.28			19.00	1.58	1.41
5.25	1.44	1.14	164.16	172.80	181.44	20.00	1.67	1.50
5.50	1.46	1.26	181.44					
5.75	1.48	1.26	181.44					
6.00	1.50	1.26	181.44					
6.25	1.52	1.29	185.76					
6.50	1.54	1.32	190.08					
6.75	1.56	1.32	190.08			21.50	1.79	1.62
7.00	1.58	1.32	190.08	197.28				
7.25	1.60	1.37	197.28					
7.50	1.63	1.43	205.92					
7.75	1.65	1.43	205.92					
8.00	1.67	1.43	205.92					
8.25	1.69	1.46	210.24			24.00	2.00	1.83
8.50	1.71	1.49	214.56					
8.75	1.73	1.54	221.76					
9.00	1.75	1.54	221.76					
9.25	1.77	1.54	221.76					
9.50	1.79	1.60	230.40					
9.75	1.81	1.60	230.40					
10.00	1.83	1.60	230.40					
10.25	1.85	1.66	239.04					
10.50	1.88	1.66	239.04					
10.75	1.90	1.66	239.04					
11.00	1.92	1.72	247.68					
11.25	1.94	1.72	247.68					
11.50	1.96	1.72	247.68			29	2.42	2.25
11.75	1.98	1.74	250.56	254.88	273.6			
12.00	2.00	1.80	259.20					
12.25	2.02	1.83	263.52					
12.50	2.04	1.83	263.52					
12.75	2.06	1.89	272.16			31	2.58	2.41
13.00	2.08	1.89	272.16	280.8				
13.25	2.10	2.00	288.00					
13.50	2.13	2.00	288.00					

Test 2D	2/13/98							
Pile	pile wt. (lbs)	9.6	Surcharge wt	51.4	Water Depth	0.17		
	γ_{water} (pcf)	62.4	γ_{sat} (pcf)	120	nitial Penetratio	1.13		
	Length	Inner dia.	Outer dia.	Wall thicknes	Chamber height	Chamber dia.		
(inches)	60.00	4.45	4.98	0.23	68.00	23.30		
(feet)	5.00	0.37	0.42	0.02	5.67	1.94		
Penetration		Pressure		Stop	Movement	Water Column Height		Corrected
inches	feet	psi	psf	psf	psf	inches	feet	feet
0.25	1.15	0.69	99.36			9.50	0.79	0.62
0.50	1.17	0.80	115.20					
0.75	1.19	0.86	123.84					
1.00	1.21	0.86	123.84					
1.25	1.23	0.91	131.04			12.50	1.04	0.87
1.50	1.25	0.97	139.68					
1.75	1.27	0.97	139.68					
2.00	1.29	1.03	148.32					
2.25	1.31	1.14	164.16			19.50	1.63	1.46
2.50	1.33	1.26	181.44					
2.75	1.35	1.26	181.44					
3.00	1.38	1.32	190.08					
3.25	1.40	1.37	197.28					
3.50	1.42	1.43	205.92			24.00	2.00	1.83
3.75	1.44	1.54	221.76					
4.00	1.46	1.54	221.76					
4.25	1.48	1.54	221.76					
4.50	1.50	1.60	230.40					
4.75	1.52	1.60	230.40					
5.00	1.54	1.66	239.04					
5.25	1.56	1.66	239.04					
5.50	1.58	1.72	247.68			28.50	2.38	2.21
5.75	1.60	1.77	254.88					
6.00	1.63	1.77	254.88					
6.25	1.65	1.83	263.52					
6.50	1.67	1.89	272.16					
6.75	1.69	1.89	272.16					
7.00	1.71	1.92	276.48					
7.25	1.73	1.95	280.80					
7.50	1.75	1.95	280.80					
7.75	1.77	2.00	288.00					
8.00	1.79	2.00	288.00					
8.25	1.81	2.00	288.00					
8.50	1.83	2.06	296.64					
8.75	1.85	2.06	296.64					
9.00	1.88	2.09	300.96					
9.25	1.90	2.12	305.28			34.00	2.83	2.66
9.50	1.92	2.17	312.48					
9.75	1.94	2.23	321.12					

Test 2E	2/18/98							
Pile	pile wt. (lbs)	9.6	Surcharge wt	51.4	Water Depth	0.17		
	γ_{water} (pcf)	62.4	γ_{sat} (pcf)	120	nitial Penetratio	1.08		
	Length	Inner dia.	Outer dia.	Wall thicknes	Chamber height	Chamber dia.		
(inches)	60.00	4.45	4.98	0.23	68.00	23.30		
(feet)	5.00	0.37	0.42	0.02	5.67	1.94		
Penetration		Pressure		Stop	Movement	Water Column Height		Corrected
inches	feet	psi	psf	psf	psf	inches	feet	feet
0.25	1.10	0.47	67.68			5.00	0.42	0.25
0.50	1.13	0.77	110.88					
0.75	1.15	0.80	115.20			10.00	0.83	0.66
1.00	1.17	0.86	123.84			11.00	0.92	0.75
1.25	1.19	0.95	136.80					
1.50	1.21	0.97	139.68			14.50	1.21	1.04
1.75	1.23	1.07	154.08					
2.00	1.25	1.09	156.96					
2.25	1.27	1.13	162.72					
2.50	1.29	1.23	177.12					
2.75	1.31	1.25	180.00					
3.00	1.33	1.27	182.88					
3.25	1.35	1.29	185.76					
3.50	1.38	1.30	187.20					
3.75	1.40	1.32	190.08					
4.00	1.42	1.35	194.40					
4.25	1.44	1.35	194.40					
4.50	1.46	1.40	201.60					
4.75	1.48	1.43	205.92			22.00	1.83	1.66
5.00	1.50	1.50	216.00					
5.25	1.52	1.56	224.64					
5.50	1.54	1.58	227.52					
5.75	1.56	1.61	231.84					
6.00	1.58	1.62	233.28					
6.25	1.60	1.63	234.72					
6.50	1.63	1.66	239.04					
6.75	1.65	1.68	241.92			26.00	2.17	2.00
7.00	1.67	1.71	246.24					
7.25	1.69	1.82	262.08					
7.50	1.71	1.83	263.52					
7.75	1.73	1.85	266.40					
8.00	1.75	1.88	270.72					
8.25	1.77	1.96	282.24					
8.50	1.79	1.98	285.12					
8.75	1.81	2.01	289.44					
9.00	1.83	2.02	290.88					
9.25	1.85	2.05	295.20					
9.50	1.88	2.06	296.64			30.00	2.50	2.33
9.75	1.90	2.08	299.52					
10.00	1.92	2.10	302.40					
10.25	1.94	2.14	308.16			33.00	2.75	2.58
10.50	1.96	2.16	311.04					

Test 2F	3/3/98							
Pile	pile wt. (lbs)	9.6	Surcharge wt	51.4	Water Depth	0.17		
	γ_{water} (pcf)	62.4	γ_{sat} (pcf)	120	nitial Penetratio	1.02		
	Length	Inner dia.	Outer dia.	Wall thicknes	Chamber height	Chamber dia.		
(inches)	60.00	4.45	4.98	0.23	68.00	23.30		
(feet)	5.00	0.37	0.42	0.02	5.67	1.94		
Penetration		Pressure		Stop	Movement	Water Column Height		Corrected
inches	feet	psi	psf	psf	psf	inches	feet	feet
0.25	1.04							
0.50	1.06							
0.75	1.08	0.68	97.92					
1.00	1.10	0.65	93.60			5.00	0.42	0.25
1.25	1.13	0.77	110.88					
1.50	1.15	0.80	115.20					
1.75	1.17	0.83	119.52					
2.00	1.19	0.85	122.40			8.00	0.67	0.50
2.25	1.21	0.87	125.28					
2.50	1.23	0.94	135.36					
2.75	1.25	0.97	139.68					
3.00	1.27	0.98	141.12			10.50	0.88	0.71
3.25	1.29	1.01	145.44			10.50	0.88	0.71
3.50	1.31	1.02	146.88					
3.75	1.33	1.03	148.32					
4.00	1.35	1.12	161.28			12.00	1.00	0.83
4.25	1.38	1.14	164.16					
4.50	1.40	1.21	174.24					
4.75	1.42	1.23	177.12			14.00	1.17	1.00
5.00	1.44	1.26	181.44					
5.25	1.46	1.26	181.44					
5.50	1.48	1.37	197.28					
5.75	1.50	1.40	201.60			18.00	1.50	1.33
6.00	1.52	1.43	205.92					
6.25	1.54	1.47	211.68					
6.50	1.56	1.49	214.56					
6.75	1.58	1.51	217.44			20.00	1.67	1.50
7.00	1.60	1.54	221.76					
7.25	1.63	1.57	226.08					
7.50	1.65	1.60	230.40					
7.75	1.67	1.60	230.40					
8.00	1.69	1.66	239.04			22.00	1.83	1.66
8.25	1.71	1.69	243.36					
8.50	1.73	1.71	246.24			23.00	1.92	1.75
8.75	1.75	1.77	254.88			24.00	2.00	1.83
9.00	1.77	1.79	257.76					
9.25	1.79	1.80	259.20					
9.50	1.81	1.81	260.64					
9.75	1.83	1.83	263.52					
10.00	1.85	1.86	267.84					
10.25	1.88	1.87	269.28					
10.50	1.90	1.90	273.60			26	2.17	2.00
10.75	1.92	1.93	277.92					
11.00	1.94	1.99	286.56			28	2.33	2.16
11.25	1.96	1.99	286.56					
11.50	1.98	2.00	288.00					
11.75	2.00	2.02	290.88					
12.00	2.02	2.06	296.64					
12.25	2.04	2.07	298.08					

Test 3A	3/3/98							
Pile	pile wt. (lbs)	9.6	Surcharge wt	63.6	Water Depth	0.17		
	γ_{water} (pcf)	62.4	γ_{sat} (pcf)	120	nitial Penetratio	1.23		
	Length	Inner dia.	Outer dia.	Wall thicknes	Chamber height	Chamber dia.		
(inches)	60.00	4.45	4.98	0.23	68.00	23.30		
(feet)	5.00	0.37	0.42	0.02	5.67	1.94		
Penetration		Pressure		Stop	Movement	Water Column Height		Corrected
inches	feet	psi	psf	psf	psf	inches	feet	feet
0.25	1.25	0.76	109.44			9.00	0.75	0.58
0.50	1.27	0.80	115.20			10.00	0.83	0.66
0.75	1.29	0.86	123.84					
1.00	1.31	0.90	129.60					
1.25	1.33	0.98	141.12					
1.50	1.35	0.99	142.56					
1.75	1.38	1.02	146.88					
2.00	1.40	1.03	148.32					
2.25	1.42	1.05	151.20					
2.50	1.44	1.06	152.64					
2.75	1.46	1.08	155.52					
3.00	1.48	1.10	158.40			15.00	1.25	1.08
3.25	1.50	1.11	159.84					
3.50	1.52	1.15	165.60					
3.75	1.54	1.21	174.24			18.00	1.50	1.33
4.00	1.56	1.29	185.76					
4.25	1.58	1.29	185.76					
4.50	1.60	1.31	188.64					
4.75	1.63	1.33	191.52			18.00	1.50	1.33
5.00	1.65	1.36	195.84					
5.25	1.67	1.41	203.04					
5.50	1.69	1.43	205.92					
5.75	1.71	1.48	213.12					
6.00	1.73	1.51	217.44			23.00	1.92	1.75
6.25	1.75	1.53	220.32					
6.50	1.77	1.62	233.28					
6.75	1.79	1.64	236.16					
7.00	1.81	1.68	241.92			26.00	2.17	2.00
7.25	1.83	1.71	246.24			26.00	2.17	2.00
7.50	1.85	1.73	249.12					
7.75	1.88	1.76	253.44					
8.00	1.90	1.78	256.32			27.50	2.29	2.12
8.25	1.92	1.81	260.64					
8.50	1.94	1.84	264.96					
8.75	1.96	1.85	266.40					
9.00	1.98	1.88	270.72					
9.25	2.00	1.89	272.16					
9.50	2.02	1.91	275.04					
9.75	2.04	1.94	279.36					
10.00	2.06	1.96	282.24					
10.25	2.08	1.99	286.56					
10.50	2.10	1.99	286.56					
10.75	2.13	2.02	290.88					
11.00	2.15	2.04	293.76			31	2.58	2.41
11.25	2.17	2.07	298.08					

Test 3B	3/3/98							
Pile	pile wt. (lbs)	9.6	Surcharge wt	63.6	Water Depth	0.17		
	γ_{water} (pcf)	62.4	γ_{sat} (pcf)	120	nitial Penetratio	1.13		
	Length	Inner dia.	Outer dia.	Wall thicknes	Chamber height	Chamber dia.		
(inches)	60.00	4.45	4.98	0.23	68.00	23.30		
(feet)	5.00	0.37	0.42	0.02	5.67	1.94		
Penetration		Pressure		Stop	Movement	Water Column Height		Corrected
inches	feet	psi	psf	psf	psf	inches	feet	feet
0.25	1.15	0.35	50.40			4.50	0.38	0.21
0.50	1.17	0.35	50.40					
0.75	1.19	0.45	64.80			6.00	0.50	0.33
1.00	1.21	0.48	69.12					
1.25	1.23	0.53	76.32					
1.50	1.25	0.53	76.32					
1.75	1.27	0.57	82.08			8.00	0.67	0.50
2.00	1.29	0.57	82.08					
2.25	1.31	0.64	92.16					
2.50	1.33	0.64	92.16					
2.75	1.35	0.70	100.80					
3.00	1.38	0.75	108.00					
3.25	1.40	0.80	115.20					
3.50	1.42	0.84	120.96					
3.75	1.44	0.88	126.72			12.00	1.00	0.83
4.00	1.46	0.90	129.60					
4.25	1.48	0.98	141.12					
4.50	1.50	1.01	145.44					
4.75	1.52	1.03	148.32					
5.00	1.54	1.06	152.64					
5.25	1.56	1.07	154.08					
5.50	1.58	1.10	158.40					
5.75	1.60	1.10	158.40			16.00	1.33	1.16
6.00	1.63	1.18	169.92					
6.25	1.65	1.20	172.80			18.00	1.50	1.33
6.50	1.67	1.26	181.44					
6.75	1.69	1.27	182.88					
7.00	1.71	1.29	185.76					
7.25	1.73	1.33	191.52			20.00	1.67	1.50
7.50	1.75	1.37	197.28					
7.75	1.77	1.41	203.04					
8.00	1.79	1.43	205.92			22.00	1.83	1.66
8.25	1.81	1.46	210.24					
8.50	1.83	1.47	211.68					
8.75	1.85	1.50	216.00			23.00	1.92	1.75
9.00	1.88	1.54	221.76					
9.25	1.90	1.56	224.64					
9.50	1.92	1.59	228.96			25.00	2.08	1.91
9.75	1.94	1.60	230.40					
10.00	1.96	1.63	234.72					
10.25	1.98	1.64	236.16					
10.50	2.00	1.67	240.48					
10.75	2.02	1.67	240.48					
11.00	2.04	1.72	247.68					
11.25	2.06	1.73	249.12			26.50	2.21	2.04
11.50	2.08	1.74	250.56			27.00	2.25	2.08
11.75	2.10	1.77	254.88					
12.00	2.13	1.80	259.20					
12.25	2.15	1.83	263.52			28.00	2.33	2.16
12.50	2.17	1.86	267.84					
12.75	2.19	1.89	272.16					
13.00	2.21	1.89	272.16					
13.25	2.23	1.89	272.16					
13.50	2.25	1.89	272.16					
13.75	2.27	1.93	277.92					
14.00	2.29	1.96	282.24					
14.25	2.31	1.96	282.24					
14.50	2.33	1.96	282.24					
14.75	2.35	1.99	286.56					
15.00	2.38	2.00	288.00					
15.25	2.40	2.02	290.88					

Test 3C	3/3/98							
3C								
Pile	pile wt. (lbs)	9.6	Surcharge wt	63.6	Water Depth	0.17		
	γ_{water} (pcf)	62.4	γ_{sat} (pcf)	120	nitial Penetratio	1.08		
	Length	Inner dia.	Outer dia.	Wall thicknes	Chamber height	Chamber dia.		
(inches)	60.00	4.45	4.98	0.23	68.00	23.30		
(feet)	5.00	0.37	0.42	0.02	5.67	1.94		
Penetration		Pressure		Stop	Movement	Water Column Height		Corrected
inches	feet	psi	psf	psf	psf	inches	feet	feet
0.25	1.10	0.52	74.88					
0.50	1.13	0.56	80.64					
0.75	1.15	0.60	86.40					
1.00	1.17	0.61	87.84			6.50	0.54	0.37
1.25	1.19	0.67	96.48					
1.50	1.21	0.67	96.48					
1.75	1.23	0.67	96.48					
2.00	1.25	0.73	105.12			7.50	0.63	0.46
2.25	1.27	0.76	109.44					
2.50	1.29	0.78	112.32					
2.75	1.31	0.83	119.52					
3.00	1.33	0.86	123.84					
3.25	1.35	0.87	125.28			10.50	0.88	0.71
3.50	1.38	0.91	131.04					
3.75	1.40	0.97	139.68			12.00	1.00	0.83
4.00	1.42	1.00	144.00					
4.25	1.44	1.03	148.32					
4.50	1.46	1.04	149.76					
4.75	1.48	1.09	156.96					
5.00	1.50	1.10	158.40			14.00	1.17	1.00
5.25	1.52	1.13	162.72					
5.50	1.54	1.14	164.16					
5.75	1.56	1.17	168.48					
6.00	1.58	1.21	174.24					
6.25	1.60	1.23	177.12					
6.50	1.63	1.27	182.88					
6.75	1.65	1.27	182.88					
7.00	1.67	1.27	182.88					
7.25	1.69	1.29	185.76					
7.50	1.71	1.32	190.08					
7.75	1.73	1.33	191.52					
8.00	1.75	1.34	192.96					
8.25	1.77	1.37	197.28					
8.50	1.79	1.40	201.60					
8.75	1.81	1.41	203.04					
9.00	1.83	1.43	205.92					
9.25	1.85	1.47	211.68			19.00	1.58	1.41
9.50	1.88	1.47	211.68					
9.75	1.90	1.49	214.56					
10.00	1.92	1.52	218.88					
10.25	1.94	1.53	220.32					
10.50	1.96	1.56	224.64			21.00	1.75	1.58
10.75	1.98	1.60	230.40					
11.00	2.00	1.60	230.40					
11.25	2.02	1.62	233.28					
11.50	2.04	1.64	236.16					
11.75	2.06	1.66	239.04					
12.00	2.08	1.69	243.36					
12.25	2.10	1.70	244.80					
12.50	2.13	1.73	249.12			24.00	2.00	1.83
12.75	2.15	1.75	252.00					
13.00	2.17	1.76	253.44					
13.25	2.19	1.79	257.76					
13.50	2.21	1.80	259.20			25.00	2.08	1.91
13.75	2.23	1.83	263.52					
14.00	2.25	1.85	266.40					
14.25	2.27	1.87	269.28			26.00	2.17	2.00
14.50	2.29	1.9	273.60					
14.75	2.31	1.95	280.80					
15.00	2.33	1.95	280.80					
15.25	2.35	1.95	280.80					
15.50	2.38	1.97	283.68					

15.75	2.40	2.00	288.00					
16.00	2.42	2.02	290.88					
16.25	2.44	2.05	295.20					
16.50	2.46	2.06	296.64					
16.75	2.48	2.07	298.08					
17.00	2.50	2.09	300.96			29.00	2.42	2.25
17.25	2.52	2.10	302.40					

Test 3D	3/3/98							
Pile	pile wt. (lbs)	9.6	Surcharge wt	63.6	Water Depth	0.17		
	γ_{water} (pcf)	62.4	γ_{sat} (pcf)	120	nitial Penetratio	1.08		
	Length	Inner dia.	Outer dia.	Wall thicknes	Chamber height	Chamber dia.		
(inches)	60.00	4.45	4.98	0.23	68.00	23.30		
(feet)	5.00	0.37	0.42	0.02	5.67	1.94		
Penetration		Pressure		Stop	Movement	Water Column Height		Corrected
inches	feet	psi	psf	psf	psf	inches	feet	feet
0.25	1.10	0.46	66.24					
0.50	1.13	0.46	66.24					
0.75	1.15	0.48	69.12					
1.00	1.17	0.49	70.56			4.00	0.33	0.16
1.25	1.19	0.51	73.44					
1.50	1.21	0.56	80.64			5.00	0.42	0.25
1.75	1.23	0.62	89.28					
2.00	1.25	0.63	90.72			6.00	0.50	0.33
2.25	1.27	0.66	95.04					
2.50	1.29	0.69	99.36			7.50	0.63	0.46
2.75	1.31	0.73	105.12					
3.00	1.33	0.76	109.44			9.00	0.75	0.58
3.25	1.35	0.81	116.64			11.00	0.92	0.75
3.50	1.38	0.84	120.96					
3.75	1.40	0.88	126.72					
4.00	1.42	0.94	135.36			12.50	1.04	0.87
4.25	1.44	0.95	136.80					
4.50	1.46	1.00	144.00					
4.75	1.48	1.02	146.88					
5.00	1.50	1.04	149.76					
5.25	1.52	1.06	152.64			14.00	1.17	1.00
5.50	1.54	1.09	156.96					
5.75	1.56	1.14	164.16					
6.00	1.58	1.15	165.60					
6.25	1.60	1.18	169.92			15.00	1.25	1.08
6.50	1.63	1.22	175.68					
6.75	1.65	1.25	180.00					
7.00	1.67	1.28	184.32					
7.25	1.69	1.31	188.64			17.50	1.46	1.29
7.50	1.71	1.35	194.40					
7.75	1.73	1.42	204.48					
8.00	1.75	1.48	213.12					
8.25	1.77	1.49	214.56					
8.50	1.79	1.51	217.44			23.00	1.92	1.75
8.75	1.81	1.57	226.08					
9.00	1.83	1.57	226.08					
9.25	1.85	1.61	231.84			24.00	2.00	1.83
9.50	1.88	1.64	236.16					
9.75	1.90	1.65	237.60					
10.00	1.92	1.67	240.48					
10.25	1.94	1.68	241.92					
10.50	1.96	1.71	246.24					
10.75	1.98	1.72	247.68					
11.00	2.00	1.74	250.56					
11.25	2.02	1.78	256.32					
11.50	2.04	1.80	259.20					
11.75	2.06	1.82	262.08					
12.00	2.08	1.85	266.40					
12.25	2.10	1.87	269.28					
12.50	2.13	1.88	270.72					
12.75	2.15	1.91	275.04					
13.00	2.17	1.94	279.36			29.00	2.42	2.25
13.25	2.19	1.97	283.68					
13.50	2.21	2.02	290.88					
13.75	2.23	2.04	293.76					
14.00	2.25	2.07	298.08					
14.25	2.27	2.08	299.52					
14.50	2.29	2.10	302.40					

APPENDIX – C CALIBRATION OF MOBILIZED SOIL EFFECTIVE FRICTION ANGLE RATIO

1D ile pen	Pressure inside pile	Total Head at utside surfac	Total Head at inside surfac	alpha	Avg. Total Head gradient
1.128	-123.84	0.1700	-1.6950	0.9370	0.8270
1.206	-139.68	0.1700	-1.7780	0.9200	0.8080
1.265	-165.6	0.1700	-2.0340	0.9090	0.8710
1.284	-172.8	0.1700	-1.9390	0.9090	0.8210
1.401	-205.92	0.1700	-2.3700	0.8730	0.9060
1.655	-230.4	0.1700	-2.3620	0.8250	0.7650
1.675	-230.4	0.1700	-2.2120	0.8250	0.7110

1C ile pen	Pressure inside pile	Total Head at utside surfac	Total Head at inside surfac	alpha	Avg. Total Head gradient
1.128	-156.96	0.1700	-1.9350	0.9450	0.9330
1.316	-205.92	0.1700	-1.7500	0.9420	0.7290
1.538	-280.80	0.1700	-2.5000	0.8800	0.8680
1.785	-387.36	0.1700	-4.1480	0.7950	1.2100

1E ile pen	Pressure inside pile	Total Head at utside surfac	Total Head at inside surfac	alpha	Avg. Total Head gradient
1.108	-156.96	0.1700	-1.9150	0.9510	0.9410
1.441	-223.20	0.1700	-2.3070	0.8780	0.8600
1.628	-263.52	0.1700	-2.5430	0.8410	0.8330
1.655	-272.16	0.1700	-2.5320	0.8400	0.8160
1.929	-313.92	0.1700	-2.8710	0.7788	0.7880

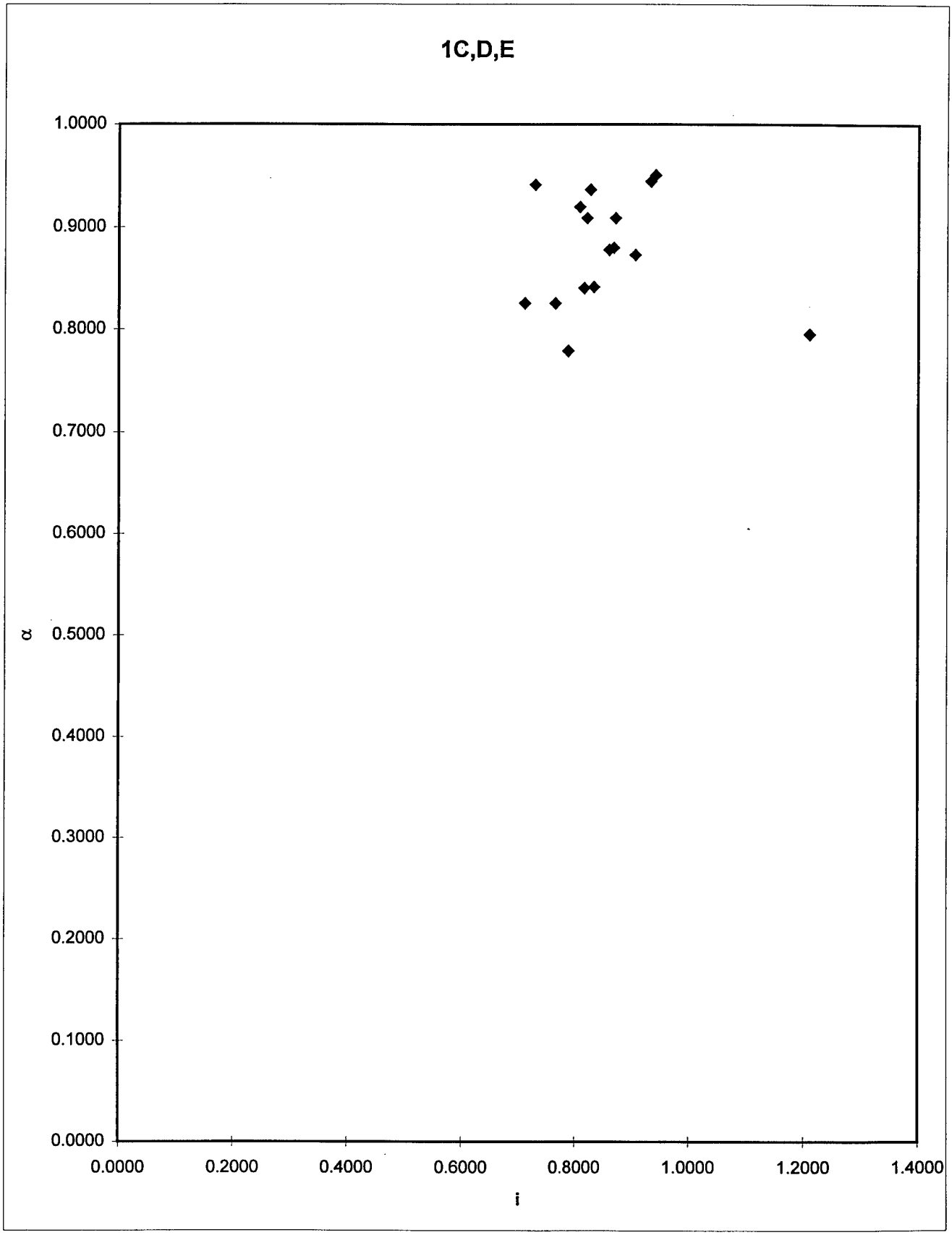
1C,D,E
1.0000
0.9000
0.8000
0.7000
0.6000
0.5000
0.4000
0.3000
0.2000
0.1000
0.0000
α
0.0000
0.2000
0.4000
0.6000
0.8000
1.0000
1.2000
1.4000
i

1D

Pile pen.	Pressure inside pile	Total Head at outside surface	Total Head at inside surface	alpha	Avg. Total Head gradient	
1.128	-123.84	0.1700	-1.6950	0.9370	0.8270	0.826684397
1.206	-139.68	0.1700	-1.7780	0.9200	0.8080	0.807628524
1.265	-165.6	0.1700	-2.0340	0.9090	0.8710	0.871146245
1.284	-172.8	0.1700	-1.9390	0.9090	0.8210	0.821261682
1.401	-205.92	0.1700	-2.3700	0.8730	0.9060	0.90649536
1.655	-230.4	0.1700	-2.3620	0.8250	0.7650	0.764954683
1.675	-230.4	0.1700	-2.2120	0.8250	0.7110	0.711044776

1C

Pile pen.	Pressure inside pile	Total Head at outside surface	Total Head at inside surface	alpha	Avg. Total Head gradient	
1.128	-156.96	0.1700	-1.9350	0.9450	0.9330	0.933067376
1.316	-205.92	0.1700	-1.7500	0.9420	0.7290	0.729483283
1.538	-280.80	0.1700	-2.5000	0.8800	0.8680	0.868010403
1.785	-387.36	0.1700	-4.1480	0.7950	1.2100	1.20952381

1E

Pile pen.	Pressure inside pile	Total Head at outside surface	Total Head at inside surface	alpha	Avg. Total Head gradient	
1.108	-156.96	0.1700	-1.9150	0.9510	0.9410	0.940884477
1.441	-223.20	0.1700	-2.3070	0.8780	0.8600	0.859472588
1.628	-263.52	0.1700	-2.5430	0.8410	0.8330	0.833230958
1.655	-272.16	0.1700	-2.5320	0.8400	0.8160	0.816314199
1.929	-313.92	0.1700	-2.8710	0.7788	0.7880	0.788232245

	2A		Total Head at	Total Head at		Avg. Total	
	Pile pen.	Pressure inside pil	utside surfac	inside surfac	alpha	Head gradient	
	1.128	-82.08	0.1700	-1.0550	1.0350	0.5430	0.542996454
	1.167	-99.36	0.1700	-1.0520	1.0310	0.5240	0.523564696
	1.265	-139.68	0.1700	-0.9660	1.0420	0.4490	0.449011858
	1.355	-181.44	0.1700	-1.1180	1.0205	0.4750	0.475276753
	1.558	-214.56	0.1700	-1.0680	0.9700	0.3980	0.397304236
	1.655	-247.68	0.1700	-1.4490	0.9485	0.4890	0.489123867
	2B		Total Head at	Total Head at		Avg. Total	
	Pile pen.	Pressure inside pil	utside surfac	inside surfac	alpha	Head gradient	
	1.42	-139.68	0.1700	-1.3280	0.9600	0.5270	0.527093596
	1.46	-156.96	0.1700	-1.4350	0.9500	0.5500	0.549657534
	1.77	-223.20	0.1700	-1.7470	0.8800	0.5410	0.540609137
	1.90	-256.32	0.1700	-2.1080	0.8500	0.5990	0.598843323
	2C		Total Head at	Total Head at		Avg. Total	
	Pile pen.	Pressure inside pil	utside surfac	inside surfac	alpha	Head gradient	
1.02	1.03	-66.24	0.1700	-0.7470	1.0844	0.4450	0.445145631
1.06	1.07	-82.08	0.1700	-0.8550	1.0105	0.4790	0.479420019
1.1	1.11	-90.72	0.1700	-0.8740	1.0600	0.4710	0.471119134
1.13	1.13	-99.36	0.1700	-0.8420	1.0600	0.4490	0.44858156
1.29	1.304	-148.32	0.1700	-1.2170	1.0100	0.5320	0.531825153
1.44	1.441	-172.80	0.1700	-1.2690	0.9750	0.5000	0.499306037
1.58	1.577	-197.28	0.1700	-1.5420	0.9350	0.5430	0.54280279
1.98	1.98	-254.88	0.1700	-1.8350	0.8300	0.5060	0.506313131
2.08	2.085	-280.80	0.1700	-2.0900	0.8100	0.5420	0.541966427
	2D		Total Head at	Total Head at		Avg. Total	
	Pile pen.	Pressure inside pil	utside surfac	inside surfac	alpha	Head gradient	
1.15	1.15	-115.20	0.1700	-1.2260	1.0400	0.6080	0.608013937
1.23	1.23	-139.68	0.1700	-1.3680	1.0200	0.6280	0.627243067
1.31	1.30	-181.44	0.1700	-1.4480	1.0200	0.6200	0.620398773
1.42	1.42	-221.76	0.1700	-1.7240	0.9950	0.6660	0.66643209
1.58	1.58	-254.88	0.1700	-1.8750	0.9600	0.6480	0.648383006
1.9	1.90	-312.48	0.1700	-2.3480	0.8800	0.6620	0.661934805
	2E		Total Head at	Total Head at		Avg. Total	
	Pile pen.	Pressure inside pil	utside surfac	inside surfac	alpha	Head gradient	
1.1	1.11	-110.88	0.1700	-1.3570	1.0400	0.6890	0.689079422
1.15	1.15	-123.84	0.1700	-1.1550	1.0500	0.5770	0.577090592
1.17	1.17	-136.80	0.1700	-1.2720	1.0450	0.6180	0.617823479
1.21	1.21	-154.08	0.1700	-1.2590	1.0430	0.5920	0.592454395
1.48	1.48	-216.00	0.1700	-1.6320	0.9750	0.6090	0.608783784
1.65	1.66	-246.20	0.1700	-1.7760	0.9300	0.5880	0.587915408
1.88	1.89	-299.52	0.1700	-2.3000	0.8805	0.6540	0.653439153
1.94	1.94	-311.04	0.1700	-2.2350	0.8700	0.6190	0.619526018
	2F		Total Head at	Total Head at		Avg. Total	
	Pile pen.	Pressure inside pil	utside surfac	inside surfac	alpha	Head gradient	
1.1	1.11	-110.88	0.1700	-1.5720	1.0310	0.7650	0.786101083
1.19	1.19	-125.28	0.1700	-1.5080	1.0140	0.7070	0.706823926
1.27	1.27	-145.44	0.1700	-1.6210	1.0000	0.7080	0.707905138
1.29	1.28	-146.88	0.1700	-1.6440	0.9895	0.7060	0.706386293
1.35	1.36	-164.16	0.1700	-1.8010	0.9700	0.7270	0.727306273
1.42	1.42	-181.44	0.1700	-1.9080	0.9550	0.7310	0.731175229
1.5	1.50	-205.92	0.1700	-1.9700	0.9450	0.7140	0.713809206
1.58	1.58	-221.76	0.1700	-2.0540	0.9300	0.7050	0.705136335
1.69	1.69	-243.36	0.1700	-2.2400	0.9000	0.7110	0.71133412
1.73	1.73	-254.88	0.1700	-2.3350	0.8950	0.7220	0.722735141
1.75	1.75	-257.76	0.1700	-2.3010	0.8900	0.7050	0.704791786
1.9	1.90	-277.92	0.1700	-2.4540	0.8550	0.6900	0.68980021
1.94	1.94	-286.56	0.1700	-2.4320	0.8500	0.6700	0.670273055

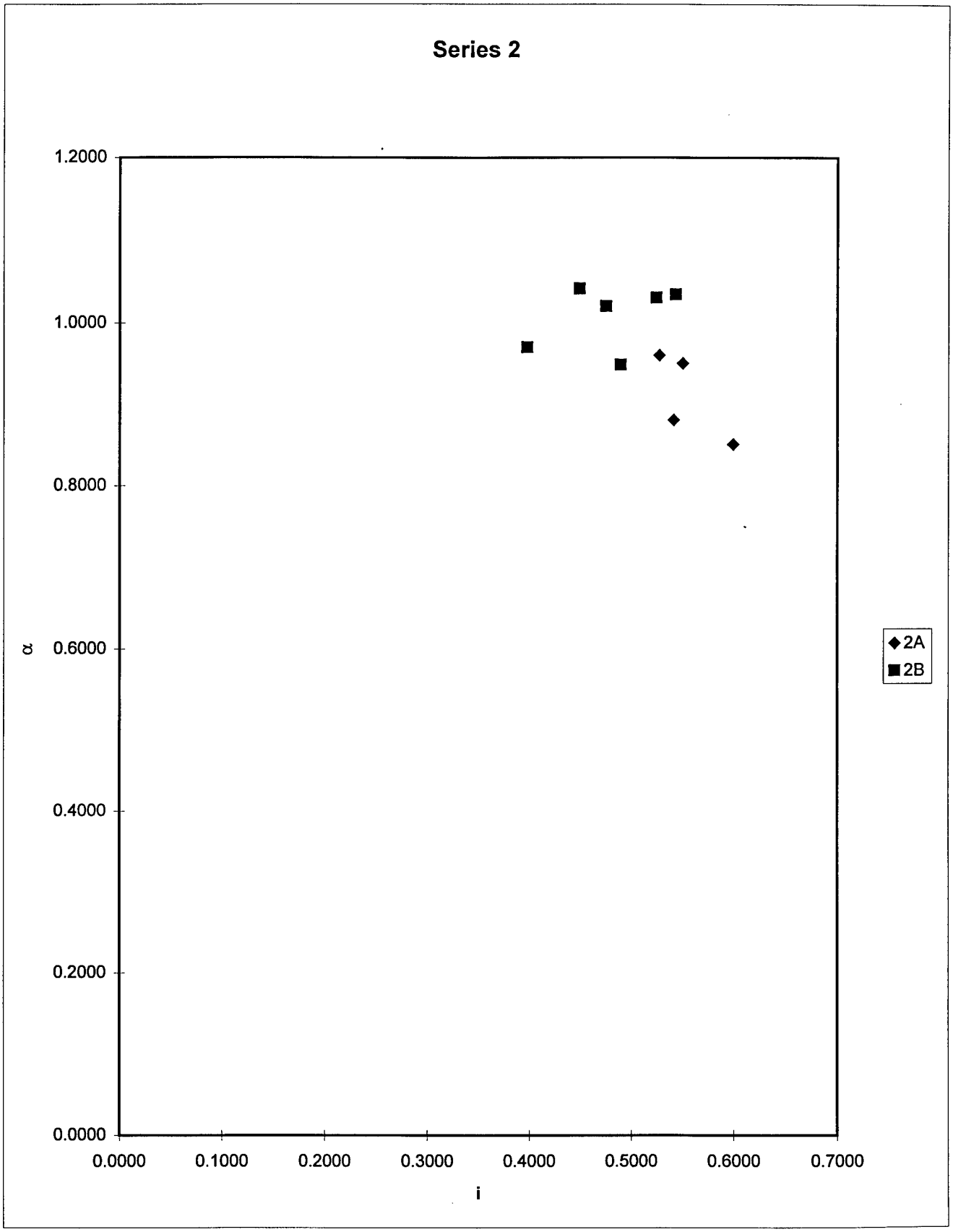
Series 2
1.2000
1.0000
0.8000
0.6000
0.4000
0.2000
0.0000
α
0.0000
0.1000
0.2000
0.3000
0.4000
0.5000
0.6000
0.7000
i
2A
2B

	3A		Total Head at	Total Head at		Avg. Total	
	Pile pen.	Pressure inside pil	utside surfac	inside surfac	alpha	Head gradient	
1.25	1.25	-115.20	0.1700	-1.2140	1.0850	0.5560	0.555823293
1.27	1.27	-123.84	0.1700	-1.2690	1.0800	0.5690	0.568774704
1.48	1.48	-159.84	0.1700	-1.4100	1.0250	0.5340	0.533783784
1.54	1.54	-185.76	0.1700	-1.6470	1.0000	0.5910	0.590702211
1.63	1.63	-195.84	0.1700	-1.8080	0.9730	0.6070	0.607493857
1.73	1.73	-220.32	0.1700	-1.7810	0.9550	0.5630	0.562896711
1.81	1.81	-246.24	0.1700	-1.9460	0.9400	0.5840	0.58388521
1.83	1.83	-249.12	0.1700	-1.9920	0.9350	0.5900	0.590387766
1.9	1.90	-260.64	0.1700	-2.0570	0.9200	0.5850	0.585436383
2.15	2.16	-298.08	0.1700	-2.3670	0.8585	0.5860	0.586453999
	3B		Total Head at	Total Head at		Avg. Total	
	Pile pen.	Pressure inside pil	utside surfac	inside surfac	alpha	Head gradient	
1.15	1.15	-50.40	0.1700	-0.5980	1.1100	0.3340	0.334494774
1.19	1.19	-69.12	0.1700	-0.7780	1.1000	0.3990	0.399326032
1.27	1.27	-82.08	0.1700	-1.0660	1.0100	0.4890	0.488537549
1.44	1.43	-129.60	0.1700	-1.2470	1.0200	0.4940	0.494417306
1.6	1.60	-169.92	0.1700	-1.5630	0.9750	0.5430	0.542579837
1.65	1.66	-181.44	0.1700	-1.5780	0.9650	0.5280	0.528096677
1.73	1.73	-197.28	0.1700	-1.6620	0.9450	0.5280	0.528563185
1.79	1.79	-210.24	0.1700	-1.7090	0.9350	0.5260	0.526330532
1.85	1.85	-221.76	0.1700	-1.8040	0.9200	0.5330	0.533225284
1.92	1.93	-230.40	0.1700	-1.7820	0.9035	0.5060	0.505961638
2.06	2.07	-250.56	0.1700	-1.9250	0.8650	0.5070	0.507263923
2.08	2.09	-254.88	0.1700	-2.0050	0.8600	0.5210	0.521582734
2.15	2.16	-267.84	0.1700	-2.1340	0.8450	0.5330	0.53259362
	3C		Total Head at	Total Head at		Avg. Total	
	Pile pen.	Pressure inside pil	utside surfac	inside surfac	alpha	Head gradient	
1.17	1.17	-96.48	0.1700	-1.1760	1.0930	0.5770	0.576692374
1.25	1.25	-109.44	0.1700	-1.2940	1.0680	0.5880	0.587951807
1.35	1.36	-131.04	0.1700	-1.3900	1.0400	0.5760	0.575645756
1.4	1.40	-144.00	0.1700	-1.4780	1.0280	0.5880	0.58815132
1.5	1.50	-162.72	0.1700	-1.6080	1.0000	0.5930	0.593062041
1.85	1.85	-211.68	0.1700	-1.9820	0.9100	0.5820	0.581307401
1.96	1.97	-230.40	0.1700	-2.1120	0.8840	0.5800	0.579776423
2.13	2.14	-252.00	0.1700	-2.2080	0.8405	0.5570	0.55664794
2.21	2.21	-263.52	0.1700	-2.3130	0.8200	0.5610	0.560749774
2.27	2.28	-273.60	0.1700	-2.3850	0.8086	0.5600	0.560307018
2.5	2.50	-302.40	0.1700	-2.5960	0.7530	0.5540	0.554308617
	3D		Total Head at	Total Head at		Avg. Total	
	Pile pen.	Pressure inside pil	utside surfac	inside surfac	alpha	Head gradient	
1.17	1.17	-73.44	0.1700	-1.0170	1.0900	0.5090	0.50856898
1.21	1.21	-89.28	0.1700	-1.1810	1.0750	0.5600	0.560116086
1.25	1.25	-95.04	0.1700	-1.1930	1.0640	0.5470	0.547389558
1.29	1.28	-105.12	0.1700	-1.2250	1.0539	0.5430	0.543224299
1.33	1.32	-116.64	0.1700	-1.2890	1.0450	0.5510	0.551398337
1.35	1.36	-120.96	0.1700	-1.1880	1.0450	0.5010	0.501107011
1.42	1.42	-136.80	0.1700	-1.3220	1.0250	0.5250	0.524982407
1.52	1.52	-156.96	0.1700	-1.5150	0.9950	0.5550	0.554641211
1.6	1.60	-175.68	0.1700	-1.7350	0.9730	0.5970	0.596430808
1.69	1.69	-194.40	0.1700	-1.8250	0.9500	0.5890	0.588842975
1.79	1.79	-226.08	0.1700	-1.8730	0.9400	0.5720	0.572268908
1.85	1.85	-236.16	0.1700	-1.9550	0.9250	0.5740	0.574014046
2.17	2.18	-283.68	0.1700	-2.2960	0.8450	0.5670	0.566896552

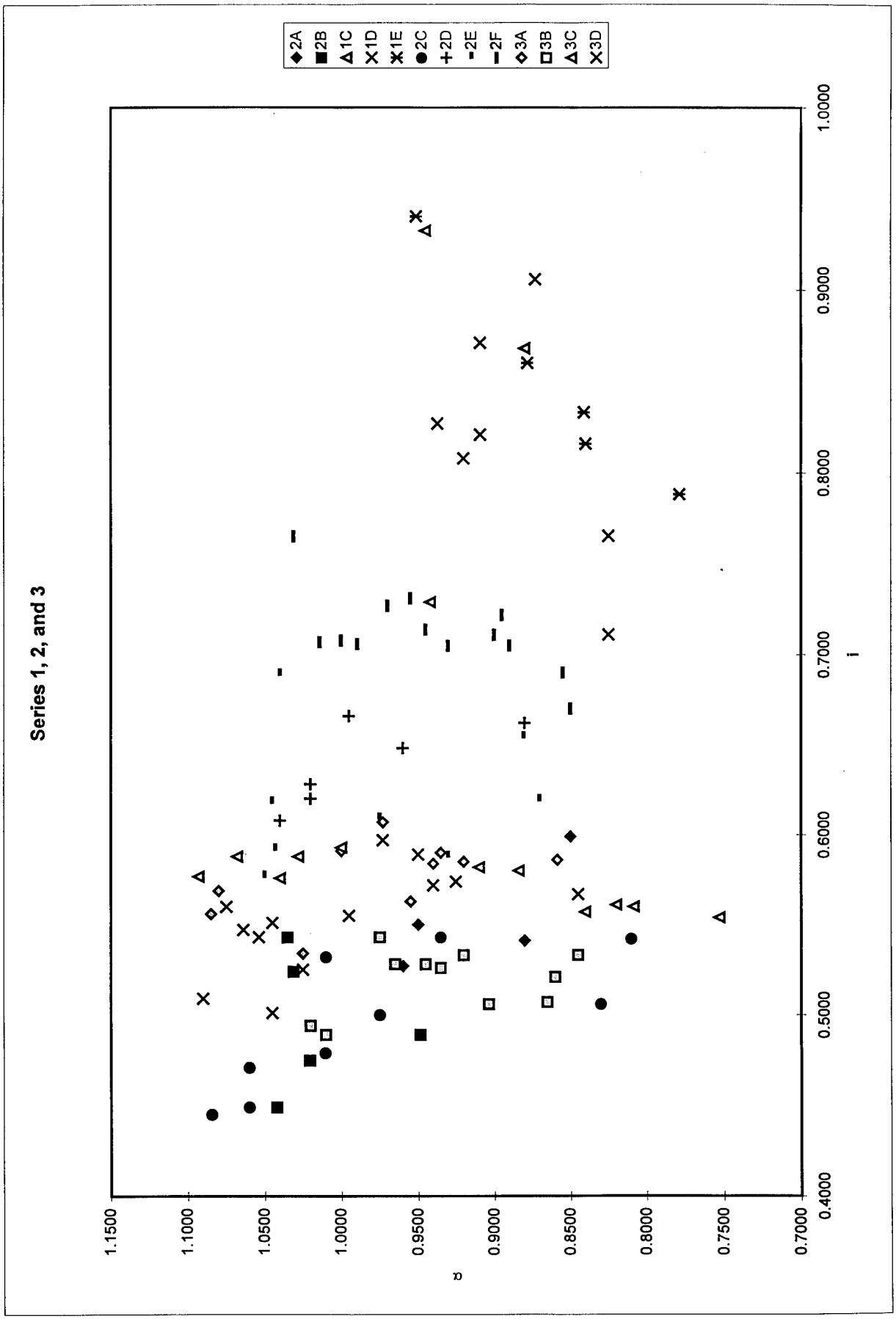

Sheet2 Chart 3

APPENDIX – D VERIFICATION OF CENTRIFUGE MODEL TEST ON CABLE MOORING LINE

VERIFICATION OF CENTRIFUGE MODEL TEST ON CABLE MOORING LINE

1. INTRODUCTION

The U.S. Naval Facilities Engineering Service Center (NFESC) conducted a series of centrifuge model tests (1) on buried mooring lines in order to validate the analytical model developed by Bang (2). Included in the tests were two series, each with three model mooring chains and one model mooring cable. The results of the centrifuge model tests on mooring chains were compared successfully with the analytical predictions previously (3). The results on mooring cables however did not compare well with the initial analytical predictions and therefore the validation procedure was incomplete. The purpose of this study is to reexamine the centrifuge test results on mooring cables and provide validation with the analytical model.

2. REVIEW OF TEST RESULTS

During the centrifuge model tests, a set of four chasing wires were attached to the mooring chains and cables. Figure - 1 shows the schematic sketch of the layout of the mooring line and chasing wires. The chasing wires were used to locate the exact geometries of the mooring chains and cables during transition from the initial to the final position due to the applied load. The effects of the chasing wires were found to be relatively insignificant to the behavior of mooring chains, since the chain diameter was much larger than that of the chasing wire. However, the effect of the chasing wires on the mooring cable might not have been negligible due to the thin nature of the mooring cable. The effects of the chasing wires therefore need to be studied in detail before any correct validation of the analytical solution can be achieved.

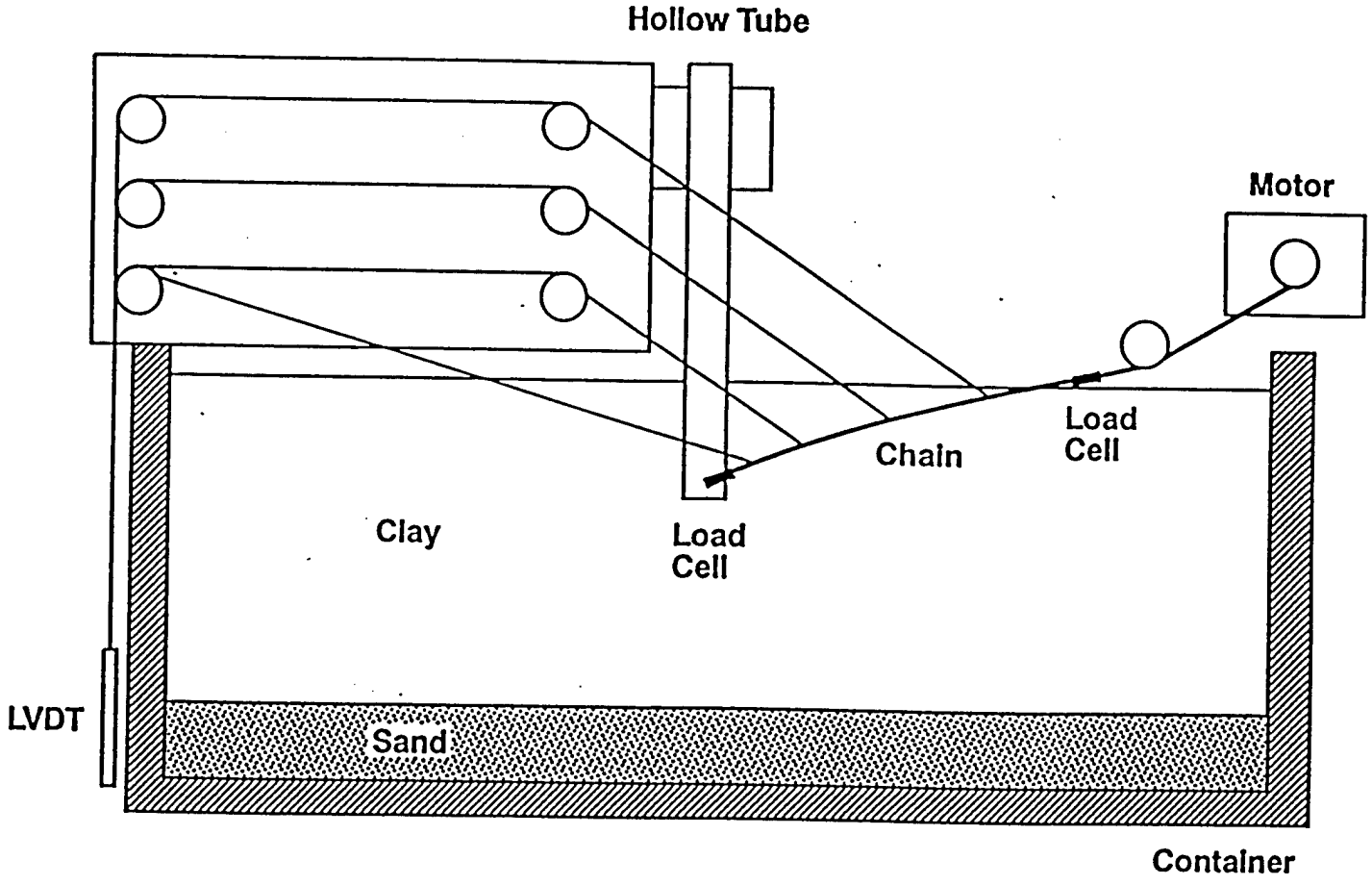

Figure - 1 Centrifuge Test Layout

3. PROCEDURES

The details of the centrifuge test results are not available, other than the technical report and photos provided by the University of Colorado, Boulder, who was contracted to conduct the tests. The dimension of the chasing wire and the locations where they were attached to the mooring cables as well as the axial force measurements are not available. With the lack of this critical information, only indirect deduction of data can be made from the reports and therefore used in this study.

Following describes the steps how the necessary data have been deduced and the validation with the analytical solution have been made.

(1) The distances from the fixed end of the mooring cable to each of the four points where the chasing wires were attached were obtained from the mooring cable deployment profile.

(2) The point of the mooring cable fixed end was back-calculated with the above information and the photograph of the final mooring cable geometry at the end of the deployment. The photograph was also used to identify the inclinations of the four chasing wires.

(3) The orientation angles of the mooring cable at the connection points with the chasing wires toward the fixed end point were measured from the final mooring cable profile at the end of the deployment. The distances along the mooring cable from the fixed end to each of the four connection points with the chasing wires were also identified.

(4) This information was then used to calculate the mooring cable configuration and axial forces with the modified analytical solution that considered the inclusion of chasing wires.

The details of these steps are described in the following sections.

3.1. Distance to Chasing Wires

Figure - 2 shows the profiles of the mooring cable of the series 1 test at various stages during deployment. It is evident from the figure that there exist points where the curvatures of the mooring cable suddenly change, indicating that those are the locations where the chasing wires were attached. The mooring cable profile that shows the most obvious changes in geometry is the one measured at 150 seconds after the test began. This profile was therefore used to pinpoint the locations where the chasing wires were attached to the mooring cable as shown in Table - 1.

Point	Length from fixed end(inches)
B	1.845
C	4.244
D	7.232
E	10.185

Table -1 Chasing Wire Distance from Fixed End
Note: Point B is the location of the first chasing wire from the fixed end. Points C through E are locations of successive chasing wires away from the point B.

3.2. Inclination of Chasing Wires and Location of Fixed End

As part of the input data, the inclination angles of the chasing wires at the point of attachment to the mooring cable were necessary. There was no information available in the report with regard to the chasing wire inclination angles. Only piece of information that indicate the geometries of the chasing wires at the end of deployment is from a still photograph (Figure - 3). The photograph however does not clearly show the position of the mooring cable fixed end.

To locate the mooring cable fixed end, an indirect extrapolation was used. First, the

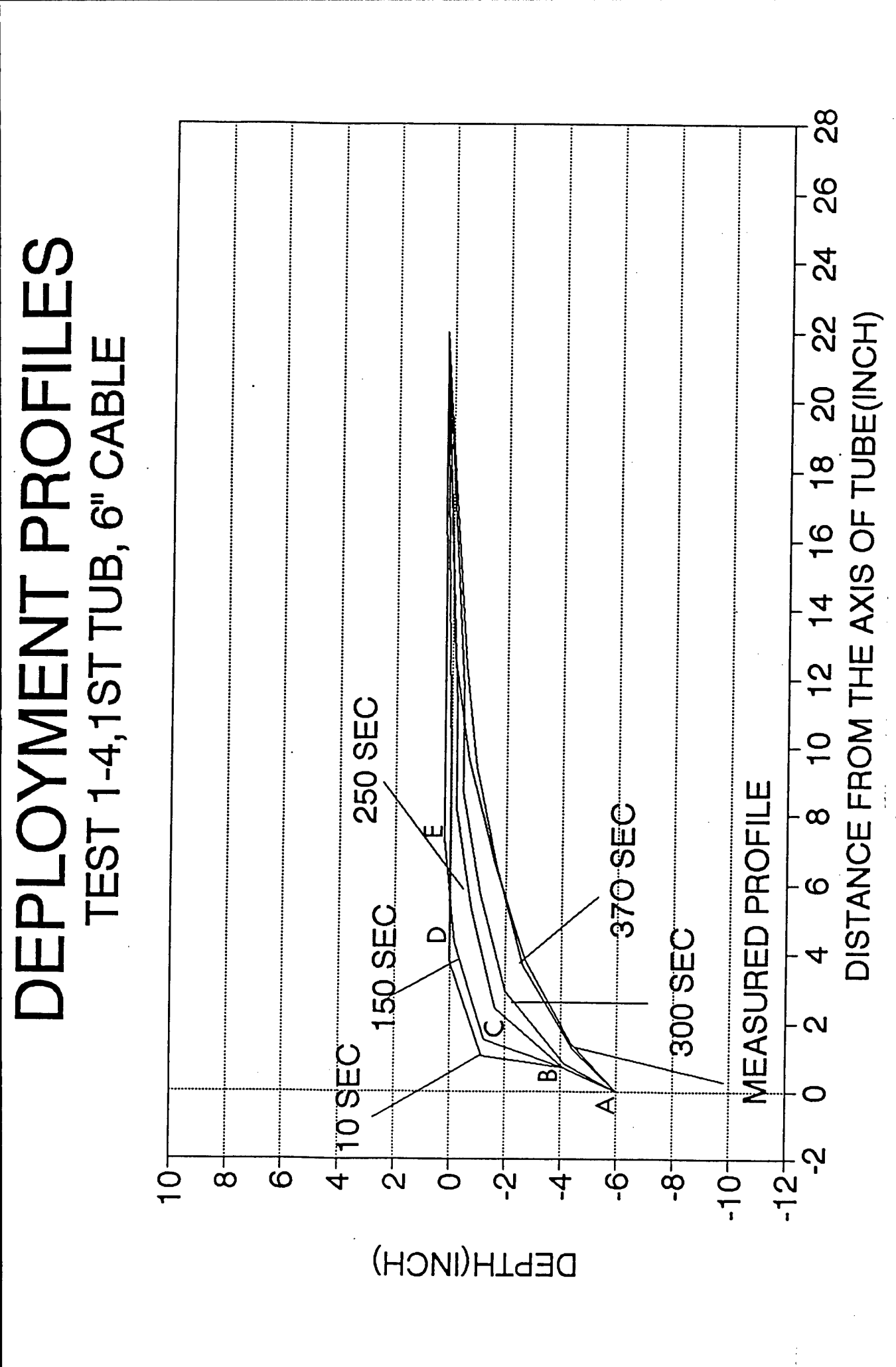

Figure - 2 Deployment Profiles

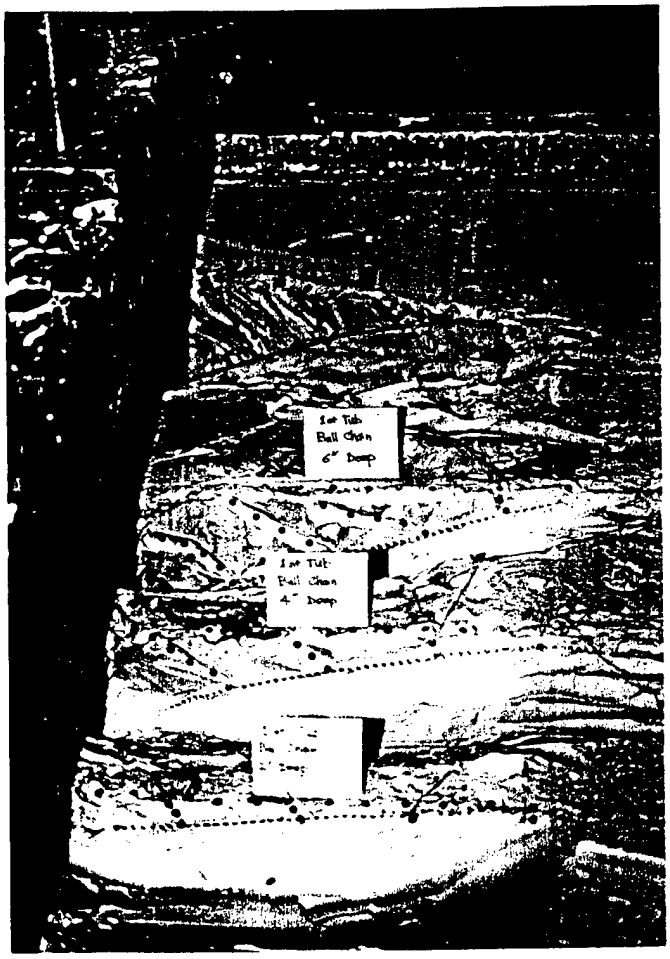

Figure - 3 Photograph of Test Series 1

distance from the fixed end (point A) to the first chasing wire (point B) was identified from the mooring cable deployment profile (Figure - 2), i.e., 1.845 inches. This distance was measured backward from the position of the first chasing wire on the photograph to locate the mooring cable fixed end. Exactly same steps were repeated to locate the mooring cable fixed ends with measured ditances from the point A to points C, D, and E. Because of potential errors in measurement, scaling, etc., the mooring cable fixed ends from these four extrapolations did not end up with a single location. The final location of the mooring cable fixed end was then taken as the average of the four locations. Figure - 4 is a duplicate of the mooring cable part of the photograph (Test 1 - 4) to indicate the positions of the mooring cable fixed end, the chasing wire attachment points to the mooring cable, the ground surface, and the vertical line from the fixed end to the ground surface. From this figure, the inclination angles of the chasing wires at the point of attachment were calculated.

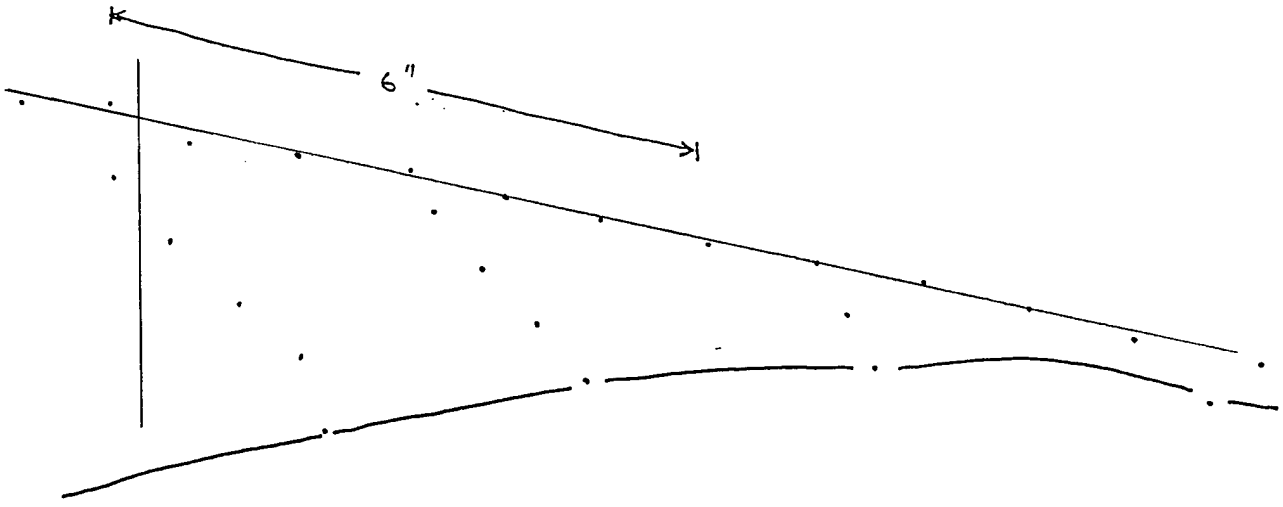

Figure - 4 Mooring Line at Final Deployment

Assuming that the tracing wires remained taut during and at the end of the deployment due to its very thin diameter, the orientations of the tracing wires could be estimated by connecting the points of the attachment and the points within the straight line portion. Figure - 5 shows the coordinates of these points used to calculate the chasing wire inclination angles as shown below. Note that θ_{CB} indicates the chasing wire inclination angle at point B to the horizontal.

$\theta_{CB}=\tan^{-1}(\frac{4.6813-1.978}{1.8375-0.2438})=59.48^0$(=1.0381 radian)

$\theta_{CC}= 57.71^0$(= 1.0072 radian)

$\theta_{CD}= 72.46^0$(=1.2647 radian)

$\theta_{CE}= 42.3^0$(=0.7383 radian)

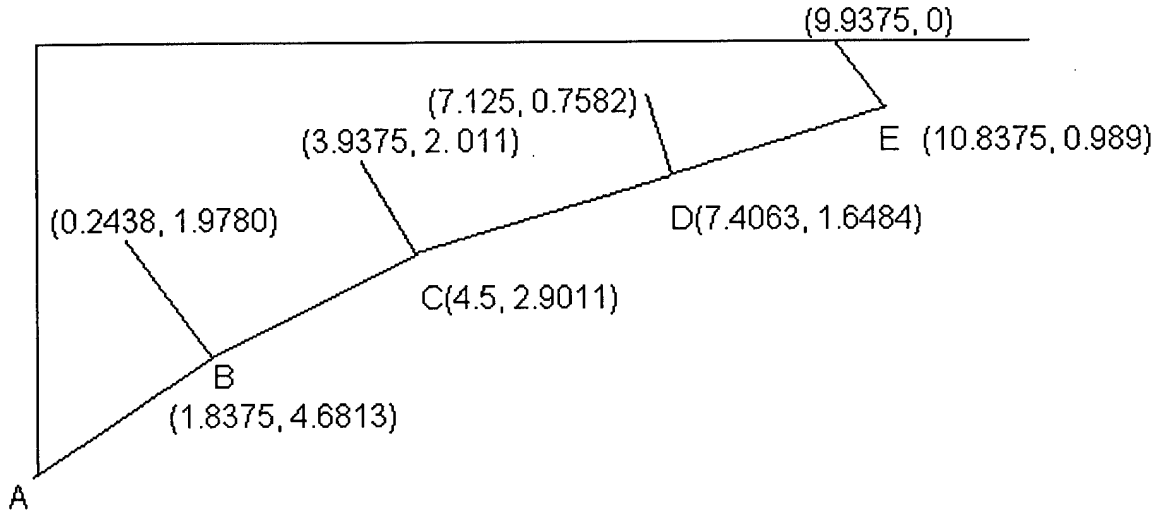

Note: numbers are in inches

Figure - 5 Horizontal and Vertical Lengths of Model Mooring Cable

3.3. Inclination Angles of Mooring Cable

The inclination angles of the mooring cable change suddenly at the points of chasing wire attachment due to the influence of the chasing wires. In order to complete the analysis, at least one inclination angle of the mooring cable at the point of chasing wire attachment needs to be known, since the chasing wire force measurements are not available. Section 3.4. provides the detailed explanation.

The mooring line inclination angles after they were affected by the tracing wires were measured from the final mooring cable deployment profile. Since the mooring cable analysis starts from the ground surface and propagates toward the fixed end through recursion formulas, the mooring line inclination angles at the chasing wire attachment points toward the fixed end (θ_2) were measured from the horizontal by locating the chasing wire attachment points as shown in Figure - 6. The measured inclination angles are indicated below. Note that θ_{2B} indicates the mooring cable inclination angle on the fixed - end side at point B.

$\theta_{2B} = 52^0$

$\theta_{2C} = 32^0$

$\theta_{2D} = 23^0$

$\theta_{2E} = 20^0$

3.4. Mooring Cable Analysis with Tracing Wires

Since the tracing wires affect the geometry and force development of the mooring cable, the effect of the tracing wires must be considered. Equilibrium of forces at the point of mooring cable - chasing wire attachment was therefore considered.

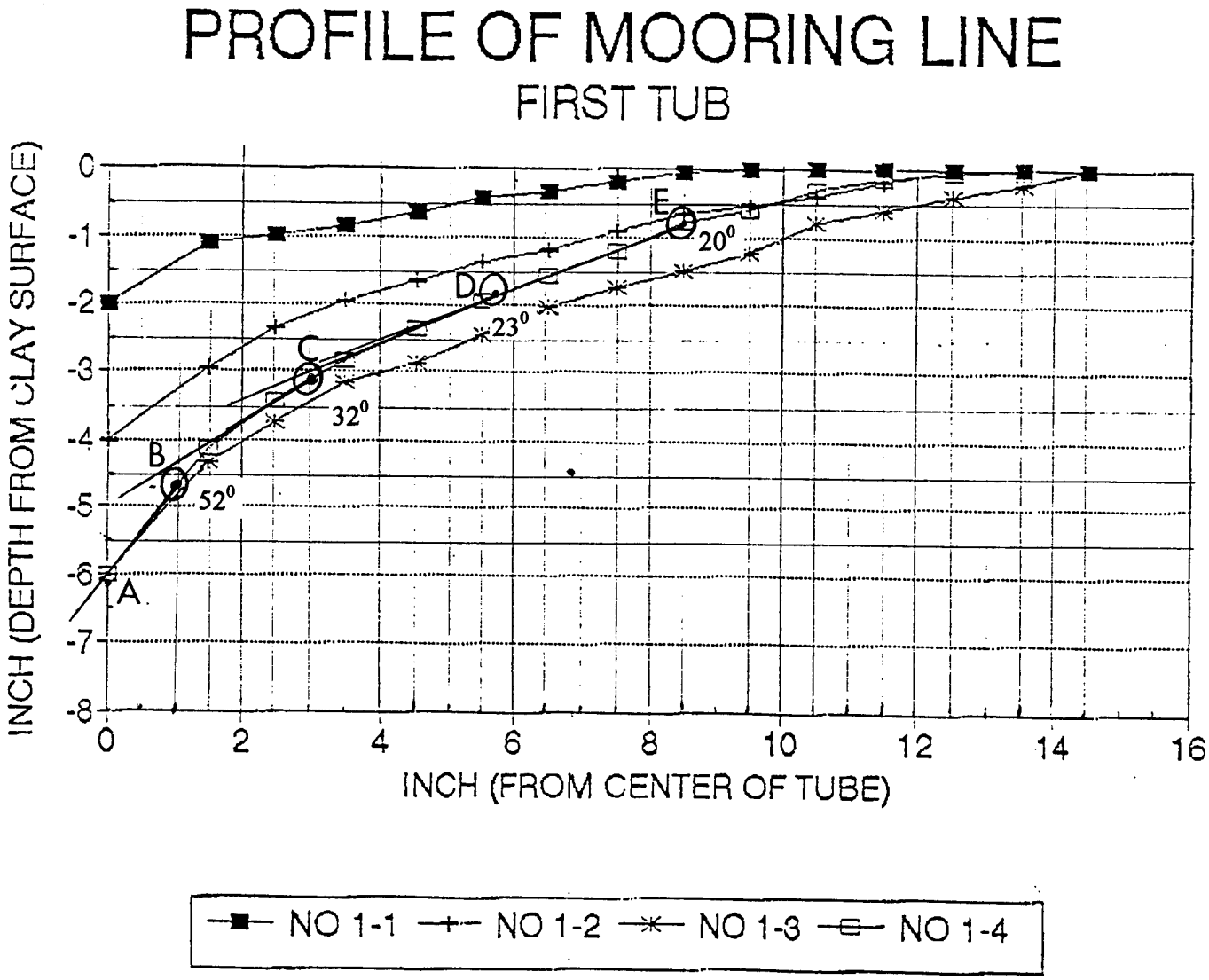

Figure - 6 Mooring Cable Inclination Angles at Point of Chasing Wires

Figure - 7 shows the schematic diagram indicating the directions and magnitudes of forces acting at the attachment point. From the equilibrium of forces along the horizontal and vertical directions, the following equations are obtained.

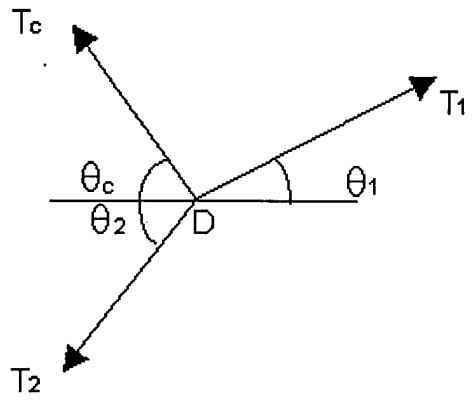

θ_1 = inclination of mooring cable before influenced by chasing wire

θ_C = inclination of chasing wire

θ_2 = inclination of mooring cable after influenced by chasing wire

T_1 = mooring cable force before influenced by chasing wire

T_2 = mooring cable force after influenced by chasing wire

T_C = force in chasing wire

Figure - 7 Definition of Angles and Forces

$$T_2*\cos\theta_2 + T_c*\cos\theta_c = T_1*\cos\theta_1 \quad (1)$$

$$T_c*\sin\theta_c + T_1*\sin\theta_1 = T_2*\sin\theta_2 \quad (2)$$

From Eq. (1),

$$Tc = \frac{T1 * \cos\theta 1 - T1 * \cos\theta 2}{\cos\theta c} \tag{3}$$

Substitution of Eq. (3) into Eq. (2) leads,

$$T_2 = T_c \frac{\sin\theta_c}{\sin\theta_2} + T_1 \frac{\sin\theta_1}{\sin\theta_2}$$

$$= T_1 \frac{\cos\theta_1 * \sin\theta_c}{\cos\theta_c * \sin\theta_2} - T_2 \frac{\cos\theta_2 * \sin\theta_c}{\cos\theta_c * \sin\theta_2} + T_1 \frac{\sin\theta_1}{\sin\theta_2} \qquad (T_c * \sin\theta_c + T_1 * \sin\theta_1 = T_2 * \sin\theta_2)$$

$$= T_1 \frac{\sin(\theta_1 * \theta_c)}{\cos\theta_c * \sin\theta_2} - T_2 \frac{\tan\theta_c}{\tan\theta_2} \tag{4}$$

Finally, T_2 can be expressed as a function of T_1, θ_1, θ_2 and θ_C.

$$T_2 = T_1 \frac{\sin(\theta_1 * \theta_c)}{\cos\theta_c * \sin\theta_2} * \frac{\tan\theta_2}{\tan\theta_2 + \tan\theta_c} \tag{5}$$

The analytical solution of the mooring line analysis was specifically modified to incorporate the effects of chasing wires. The solution method calculates the geometry and axial force of the mooring line from the ground surface toward the fixed end using recursion formulas based on the force and moment equilibrium conditions. Please refer to reference (2) for the datails of the analytical solution.

The modification of the solution method is at the end of the mooring line element where the chasing wire is attached. Without the chasing wire, the calculated orientation angle and the axial force at the end of the previous element become those at the beginning of the new element

due to the compatibility requirements. However, when the chasing wire is attached, the orientation angle and the axial force at the beginning of the current element are altered. Because of the available equilibrium conditions, only two unknowns can be calculated. With known measured information described previously, the axial forces of the chasing wire and the mooring cable of the new element could be calculated. The procedure continues with or without the chasing wires until the fixed end is reached.

4. RESULTS

The following input data were used for the mooring cable validation study. Please note that the numbers inside the parenthesis indicate the prototype values, considering the acceleration level used in the centrifuge testing.

Mooring cable diameter = 3/16 inches (15 inches)

Mooring cable tension = 52 lbs (332,800 lbs)

Depth to fixed end = 6 inches (40 ft.)

Distance from fixed end to chasing wire attachment

: point B = 1.845 inches (12.3 ft.)
: point C = 4.244 inches (28.293 ft.)
: point D = 7.232 inches (48.213 ft.)
: point E = 10.185 inches (67.9 ft.)

Water depth = 0 (0)

Horizontal distance from fixed end to load application = 13.5 inches (90 ft.)

Soil undrained shear strength = 65 psf from 0 ~ 1.5 inches (0 ~ 10 ft.)

43 psf/in. from 1.5 inches (6.5 psf/ft.)

To validate the analytical solution, the effects of the following parameters have been studied; the bearing capacity factor (N_{cw}) and the diameter conversion factor (α_w). Note that the effect of the cable slide area factor (β_w) was not studied. Instead the value of β_w remained as 1.0. This was because the tangential force developed at the bottom side of the mooring line is influenced by the product of α_w and β_w and no attempt was made to separate the effects of these two parameters during the model test.

4.1. Effect of N_{cw} on Mooring Cable Geometry

Figure - 8 shows the effect of N_{cw} on the mooring cable geometry. Note that the value of α_w is 1.0 for all values of N_{cw}. It indicates that the effect of N_{cw} is relatively insignificant for the magnitudes considered ($N_{cw} = 7 \sim 13$). Values of N_{cw} between 7 and 9 provide very good comparsions with the experimental measurement. As the value of N_{cw} increases, the mooring cable profile tends to shift upward.

4.2. Effect of α_w on Mooring Cable Geometry

Figure - 9 shows the effect of α_w on the mooring cable geometry with N_{cw} of 9. The results indicate that the influence of α_w is virtually non-existing except near the ground surface when the value of α_w varies from 0.5 to 3.2.

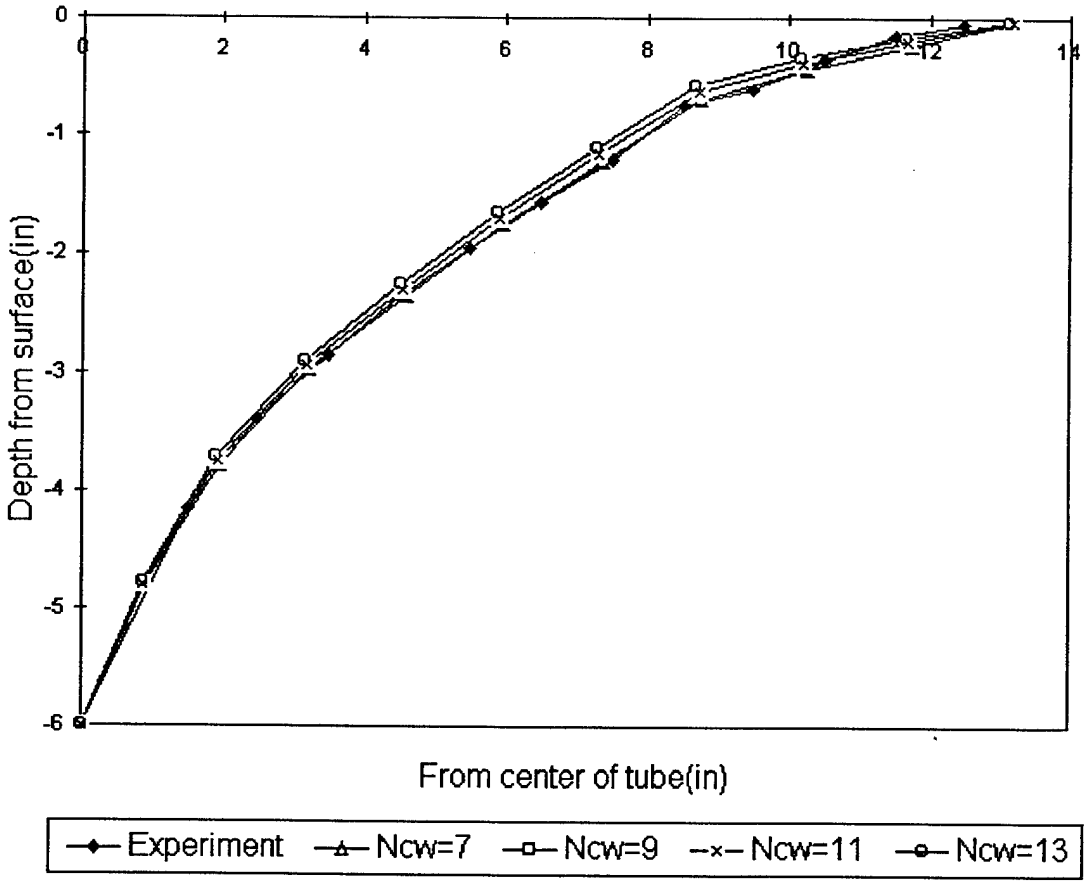

Figure - 8 Mooring Line Geometry with Various Values of N_{cw}

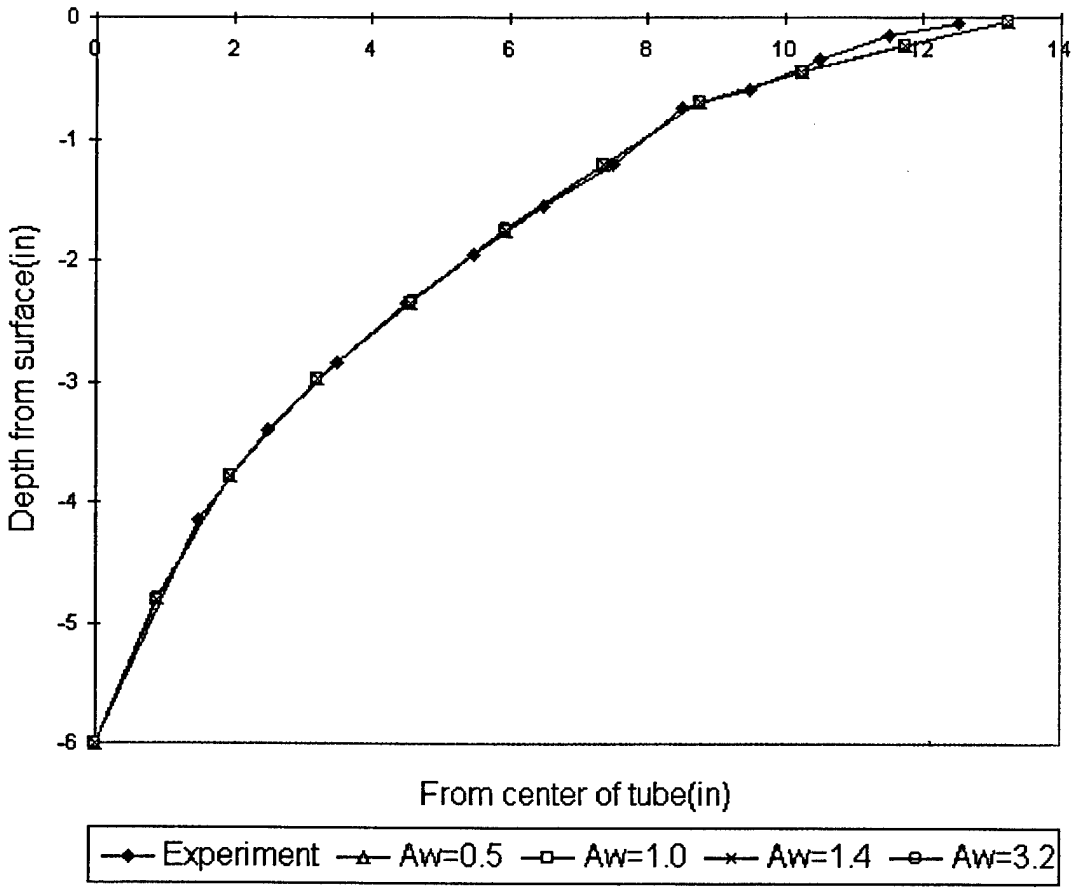

Figure - 9 Mooring Line Geometry with Various Values of α_w

4.3. Mooring Cable Axial Force

Figure - 10 shows the changes in mooring cable forces at the ground surface and at the fixed end as a function of α_w. Figure - 11 shows a similar variation of the mooring line force at the fixed end as a function of N_{cw}. Note that all predictions overestimate the measured mooring cable force at the fixed end of 263,040 lbs.

4.4. Discussion

Results indicate that the mooring cable geometry as influenced by the chasing wires can be estimated very accurately with the modified formulation using the values of $N_{cw} = 7 \sim 9$ and $\alpha_w = 0.5 \sim 3.2$. However, the measured mooring cable force at the fixed end is significantly influenced by the values of N_{cw} and α_w. The measured mooring cable force at the fixed end could be obtained if the values of α_w of 3.2 and N_{cw} of 9 are used. This seems relatively high, since α_w describes the ratio between the soil adhesion and cohesion. When α_w of 1.0 is used, the mooring cable force at the fixed end is calculated to be 294,624.3 lbs, resulting in ratios of $T_{\text{fixed end}} / T_{\text{surface}} = \frac{294624.3}{332847.6} = 0.885$, and $T_{\text{fixed end calculated}} / T_{\text{fixed end measured}} = \frac{294624.3}{263040} = 1.12$

The results included in this study are based on approximations, interpolation, and extrapolations of limited data available. Accurate comparisons were not possible because of the lack of measurement records on the chasing wires.

It is noted that the results from the second series centrifuge test on mooring cable could not be used in this verification study, since the deployment profile of the mooring cable was not measured during the test due to the malfunction in LVDT's.

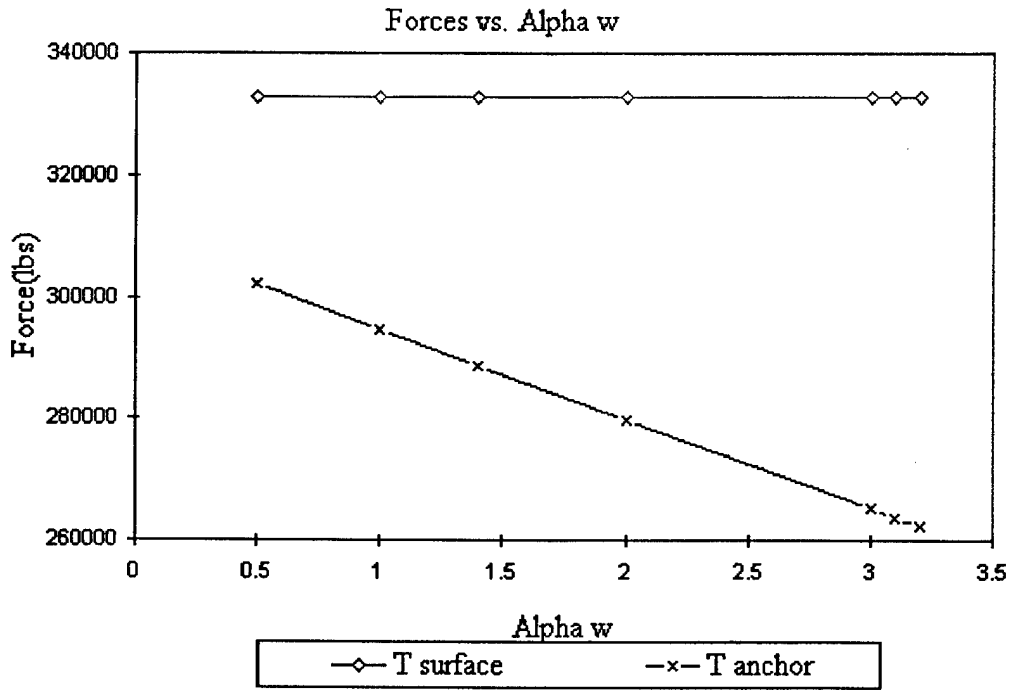

Figure - 10 Mooring Cable Force Variation with α_w

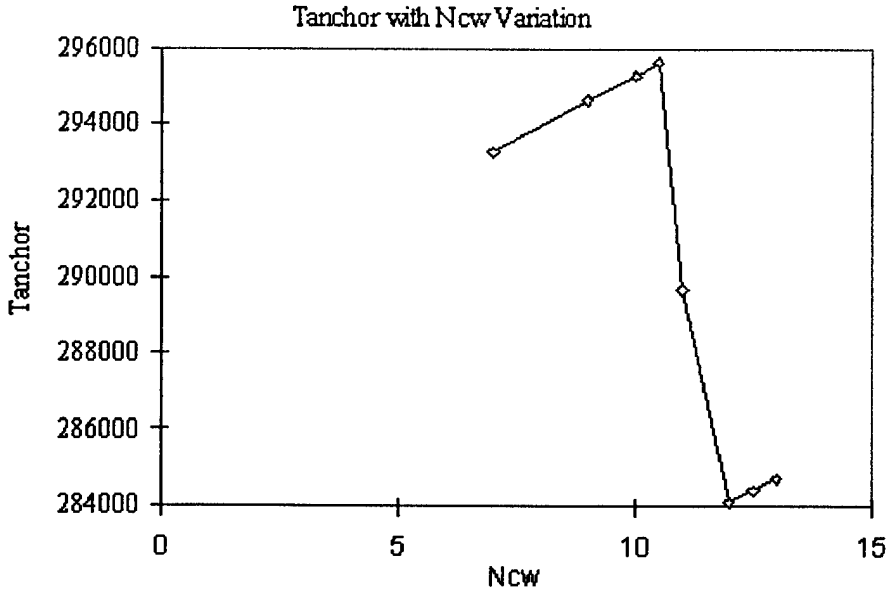

Figure - 11 Mooring Cable Force Variation at Fixed End with N_{cw}

5. REFERENCES

1. Law, H. K., et. al., "Centrifuge Testing for Dynamic Anchor Line Modeling," A Report submitted to Naval Facilities Engineering Service Center, Univ. of Colorado, Boulder, Oct., 1994.

2. Bang, S., "Anchor Mooring Line Computer Program User Manual," Contract Report CR - 6020 - OCN, Naval Facilities Engineering Service Center, June, 1996.

3. Bang, S., R. J. Taylor, Y. Jie, and H. T. Kim, "Analysis of Anchor Mooring Line in Cohesive Seafloor," Transportation Research Record, No. 1526, 1996.

REPORT DOCUMENTATION PAGE

Form Approved
OMB No. 0704-0188

1. AGENCY USE ONLY *(Leave blank)*	2. REPORT DATE	3. REPORT TYPE AND DATES COVERED
	11 June 1998	Annual Report, 1 June 97 - 31 May 98

4. TITLE AND SUBTITLE

Use of Suction Piles for Mooring of Mobile Offshore Bases

5. FUNDING NUMBERS

Grant
N00014-97-1-0887

6. AUTHOR(S)

Sangchul Bang

7. PERFORMING ORGANIZATION NAMES(S) AND ADDRESS(ES)

South Dakota School of Mines and Technology
501 E. St. Joseph St.
Rapid City, SD 57701

8. PERFORMING ORGANIZATION REPORT NUMBER

9. SPONSORING / MONITORING AGENCY NAMES(S) AND ADDRESS(ES)

Office of Naval Research
800 North Quincy St.
Arlington, VA 22217-5660

10. SPONSORING / MONITORING AGENCY REPORT NUMBER

11. SUPPLEMENTARY NOTES

a. DISTRIBUTION / AVAILABILITY STATEMENT

APPROVED FOR PUBLIC RELEASE

12. DISTRIBUTION CODE

13. ABSTRACT *(Maximum 200 words)*

The research includes a feasibility study to determine the practicality, efficiency, and applicability of the suction piles for their use as part of the mooring system in deep water. It examines the effects of various pertinent geometric and material parameters of suction piles through analytical and experimental studies. Laboratory experiments on small scale model suction piles have been conducted to provide technical data that are essential in evaluating the relative performance of suction piles under various conditions and providing means of verifying the analytical solution methods.

14. SUBJECT TERMS

Suction pile, deep water mooring, critical suction pressure, mooring line, experimental model testing

15. NUMBER OF PAGES

263

16. PRICE CODE

17. SECURITY CLASSIFICATION OF REPORT	18. SECURITY CLASSIFICATION OF THIS PAGE	19. SECURITY CLASSIFICATION OF ABSTRACT	20. LIMITATION OF ABSTRACT
			UL